

**GEOLOGICAL AND PRECIOUS METAL EVOLUTION AT  
FREEGOLD MOUNTAIN, DAWSON RANGE, YUKON**

GEOLOGICAL AND PRECIOUS METAL EVOLUTION AT  
FREEGOLD MOUNTAIN, DAWSON RANGE, YUKON

By

BRENT IAN ALEXANDER McINNES, B.Sc (Hons.)  
(Geology, McMaster University)

A Thesis

Submitted to the School of Graduate Studies  
in Partial Fulfilment of the Requirements  
for the Degree  
Master of Science

McMaster University

October, 1987

Master of Science (1987)  
(Geology)

McMaster University  
Hamilton, Ontario

Title: Geological and Precious Metal Evolution at  
Freegold Mountain, Dawson Range, Yukon

Author: Brent Ian Alexander McInnes, B.Sc. (Hons.)  
(Geology, McMaster University)

Supervisor: Dr. James H. Crocket

Number of Pages: xiii, 230

## Abstract

Freegold Mountain is part of a northwesterly trending volcanoplutonic arc comprising the eastern portion of the Yukon Crystalline Terrane. Plutonic rocks in the area intrude Paleozoic metasediments and consist of a Late Triassic to Early Cretaceous granodiorite intruded by the Big Creek Syenite dated at  $138 \pm 10$  Ma. A suite of K-rich intrusive volcanic rocks comprise an early period of basalt-andesite-dacite volcanism and a later rhyolitic volcanism dated at  $78 \pm 6$  Ma. Volcanic rocks at Freegold Mountain can be correlated with Mt. Nansen Volcanics.

Two sets of fracture planes, oriented at 165/70E and 18/80W, show dextral and sinistral displacement, respectively. Rhyolite dykes and gold-quartz veins predominantly oriented NNE have been emplaced along the 18/80W extensional fracture systems. These fractures may be modelled as high-angle Reidel shears, although evidence indicates that fracture orientations and fault movement have been complicated by changing stress fields from middle Cretaceous to Tertiary time.

The gold-bearing quartz veins at Freegold Mountain are high grade, low-tonnage deposits with grades ranging from 0.4 to 1.0 oz/t. Fluid inclusions from the lower portions of the Laforma mine homogenize at 185° C with salinity ranging between 2 and 4.5 wt. % NaCl equivalent. A boiling zone has been detected above the deeper ore where fluid

inclusions show extreme ranges in homogenization temperatures (165-430° C) and salinity (4 - 43 wt. % NaCl). Fluid inclusion waters have stable isotopic signatures indicative of meteoric water with  $\delta D = -138$  and  $\delta^{18}O = -18.4$ . Boiling of the Laforma fluid has caused a shift towards heavier hydrogen and oxygen isotopic values, mineral deposition and appears to enhance gold precipitation over non-boiling zones. Stable isotopic evidence indicates that the paleolatitude of Freegold Mountain during late Cretaceous time was south of the present day Yukon-B.C. border.

The Emmons Hill (Dart) prospect is a gold-bearing vein-breccia with a mineral assemblages of barite, stibnite, marcasite, cinnabar, orpiment, Fe and Mn carbonates and chalcedonic silica. Fluid inclusions from these deposits homogenize between 140-185° with salinities of 0-0.5 wt. % NaCl. This property shows marked similarities to acid-sulphate type precious metal deposits in New Zealand and western United States.

Large (x to xx Mt) northwesterly trending diatremes appear to be structurally controlled by small transcurrent faults parallel to and coeval with displacement along the Tintina fault. The Antoniuk diatreme (3.7 Mt @ 1.14 g/t Au) consists of heterolithic and monolithic breccias intruded by dacite and rhyolite dykes. Diamond drilling indicates that a large body of fine to medium grained alaskite is present beneath the auriferous breccia. The deposit formed by the

explosive escape of volatile components evolved from the retrograde boiling of a silicic magma chamber. Gold mineralization in the breccia is associated with pyrite and arsenopyrite formed at temperatures around 300°C and salinities of about 4.5 wt. % NaCl.

## Acknowledgements

Working in the Dawson Range would be an impossible undertaking without the co-operation and help of many individuals and corporations. Logistic and technical support was provided by Archer, Cathro and Associates Ltd., and I would particularly like to thank geologists Bob Cathro, Sandy Main, Jessie Duke and Kevin Capenhurst for their advice and discussions. A debt of thanks is due Ron Granger and family for their hospitality and guidance in familiarizing me with every aspect of the field area. Access to the Dart claims (Emmons Hill) was permitted by Noranda Min. Corp., and company files covering the property were provided by Wayne Reid and Craig Hart. Jim Morin of the Department of Indian and Northern Development provided access to Laforma files.

Samples for radiometric dating were prepared by Katrina Jager and Mike Franklyn, and analysed by Dave Jones using the facilities of Dr. R.H. McNutt, McMaster University. I am grateful to Steve Prevec for aid in data interpretation.

Special thanks to Fereydoun Ghazban for helping to set up the crushing line for hydrogen isotopic analysis, and for analyzing the quartz for oxygen isotopes. Caroline Leblanc and Martin Knyf performed the calcite isotopic analyses using the facilities of Dr. H.P. Schwarcz, McMaster University. Hydrogen isotope analyses were performed by Dr. R.H. Krouse, University of Calgary.

Black and white photos were prepared by Jack Wharwood

and thin sections by Len Zwicker.

This project was initiated and partially funded by Dr. Wayne Goodfellow, Mineral Resources Division, Geological Survey of Canada. I wish to sincerely thank him for his ongoing support, encouragement, and enthusiasm for the project.

Dr. Jim Crocket has allowed me latitude and diversity in tackling the geological problems at Freegold Mountain, and provided unencumbering supervision. Partial funding for this project was supplied from an NSERC grant, awarded Dr. Crocket.

Finally, words cannot describe my appreciation to my wife, Noreen, who carefully drafted the diagrams and whose patience and sacrifice was unmatched during the preparation of the thesis.

## Table of Contents

	PAGE
Abstract .....	iii
Acknowledgements .....	vi
List of Figures .....	xi
List of Tables .....	xii
List of Photos .....	xiii
<b>PART A: GEOLOGY AND GEOCHEMISTRY OF FREEGOLD MOUNTAIN</b> .....	<b>1</b>
<b>Chapter 1: Introduction</b> .....	<b>1</b>
1.1 Location .....	3
1.2 History .....	3
1.3 Methodology .....	8
1.3.1 Field studies .....	8
1.3.2 Laboratory studies .....	10
1.4 Thesis .....	11
<b>Chapter 2: Regional Geology</b> .....	<b>13</b>
2.1 A review of Cordilleran evolution ....	13
2.1.1 Proterozoic to Cretaceous evolution .	15
2.1.2 Cretaceous to Present evolution ....	16
<b>Chapter 3: Geology of the thesis area</b> .....	<b>19</b>
3.1 Regional geology .....	19
3.2 Local geology .....	20
3.2.1 Introduction .....	20
3.3 Thesis map .....	23
3.3.1 Rock types .....	23
3.3.2 Lithologies of Freegold Mountain ...	25
<b>Chapter 4: Rock geochemistry and chemical classification</b> .....	<b>39</b>
4.1 Methodology .....	39
4.2 Results of major and trace element analysis .....	44
4.2.1 Classification of rock types .....	44
4.2.1.1 Plutonic rocks .....	44
4.2.1.2 Volcanic rocks .....	45
4.2.2 Rare earth element data and petrogenesis .....	50
4.2.2.1 Granodiorite .....	50
4.2.2.2 Syenite .....	51
4.2.2.3 Basalt-Andesite-Dacites .....	54
4.2.2.4 Rhyolites .....	57

	PAGE
Chapter 5: Geochronology .....	60
5.1 Introduction .....	60
5.1.1 Metasedimentary rocks .....	60
5.1.2 Syenite and granodiorite plutons ...	61
5.2 Rb-Sr dating of the syenite porphyry .	65
5.2.1 Methodology .....	66
5.2.2 Analytical results .....	68
5.2.3 Discussion of Rb-Sr dating results .	73
5.3 Andesites, dacites and rhyolites .....	75
 Chapter 6: Structural geology .....	 80
6.1 Introduction .....	80
6.2 Regional structures and their implications on the structure of Freegold Mountain .....	  84
6.3 Structural deformation in the thesis area .....	 85
6.4 Interpretation of structural deformation in the thesis area .....	 89
 PART B. GEOLOGY AND GEOCHEMISTRY OF PRECIOUS METAL DEPOSITS .....	  95
 Chapter 7: Geology of precious metal deposits .	 95
7.1 Laforma Mine .....	95
7.1.1 Mineralogy .....	101
7.2 Antoniuk Deposit .....	108
7.2.1 Geology .....	108
7.2.2 Genetic implications of breccia formation .....	 120
7.2.3 Mineralogy .....	123
7.3 Emmons Hill .....	126
 Chapter 8: Fluid inclusion study .....	 136
8.1 Method of study .....	140
8.2 Fluid inclusion studies of ore deposits and quartz veins at Freegold Mountain .....	  144
8.2.1 Laforma Mine .....	146
8.2.1.1 TU 10-271 .....	146
8.2.1.2 TU 6-248 .....	150
8.2.1.3 4th level .....	152
8.2.1.4 2nd level and surface exposures of the Laforma vein .....	 164
8.2.2 Antoniuk Deposit .....	165
8.2.3 Emmons Hill .....	172
8.2.4 Barren quartz veins .....	176
 Chapter 9: Stable isotope studies .....	 179
9.1 Introduction .....	179
9.2 Analytical methods .....	180

	PAGE
9.2.1 Hydrogen .....	180
9.2.2 Oxygen and Carbon .....	181
9.2.3 Sulfur .....	182
9.2.4 Analytical standards .....	182
9.3 Laforma Mine .....	182
9.3.1 Hydrogen and oxygen isotope results .	182
9.3.2 The effects of boiling on isotopic ratios .....	189
9.3.3 The effect of boiling on gold deposition .....	191
9.3.4 Carbon isotope results .....	193
9.3.5 Sulfur isotope results .....	193
9.4 Antoniuk Breccia .....	194
9.4.1 Sulphur isotopes .....	194
9.5 Emmons Hill .....	195
9.5.1 Oxygen and Hydrogen results .....	195
9.6 Metal inventory - considering the genesis of gold deposits at Freegold Mountain .....	195
 Chapter 10: Conclusions and summary .....	 199
 References cited .....	 203
 Appendix A: Geochemical data .....	 215
 Appendix B: Structural data .....	 220
 Appendix C: Fluid inclusion data .....	 223

List of Figures

FIGURE	PAGE
1. Location Map .....	4
2. Location of gold occurrences at Freegold Mountain .....	7
3. Geological subdivision of the Canadian Cordillera .....	14
4. Geology (1: 250,000) of southeastern Dawson Range .....	21
5. Geology (1: 5,000) of southeastern Freegold Mountain .....	24
6. (a) Binary alkali - silica discrimination diagram	
(b) Ternary AFM discrimination plot .....	46
7. Binary K <sub>2</sub> O - silica discrimination diagram for volcanic rocks .....	49
8. Chondrite normalized REE pattern for plutonic rocks .....	52
9. Chondrite normalized REE pattern for volcanic rocks .....	56
10. Sample locations for Rb-Sr and K-Ar geochronology .....	67
11. Rb-Sr isochron diagram for Big Creek Syenite .	72
12. Pole to fracture plot of fracture planes .....	86
13. Rose diagrams of dyke orientations .....	88
14. Reidel fracture orientations and observed fracture orientations at Freegold Mountain ..	91
15. Cross section of Laforma Deposit .....	96
16. Ore shoot development along a non-linear fault zone .....	97
17. Plan sections of various levels of Laforma ...	99
18. Geology of the Antoniuk Breccia deposit .....	109
19. Cross-sections of Antoniuk Breccia deposit .. pocket	
20. Calibration curve for fluid inclusion stage ..	139
21. Typical freezing run for salinity determination	143
22. Typical heating run for homogenization temp ..	145
23. Histogram of homogenization temperatures for Laforma sample TU 10-271 .....	148
24. CO <sub>2</sub> -H <sub>2</sub> O inclusions .....	149
25. Histogram of homogenization temperatures for Laforma sample TU 6-248 .....	151
26. Fluid inclusions and minerals from boiling zone .....	153
27. Histogram of homogenization temperatures for fluid inclusions for the 4th level Laforma sample .....	155
28. Multiphase inclusions hosted within quartz from the Laforma 4th level boiling zone .....	157
29. Heating run for multiphase inclusion .....	160
30. Fluid inclusions from intergrown quartz-carbonate-pyrite within vugs in the Antoniuk Breccia gold deposit .....	166

Figure	Page
31. Homogenization temperatures for Antoniuk fluid inclusions .....	168
32. Homogenization temperature vs. salinity diagram for Antoniuk inclusions .....	170
33. Isotherm diagram for CO <sub>2</sub> -H <sub>2</sub> O system .....	171
34. Fluid inclusion and mineralogy of Emmons Hill	173
35. Homogenization temperatures and salinity histograms for Emmons Hill barite .....	175
36. Homogenization temperatures and salinity histograms for barren quartz sample .....	178
37. Stable isotopic signatures for ore fluids ..	186
38. Geologic reconstruction of Canadian Cordillera before strike-slip movement along Tintina fault .....	188

#### List of Tables

Table	Page
1. Detection limits for elements analysed by neutron activation .....	40
2. GSC laboratory duplicate results .....	42
3. Relative errors on major and trace elements ..	43
4. Rb-Sr data table for Big Creek Syenite .....	69
5. K-Ar data table for rhyolite dyke .....	78
6. Orientation and displacement of structures at Freegold Mountain .....	82
7. Temperature data for calibration substances used for McMaster heating-freezing stage ....	138
8. Isotopic composition of Laforma ore fluid ...	184
9. Isotopic composition of calcite at Laforma ...	191
10. Sulphur isotope data for the Laforma Mine ...	194
11. Sulphur isotope data for Antoniuk Breccia ...	194

#### List of Maps

Map	Page
1. Geology (1: 5,000) of southeastern Freegold Mountain .....	pocket
2. Cross-sections of Antoniuk Breccia deposit ..	pocket



## PART A. GEOLOGY AND GEOCHEMISTRY OF FREEGOLD MOUNTAIN

### CHAPTER 1. INTRODUCTION

During the past two decades our understanding of precious metal deposits, particularly in Cordilleran settings, has increased considerably due to the recognition that these deposits often show similarities to geothermally active areas such as North Island, New Zealand and Yellowstone National Park, Wyoming. The exploitation of these areas for power generation led to a detailed geological and geochemical study of the interaction between water and upper crustal rocks in areas of high heat flow. Geochemical analyses of these geothermal fluids and their deposits showed anomalous concentrations of Au, Ag, As, Sb, Hg and Tl (Weissberg, 1969), a suite of elements which also occur in precious metal deposits mined in southwest United States and Mexico. This occurrence of precious metals and a distinctive minor element suite combined with data on the geology, structure and chemistry of active hydrothermal systems led to the corroboration of White's (1955) postulation that epithermal Au-Ag vein deposits are actually fossil geotherms.

Although much attention has been paid to deposits in the United States, comparatively little research work has been conducted on precious metal areas in the Cordilleran regions of Canada, particularly in the Yukon. In 1985 the federal government of Canada and the territorial government of the Yukon signed a mineral development agreement to conduct large scale regional geochemical surveys in order to

Photo 1. A westward view of Freegold Mountain (centre) showing the typical rolling nature of the Dawson Range. Emmons Hill is just to the right and the Antoniuk Breccia to the left on the photo.



promote the growth of the mineral resource industry in the Yukon. A minor portion of the total expenditure was allocated to research projects whose purpose was to investigate the nature of mineral deposits in Yukon, particularly in those areas where precious metal deposits had been or were being developed. It is hoped that detailed research into the physical and chemical environments of precious metal deposition will permit a thorough understanding of the geological factors that were vital to the generation of such gold deposits and that this knowledge may be utilized in the search for new deposits. The area chosen for this project was Freegold Mountain, situated within the Dawson Range in southwest Yukon.

### 1.1 Location

Freegold Mountain is located at 137° 07' W and 62° 18' N on NTS mapsheet 115 I/6 (see figure 1). The area is accessible by a 65 km all-weather road from the town of Carmacks to the southeast. The condition of some of the trails in the area, particularly in wet weather, necessitates the utilization of a four wheel drive vehicle.

### 1.2 History

Tourism is now the major industry in the Yukon, but until recently and since its first significant discovery by George Carmack in the Klondike in 1895, gold mining has been the primary industry in the territory. Since its discovery

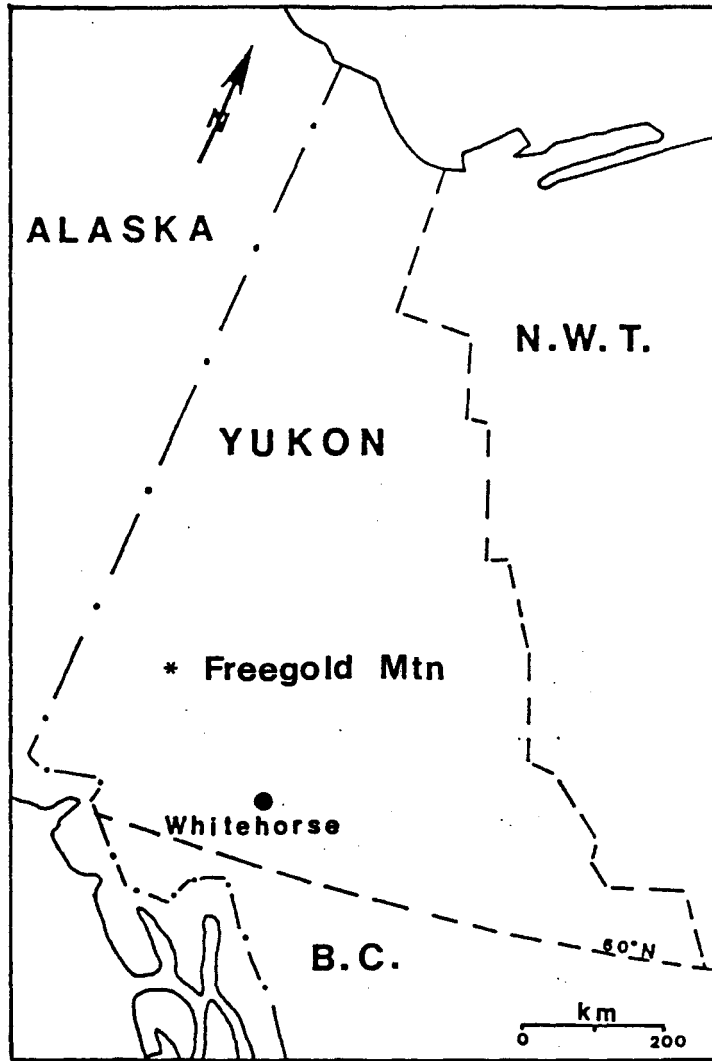


Figure 1. Location Map

the Klondike alone has produced over 12,000,000 ounces of placer gold<sup>1</sup>, a figure which is more often associated with Archean gold systems than with Phanerozoic systems.

Although the area has undergone considerable mining and prospecting activity, no lode source has been found to account for the large amount of gold mined. Mining activity decreased considerably in the early 1900's, and small mining companies and individual operations became unprofitable when the richer claims were mined out. Many sold out to big mining conglomerates that employed large floating dredges to scour the creek beds, and left the area either to return to their native homelands or to venture into the wilderness in search of other gold mines. Consequently some did, and it is this period of Yukon history that many of the lode gold occurrences were first discovered.

One of the areas that received much attention was the Mount Freegold and Mount Nansen area in the Dawson Range located in southwest Yukon, where placer gold had been discovered in 1911 on a small scale (Cairnes, 1914). The mining operations were not profitable and activity in the area was minimal until 1930 when P.F. Guder discovered a gold-bearing magnetite skarn on Freegold Mountain. This discovery led to a staking rush in the spring of 1931 (Johnston, 1937), where systematic prospecting on a few claims uncovered gold bearing quartz-sulphide veins on the

---

<sup>1</sup>. The exact amount of gold mined will never be known since many of the early miners reported lower than actual recoveries to avoid paying hefty taxes to the Canadian government.

1'southwest side of the mountain. Since then many different precious metal showings have been discovered on Freegold Mountain, and some are still being actively exploited for their precious metal potential.

This thesis incorporates detailed studies of three of eight known gold prospects on Freegold Mountain shown in Figure 2: the Laforma Mine, the Antoniuk Breccia and the Emmons Hill Barite-Stibnite occurrence. Of these, only the Laforma Mine has been mined extensively. Its production history includes a brief but successful period in 1939-40 when T.C. Richards mined under lease 1,437 ounces of gold from 1,414 tons of ore (average = 1.02 oz/ton) from the upper section of the vein. The owners of the mine refused to renew the agreement and the property remained dormant until 1960 when Ormsby Mines Limited purchased the property. In 1965-66, 1610 oz of Au and 570 oz of Ag were mined from the lower (4th) level of the mine by Discovery Mines Ltd. Since then, sporadic attempts to develop the Laforma property and other showings by diamond drilling and geochemical surveys have failed to produce further development on the property. Ore reserves calculated for the mine are 181, 000 tonnes with an average grade of 11.3 g/t Au over a 1.5 m mining width.

The Antoniuk breccia was discovered in 1975 by T. Antoniuk of Rayrock Mines Ltd. during diamond drilling of geochemical anomalies to the east of the Laforma vein. The potential of the property for gold mineralization was

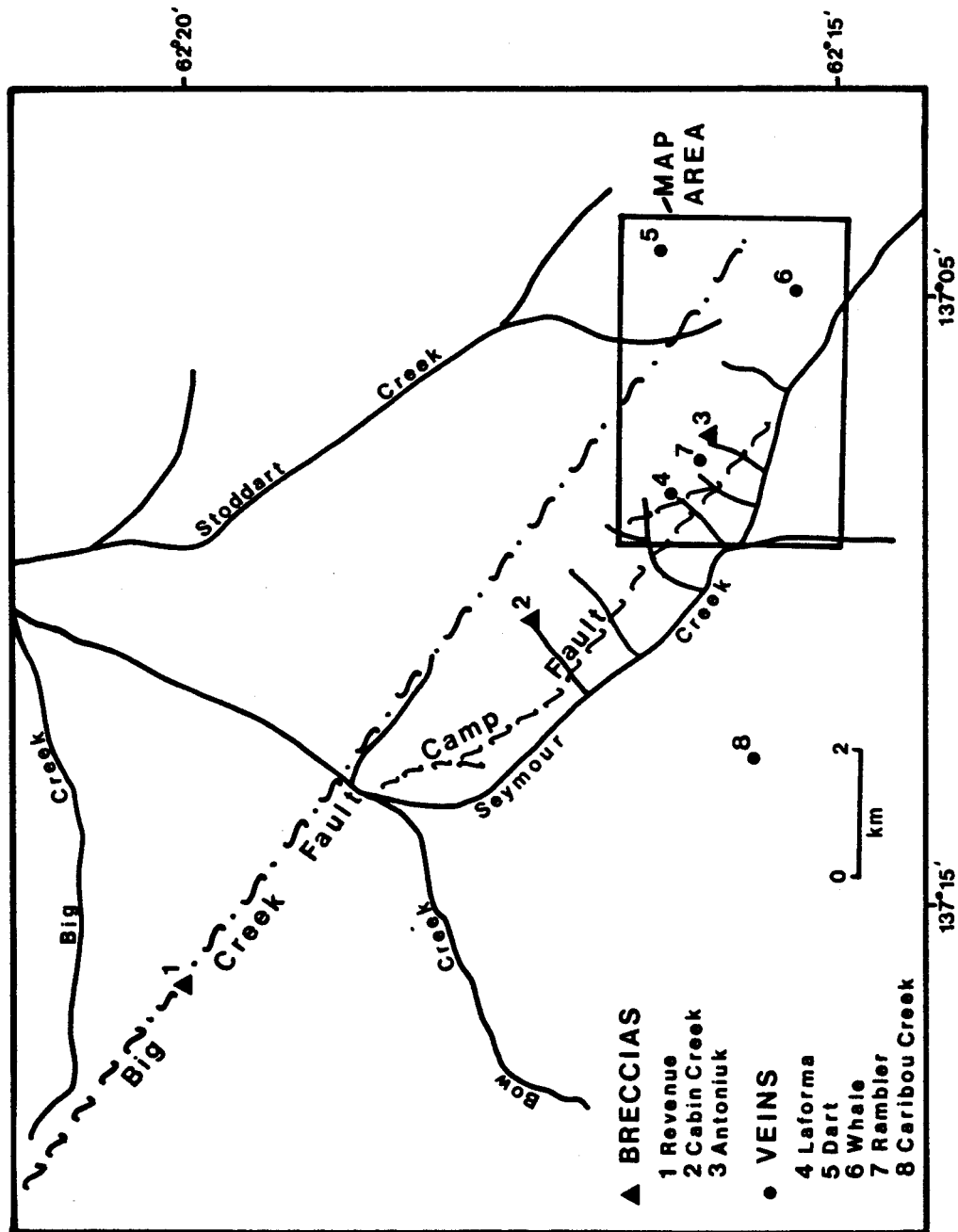


Figure 2. Location of gold occurrences at Freegold Mountain in relation to major structural features and thesis map area.

realized but it remained dormant until 1985 when Archer, Cathro and Associates Ltd. began doing assessment work on the property. Development of the prospect was spurred by the promise of a new gold extraction technique, "heap-leaching", a technology currently enjoying success in western United States for the mining of low grade, bulk tonnage gold deposits. An extensive diamond drilling program operated during 1986 to test the grade and tonnage of the deposit which is presently estimated to contain 3.7 million tonnes @ 1.14 g/tonne (0.5 g/tonne cutoff, Cathro and Main, (1986)).

The Emmons Hill prospect is an occurrence of stibnite-barite mineralization with anomalous Au, Ag, Hg, Tl, Pb and Zn concentrations. The property underwent development in the mid-1930's when a shaft was sunk to a depth of 92 feet, with crosscuts at 40 and 92 feet (Johnston, 1937). Gold values were reported to be greater than 1 oz/ton at the time of working. The ground was drilled in 1980 with poor results and is currently (1987) being reassessed by Noranda Minerals Inc. by diamond drilling.

### 1.3 Methodology

#### 1.3.1 Field Studies

Field work was conducted during the summers of 1985 and 1986 while the author was employed by the Mineral Resources Division of the Geological Survey of Canada. Detailed field mapping was conducted of the area at a scale of 1:5000 (Map

1). The Antoniuk Breccia was mapped during 1986 at a scale of 1:1000 (Map 2). The 3-dimensional interpretation of the Antoniuk Breccia was produced by combining surface mapping with drill core logging conducted by Mr. Jesse Duke, an employee of Archer, Cathro and Associates Ltd. at the time of the authors visit. The interpretation provided within is the sole responsibility of the author and is not necessarily subscribed to by the geological staff of Archer, Cathro and Associates Ltd. of Vancouver. Base maps and air photographs utilized in mapping were provided by Archer, Cathro and Associates Ltd. The Laforma Mine property was reinterpreted at a 1:100 scale from company maps prepared by Rayrock Resources in 1966.

Rock samples for petrographic examination and geochemistry were collected during mapping. Drill core from the Laforma Mine, Antoniuk Breccia and Emmons Hill was also sampled. This material is stored on site except for the latter which is stored at the H.S. Bostock Core Library in Whitehorse.

Field mapping is a necessary prerequisite when studying the evolution of precious metal systems since their formation is influenced strongly by the regional geology. Ore formation requires extensive ground preparation by tectonic processes to provide fault conduits utilized by large scale hydrologic convection cells, and by rising subvolcanic dykes and plutons necessary for the high thermal gradients needed to drive these cells. The structural,

plutonic and volcanic history of the area can only be determined by detailed field studies and the interpretation of geochemical data associated with ore formation may be misleading if geological control is inadequate.

### 1.3.2 Laboratory Studies

Selected samples were examined by reflected and transmitted light microscope to determine mineralogical, textural and paragenetic relationships of rock and ore-forming minerals. The identification of ore minerals was confirmed qualitatively by ion microprobe and scanning electron microscope at the Geological Survey of Canada. Geochemical analysis for major, minor and trace elements were conducted for some samples to aid in the chemical classification of rock types, and to evaluate chemical variations related to ore forming processes.

To estimate the thermochemical and physical environment of ore mineralization, gangue and ore minerals associated with the gold event were investigated using fluid inclusion and stable isotopic techniques as follows:

- 1) Fluid inclusions in quartz and barite were examined petrographically and analyzed using a heating-freezing stage;
- 2) H<sub>2</sub>O extracted from fluid inclusions was analyzed for its hydrogen isotopic composition;
- 3) The oxygen isotopic compositions of the hydrothermal fluids were determined by measuring the oxygen isotopic

composition of the gangue minerals hosting fluid inclusions;  
4) Calcite and pyrite associated with ore deposition were analyzed for their carbon and sulfur isotopic composition.

The radiometric ages of two major lithologies in the Freegold Mountain area was documented using Rb/Sr and K/Ar dating methods.

#### 1.4 Thesis

By considering the results of field and laboratory research, it is argued that gold mineralization at Freegold Mountain, Yukon is closely related to a period of tectonic deformation, during which, near surface rhyolitic subvolcanic activity drove groundwater dominated hydrothermal systems, both of which were controlled by fault systems in a compressional-tensional tectonic deformation region. Gold, silver, arsenic, antimony, mercury and barium were deposited from boiling, volatile-rich solutions, although boiling was not the only factor controlling mineral deposition. The area has undergone a relatively low rate of denudation since ore deposit formation, possibly less than 1 km in the last 70 Ma.

Isotopic evidence from water trapped in fluid inclusions strongly suggests that the area has been tectonically displaced a considerable distance northward since the time of its original formation. Combined with geological reconstruction of the Yukon by Templeman-Kluit (1979), it is conceivable that the area has moved on the

order of 350 to 450 km since ore deposit formation.

## CHAPTER 2. REGIONAL GEOLOGY

### 2.1 A Review of Cordilleran Evolution

Before a detailed account of the local geology is given it is useful to review the geological evolution of the Northern Cordillera as it is currently understood.

Interpretations of the geological evolution of the Freegold Mountain area can then be made and understood as part of a dynamic plate tectonic environment. The evolution of the Freegold Mountain area is closely tied to the tectonic events that occurred from the Cretaceous period to the present, and thus that period will be dealt with in more detail. While the formation of the North American Cordillera is complex and not yet fully understood, much less is known about the Yukon portions of the Cordillera. Most of the regional geological knowledge of the Northern Cordillera as it applies to the Freegold Mountain area is taken from mapping and synthesis studies of Templeman-Kluit (1976).

A complete synthesis of the current theories of Cordillera formation is beyond the scope of this thesis and the reader is referred to the work of Monger and Price (1979), Ewing (1980), Coney (1978), Monger et al. (1972) and Monger et al. (1982).

The Canadian Cordillera is subdivided into five northwesterly trending belts (Figure 3) defined by unique lithological, structural and physiographic criteria. These

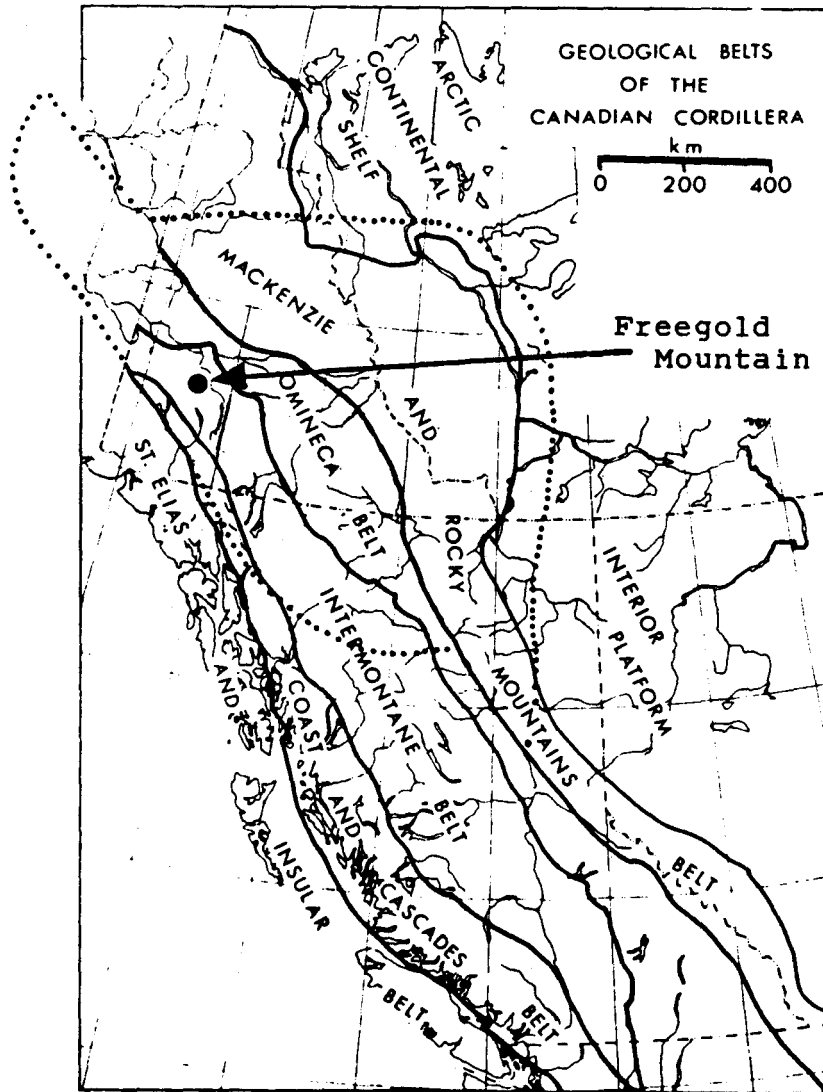


Figure 3. Geological subdivision of the Canadian Cordillera (from Templeman-Kluit, 1979).

belts are termed from east to west: Rocky Mountain, Omenica Crystalline, Intermontane, Coast Plutonic Complex and Insular Belt. The belts west of the Rocky Mountain Belt are interpreted to be allocthonous terranes accreted onto the North American continent along a convergent plate margin. Following is a brief chronological history of the Northern Cordillera from the Proterozoic to the present.

### 2.1.1 Proterozoic to Cretaceous Evolution

From mid Proterozoic until mid Devonian time a voluminous sedimentary wedge accumulated off the western North American craton in a miogeoclinal basin. On the shelf of the craton an extensive carbonate-orthoquartzite bank (Wheeler and Gabrielse, 1972) formed from Cambrian to mid-Triassic. From Late Cambrian to Middle Devonian an island arc complex is inferred to have appeared to the west of the craton due to the presence of a volcanic-greywacke sedimentary suite of this age. Thus it appears that the oceanic-continental plate boundaries had decoupled and oceanic plate consumption in an easterly dipping subduction zone occurred at this time.

Compressive deformation in Late Devonian to Mississippian time thrust thick sequences of pelagic sediments eastward onto the carbonate shelf and over the continental margin. This period of uplift is known as the Antler Orogeny and was significant in producing voluminous clastic detritus and significant crustal thickening eastward

onto the craton.

The Pennsylvanian to Permian period was significant in that during this time a major deep crustal fracture, the Tintina fault, developed on the craton. Vertical and possibly strike-slip movement occurred during this period (Templeman-Kluit, 1976) of compression. From mid-Permian to Late Mesozoic numerous island arc allocthonous terranes were accreted onto the western margin of North America by the consumption of their interarc basins in as many as three concordant subduction zones (Windley, 1977). By the end of the Triassic the Omenica Crystalline and the Intermontane Belts were accreted. The Cretaceous was marked by the accretion of the Coast Plutonic Complex and the Insular Belts. This phase of development of the Cordillera from a series of island areas to a consolidated emergent Cordilleran belt culminated in a physiographic province much similar in nature to the present-day Andes.

#### 2.1.2 Cretaceous to Present Evolution

Consumption of oceanic plate material from the Cretaceous to the Tertiary in a subduction zone west of the Insular Belt led to the emplacement of large scale plutons into, and the metamorphism of, the miogeoclinal sediments and earlier emplaced plutons to the east of the subduction zone in the Coast Plutonic Complex (CPC). This development of arc magmatism created crustal thickening and uplift in the CPC. During this time major right lateral strike slip

movement initiated on the Tintina - Northern Rocky Mountain Trench fault system, totalling up to 1,000 km (Templeman-Kluit, 1976; Gabrielse, 1985). It is also possible that some vertical movement occurred on the Tintina at this time due to compression (Templeman-Kluit, 1976).

From approximately 95 to 40 Ma, oblique subduction of the northward spreading Kula Plate was occurring along the western margin of the Northern Cordillera. This type of plate motion is believed to be responsible for dextral strike-slip movement on the Tintina fault zone of as much as 450 km (Roddick, 1967), which occurred while the fault zone was as much as 1000 km eastward of the plate margin. Major strike-slip motion along the Shikwak-Denali fault system, to the west of the Tintina began around 55 Ma, and continued until 38 Ma totalling about 300 km of movement (Eisbacher, 1976; Lanphere, 1978).

Accompanying this period of compression and transcurrent movement was a sympathetic regime of tensional and extensional stresses which controlled the development of NE-trending normal block faulting (Gabrielse, 1985) and emplacement of the northerly trending peralkaline Stikine Lavas in northern B.C. (Souther, 1977). Other phenomenon temporally and spatially related to dextral transcurrent faulting were granitic plutonism in two periods from middle to late Cretaceous (ca. 100 to 70 Ma) and early Cenozoic (ca. 50 Ma), early Cenozoic volcanism with emplacement of the northerly trending Nisling Range alaskite pluton and

dykes in the Snag district, Yukon (Templeman-Kluit, 1976) and the intrusion of northerly trending lamprophyre dykes in northern B.C. (Gabrielse, 1985). Dramatic uplift of up to 1000 m (Monger and Price, 1979) occurred during this period of active plutonism and volcanism in the Coast Plutonic Complex, and resulted in the present topography of deeply dissected river valleys, highly eroded Cretaceous plutons and the removal of most pre-Tertiary volcanic rocks in the Freegold Mountain area.

During the late Eocene (ca. 40 Ma) a major transition in the tectonic evolution of the Northern Cordillera occurred. Transcurrent motion along the Denali-Shakwak fault terminated and migrated westward to the plate margin where a transform fault was initiated along the former subduction zone (Coney, 1978; Atwater, 1970). This transform fault known as the Queen Charlotte fault replaced subduction in the Northern Cordillera except along the Aleutian trench, where the Kula plate was consumed by about 30 Ma. Volcanism and plutonism in the Northern Cordillera diminished considerably during this subduction to transform transition. The compressional and extensional stress regimes accompanied this westward transition and had less importance in the structural development of the interior belts.

## CHAPTER 3. GEOLOGY OF THE THESIS AREA

### 3.1 Regional Geology

The Freegold Mountain area has undergone relatively little detailed geological work in the past. The first geologist in the area was D.D. Cairnes (1914) who investigated the placer deposits to the south at Mt. Nansen in 1914. The Carmacks District, including Freegold Mountain and Mt. Nansen areas, were investigated by H.S. Bostock (1935) in the early 1930's and mapped at a 1 inch to 4 mile scale. During a three year period, he documented the rock types in the region and assigned astonishingly accurate relative ages to the major lithologies based on contact relationships.

Bostock's field assistant in 1932 and 1933, J.R. Johnston, returned to the Carmacks District in 1936 to investigate the geology of the gold deposits recently discovered in the Freegold Mountain area (Johnston, 1937). The entire length and width of the northwest trending Freegold Mountain were mapped by Johnston at a scale of 1 in to 1,000 ft. Although the exposure of outcrop is poor in the Dawson Range, he prepared a good quality map by tracing surficial float material in areas devoid of outcrop. This method is useful in most of the Dawson Range since Pleistocene glacial advance was arrested to the southeast. In fact, geochemical soil surveys are quite successful in delineating mineral deposits because of the absence of

glacial scouring and extended periods of residual soil formation. Much of the description of the geology of gold deposits at Freegold Mountain by Bostock and Johnston have proven invaluable since many of the early workings are now inaccessible.

The area saw little further work until Dirk Templeman-Kluit conducted a reconnaissance scale (1: 250,000) geological survey of the Carmacks sheet (115 I) in 1978 (Templeman-Kluit, 1984). This work was the first attempt to discern structure and age relationships via radiometric age dating within the Carmacks map area.

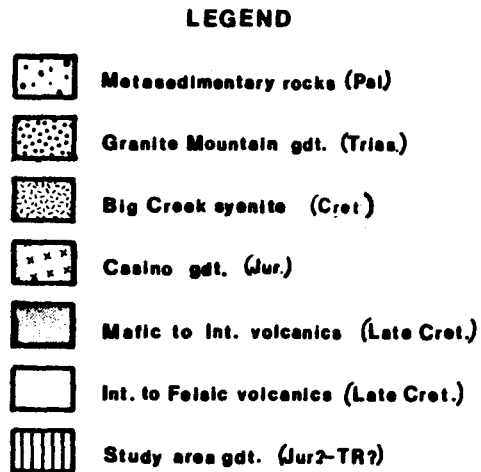
During 1986, the Freegold Mountain - Mt. Nansen areas (115 I/6) were mapped at a 1: 50,000 scale by G.G. Carlson under contract with the Department of Indian and Northern Affairs. This report was not available at the time of writing.

During 1985 and 1986 the author conducted detailed investigations of the geology of gold deposits on the east side of Freegold Mountain, and mapped the surrounding terrain at a scale of 1: 5,000.

### 3.2 LOCAL GEOLOGY

#### 3.2.1 Introduction

The Dawson Range (Figure 4) is a northwest trending volcanoplutonic arc representing the eastern portion of the accreted Stikinia terrane (Monger, 1984). The area is



1:250,000

modified from Templeman-Kluit 1984

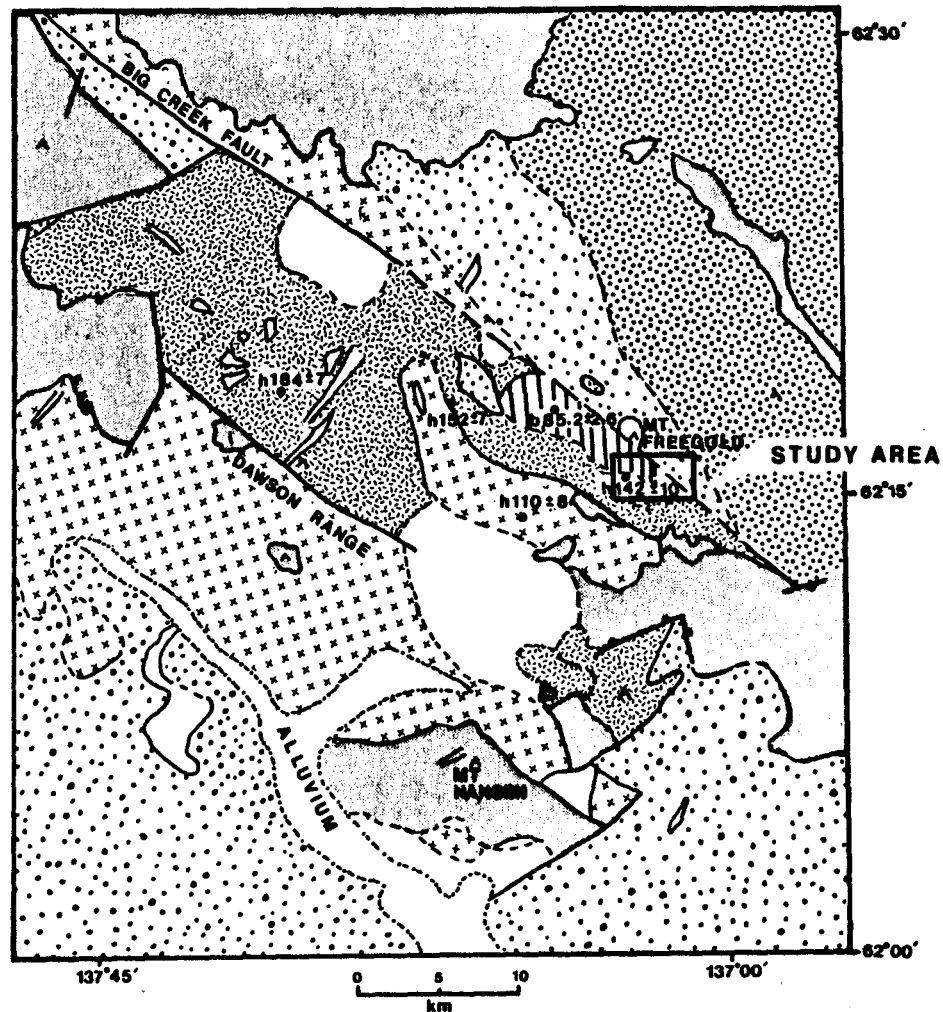
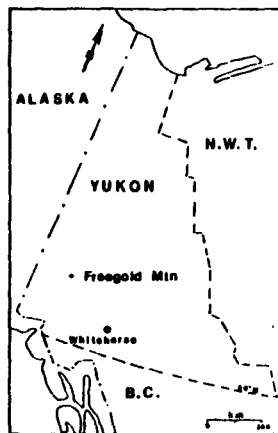


Figure 4. Geology (1: 250,000) of southeastern Dawson Range. (modified from Templeman-Kluit, 1984)

dominated by large northwesterly trending syenitic and granodioritic plutons of batholithic proportions. These were emplaced into Paleozoic? sediments, which commonly occur as roof pendants. Metamorphism of these sediments to schists and gneisses probably occurred during plutonism.

The batholiths in the area are cut by two younger intrusive units: andesitic to dacitic dykes, and small granitic subvolcanic plutons with apophyses of rhyolite. The emplacement of these dyke units is generally structurally controlled. This period of granite and rhyolite emplacement resulted in near surface hydrothermal activity, explosive brecciation and the deposition of quartz, precious metals and sulphides in breccia zones, fractures and fault zones.

Prior to this subvolcanic activity, there appears to have been a significant period of erosion as the batholiths were exposed and the Paleozoic sediments isolated into small islands. The area had slightly rolling to planated physiographic characters as evidenced by the rounded nature of many of the mountain tops in the Dawson Range (Photo 1). During the latter intrusive event there appears to have been a period of uplift evidenced by present day river valleys which are deeply incised and have a distinctive "V" shape with relatively steep sloping walls. These walls begin to lower in grade approximately 200 m above the valley floor, indicating a possible 200 m vertical uplift, which is corroborated by Bostock's (1935) estimate of a 150 m uplift

in the Big Creek valley north of Freegold Mountain.

As mentioned previous, the area has escaped Pleistocene glaciation and developed a relatively deep regolith. This regolith is overlain by the last geological deposit of significance, the 10 - 30 cm White River ash, which was erupted 1200 years ago from a volcano in Alaska (Lerbekmo and Campbell, 1969).

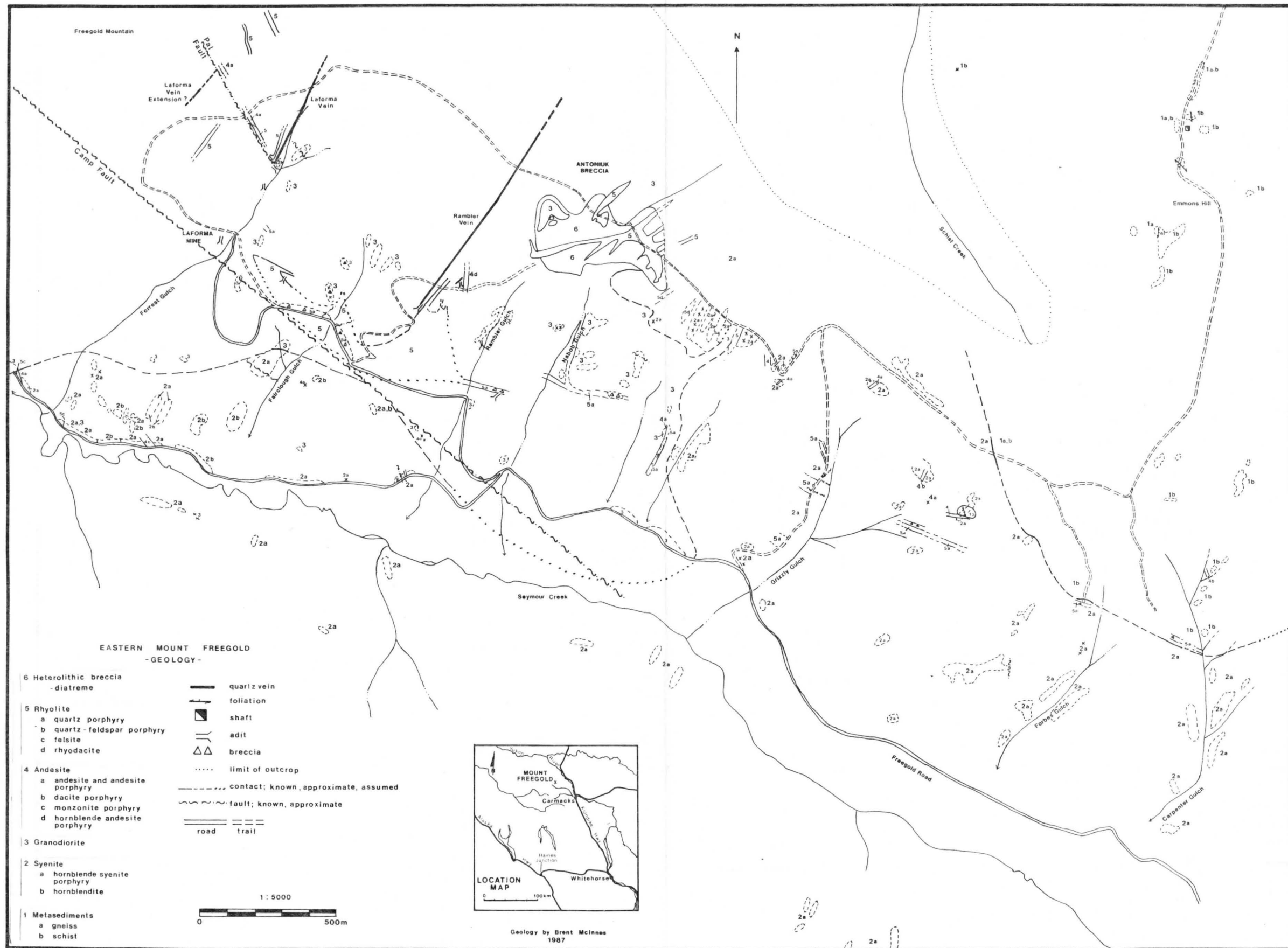
### 3.3 THESIS MAP

Mapping of the thesis area at a scale of 1: 5,000 was conducted in 1985 and 1986 (Map 1 and Figure 5). The map area (4.5 km by 3.5 km) was restricted to the eastern side of Freegold Mountain to encompass the gold deposits which have undergone the most development since Johnston's (1937) work. Extensive drilling and underground development at the Laforma Mine and the recent drilling and trenching at the Antoniuk Breccia enabled a reinterpretation of the geology in those immediate and surrounding areas. Numerous roadcuts and exploration trenches constructed by exploration companies and prospectors were utilized in areas where no outcrop was exposed.

#### 3.3.1 Rock Types

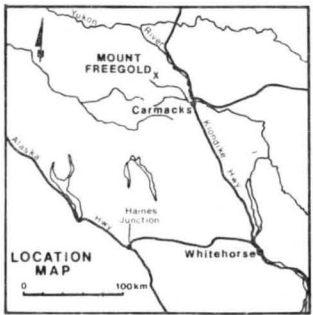
Five major rock types occur in the map area (Map 1): metasediments, syenite, granodiorite, andesite and rhyolite. These are further divided into subtypes, designated by the presence or absence of phenocrysts, physical differences

Figure 5. Geology (1: 5,000) of southeastern Freegold Mountain.



**EASTERN MOUNT FREEGOLD  
-GEOLOGY-**

- |                                     |  |
|-------------------------------------|--|
| 6 Heterolithic breccia<br>-diatreme | — quartz vein                              |
| 5 Rhyolite                          | — foliation                                |
| a quartz porphyry                   | ▣ shaft                                    |
| b quartz-feldspar porphyry          | — adit                                     |
| c felsite                           | △△ breccia                                 |
| d rhyodacite                        | ..... limit of outcrop                     |
| 4 Andesite                          | ----- contact; known, approximate, assumed |
| a andesite and andesite porphyry    | ~~~~~ fault; known, approximate            |
| b dacite porphyry                   | == road                                    |
| c monzonite porphyry                | --- trail                                  |
| d hornblende andesite porphyry      |  |
| 3 Granodiorite                      |  |
| 2 Syenite                           |  |
| a hornblende syenite porphyry       |  |
| b hornblendite                      |  |
| 1 Metasediments                     |  |
| a gneiss                            |  |
| b schist                            |  |



Geology by Brent McInnes  
1987

(ie. schist or gneiss) and compositional variations. These descriptive parameters are useful for field classification, and do not have any genetic implications. A chemical classification of rock types is provided later in the next chapter.

### 3.3.2 Lithologies of Freegold Mountain

#### **Metasedimentary Rocks**

The northeast portion of the map area is dominated by schists and gneisses, the dominant lithology being quartz-biotite schist, characterized by strongly foliated light and dark layers (Photos 2 and 3). The light coloured layers are rich in quartz and plagioclase, the darker layers, in biotite. In some areas thin, discontinuous lenses of coarse grained quartz-feldspar-hornblende gneiss occur interbanded with quartz-biotite schist.

An exploration trench south of the head of Schist Creek revealed the contact between the metasedimentary package and the syenite intrusion. Along this contact, the syenite is hornblende rich with the hornblende grains aligned parallel to the contact. Along the contact the metasediments are strongly foliated and indurated and contain porphyroblasts of K-feldspar elongated parallel to the foliation. In general, the orientation of schistosity in the metasediments is concordant with the syenite contact.

These rocks are thought to represent quartzites and greywackes of Paleozoic age (Johnston, 1937; Templeman-

Photo 2. Close-up of quartz-biotite schist with biotite and quartz-feldspar rich banding.

Photo 3. Outcrop of steeply dipping quartz-biotite schist east of Emmons Hill. The schistosity dips to the east at this location, away from major igneous intrusives.



Kluit, 1984), which have been regionally metamorphosed during plutonic emplacement.

### **Granodiorite**

Granodiorite occupies the north-central and northwest portions of the map area (Fig.5), and continues in the northwesterly direction for another 8 km. This intrusion was named the Seymour Creek stock by Johnston (1937). It is the eastern outlier of two larger granodiorite bodies mapped by Templeman-Kluit (1984) (Fig. 4) as the Casino Granodiorite. Although Johnston (1937) reports a granitic phase of this intrusion to the northwest of the map area, the granodiorite in the map area is of uniform composition and character.

The rock is medium to coarse grained, equigranular to porphyritic with phenocrysts of pink and white feldspar (Photo 4). It contains oligoclase, quartz, orthoclase, hornblende and biotite with accessory sphene, iron oxide and apatite. The feldspars commonly show oscillatory zoning, and albite, pericline and Carlsbad twinning. Twinning is also common in the hornblende.

### **Syenite**

Syenite occurs in the central and southern portions of the map area (Fig. 5). This unit consists of hornblende syenite porphyry and hornblendite. The two lithologies are clearly related, the hornblendite being the cumulate zone of

Photo 4. Hand sample of typical granodiorite.

Photo 5. Hand sample of typical syenite.



a magma chamber and the hornblende syenite porphyry, the residual material which crystallized above the cumulate zone. The contact between the two is subhorizontal and sharp, and can be observed by walking 100 m upslope from the road at a point 400 m east of Forrest Gulch.

The hornblendite is intruded by hornblende syenite porphyry and veins of potassium feldspar. Hornblendite occurs predominantly on the north side of Freegold road, east of Forrest Gulch, but can also be observed in trenches south of the head of Schist Creek where it is in contact with the gneiss. This latter type of occurrence is also found at Emmons Hill. The hornblendite generally contains between 80-100% hornblende, with plagioclase making up the remainder. Sphene, magnetite and apatite occur as accessory minerals.

The hornblende syenite porphyry is the dominant lithology making up 95% of the total syenite exposed. This rock is characterized by the trachytoidal texture of tabular orthoclase megacrysts which can be up to 5 cm in length, but are commonly about 3 cm long (Photo 5). The average rock has been estimated visually to contain 50% orthoclase, 20% oligoclase, 5-10% quartz and 20-25% hornblende (Johnston, 1937). Outcrops of this rock type are massive and well jointed.

Tabular orthoclase crystals observed in outcrop are generally horizontal to subhorizontal. The subhorizontal crystals are oriented in a northwesterly direction and dip

to the east. The significance of this observation may be to indicate that tectonism has either uplifted the southwest or downdropped the northeast portion of the pluton in the area. If the assumption is correct that the original orientation of the megacrysts was horizontal due to the floating of the low density orthoclase crystals in the melt during crystallization, then the reorientation is post magmatic and of tectonic origin. This would support later evidence suggesting that block faulting may have occurred during the geological evolution of the area.

### **Dykes**

The area is frequently dissected by two types of subvolcanic intrusives: andesitic to dacitic dykes and rhyolite dikes. No volcanic rocks have been preserved in the Freegold Mountain area.

### **Andesite and Dacite Dykes**

These green to grey, aphanitic to porphyritic dykes occur sporadically throughout the thesis area and are not volumetrically significant. Johnston (1937) reports that they are abundant near the summit of Freegold Mountain, but in the thesis area they make up a very small proportion of exposed rock. Hand samples can vary from aphanitic to porphyritic, with phenocrysts of plagioclase, quartz and occasionally biotite or hornblende. Some dacite dykes contain xenoliths of granodiorite and metasedimentary

Photo 6. Andesite dyke containing xenoliths of metasedimentary country rock.

Photo 7. Small andesite porphyry dyke intruding into syenite.



country rock (Photo 6). There are too few dykes in the map area to establish a dominant orientation, however those prevalent near the summit of Freegold Mountain strike northwest (Johnston, 1937). These dykes cut all rock types in the area (Photo 7) except rhyolite.

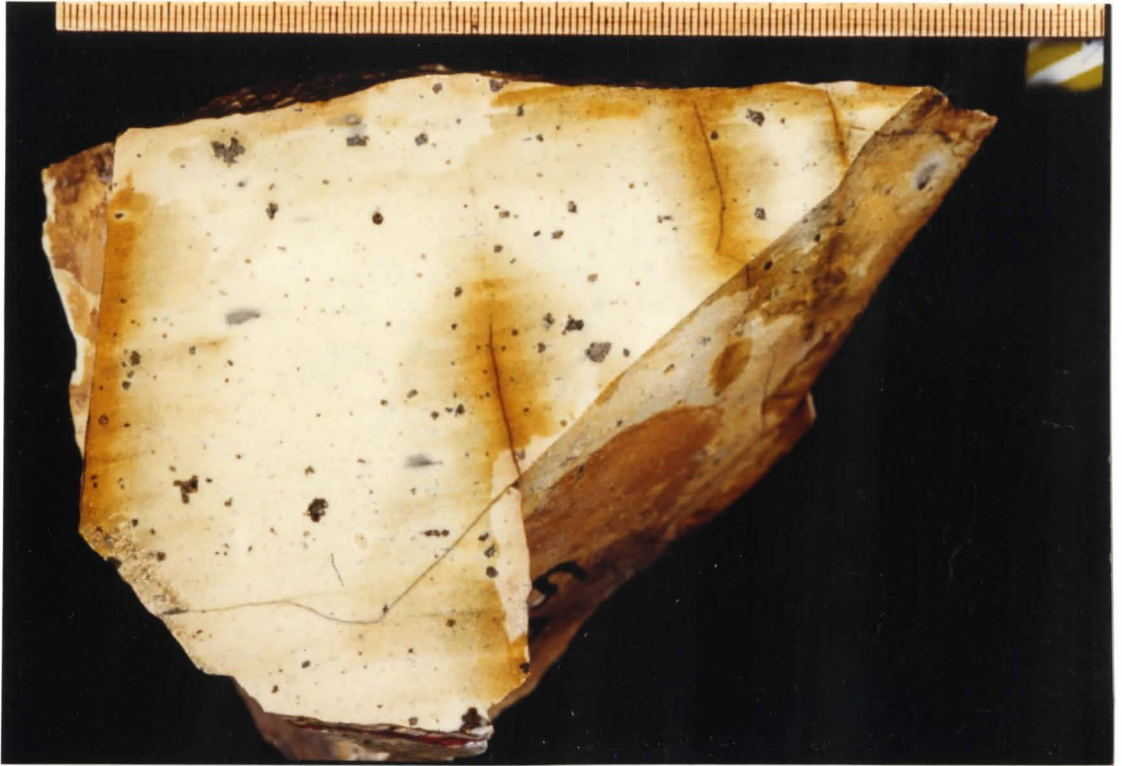
For simplicity, monzonite porphyry and granophyre dykes (Johnston, 1937) have not been differentiated and occur on Map 1 as monzonite porphyry. They are relatively rare and only observed to crosscut syenite and granodiorite. Crosscutting relationships suggest that they were intruded after pluton and before andesite-dacite dyke emplacement. They have a distinctly granitic character in comparison to the andesite and rhyolite dykes and it is probable that they are the residual components of a granitic magma introduced after batholith emplacement.

### **Rhyolite Dykes**

Rhyolite dykes are conspicuous in the area in that they often form walls of outcrop, especially on the hillsides. They are generally white to buff coloured and aphanitic to porphyritic with phenocrysts of quartz and occasionally feldspar. There are three main varieties as indicated on Map 1: quartz porphyry, quartz-feldspar porphyry and felsite. The porphyritic varieties contain phenocrysts of quartz and/or alkali feldspar, often strained and brecciated (Photo 8). Quartz phenocrysts commonly show resorption by the matrix, possibly resulting from silica undersaturation

Photo 8. Highly altered rhyolite dyke in hand specimen. Feldspar phenocrysts have been altered and replaced by pyrite. Flow banding can be detected in the oxidized portions of the sample.

Photo 9. A rhyolite dyke with well developed flow banding enhanced by weathering.



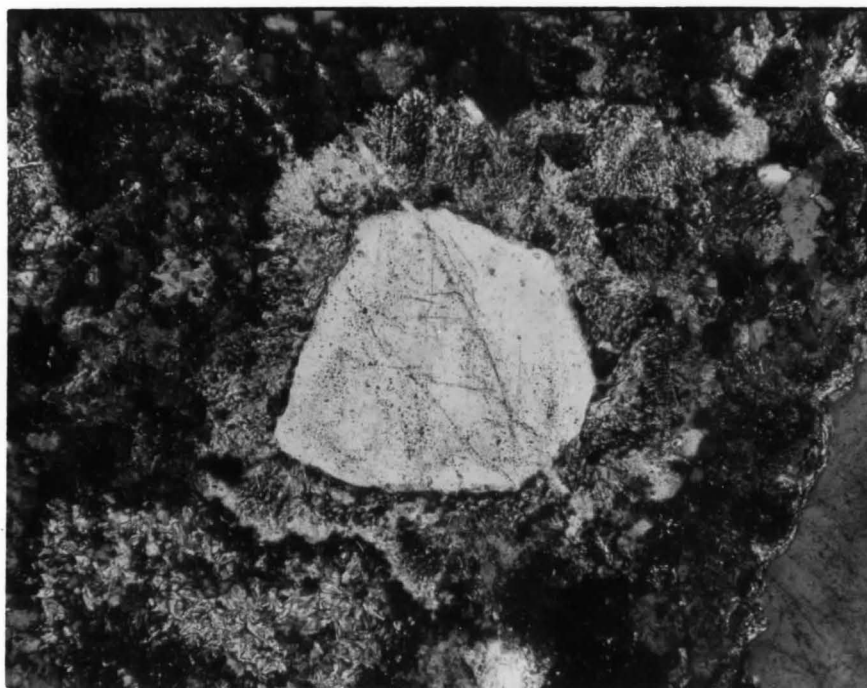
of the matrix during intrusion (Photo 10). The matrix consists of fine grained quartz and feldspar, which occurs either as a microcrystalline groundmass or as micrographic intergrowths. Sericite, chlorite, tourmaline and pyrite occur occasionally as accessory phases, and probably are secondary. The felsitic variety contains no phenocrysts and is homogeneously cryptocrystalline.

Banding is common in small dykes (Photo 9) and along the contacts of larger ones. The rhyolite is also frequently brecciated and evidence indicates that both autoclastic brecciation (syn-emplacement) and tectonic brecciation (post-emplacement) have occurred. The resistant nature of these rhyolite dykes in outcrop is due to silicification, with quartz cementing brecciated dyke fragments or adjacent country rock, or occurring as vein material within or concordant to the dyke (Photos 11 and 12).

Two centers of rhyolitic activity appear to be present in the area. A major swarm of dykes occur within the Antoniuk Breccia in the north central portion of Map 1 above Nabob Gulch. These quartz porphyritic to felsitic dykes, which strike dominantly at  $45^{\circ}$ , and dip vertically, are interpreted from diamond drill core observation to be apophyses of a shallow, buried intrusive which generated the explosive brecciation event (Maps 2 and 3, in pocket). This will be discussed in detail in Chapter 7.

A second inferred centre of rhyolitic activity is

Photo 10. Embayed quartz phenocryst within rhyolite.  
Phenocryst is approx. 3 mm in diameter.



located north of the Camp Fault between Forrest and Rambler Gulches. Although this area is considerably less exposed, a 350 m long outcrop of brecciated rhyolite occurs along the north side of the Laforma road, east and west of Fairclough Gulch. The Alpha adit, between Forrest and Fairclough Gulch is 75 m long and Johnston (1937) reports that most of it is in quartz porphyry. To the east subcroppings of rhyolite are abundant south of the Rambler Vein and towards Rambler Gulch. A dyke cuts across Rambler Gulch above the Laforma road. The southern portion of this area is bounded by the Camp Fault, which may have displaced vertically or dextrally the southerly portion of the rhyolite intrusion (if one existed).

Isolated rhyolite dykes are present throughout the map area. A long, possibly continuous set of rhyolite dykes oriented in a northwesterly direction outcrop discontinuously from west of Grizzly Gulch to Carpenter Gulch. These exposures, called the Whale Vein by Johnston (1937), are often brecciated and silicified. An impressive northeasterly trending "wall" of silicified rhyolite occurs along the east side of Nabob Gulch and joins a northwesterly trending wall which is well exposed in Nabob Gulch. It may be connected to the Whale Vein to the east. This wall is 3 to 10 m in width and up to 10 m high (Photo 11).

An important field observation concerning the presence of rhyolite is that there is a close spatial relationship between dykes and gold bearing quartz veins and breccias,

Photo 11. Ten metre high silicified rhyolite dyke.

Photo 12. Photograph of 1.5 metre wide quartz vein  
(right) parallel to a 2 metre wide rhyolite  
dyke.



and therefore sites of hydrothermal activity (Photo 12). A rhyolite dyke exposed at surface and depth concordant to the trend of the Laforma Vein (Figures 5, 15 and 17). This phenomenon also occurs along the southern portion of the Rambler Vein. As discussed before, rhyolite dykes are common in the Antoniuk Breccia. Samples of stibnite-barite cemented breccia from the Emmons Hill prospect contain clasts of rhyolite and recent trenching of the property by Noranda Minerals Corp. indicates that rhyolite dykes are present in the vicinity (C. Hart, Noranda geologist, pers. comm., 1987).

## CHAPTER 4. ROCK GEOCHEMISTRY AND CHEMICAL CLASSIFICATION

### 4.1 Methodology

Samples of plutonic and volcanic rocks in and around the thesis area were analyzed for major and trace elements in order to aid in the classification of rock types and the interpretation of the igneous processes which led to the present geological character of the area. The freshest samples were crushed to -200 mesh using a jaw crusher, ceramic pulverizer and tungsten-carbide shatterbox. One split of these samples was submitted to the Geological Survey of Canada Geochemical Laboratories in Ottawa for major and trace element analysis and another was analyzed for trace elements by Nuclear Activation Services Ltd., using the McMaster Nuclear Reactor at McMaster University.

All analyses at the GSC laboratories were conducted by ICP-MS except H<sub>2</sub>O TOTAL, CO<sub>2</sub> TOTAL, C, S, and LOI (loss on ignition) which were done via standard chemical methods. A solution for major and trace element analysis was obtained by fusing 0.5 g of sample with lithium metaborate, dissolving the fusion cake in 5% HNO<sub>3</sub> and diluting the solution to 250 ml.

Instrumental Neutron Activation Analysis (INAA) was conducted for elements listed in Table 1 (detection limits as quoted by NAS). For some samples (particularly Sb-rich ores) poorer detection limits prevailed (Appendix A). Large

Table 1. Elements Analyzed by Instrumental Neutron Activation and Quoted Detection Limits (NAS Ltd.)

<u>Element</u>	<u>Detection Limit</u>	<u>Units</u>
Ag	5.0	ppm
As	2.0	ppm
Au	5.0	ppb
Ba	100.0	ppm
Ca	1.0	%
Co	5.0	ppm
Cr	10.0	ppm
Fe	0.02	%
Hf	1.0	ppm
Mo	5.0	ppm
Na	0.05	%
Ni	200.0	ppm
Rb	30.0	ppm
Sb	0.2	ppm
Sc	0.1	ppm
Se	5.0	ppm
Ta	1.0	ppm
Th	0.5	ppm
U	0.5	ppm
W	4.0	ppm
Zn	50.0	ppm
La	1.0	ppm
Ce	3.0	ppm
Sm	0.1	ppm
Eu	0.2	ppm
Yb	0.2	ppm
Lu	0.05	ppm

sized polyethylene vials were filled with 10 to 13 g of rock powder for analysis of rare earth elements La, Ce, Sm, Eu, Yb and Lu. Gd was analyzed using a prompt gamma counting method on approximately 2 g of rock powder sealed in small polyethylene vials.

The results of duplicate samples submitted to the GSC laboratories are provided in Table 2. Each laboratory received two duplicate samples and the relative errors quoted in Table 3 are the greater of the two relative errors calculated for each duplicate and not the average. Some of the errors are quite large due to elemental concentrations close to the limit of detection for that element. These errors probably overestimate the error applicable to those samples containing elemental concentrations well above the limit of detection. Some relative errors are unknown because the elemental concentrations were below the limit of detection for the method. The NAS errors were calculated on replicates from quartz-rich precious metal mineralized samples and therefore many of the lithophile trace element concentrations were below the limit of detection.

In general it can be stated that the precision of the major element analysis is good (<5%). Relative errors calculated on trace elements whose concentrations exceeded their limit of detection by a factor of two were generally less than 11%.

Table 2. GSC laboratory duplicate results

SAMPLE #	F86-16	F86-16d	TR18-660E	TR18-660Ed
SiO2	67.2	66	65.2	65.4
TiO2	0.44	0.41	0.41	0.41
Al2O3	15.6	15.7	14.7	16.1
Fe2O3T	4.02	4.02	3.79	3.75
MnO	0.09	0.09	0.09	0.09
MgO	1.92	1.78	1.59	1.58
CaO	3.47	3.57	3.01	2.99
Na2O	3.76	3.76	3.75	3.6
K2O	3.16	3.3	3.62	3.66
P2O5	0.15	0.14	0.17	0.17
H2OT	1.1	0.8	1.8	1.8
CO2T	0.2	0.1	0.7	0.7
S	0	0.01	0.01	0.01
AG	0	0	2	3
BA	1400	1400	2300	2300
BE	1.6	1.5	1.6	1.6
CO	35	11	42	42
CR	20	18	18	16
CU	11	9	19	20
LA	29	23	22	23
NI	3	2	0	0
PB	15	12	17	19
SR	580	580	420	430
TL	0.7	0.7	1.1	1.3
V	67	66	67	67
YB	1.4	1.3	1.4	1.4
ZN	47	47	170	45
ZR	140	140	170	150

Major elements expressed as wt. %

Trace elements as ppm

d = duplicate

Table 3. Relative Errors on Major, Minor and Trace Element Analysis Calculated from Replicate Analyses

<u>GSC Data</u>		<u>NAS Data</u>	
<u>Element/Oxide</u>	<u>± % Relative Error</u>	<u>Element</u>	<u>% Relative Error</u>
SiO <sub>2</sub>	0.9	Ag	unknown <sub>2</sub>
TiO <sub>2</sub>	3.5	As	9.2
Al <sub>2</sub> O <sub>3</sub>	4.5	Au	4.6
Fe <sub>2</sub> O <sub>3</sub>	0.5	Ba	0.0 <sub>1</sub>
MnO	0.0	Ca	unknown <sub>2</sub>
MgO	3.8	Co	1.8
CaO	1.4	Cr	60.0 <sub>1</sub>
Na <sub>2</sub> O	0.7	Fe	6.1
K <sub>2</sub> O	2.2	Hf	unknown <sub>2</sub>
P <sub>2</sub> O <sub>5</sub>	3.4	Mo	"
		Na	"
H <sub>2</sub> O <sub>total</sub>	15.8	Ni	"
CO <sub>2</sub>	0.0	Rb	"
S	0.0	Sb	3.2
		Sc	33.0 <sub>1</sub>
Ba	0.0	Se	unknown <sub>2</sub>
Ag	20.0 <sup>1</sup>	Ta	"
Be	3.2	Th	11.1 <sub>1</sub>
Co	52.0 <sub>1</sub>	U	16.3
Cr	6.0	W	unknown <sub>2</sub>
Cu	10.0	Zn	11.0
La	11.5	La	0.0 <sub>1</sub>
Ni	unknown <sub>2</sub>	Ce	unknown <sub>2</sub>
Pb	11.1	Sm	0.0 <sub>1</sub>
Sr	1.2	Eu	unknown <sub>2</sub>
V	0.8	Yb	"
Yb	3.7	Lu	"
Zn	60.0		
Zr	6.3		

1. calculated on concentrations near limit of detection
2. replicate sample concentration below limit of detection for this element

## 4.2 RESULTS OF MAJOR AND TRACE ELEMENT ANALYSIS

Twenty-two samples were analyzed at the Geological Survey of Canada and eighteen by Neutron Activation Services. The combined major and trace element data from both sets are given in Appendix A.

### 4.2.1 Classification of Rock Types

#### 4.2.1.1 Plutonic Rocks

Two varieties of plutonic igneous rocks outcrop in the thesis area. These have been given field classifications of granodiorite and syenite based on estimated modal percentages of felsic minerals following the standard IUGS classification scheme (Streckeisen, 1975). Major element chemical compositions calculated into CIPW normative mineral compositions have also been used to verify this classification following the method of Streckeisen and Le Maitre (1979).

Both modal and normative schemes classify the samples as granodiorite on Streckeisen's plot. Thus 'granodiorite' is the proper name based on these schemes. The rock type termed syenite in the field is actually a quartz syenite on the Streckeisen plot based on the estimated modal composition of 50% orthoclase, 20% plagioclase and 5-10% quartz; however, these rocks plot as quartz monzonite to quartz monzodiorite on the normative classification scheme. Streckeisen and Le Maitre (1979) point out that the concordance between fields on the normative and modal

classification schemes is not perfect, as seems apparent in this case. Since the normative classification scheme relies on two separate calculation methods dependant on a chemical analysis, the rock will be named according to the less interpretive IUGS classification of quartz syenite.

#### 4.2.1.2 Volcanic Rocks

Two types of intrusive volcanic rocks are present in the thesis area and have been given the field terms of andesite and rhyolite based on Johnston's (1937) nomenclature. Chemical analyses of these rock types has allowed their classification to be refined according to schemes proposed by Irvine and Baragar (1971), and Pecерillo and Taylor (1976). The classification scheme widely accepted for volcanic rocks is based on a binary alkalies-silica diagram and a ternary AFM plot (Figures 6 A and B) using raw chemical data (Irvine and Baragar, 1971).

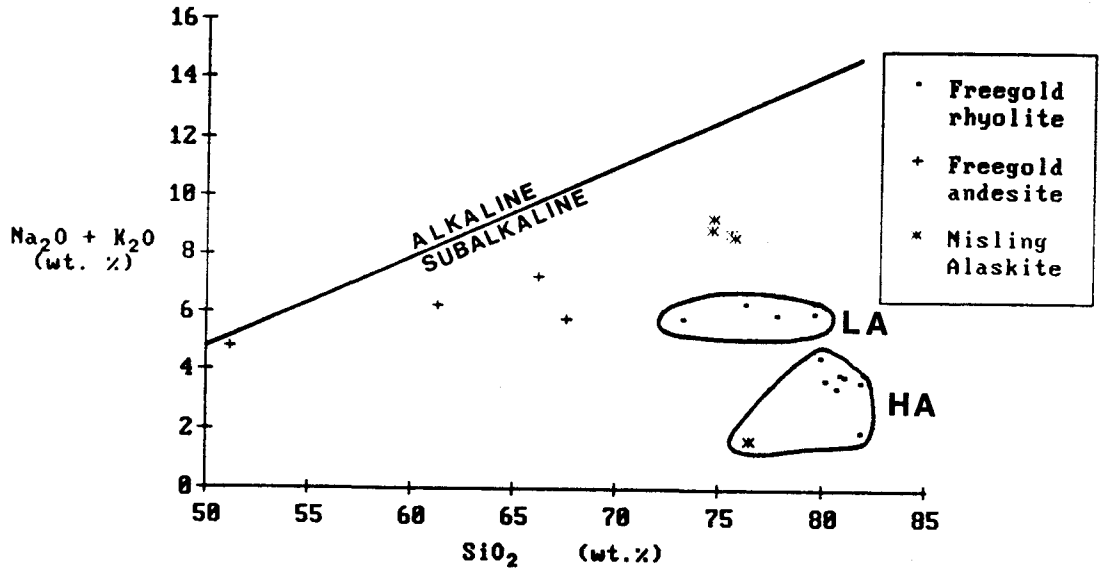
Fresh samples of 'andesitic' rocks from the Freegold Mountain area plot within the subalkaline field of Fig. 6A and within the calc-alkaline field of Fig. 6B. Also plotted on Figure 6B are rocks found elsewhere in the Dawson Range thought to be contemporaneous (Dawson Range Quartz Porphyry) with the Freegold Mountain samples. These also plot within the calc-alkaline field.

Unlike the andesite samples, most of the rhyolitic rocks in the Freegold Mountain area have been hydrothermally altered. Brecciated portions of the dykes are silica

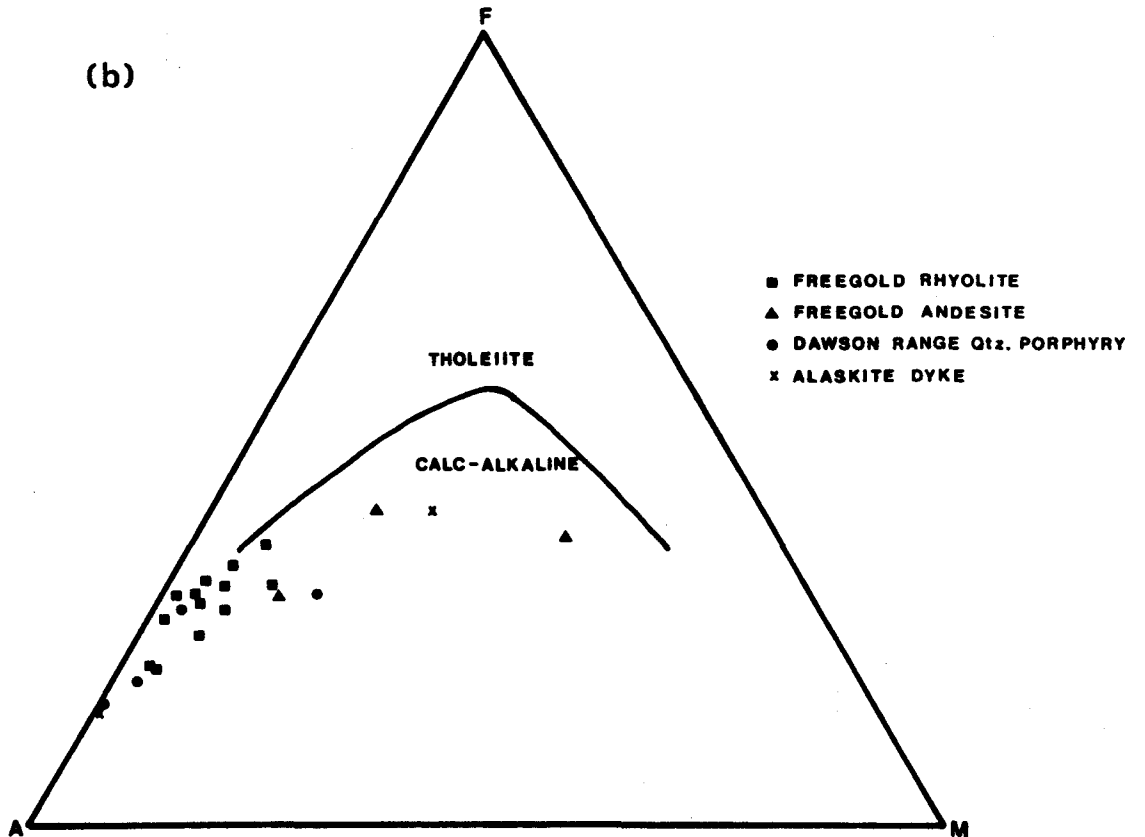
Figure 6. (a) Binary alkali - silica discrimination diagram (after Irvine and Baragar, 1971).  
(HA) = highly altered rhyolite samples  
(LA) = least altered rhyolite samples

(b) Ternary AFM discrimination plot (after Irvine and Baragar, 1971).

(a) Dawson Range Intrusive Volcanics



(b)



cemented and quartz veins within and parallel to the dykes are common (Photo 12). The rhyolite samples submitted for geochemical analysis appeared fresh in hand specimen but on a thin section scale, some samples contained small microveinlets of quartz and secondary sericite.

Hydrothermal alteration appears to have been pervasive, even in massive samples, to the extent that  $\text{Na}_2\text{O}$  concentrations are all less than 0.15 wt. %. Compilation studies of the chemical composition of fresh Cordilleran rhyolites (Ewart, 1979; Le Maitre, 1976; and Chayes, 1975) show average  $\text{Na}_2\text{O}$  and  $\text{K}_2\text{O}$  contents to be between 3.5 - 4.2 wt. % and 3.3 - 4.8 wt. %, respectively. If the Freegold rhyolites were of 'average' composition upon intrusion, during hydrothermal alteration Na has been flushed from them. Although the average  $\text{K}_2\text{O}$  content of Freegold rhyolites ( $4.0 \pm 1.25$  wt. %), is similar to the Cordilleran rhyolite average ( $4.1 \pm 0.7$  wt. %; Ewart, (1979)), the spread in the uncertainty associated with the Freegold data (Fig. 7) suggests that some remobilization of K has occurred.

Sodium and potassium mobilization from the rhyolitic samples precludes their classification as alkaline or subalkaline rocks (Fig. 6A) when that classification depends on alkali content. Freegold rhyolite samples have been subdivided into highly altered (HA) and least altered (LA) fields and plotted (Fig. 6A) with fresh samples of Nisling Range alaskite which are chemically and physically similar to the rhyolites. By virtue of this similarity, it is

proposed that unaltered Freegold rhyolite samples would plot near the Nisling Alaskite samples on Figure 6A, still within the subalkaline field.

The calc-alkaline classification of rhyolite samples on Figure 6B is little affected by the Na removal and K remobilization. On this ternary plot samples with higher  $\text{Na}_2\text{O}$  contents plot closer to the alkali (A) axis, still within the calc-alkaline field. Unaltered rhyolite would yield the same general classification as the altered samples do.

A simple but useful chemical classification, particularly for relatively young (ie. not Archean) fine grained volcanic rocks, was proposed by Peccerillo and Taylor (1976) and modified by Ewart (1979). Figure 7 is a binary plot of  $\text{K}_2\text{O}$  (wt. %) vs.  $\text{SiO}_2$  (wt. %) with the type fields as proposed by Peccerillo and Taylor (1976). Samples plotted in Fig. 6B are replotted on Fig. 7 and fall within the basalt, andesite, dacite and rhyolite fields. Of the four samples classified as andesite on Map 1 (Fig. 5), two plot as high-K dacites, one as high-K andesite and the other as a shoshonite (above the high-K basalt field). This shoshonitic sample was obtained from a dyke intruded into quartz syenite and the high  $\text{K}_2\text{O}$  content of the basalt may reflect partial melting and incorporation of K-feldspar from the syenite, although no evidence for this was observed during petrography.

The rhyolitic rocks in the Freegold Mountain area span

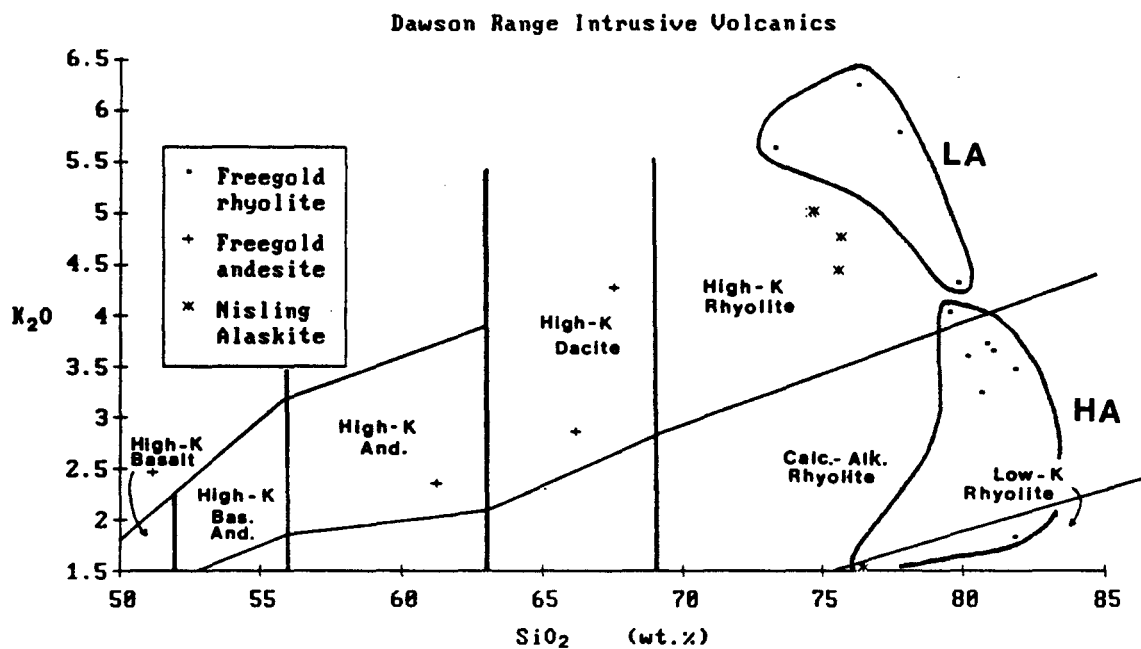


Figure 7. Binary K<sub>2</sub>O - silica discrimination diagram for volcanic rocks with fields by Pecerillo and Taylor, (1976).  
 (HA) = highly altered rhyolite samples  
 (LA) = least altered rhyolite samples

the low-K, calc-alkaline (highly altered samples), and high-K rhyolite (least altered samples) fields. Samples of Tertiary Nisling Alaskite and related quartz-feldspar porphyry dykes from the Snag map sheet to the west, have been plotted on Figure 7 for comparison purposes. Since the initial  $K_2O$  content of these rocks is uncertain, it is futile to attempt to discern whether they are calc-alkaline or high-K rhyolites. It should be noted that the average  $K_2O$  content (4.1 wt. %) is within the high-K rhyolite field.

Disregarding the problems associated in classifying the Freegold rhyolites, it is apparent that subvolcanic rock types in the Dawson Range are K-rich.

#### **4.2.2 Rare Earth Element Data and Petrogenesis**

This section will examine the petrogenesis of rock types common in the Freegold area based on lithogeochemical data. Although many elemental composition scatter diagrams are commonly used to discriminate geochemical processes, it is perhaps most valuable to look at the rare earth element (REE) data to discuss petrogenesis. Figures 8A & B and 9A & B contain the chondrite normalized REE plots for each rock type where adequate sample material was available.

##### **4.2.2.1 Granodiorite**

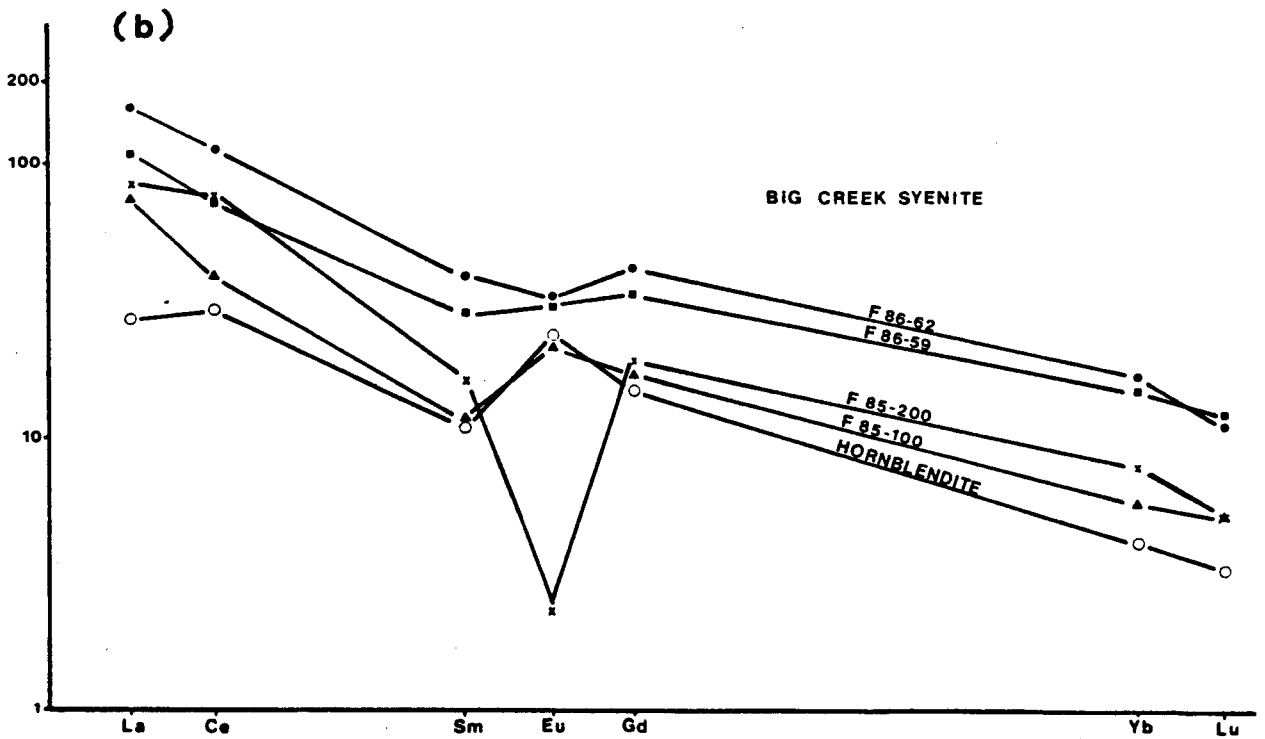
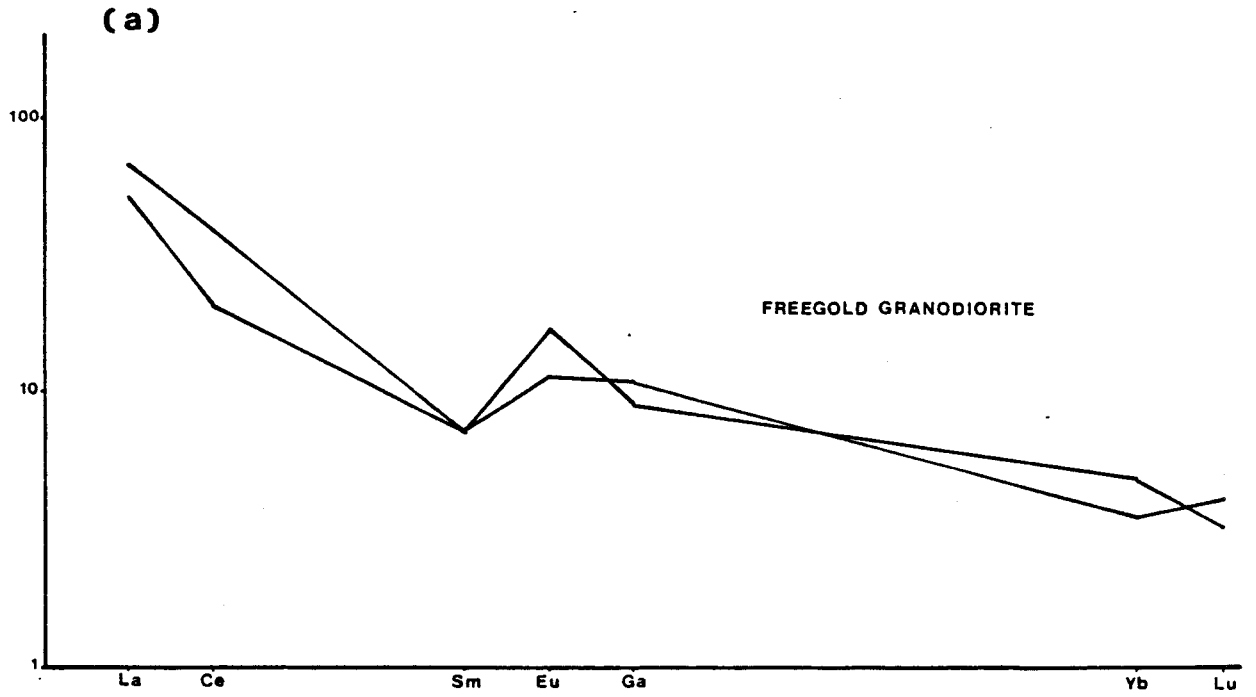
The granodiorites and granites in the Dawson Range are of batholithic proportions and analogous to composite tonalite-granodiorite-granite batholiths formed in other

Cordilleran-type orogenic environments in Peru (Atherton et al., 1979), California (Bateman, 1983) and Alaska (Buddington, 1927). These authors have identified complex histories of emplacement and evolution but recognize some broad geochemical trends. For example, where "toward continent" (ie. eastward) dipping subduction zones are involved, elements such as potassium, silica, uranium, thorium, beryllium, rubidium, total rare earths and  $^{87}\text{Sr}/^{86}\text{Sr}$  increase with increasing eastwards distance from the trench. Samples of fresh granodiorite in the thesis area are, however, too limited to recognize any such variations. The REE patterns for two granodiorite samples are plotted on Fig. 8A. The granodiorite shows enrichment in LREE's with a positive europium anomaly. The proposed petrogenetic interpretation of the REE patterns in these samples is consistent with melt generation in a mantle-wedge environment above an active subduction zone, similar to other granodiorites in Cordilleran regions of the Americas. (Middlemost, 1985).

#### 4.2.2.2 Syenite

Individual REE trends of syenitic rocks are plotted on Fig. 8B. The sample of hornblendite from the cumulate zone shows low abundances of light and heavy REE and a positive europium anomaly. This is consistent with its cumulate nature as most REE prefer the residual magma over crystallization in hornblende because of their small ionic

Figure 8. Chondrite normalized REE pattern for  
(a) granodiorite.  
(b) syenite



size. The positive europium anomaly is the result of  $\text{Eu}^{2+}$  (larger ionic size than trivalent REE's) substituting for  $\text{Sr}^{2+}$  in the Ca sites of hornblende during the early crystallization of the melt. Apart from this positive Eu anomaly, the shape of the REE trend for the hornblendite is similar to that of hornblende mineral separates (Gromet and Silver, 1983).

Sample F86-62 is a hornblende-rich rock within 5 m of a syenite-metasediment contact. It has the highest REE concentration of any syenite sample. The LREE enrichment is inconsistent with normal hornblende crystallization from a melt and is probably due to contamination by assimilation of adjacent biotite-quartz schists. This finding is consistent with the high  $\text{Sr}^{87}/\text{Sr}^{86}$  ratio of the sample as outlined in Chapter 5.

Sample F85-200 is characterized by a relative enrichment in the LREE's and by a strong negative europium anomaly. This sample is relatively quartz-rich and hornblende-poor and the shape of the trend suggests that F85-200 is a more highly evolved sample which may have been one of the later crystallizing phases. The strong negative Eu anomaly may reflect significant substitution of Eu in earlier crystallized plagioclase and alkali feldspar thereby depleting the residual liquid in Eu. Minor alteration in this sample may have affected the REE pattern by destruction of feldspar and the leaching of Eu, but the alteration does not seem significant enough to remove the amount of Eu

necessary to cause a negative anomaly.

Sample F86-59 is a hornblende-rich and plagioclase-rich sample. The relatively high REE abundances in this rock are attributed to the high modal abundance of feldspar with Eu substituting for Ca in hornblende which overprints any vestige of a positive europium anomaly contributed by plagioclase.

Sample F85-100 is a common quartz syenite with approximately 50% alkali feldspar, 20% oligoclase, 25% hornblende and 5% quartz. The REE pattern of this sample showing relatively high LREE abundances and a positive europium anomaly is possibly the result of the combined REE concentrations of each mineral (Gromet and Silver, 1983) and their formation from a lesser evolved residual liquid than sample F85-200.

#### 4.2.2.3 Basalt-Andesites-Dacites

The range of REE patterns of this group of rocks is plotted on Fig. 9A. The upper limit is defined by the high-K basalt and the lower limit by the high-K dacite. The generally parallel trends in REE patterns, the positive Eu anomaly and the high-K content prevalent in this group suggest that they may have been derived from a single parental source melt. The similarity in shape of the REE pattern between the 'andesitic' clan and the granodiorites on Figure 8A suggest that the andesites may have been produced from a melt similar to the Freegold Granodiorite

which has undergone a minor amount of fractional crystallization. Temporal relationships do not however suggest that the Freegold Granodiorite itself is the parent magma.

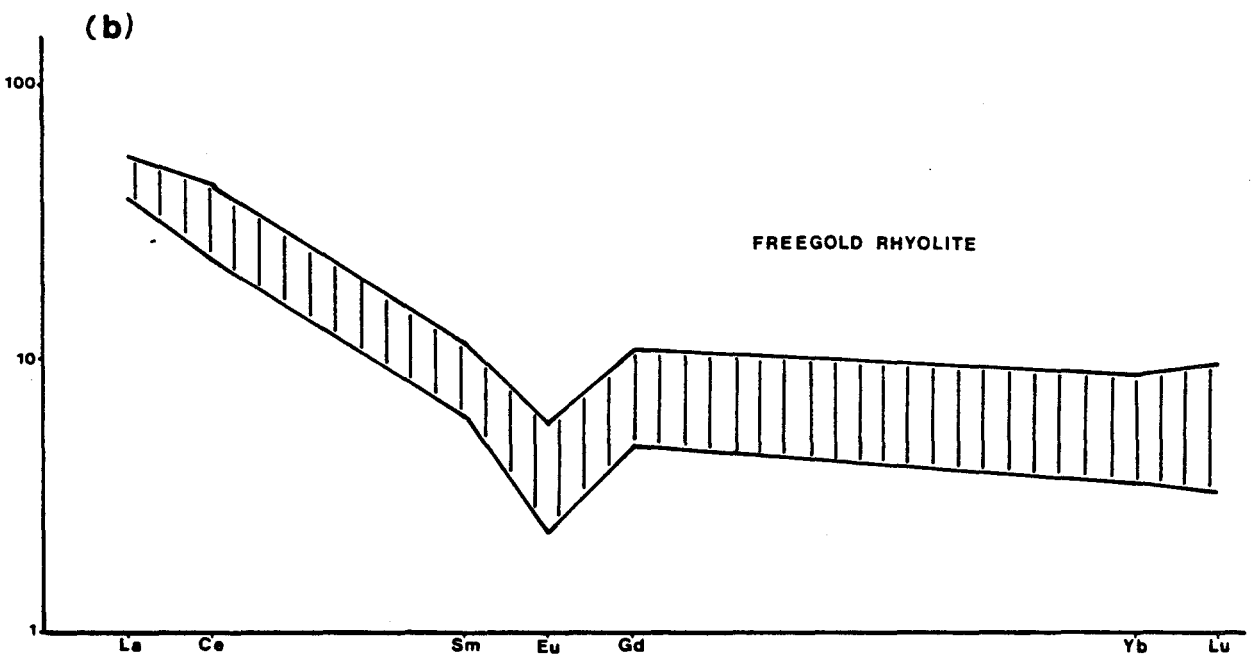
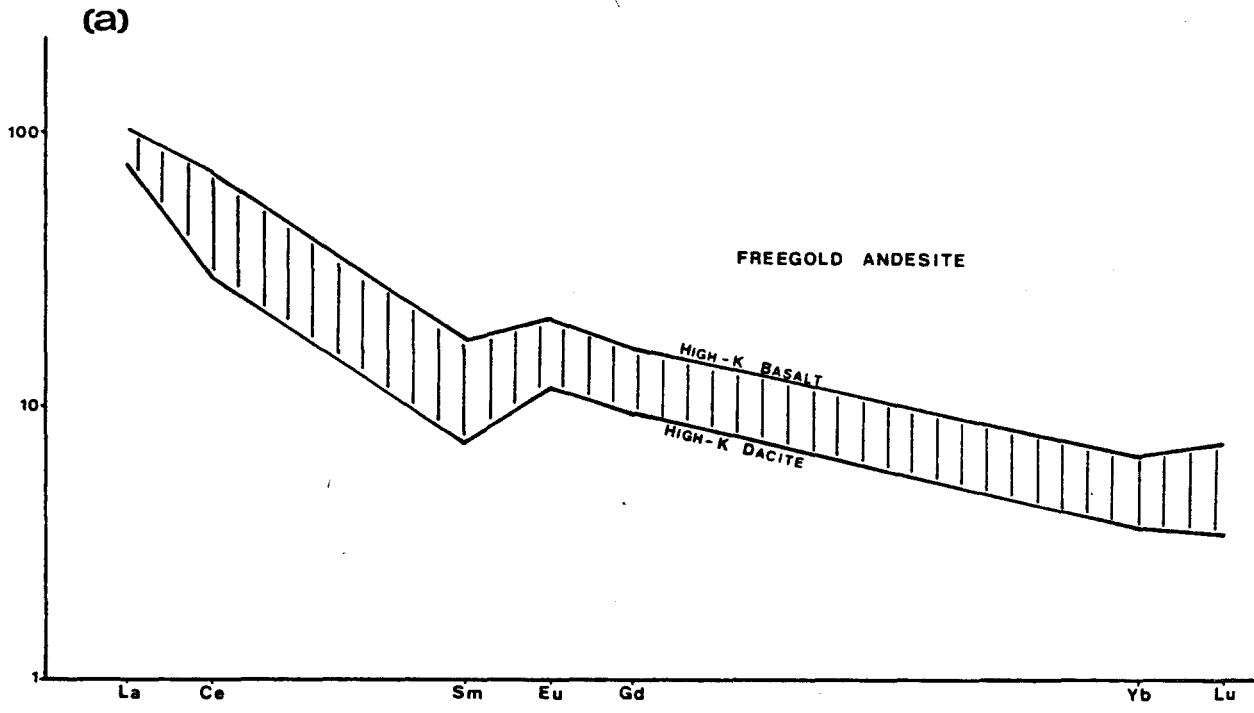
The basaltic sample is aphanitic, while the andesite and dacite samples contain phenocrysts of plagioclase, hornblende and quartz. If the basaltic sample is interpreted to be the earliest intrusive phase from an undifferentiated source melt, then the decreasing REE abundances in the andesitic and dacitic samples may be attributed to some type of crystallization process. The partition coefficient for most minerals in basaltic to andesitic melts is less than 1 (Henderson, 1982, Table 5.2a, p. 91), and therefore crystallization of mineral phases would tend to enrich the residual liquid in REE's, particularly the LREE's. The REE pattern for this group of rocks, however, shows the opposite trend in that the more 'evolved' dacitic rocks have lower total REE abundances.

The REE data does not suggest that this group of rocks has evolved from a basaltic to a dacitic composition by fractional crystallization of a mafic melt according to the theory of REE partitioning during fraction crystallization. An alternate explanation is mixing of mantle derived magmas and magmas generated by partial melting of lower crustal material depleted in total REE's, which is consistent with the tectonic setting of these rocks.

Figure 9. Chondrite normalized REE pattern for

(a) andesite group

(b) rhyolites



#### 4.2.2.4 Rhyolites

The REE pattern for rocks of rhyolitic composition are shown in Fig. 9B. LREE show relative enrichment in comparison to HREE and a negative Eu anomaly is present in all samples. The negative Eu anomaly can be accounted for by the fractionation of plagioclase or sanidine from the original liquid. The partition coefficient ( $K_{\text{mineral-liquid}}$ ) for Eu partition between plagioclase and sanidine with respect to silicic melts is 3.8-7.9 and 3.3-6.5 respectively (Nash and Crecraft, 1985), and therefore the crystallization of either phase could produce a negative Eu anomaly in a rock forming from the residual liquid. The low absolute abundances of LREE's cannot be attributed to fractional crystallization of feldspar, but may be due to the fractionation of LREE-rich accessories such as allanite ( $K_{\text{LREE}}=750-2800$  (Mahood and Hildreth, 1983)) or monazite as suggested by Miller and Mittlefehldt (1982).

Aplite dykes of rhyolitic composition associated with the Nisling Range Alaskites to the west are interpreted by Lynch and Pride (1984) to be the residual phases of a fractionally crystallized, coarse to medium grained, alaskitic alkali granite. These residual phases are chemically and texturally similar to Freegold Mountain rhyolites. The Nisling Range dykes, which have REE patterns comparable to Freegold rhyolites, are LREE depleted, HREE enriched and have a more negative Eu anomaly relative than

the coarse grained, allanite-bearing alaskite. Lynch and Pride (1984) argue that fractional crystallization of allanite in the early coarse and medium grained phases accounts for the REE trend.

An alternate interpretation is that the Freegold rhyolites were derived by partial melting of an upper crustal source region already depleted in residual plagioclase (Alburquerque, 1977) such as an arenaceous sandstone or greywacke. Anatexis of such a rock type would explain the low total REE abundances, and fractional crystallization of such a melt would account for the Eu anomaly. Partial melting of a sialic source also accounts for the absence of mafic components which might be expected from a fractionally crystallized mafic melt.

The REE abundances for the Freegold Mountain rhyolites are very low compared to Twin Peaks, Utah (Nash and Crecraft, 1985), Taupo Volcanic Zone, N.Z. (Cole, 1979), and the Sierra La Primavera, Mexico and Bishop Tuff, California (Mahood and Hildreth, 1983) rhyolites. They are comparable however, with high level rhyolite intrusives of the Mt. Skukum, Yukon area (Smith, 1983). Smith also attributed the low LREE abundances and negative Eu anomaly of the Skukum rhyolites to the fractionation of feldspar and LREE-rich accessory minerals.

Superimposing the rhyolite REE pattern (Fig. 9B) over those of the 'andesite' clan (Fig. 9A) shows that the rhyolites are more depleted in LREE and Eu. The HREE

abundances are about the same in both series. Whether the rhyolites are derived from a highly fractionated melt of original andesitic to dacitic composition is uncertain. In theory, fractional crystallization of mineral phases from a dacitic melt should enrich the residual silicic liquid in both light and heavy REE and produce a negative Eu anomaly (Arth, 1976). The Freegold rhyolites do show a negative Eu anomaly, but are not enriched in LREE or HREE although the LREE depletion may be the result of fractionation of LREE-rich accessory minerals. The lack of HREE enrichment in the rhyolite suggests that their origin is not simple fractional crystallization of a dacitic source melt. Rhyolitic volcanism at Freegold Mountain may have resulted from a separate melting event of sialic crust occurring after andesitic-dacitic volcanism.

## CHAPTER 5. GEOCHRONOLOGY

### 5.1 Introduction

Radiometric data has been used extensively to sort out the complex geological history of the Yukon Crystalline Terrane. Unfortunately, many of the dates are from samples collected during reconnaissance geological surveys in which the degree of geological control was less than desirable (Wilson et al., 1985). Consequently, they actually add to the complexity of delineating intrusive events. The common usage of the K-Ar method (Templeman-Kluit and Wanless, 1975; Wanless et al., 1970; and Godwin, 1975) in areas of multiple batholith emplacement where the resetting of the K-Ar age towards the youngest intrusive event is commonplace (Dalrymple and Lanphere, 1969) can further complicate interpretations.

This section is an attempt to review radiometric data in the Freegold Mountain - Mt. Nansen area, and provide information on the field relationships and age discrepancies of the major rock types in the thesis area.

#### 5.1.1 Metasedimentary Rocks

The metasedimentary rocks are the oldest lithology in the area based on field relationships showing that all igneous rocks cut them. They are considered to be Late Paleozoic (Templeman-Kluit, 1984).

### 5.1.2 Syenite and Granodiorite Plutons

The relationship between time of granodiorite and syenite intrusion is enigmatic. Johnston (1937) cited the following as evidence for his interpretation that the granodiorite is the younger of the two:

"Close to its contact with syenite porphyry at the head of Liberty Gulch the granodiorite porphyry becomes light grey and finer grained."

The actual contact between the two rock types, however, was not observed by him.

Contacts between syenite and granodiorite were observed by the author in outcrop exposed along the road 50 m east of Forrest Gulch and on the south side of Seymour Creek about one km to the west of the map area. These contacts clearly showed evidence that the syenite intrudes into the granodiorite. Photos 13, 14 and 16 show xenoliths of granodiorite within syenite and hornblendite. Photos 17 and 18 are from an outcrop which contains small "dykes" of coarse grained syenite intruding along joint patterns in the granodiorite. Photo 15 shows a small sill-like feature with modal variation in mineralogy. This variation is due to the settling of the dense amphibole crystals at the base and "floating" of the less dense crystals of K-feldspar towards the top of the sill. The appearance of the granodiorite in this area was similar to that in the map area and it is concluded on this field evidence that the syenite porphyry is younger than the granodiorite.

This conclusion is problematic however, in that

Photo 13. Xenoliths of granodiorite within syenite.

Photo 14. Xenoliths of granodiorite within syenite.



Photo 15. A 45 cm thick "sill" of syenite within granodiorite showing a hornblende-rich lower cumulate zone and K-feldspar-rich upper zone.

Photo 16. Xenolith of granodiorite within cumulate hornblendite.

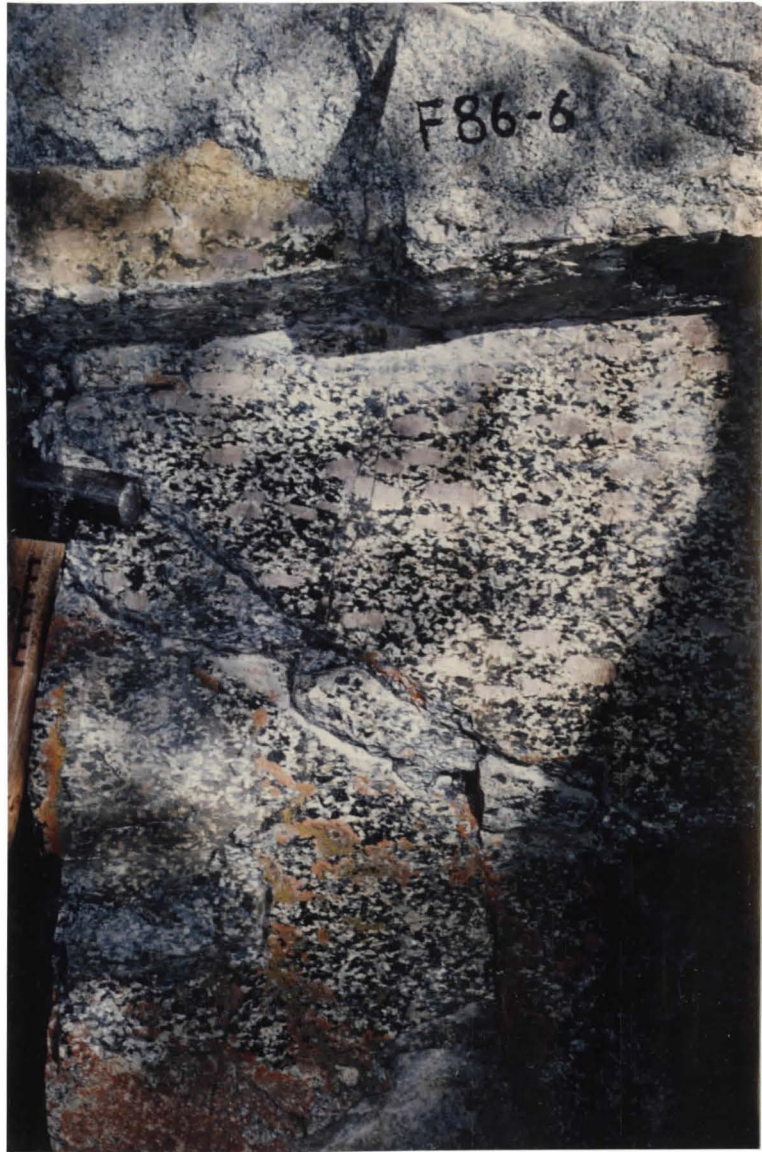
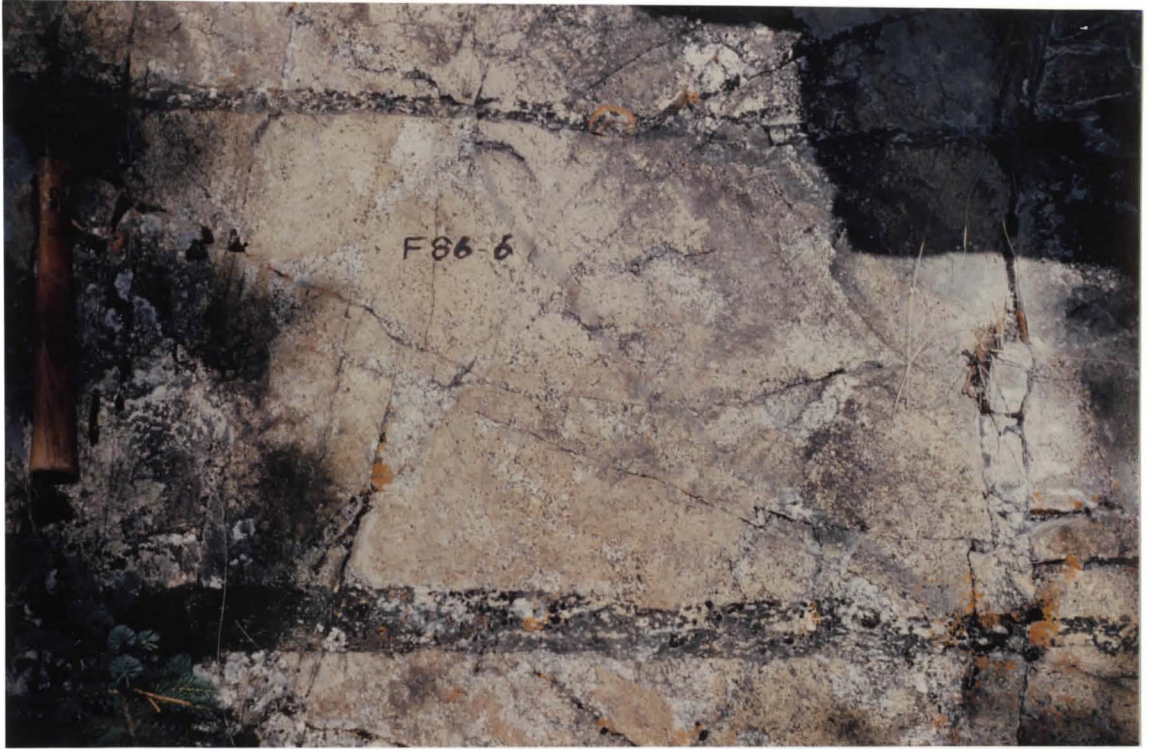


Photo 17. Small dykes of syenite intruding joint planes in granodiorite.

Photo 18. A close-up showing the coarse-grained nature of the right portion of the lower dyke in Photo 17. Scale is in cm.



radiometric ages for the granodiorite by K-Ar methods are  $110 \pm 8$  Ma (hornblende separate, 7.2 km southwest of study area, see Figure 4) and  $85 \pm 3$  Ma (biotite separate, 4.5 km northwest of study area, see Figure 4) while syenite ages are reported to be:

$142 \pm 10$  Ma (hornblende, within study area),  $184 \pm 7$  Ma (hornblende, 22 km west of study area), and  $152 \pm 7$  Ma (hornblende, 11 km west of study area) (Templeman-Kluit, 1974).

Of the two granodiorite samples, the latter sample was taken from a rock type which does not resemble the granodiorite in the Freegold Mountain area, but is more characteristic of a fine grained granite. It may therefore, represent an intrusive different in age from the Freegold granodiorite.

The sample yielding the  $110 \pm 8$  Ma age is from a granodiorite pluton 7 km southwest of the thesis area. No estimates of the reliability of this age are available and the sample site was not visited by the author to observe the nature of the granodiorite. Due to the discrepancies between field relationships and radiometric dates it was decided to further investigate this problem using Rb-Sr dating.

## 5.2 Rb-Sr Dating of the Syenite Porphyry

Of the two lithologies, it was decided to date the syenite porphyry because:

1. It is more difficult to obtain fresh samples of granodiorite in the map area because of widespread alteration within the granodiorite.

2. Different crystallization products of syenite including hornblendite and syenite porphyry should give a good spread in Rb/Sr ratio within the available outcrop scale, therefore minimising the chance of getting non-comagmatic samples.

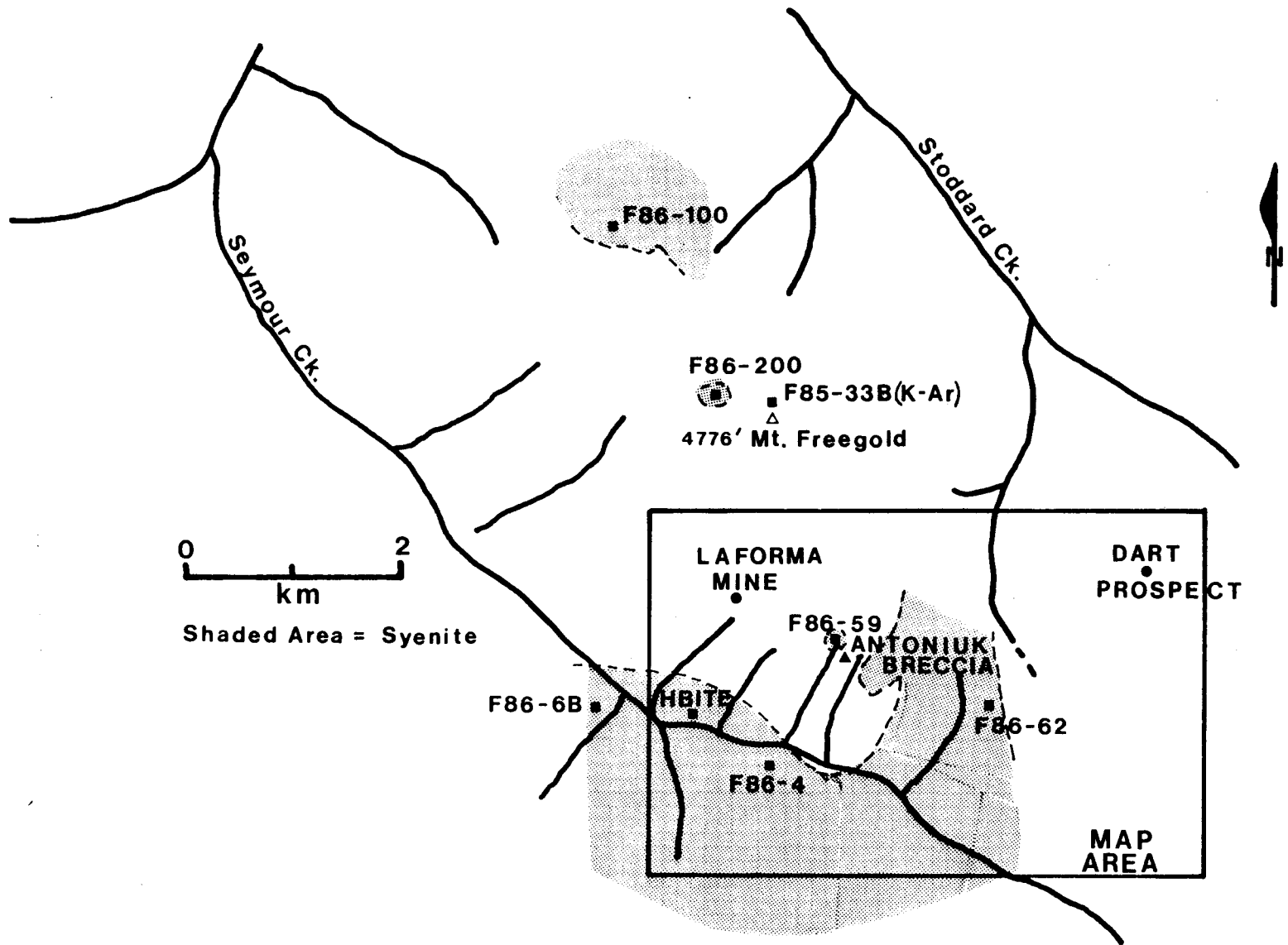
3. The coarse grain size of the syenite made mineral extraction easier and minimized the potential of contamination by other minerals during mineral separation.

4. The previous syenite dates were thought more likely to be in error because of the common occurrence of excess  $^{40}\text{Ar}$  in amphiboles (Dalrymple and Lanphere, 1969; Gilbert and Foland, 1986), thereby giving an age older than the actual crystallization age.

#### 5.2.1 Methodology

Eight large syenite samples weighing between 5 and 10 kg were collected for age dating purposes within and around the map area as shown on Figure 10. These samples were crushed and ground to - 200 mesh using a Chipmunk jaw crusher, a ceramic pulverizer, and a tungsten-carbide shatterbox. Mineral separates were obtained from cut slabs by a drill fitted with a masonry bit. This method was found to be useful in that contamination by neighboring minerals was easily avoided, and any contaminants in the drill

Figure 10. Sample locations for Rb-Sr and K-Ar geochronology.



cuttings were obvious and could be removed or the sample rejected.

The samples were then homogenized and split, with half submitted for chemical dissolution and isotopic determination, and the other half prepared for Rb and Sr concentration determination by XRF. Rb and Sr concentrations were determined by a Phillips PW 1450 automated X-Ray Fluorescence spectrometer using the Mo-Compton peak method described by Reynolds (1963; 1967) and Turek et al. (1977). Triplicate samples were prepared in powder pellet form by combining the sample powder (3 to 4 grams) with 3 drops of Mowiol binding solution in a 5 dram glass vial. This mixture was then compressed under 20 tons pressure in a chemplex aluminum pellet cup using a Spex 30 ton press.

The aliquot of sample submitted for isotopic determination was dissolved and strontium separated by wet chemical techniques (adapted from Beakhouse and Heaman, 1980). The  $^{87}\text{Sr}/^{86}\text{Sr}$  ratio was determined on a VG 354 five-collector solid-source mass spectrometer with magnetic field switching and data processing controlled by a Hewlett-Packard computer.

### 5.2.2 Analytical Results

The results obtained by XRF analyses and mass spectrometry are provided in Table 4. Reproducibility of XRF results was generally less than 3% relative error at the

Table 4. Rb-Sr Data Table for Big Creek Syenite, Freegold Mountain

Sample # (UTM Location)	Rb conc.	Sr conc.	Rb/Sr (2 $\sigma$ rel. error)	$^{87}\text{Sr}/^{86}\text{Sr}$ (2 $\sigma$ rel. error)	$^{87}\text{Rb}/^{86}\text{Sr}$ ( $\pm 0.5\%$ error)	Comments
Hornblende 389758 mE 6984788 mN	19.8 21.2 21.1	384.5 385.1 388.3	0.054885	0.786253 $\pm 0.003\%$	0.15545	
	$\bar{x} = 20.7 \pm 0.8$	$\bar{x} = 383.3 \pm 2.6$				
	Rb. I.O. = 19.8					
FB6 - 188H	13	238	0.05824	0.786334 $\pm 0.002\%$	0.16764	hornblende separate
FB6 - 188K	87	417	0.28961	0.787164 $\pm 0.002\%$	0.68339	orthoclase separate
FB6 - 6C	38 38 37	853 836 835	0.04438 0.04578 0.04463			sample lost during preparation
	$\bar{x} = 38 \pm 1$	$\bar{x} = 841 \pm 18$	$\bar{x} = 0.04463$ $\pm 3.6\%$			
FB6 - 4 398588 mE 6984288 mN	59 61 59	542 551 548	0.10884 0.11153 0.10768	0.786564 $\pm 0.002\%$ 0.786555 $\pm 0.002\%$	0.31574	
	$\bar{x} = 60 \pm 1$	$\bar{x} = 547 \pm 5$	$\bar{x} = 0.10932$ $\pm 3.8\%$			
FB6 - 288 398888 mE 6987788 mN	114 111 113	973 955 976	0.11689 0.11588 0.11589	0.786478 $\pm .002\%$	0.33683	
	$\bar{x} = 113 \pm 2$	$\bar{x} = 968 \pm 11$	$\bar{x} = 0.11619$ $\pm 0.9\%$			
FB6 - 59 391188 mE 6985358 mN	54 55 54	262 268 258	0.28967 0.21892 0.21872	0.787142 $\pm 0.003\%$	0.59786	
	$\bar{x} = 54 \pm 1$	$\bar{x} = 268 \pm 2$	$\bar{x} = 0.21844$ $\pm 0.5\%$			

Sample # (UTM Location)	Rb conc.	Sr conc.	Rb/Sr (2 $\sigma$ rel. error)	87Sr/86Sr (2 $\sigma$ rel. error)	87Rb/86Sr ( $\pm$ 0.5% error)	Comments
FB6 - 100 389100 mE 6909300 mN	96	1110	0.08642	0.706460 $\pm$ 0.003%	0.25008	
	95	1099	0.08623			
	96	1107	0.08647			
	-----		$\bar{x}$ =0.08637			
	$\bar{x}$ = 96 $\pm$ 1	$\bar{x}$ =1105 $\pm$ 6	$\pm$ 0.2%			
FB6 - 68 388900 mE 6904800 mN	130	1277	0.10189	0.706570 $\pm$ 0.002%	0.29585	
	135	1307	0.10342			
	133	1299	0.10269			
	-----		$\bar{x}$ =0.10267			
	$\bar{x}$ = 133 $\pm$ 3	$\bar{x}$ = 1294 $\pm$ 16	$\pm$ 1.2%			
FB6 - 62 392600 mE 6904700 mN	48	618	0.07787	0.706624 $\pm$ 0.004%	0.22576	high REE signature
	46	603	0.07624			
	49	614	0.07624			
	-----		$\bar{x}$ =0.07843			
	$\bar{x}$ = 48 $\pm$ 2	$\bar{x}$ = 612 $\pm$ 8	$\pm$ 3.4%			

$2\sigma$  level for the Rb/Sr ratio. Blanket errors of 0.5% and 3.0% were assigned to the  $^{87}\text{Rb}/^{86}\text{Sr}$  ratio when calculating the radiometric age of the syenite. The error in the  $^{87}\text{Sr}/^{86}\text{Sr}$  ratio was less than 0.004% at the  $2\sigma$  level. Replicate analysis of F86-4 ( $\pm 0.001\%$  relative error at  $2\sigma$ ) confirmed the machine generated output error. Figure 11 is a plot of the data in Table 4. A value of  $1.42 \times 10^{-11} \text{ yr}^{-1}$  was used for the decay constant of  $^{87}\text{Rb}$ . A regression line calculated using a modified York (1969) regression model on all nine samples yields an age of  $131 \pm 30 \text{ Ma}$  ( $2\sigma$  error, MSWD = 12.47) with an  $R_1 = 0.7060 \pm 0.0001$ . In an attempt to refine the age, sample F86-62 was excluded from the regression calculation because it is thought that this sample is affected by assimilation of the older sedimentary rocks during its crystallization. Evidence for this conclusion is the high REE content of this sample compared to other syenite samples (Figure 8B) and the high  $^{87}\text{Sr}/^{86}\text{Sr}$  ratio, both observations suggesting that F86-62 was collected too close (5m) to the syenite-sediment contact so that contamination by older crustal material occurred. The age calculated on the remaining eight samples is  $138 \pm 20 \text{ Ma}$  ( $2\sigma$  error, MSWD = 5.29) with an  $R_1 = 0.7060 \pm 0.0001$ . Thus, while the age and initial ratio are changed only modestly the error in the age is reduced by ca. 30%.

A close examination of F86-200 revealed the presence of small, pervasive, post-crystallization quartz microveinlets not present in other samples submitted for geochronology.

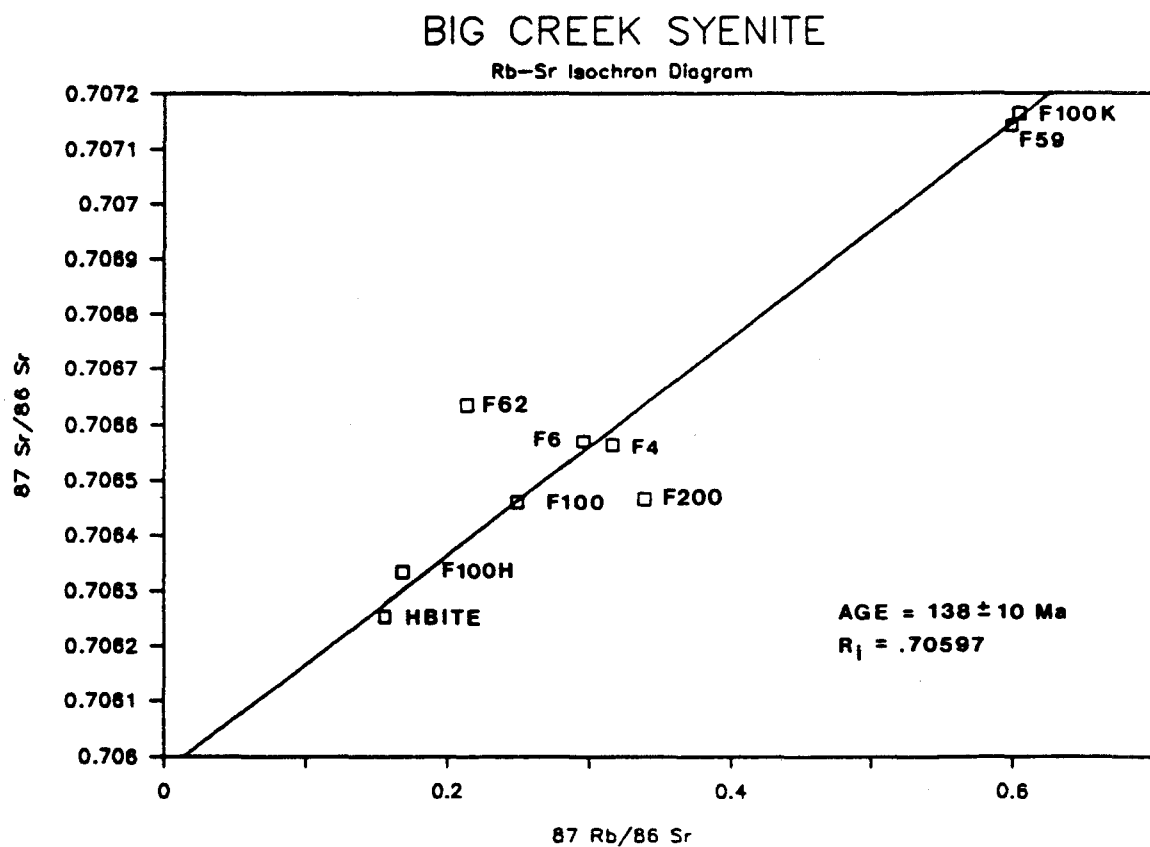


Figure 11. Rb-Sr isochron diagram for Big Creek Syenite.

Chemical analysis of this rock (Appendix A) show that it has a gold concentration of 44 ppb, while all other syenite samples have less than 5 ppb suggesting that the gold enrichment is related to the vein material. The exact effect of these microveinlets and associated alteration on the Rb/Sr ratio and the isotopic integrity of the rock sample is uncertain. However, it is apparent that F86-200 deviates from the regression line on Figure 11. A recalculation of the regression line using 7 data points (excluding F86-62 and F86-200) results in an age of  $138 \pm 10$  ( $2\sigma$  error, MSWD = 0.62) with an  $R_1 = 0.70597 \pm 0.00002$  using blanket errors of 0.004% for  $^{87}\text{Sr}/^{86}\text{Sr}$  and 3.0% for  $^{87}\text{Rb}/^{86}\text{Sr}$ . A smaller blanket error for the latter of 0.5% made no significant difference in the regression line calculation, yielding an age of  $138 \pm 8$  Ma ( $2\sigma$  error, MSWD = .77). Again, the main effect on the analysis is a reduction of error on the Rb-Sr age.

### 5.2.3 Discussion of Rb-Sr Dating Results

The age of  $138 \pm 10$  Ma is in agreement within error of 2 of the 3 K-Ar ages reported by Templeman-Kluit (1984) for the Big Creek Syenite and very similar to the K-Ar date of  $142 \pm 10$  Ma from a sample located in the vicinity of the thesis area. Thus it appears that the granodiorite in the thesis area is older than the reported age of  $110 \pm 8$  Ma for the sample taken 7.2 km to the southwest. This leads to two possibilities: either the K-Ar date for the granodiorite has

been reset and is in error or the granodiorite in the thesis area is not equivalent to the type sampled to the southwest.

No comment can be made as to the accuracy of the K-Ar date or whether the granodiorite was similar in character to the type present in the study area. It can be stated however that an age for the granodiorite greater than 140 Ma would make it comparable in age to a large granodioritic body located to the immediate northeast of the thesis area which has yielded K-Ar ages of:  $142 \pm 10$  Ma (hornblende),  $174 \pm 6$  Ma (biotite),  $177 \pm 9$  Ma (bi), and  $180 \pm 9$  Ma (bi). The last three ages are supplemented by a zircon age of 192 Ma (no errors given)(Templeman-Kluit, 1984).

Based on physical characteristics, this Triassic granodiorite cannot be correlated with the the study area granodiorite since it has a lighter colour, lesser potassium feldspar and a well developed penetrative foliation. Based on the available radiometric age data, the portion of the granodiorite in the Freegold Mountain area known as the Seymour Creek stock (see Fig. 4) is a separate entity in time and space. Clearly more isotopic age dating studies are required. Samples of granodiorite from the thesis area have been submitted to the geochronology laboratories at the Geological Survey of Canada where U-Pb dating on zircons and sphene will be undertaken in an attempt to further clarify the situation.

Initial ratios greater than about 0.706 reflect the contribution of radiogenic strontium from Precambrian rocks

to rising magma bodies according to Rodgers et al., (1974) and Le Couteur and Templeman-Kluit, (1976). If a Mesozoic aged magma ascended through oceanic crust of Phanerozoic age the initial  $^{87}\text{Sr}/^{86}\text{Sr}$  ratio of about 0.704 would not be significantly affected by assimilation of wallrock Sr since the crust would not have accumulated much radiogenic strontium. The Big Creek Syenite is interpreted to be on the hinge line which marks the transition zone between regions floored by older Precambrian continental crust and younger oceanic crust probably having been emplaced during subduction related melting of the younger oceanic plate (Le Couteur and Templeman-Kluit, 1976). The initial Sr isotope ratio of 0.706 of Big Creek Syenite suggests that the pluton was emplaced during subduction related melting and contaminated to a minor extent by Precambrian continental crust ( $^{87}\text{Sr}/^{86}\text{Sr}=0.0707-0.709$  (Faure and Powell, 1972)) upon ascent. Thus the isotopic data are compatible with the model that the Big Creek Syenite marks the western boundary of continental crust in the Early Cretaceous.

### 5.3 Andesites, Dacites and Rhyolites

The dykes of these rock types cut all other rocks and represent the last intrusive events in the Freegold Mountain area. The age difference of the above three are probably small although one outcrop between Grizzly and Nabob Gulches shows a rhyolite dyke crosscutting a dacite dyke. Johnston (1937) arrived at a similar conclusion although no concrete

evidence was provided. Mining consultants on the early workings of the Laforma Mine also reported rhyolite dykes crosscutting andesite but this information could not be corroborated. It is evident from the authors reconstruction of the Laforma Mine workings (Chapter 7) that fault structures cutting and displacing andesite dykes were parallel to faults acting as conduits for rhyolite intrusion. The age of rhyolitic volcanism is important to define because many precious metal systems in the Freegold Mountain area have unequivocal temporal and spatial relationships with shallow seated silicic volcanism. The dating of rhyolite emplacement may therefore help constrain the age of these gold deposits. The timing of fault activation and rhyolite intrusion will be discussed in more detail in Chapter 6.

The age of these dykes in the thesis area has until now been unknown, but they have generally been correlated by Templeman-Kluit (1984) as the equivalents of the Mount Nansen Volcanics. These rocks have recently been dated as Late Cretaceous (Grond et al., 1984) with samples near the village of Carmacks giving ages of  $73.1 \pm 2.5$ ,  $67.9 \pm 2.3$ , and  $68 \pm 2.2$  Ma (all errors reported as  $1\sigma$ ).

Samples of the rhyolite, particularly the coarser grained varieties have been submitted to the Geological Survey of Canada Geochronology Laboratory for U-Pb radiometric dating on zircons. A sample of a coarse grained rhyolite dyke from the summit of Freegold Mountain, F85-33B

(see Figure 10), was submitted to Geochron Laboratories, Cambridge, Mass. for K-Ar dating in order to determine the approximate age of rhyolitic volcanism and by association the age of precious metal deposition. The duplicate analytical results are provided in Table 5. This sample yielded an age of  $77.5 \pm 6.2$  ( $2\sigma$  error).

F85-33B, like most other rhyolite samples in the Freegold Mountain area, has undergone hydrothermal alteration during intrusion. Thus the age may not reflect the actual time of intrusion and cooling but could possibly be the age where the hydrothermal system cooled below the blocking temperature of argon in sericite or other K-bearing hydrothermal minerals. This period of time between intrusion and cessation of alteration is probably minimal and well within analytical error.

The model age of  $78 \pm 6$  Ma is similar to the age of Mount Nansen and Carmacks group volcanics (Grond et al., 1985) within error. The intrusive volcanic rocks in the Freegold Mountain area can therefore be correlated with Mount Nansen volcanics as suggested by Templeman-Kluit (1984). The temporal and spatial relationship of precious metal deposits with rhyolitic volcanism in and around the thesis area suggests that the age of mineralization is Late Cretaceous. The Casino porphyry copper complex which has precious metal mineralization and is located 100 km NW of Freegold Mountain has been dated at  $70 \pm 5$  Ma (Godwin, 1975). The occurrence of gold bearing quartz veins and

Table 5. Analytical Data for K-Ar age determination for rhyolite sample F85-33B

Argon Analyses:

$^{40}\text{Ar}$ , ppm	$^{40}\text{Ar}/\text{Total } ^{40}\text{Ar}$	Average $^{40}\text{Ar}$ , ppm
0.01529	0.562	
0.01518	0.568	0.01523

Potassium Analyses:

% K	Ave. % K	$^{40}\text{K}$ , ppm
2.806	2.776	3.311
2.745		

Apparent Age =  $77.5 \pm 3.1$  (1 $\sigma$  error)

Constants Used:

$$\lambda_{\beta} = 4.962 \times 10^{-10}/\text{year}$$

$$(\lambda_{e} + \lambda'_{e}) = 0.581 \times 10^{-10}/\text{year}$$

$$^{40}\text{K}/\text{K} = 1.193 \times 10^{-4} \text{ g/g}$$

$$^{40}\text{Ar} = \text{radiogenic } ^{40}\text{Ar}$$

breccia bodies associated with felsic volcanism at Freegold Mountain and Mount Nansen, and of large porphyry copper systems during a similar period of volcanic activity, may suggest a regional Dawson Range volcanogenic-metallogenetic event.

The Late Cretaceous age for Freegold Mountain rhyolitic volcanism discounts any temporal correlations with Skukum rhyolites ( $53 \pm 2$  Ma; Pride and Clark, 1985), and may preclude correlation with the Nisling Range Alaskite (52-67 Ma: Templeman-Kluit and Wanless, 1975; Le Couteur and Templeman-Kluit, 1976).

## CHAPTER 6. STRUCTURAL GEOLOGY

### 6.1 Introduction

The determination of the structural geology of the Freegold Mountain area is more than of academic interest in that most ore deposits, particularly vein deposits, are structurally controlled phenomenon. Figure 2 shows the location of major structures, precious metal vein deposits and breccias in the Freegold Mountain area. The development of a gold deposit requires tremendous volumes of fluid flow to transport and deposit sufficient quantities of low solubility metals. Ground preparation by structural deformation is a prerequisite for the creation of high permeability, particularly in non-permeable igneous rocks. The emplacement of highly viscous rhyolite dykes is also dependant on the existence of fracture zones since high viscosity material cannot induce fracture propagation during intrusion.

Structural studies in the Dawson Range are limited by lack of good outcrop. Large structural features can be mapped as linear valley systems (Big Creek fault) with displaced rock types on either side (Templeman-Kluit, 1984) or as linear to curvilinear notches in topography which can be interpreted by ground observation or from air photographs. An example of the latter is the Camp fault which cuts along the SW side of Freegold Mountain (Map 1, Photo 19). Careful observation of fracture trends during

Photo 19. View east across Seymour Creek valley towards Freegold Mountain. The dashed line represents the Camp Fault which cuts a distinct notch into the side of Freegold Mountain. The Laforma Mine is to the left.

Photo 20. Vertically oriented slickenslide development along northerly trending fracture planes.



mapping of outcrop, exploration trenches, and detailed mapping of faults and fracture systems within the Laforma mine have allowed a preliminary structural interpretation of deformation in the thesis area.

The orientation of known major fault structures in the thesis area are presented in Table 6.

Table 6.

<u>Structure</u>	<u>Orientation</u>	<u>Direction and Displacement</u>
Big Creek fault	130°	dextral, 14 km
Camp fault	130°	dextral?/vertical?
Pal fault	150°	dextral, 400 m
Laforma Vein/fault	22°	sinistral, 75 m
Rambler Vein/fault	32°	unknown

The Big Creek fault has been documented by Templeman-Kluit (1984) to cut through Big Creek Valley to the northwest of Freegold Mountain (see Fig. 4). The dextral displacement of a granite by this fault system is a minimum of 14 km. The fault has been interpreted by Templeman-Kluit to bisect Freegold Mountain, although no physical evidence of such a major fault system was observed by this author in the area. It is possible that the Camp fault is a splay of the Big Creek fault and represents the plane of deformation in the Freegold Mountain area, although not enough data is available as to its sense of motion and displacement to verify this.

The Camp fault outcrops along the Freegold Mountain road just after the Laforma road turnoff (Fig. 5). The fault zone cutting through syenite leaves the rock highly brecciated and friable, suggesting brittle deformation. No

markers have been identified to indicate the sense of displacement along this shear zone, but the occurrence of hornblendite on the south side of the fault zone may suggest that some vertical movement has taken place, raising the cumulate zone of the syenite above the elevation of syenite to the north of the Camp fault. This evidence is speculative however since the cumulate hornblendite cannot be considered a well defined marker horizon.

The Pal fault is a major structure against which the southern end of the Laforma vein abruptly ends. It is apparent from Map 1 and Figure 17 (see Chapter 7) that rhyolite dykes near the Pal fault turn westward, parallel to the direction of fault movement. The dykes have intruded along curving splay fractures created during dextral movement on the Pal fault. Intrusion of rhyolite into such a fracture system would account for the lack of brittle deformation that would normally accompany drag folding.

In 1975 diamond drilling on the south side of the Pal fault intersected a quartz vein with mineralogy and gold grades similar to that of the Laforma Vein which was interpreted to represent the southern displaced portion of the Laforma Vein (Antoniuk, 1975). This would suggest that about 400 m of dextral displacement has occurred on this structure. Diamond drilling into the Pal fault discovered a highly brecciated zone with anomalous gold values interpreted to represent the brecciated remnants of the Laforma Vein caught up in the shear zone.

The Laforma Vein has been emplaced along a shear structure which has sinistrally displaced an andesite dyke (Beavan, 1963) on the order of 75 m (see Figure 17). The shear zone is highly brecciated, silicified and altered. Slickenslides suggest that only lateral movement has occurred along this structure. Mining operations at the Laforma Mine were hampered by ground control problems and timbering was necessary to prevent cave-ins of the non-consolidated gouge material surrounding the vein.

## 6.2 Regional Structures and their Implications on the Structure of Freegold Mountain

The Freegold Mountain area is located between two megastructures, the Tintina fault and Shakhwak-Denali fault, major lineaments along which extensive dextral transcurrent motion has occurred (Gabrielse, 1985). Displacement along the Tintina fault from the Cretaceous to the Eocene is estimated to be a minimum of 450 km (Roddick, 1967; Templeman-Kluit, 1979). The Shakhwak-Denali fault system has an estimated displacement of about 300 km (Eisbacher, 1976; Lanphere, 1978). Initiation of movement along this major structure is not considered to have begun until 55 Ma, transferring the regional stress field to the west. If initiation of movement along the Shakhwak-Denali fault did not occur until the Eocene, it postdates the period of structural deformation and silicic volcanism in the Freegold Mountain area.

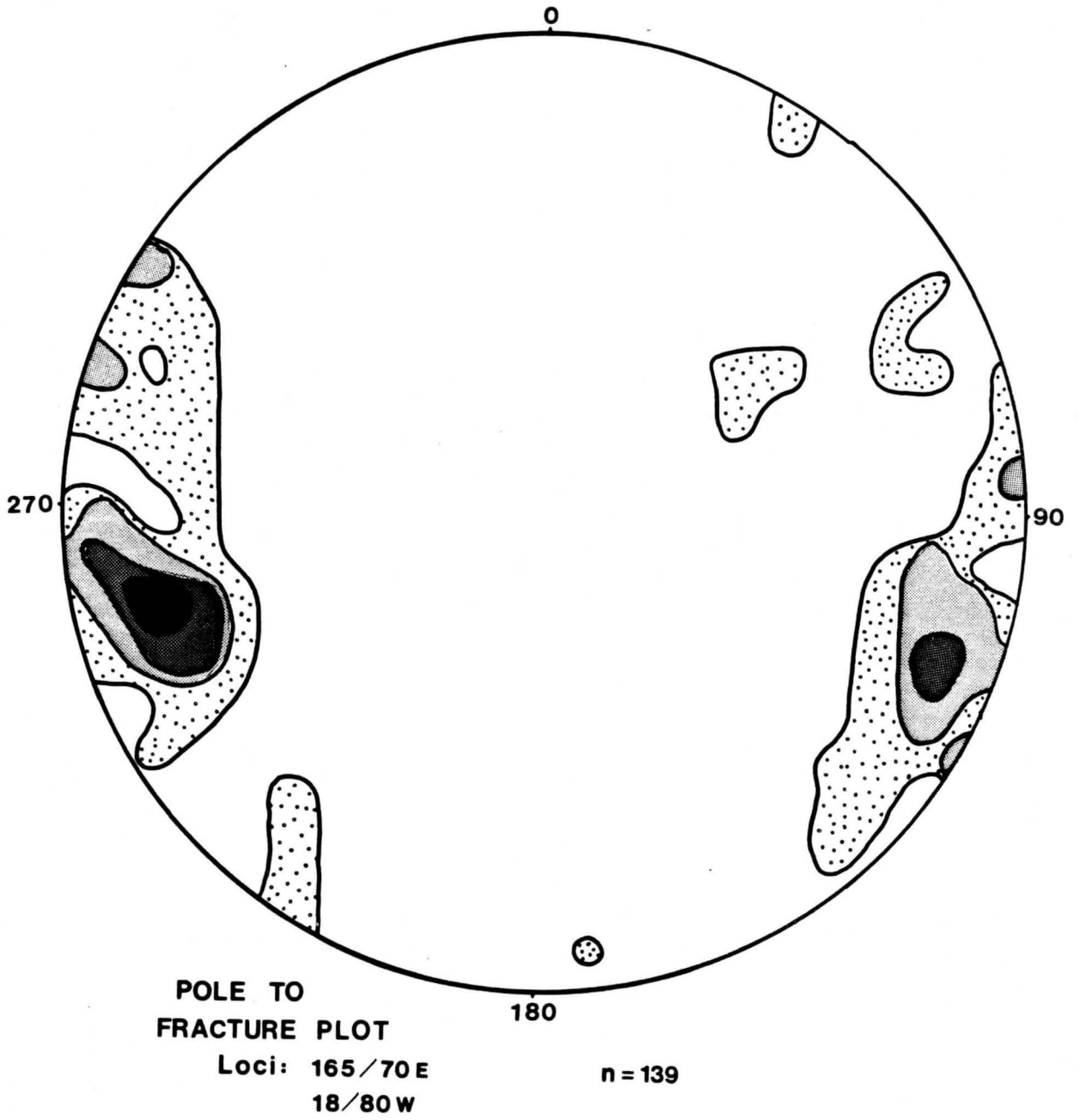
The orientation of both fault systems is  $130^{\circ}$ . Concordant to these systems are structures such as the Big Creek and Camp faults where small amounts of displacement may have taken up stress in the regions away from the major shear zones. The direction of principal stress in the region through the Cretaceous was  $165^{\circ}$  (Gabrielse, 1985), similar to the direction of the northward subducting Kula plate. The spatial orientation of faults, fractures, veins and dykes in the Dawson Range must be controlled by the orientation of principal stress fields acting on major shear structures such as the Tintina fault and parallel subordinate structures such as the Big Creek fault.

### 6.3 Structural Deformation in the Thesis Area

Figure 12 is a pole to fracture plot of 139 fracture and fault planes measured within the thesis area, the majority at outcrop scale. The individual measured orientations and locations are provided in Appendix B. Figure 12 shows two distinct trends consisting of a dominant orientation of  $165/70E$  and a secondary trend of  $18/80W$ .

Figure 13 contains rose diagrams of dyke orientations within the thesis area. Figure 13A displays the cumulative orientation of 46 different dykes of varying composition, as listed in Appendix B. From this plot there are two principal directions, a NNE and a NE trend. In order to constrain dyke emplacement to a relatively short period of time, it was decided to look only at the orientation of

Figure 12. Pole to fracture plot of fracture planes at  
Freegold Mountain.



rhyolite dykes. Figure 13B is an isolated plot of rhyolite dykes within the Antoniuk Breccia, and it is apparent that a preferred orientation exists between  $40^{\circ}$  and  $60^{\circ}$ . These dykes are interpreted to have intruded through a semi-consolidated matrix of highly brecciated rock and therefore the alignment of the dykes within the breccia are probably dependant on the attitude of inferred magma source below the breccia (see Chapter 7), and not controlled by regional stress conditions.

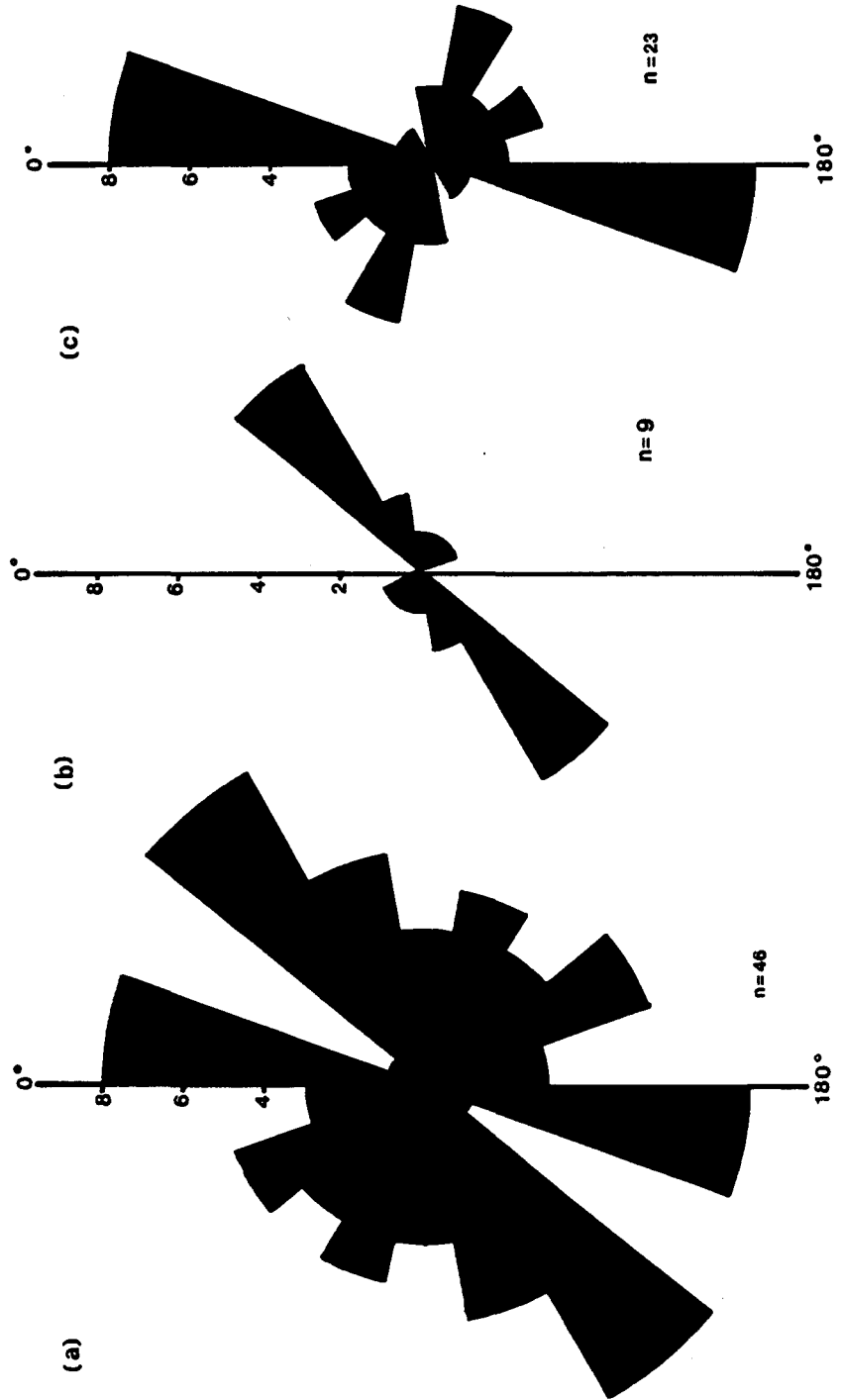
Figure 13C is a plot of remaining rhyolite dykes in the thesis area. These dykes show a dominant principal orientation between  $0^{\circ}$  and  $20^{\circ}$ , and two minor trends at approximately  $100-120^{\circ}$  and  $140-160^{\circ}$ . The orientation of dykes along a  $0^{\circ}$  and  $20^{\circ}$  trend similar to the secondary fracture orientation on Figure 12 is interpreted to represent emplacement of rhyolites along these secondary extensional fracture zones. Further evidence to suggest that extension occurs along these secondary fractures are the Laforma and Rambler gold-quartz veins (up to 2 m in width and displaying open-space filling textures) oriented at  $22^{\circ}$  and  $32^{\circ}$ , respectively. Furthermore, the permeability provided by extensional fractures and faults is a necessary prerequisite to fluid flow, mineral deposition and vein formation. On a more regional scale, rhyolite dykes emanating from the Nisling Range alaskite have a preferred northerly trend (Templeman-Kluit, 1976). The similar orientation of rhyolite dykes of Freegold Mountain and the

Figure 13. Rose diagrams for dyke orientations at Freegold Mountain.

(a) Cumulative orientations for all dykes.

(b) Rhyolite dyke orientations in Antoniuk Breccia.

(c) Rhyolite dyke orientations for thesis area excluding Antoniuk.



Nisling Range suggests a northerly oriented extensional fracture system may have persisted throughout the Dawson Range during Late Cretaceous to Tertiary in response to regional stress conditions.

Tensional and extensional processes operating in northern British Columbia (similar to those acting in Yukon) have been interpreted to have controlled NE-trending normal block faulting (Gabrielse, 1985) and the emplacement of northerly trending peralkaline Stikine Lavas (Souther, 1977) and lamprophyre dykes. Three occurrences of slickenslides observed in the thesis area indicate that some fracture systems oriented north to northeast (see Photo 20) have had a vertical component of movement. Although no indication of the amount of displacement was evident, the presence of such features oriented north to northeasterly does indicate that block faulting is possible.

#### 6.4 Interpretation of Structural Deformation in the Thesis Area

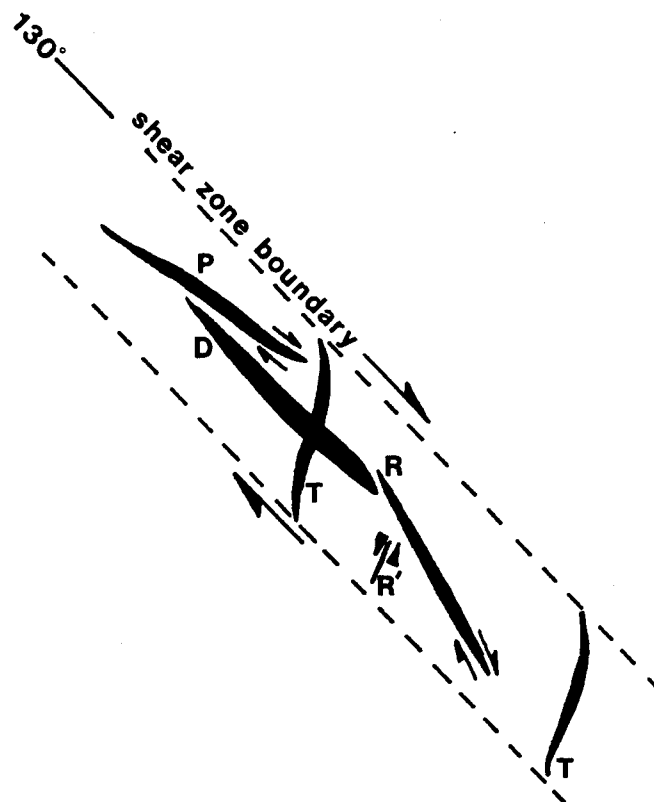
Shearing within the competent rocks of the Freegold Mountain area has led to brittle deformation characterized by the abrupt offset of markers and the occurrence of faults and fault breccias as defined by Ramsay (1980).

Experimental deformation in the laboratory of material acting under brittle conditions by Reidel in 1929 and later confirmed by Tchalenko (1968), show that the material within the shear zone develops fracture systems in a systematic and

orderly fashion. Figure 14a, redrawn from Gwilym Roberts (1987) and O'Brien (1985), shows the orientation of shear fractures, and the direction of movement across them. The first fractures to form are the low-angle Reidel (R) and the high-angle Reidel (R') shears. The next to form are the reverse or pressure shears (P), followed by principal shear fractures (D). Extension fractures (T) are also formed during shearing. Their location is on a plane generally perpendicular to the X axis on a strain ellipsoid (principal stress direction =  $\sigma_1$ ).

Since the Freegold Mountain area occurs between two megastructures where well documented shearing has occurred, it is probable that fractures and vein orientations within the area are controlled by conditions similar to those of the Reidel model. The area shows brittle deformation and shear development which would provide favorable conditions for Reidel shear development. Figure 14b shows the orientation of known fractures and shear fractures in the Freegold Mountain area. The Tintina fault and smaller faults in the area such as the Big Creek and Camp faults are designated as the major shear zone boundaries. The principal stress direction during Cretaceous deformation is  $160^\circ$  (Gabrielse, 1985). The orientation of known fractures in the Freegold Mountain area from Fig. 14b, and known shear zones from Table 6, do not compare favorably to a Reidel model of fracture orientation (Fig. 14a) since only one of the observed fracture orientations, at  $18^\circ$ , fits into the

(a)



(b)

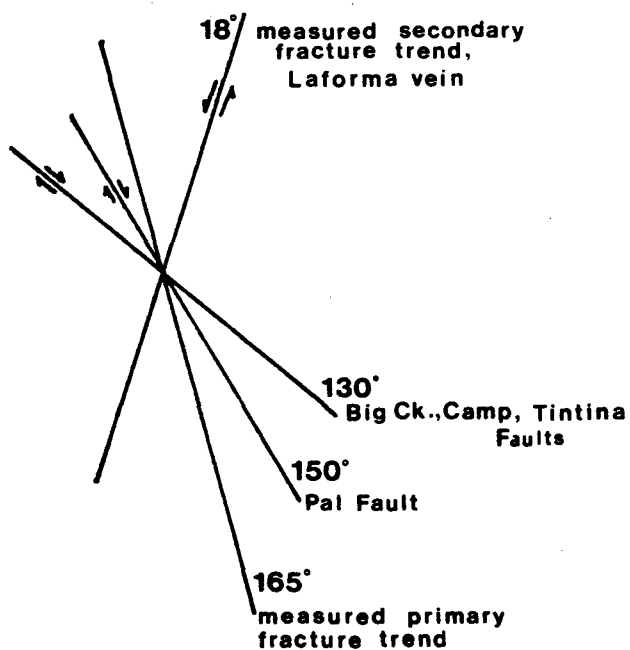


Figure 14. (a) Reidel fracture orientations for an area with shear zone boundaries (SZB) oriented at 130°.

(b) Orientation of fault and fracture planes at Freegold Mountain.

predicted pattern as a high-angle Reidel shear fracture. Sinistral displacement along the Laforma vein/fracture system (which at  $22^{\circ}$ , represents the general  $18^{\circ}$  trend within error of measurement) is similar to that predicted by the model and therefore it may be a high-angle Reidel fracture. None of the other observed shears, however, fit particularly well with the model and it is possible that shear activity at Freegold Mountain is not controlled by a Reidel shear zone model. The possible reasons are:

1. The area between the principle bounding shear zones is too large to be modelled according to laboratory experiments.
2. A vertical component of movement along the shear zones affects the predicted orientation of fracture patterns.
3. Fracture patterns in the Freegold Mountain area are the result of non-uniform continually changing stress conditions and do not reflect a state of constant deformation conditions.
4. Most of the stress is taken up along the major shear zones with low competency rocks and that the interior regions undergo a stress regime too low to produce Reidel shears.

If the latter is true then shear zones closer to the Tintina fault may show orientations consistent with the Reidel shear model. Mapping of fracture orientations in areas near the Tintina fault may be a valuable exploration strategy in predicting the attitude and possibly the

location of precious metal veins.

The 18° fracture orientation is interpreted to have had both shear and extensional components and thus may represent a modified extension fracture (Figure 14a). Fractures at 165° orientation show dextral displacement and do not appear to be in zones of major extension, although some dyke units do have this orientation. The Pal fault (150°) may be a member of this fracture family. If this is the case, then fractures and dykes with 165° orientation postdate those striking at 18°.

Gabrielse (1985) documents the change in general orientation of principal stress in the northern Cordillera using fold axes trends and the orientation of transcurrent faults in conjunction with their presumed ages. There appears to have been a change of  $\sigma_1$  from northeast in pre-Albian time, to north-northwest in the middle Cretaceous, followed by north to northeast in Late Cretaceous to early Cenozoic time. If the Big Creek and Camp faults represent the middle Cretaceous shear zones in that they are parallel to the Tintina fault, they would represent transcurrent faulting under a northwesterly principal stress direction. The timing of rhyolite dyke and vein emplacement along the 18° fracture orientation of Late Cretaceous (78 Ma) may represent regional  $\sigma_1$  orientation to the northeast. Later offset of 18° fractures by movement on 165° fractures may have resulted from the reorientation of principal stress to a more northerly orientation.

Changing stress conditions through time may explain the spatial orientation and crosscutting relationships of fracture zones observed in the study area, which are similar to those documented by Gabrielse (1985). The presence of non-unidirectional stress fields operating over long periods of time may explain why fracture orientations cannot be modelled as composite Reidel shears.

## PART B. GEOLOGY AND GEOCHEMISTRY OF PRECIOUS METAL DEPOSITS

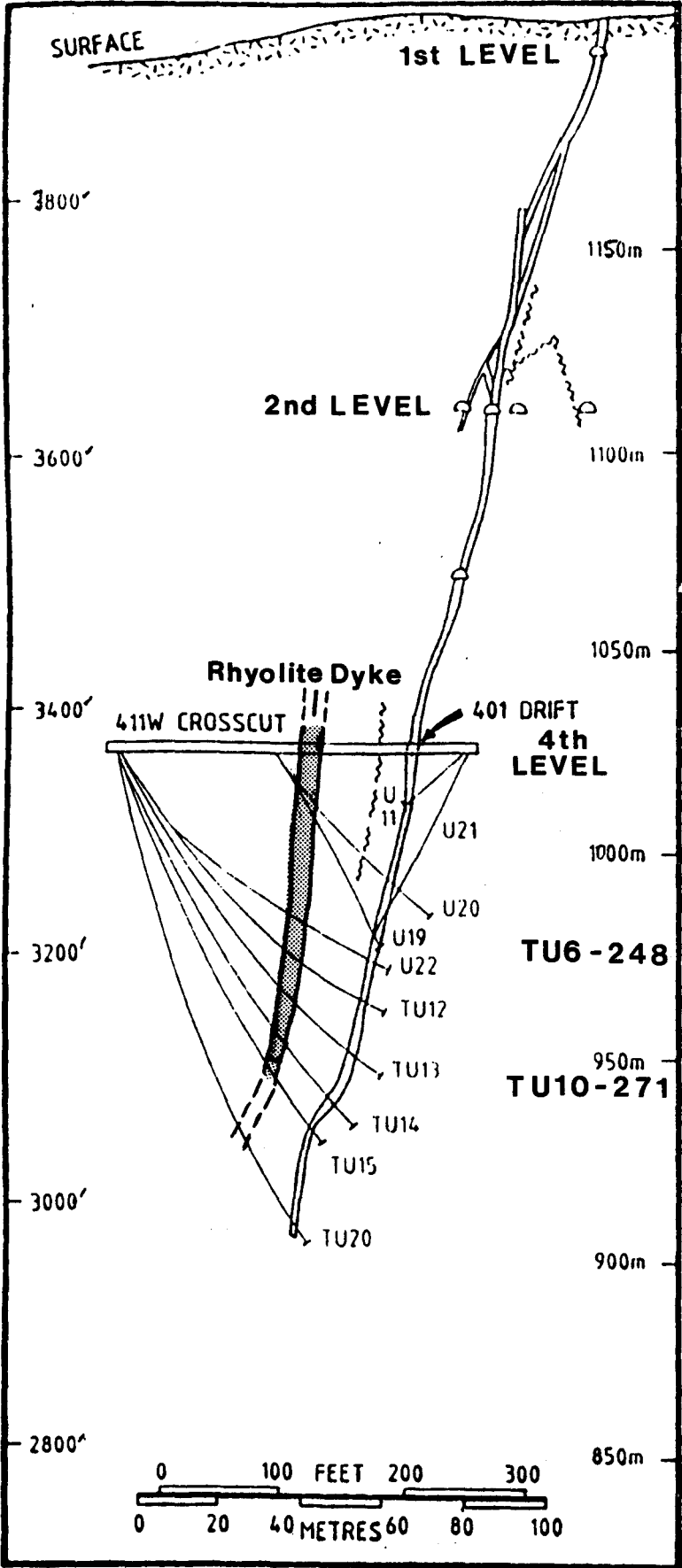
### CHAPTER 7. GEOLOGY OF PRECIOUS METAL DEPOSITS

#### 7.1 Laforma Mine

The geology of the Laforma mine was reconstructed using unpublished company reports on file at DIAND (Whitehorse Geology Office), from relogging and plotting drill core profiles in conjunction with company files of drill sites and attitudes, and from surface mapping of trenches and adits where accessible. Underground mapping was only conducted on Level 4 and was restricted due to a cave-in.

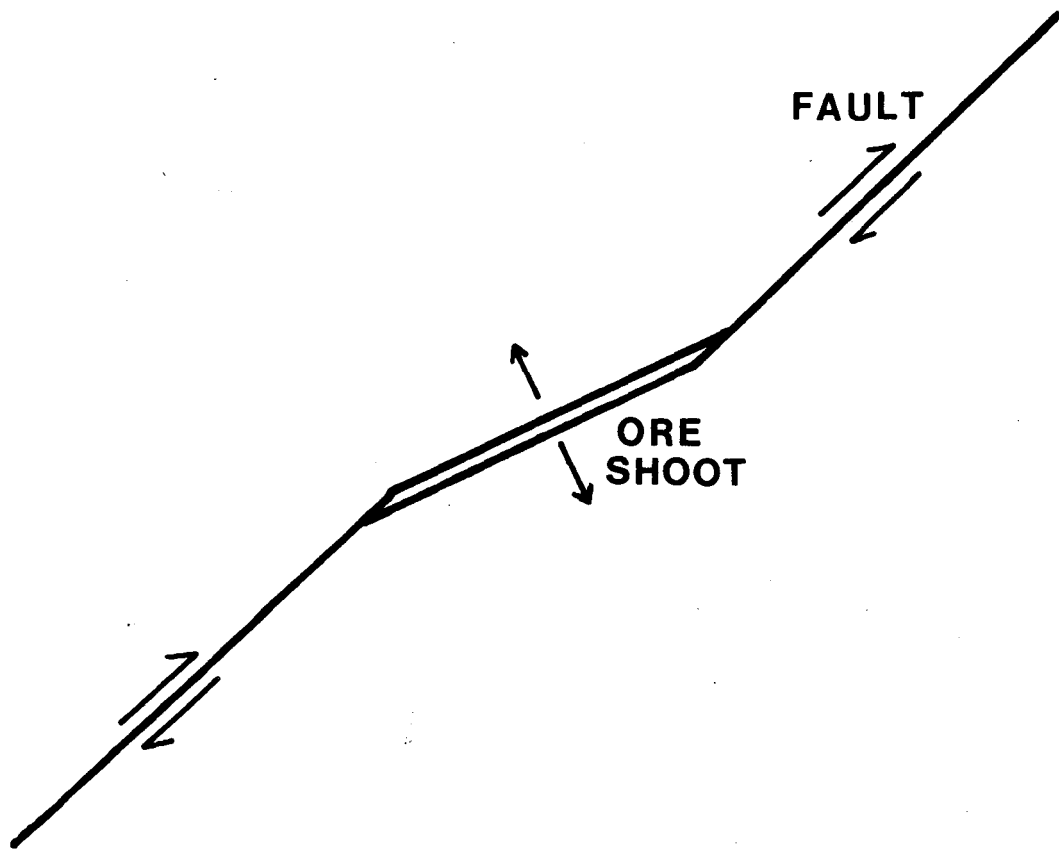
The Laforma Mine is located on a gold-bearing quartz vein within a shear zone in granodiorite. The mine has been developed on three levels (all elevations above sea level): Level 2 at 1110 m , Level 3 at 1065 m and Level 4 at 1025 m elevation. Exploratory drifting was initiated on Level 1 at 1200 m elevation early in the mines history. Figure 15 is a cross section of the deposit. The shear zone is present at the surface (1210 m elevation) and continuous to a depth of 900 m. This zone is silicified throughout but quartz vein development has been limited to two zones called the north and south ore shoots. These ore shoots have developed in parts of the shear zone where extension and permeability were greatest. The formation of fissures may be related to movement along the fault where minor deviations in fault orientation led to the creation of rectangular conduits as

Figure 15. Cross-section through Laforma Deposit looking north showing concordance of rhyolite dyke and gold-quartz vein. The relative elevations of fluid inclusion samples TU 10-271 and TU 6-248 are plotted in relation to the 4th Level.



depicted in Figure 16 (Mitcham, 1974). Veins are often not continuous and occasionally pinch and swell due to shearing along the fault during vein deposition.

Figure 16. Ore shoot development along a non-linear fault zone



Surface mapping (Map 1) shows that a rhyolite dyke near the Laforma vein bends to the west near the Pal fault zone. Away from the Laforma structure to the west rhyolite dykes do seem to be oriented parallel to the Pal fault. Andesite and rhyolite dykes appear to crosscut each other concordant to the Laforma structure but the nature of this relationship is unclear due to poor exposure. The vein, as it is exposed at the surface south of the trail (see Figure 5), is fine-

grained, dark, sulfide-rich and shows multiple periods of brecciation and silicification. North of the trail the vein is discontinuous and non-linear and may be offset slightly by faults.

Figure 17a, of Level 1 shows that the Laforma vein is hosted within a rhyolite dyke which has intruded along, and is cut, by the Pal fault. Quartz veins exposed in drifting on Level 1 were small and discontinuous and not suitable ore material.

Level 2 (Figure 17b) contains both andesite and rhyolite dyke units which are parallel or subparallel to the strike of the fault structure. Andesite dykes are displaced (about 75 m) on the eastern and western portions of the fault zone with a left-handed sense of motion. Cross faults parallel to the Pal fault have displaced the andesite and rhyolite dykes by a few metres. The rhyolite dykes show trends oriented parallel to the Laforma fault away from the Pal fault, gently curving to concordance with the Pal fault near the junction between the Pal and Laforma structures.

Level 4 (Figure 17c) is similar to Level 2 in that an andesite dyke on the west side of the shear zone has been displaced approximately 75 m south. A crosscut to the west of the vein intersected a rhyolite dyke trending parallel to the vein. Diamond drilling from the end of the crosscut to the deeper portions of the vein also intersected this dyke (Figure 15) and verifies that rhyolite dykes intruded along structures parallel and similar to the Laforma shear zone.

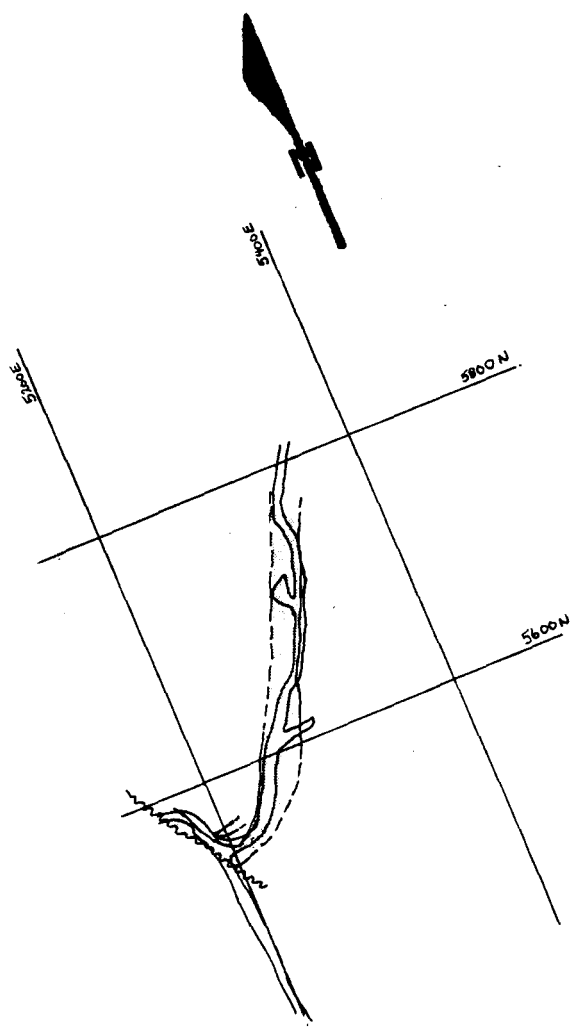
Figure 17. Plan sections of various levels of the Laforma Mine.

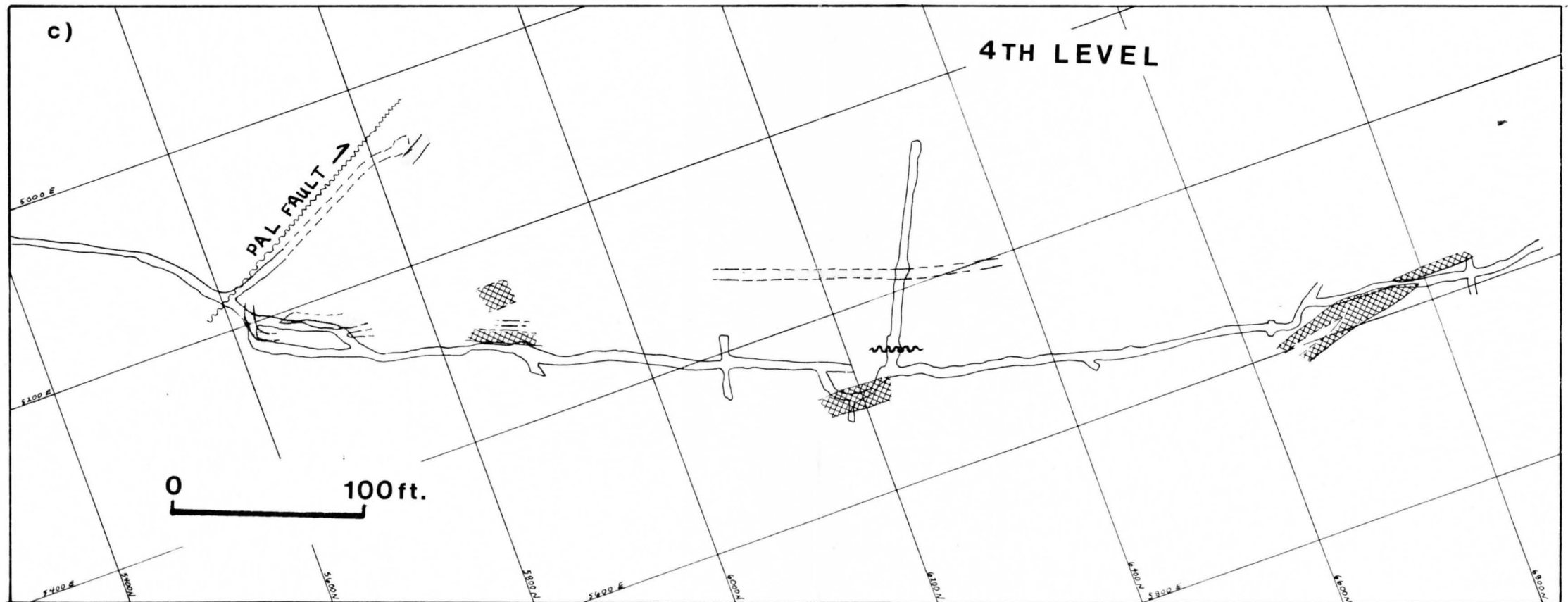
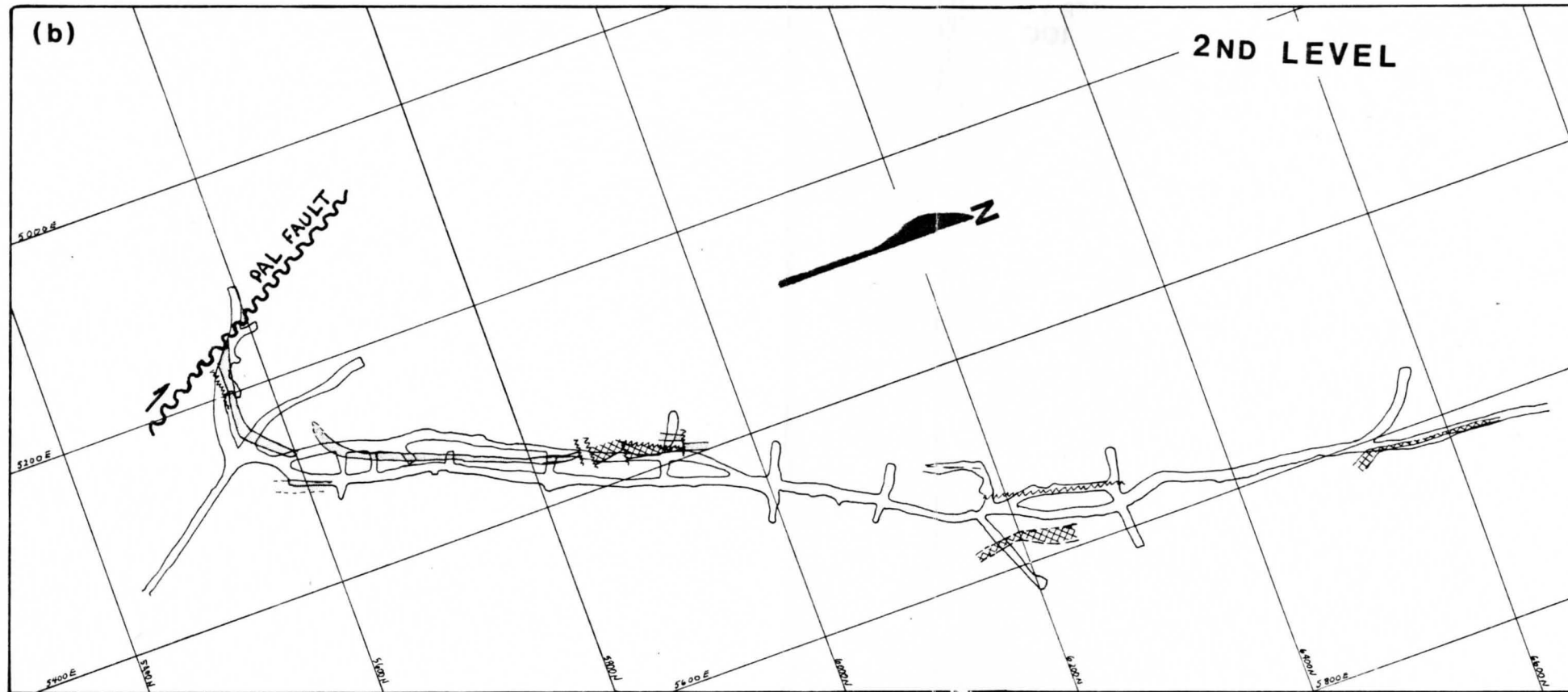
(a) Level 1

(b) Level 2

(c) Level 4

(a) 1ST LEVEL





Diamond drilling from another west crosscut at the southern portion of the mine near the Pal fault suggests that rhyolite dykes also intruded along other fault structures.

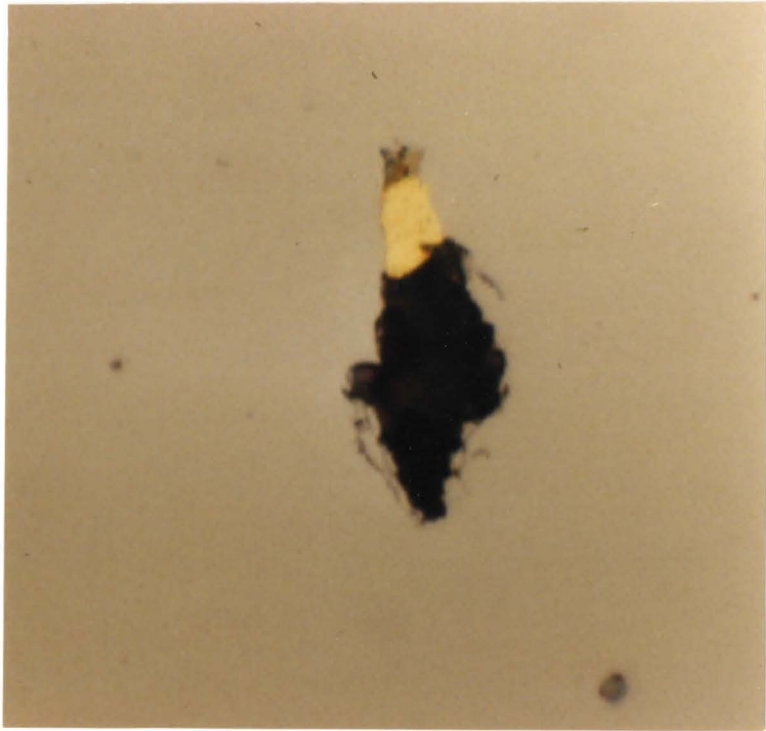
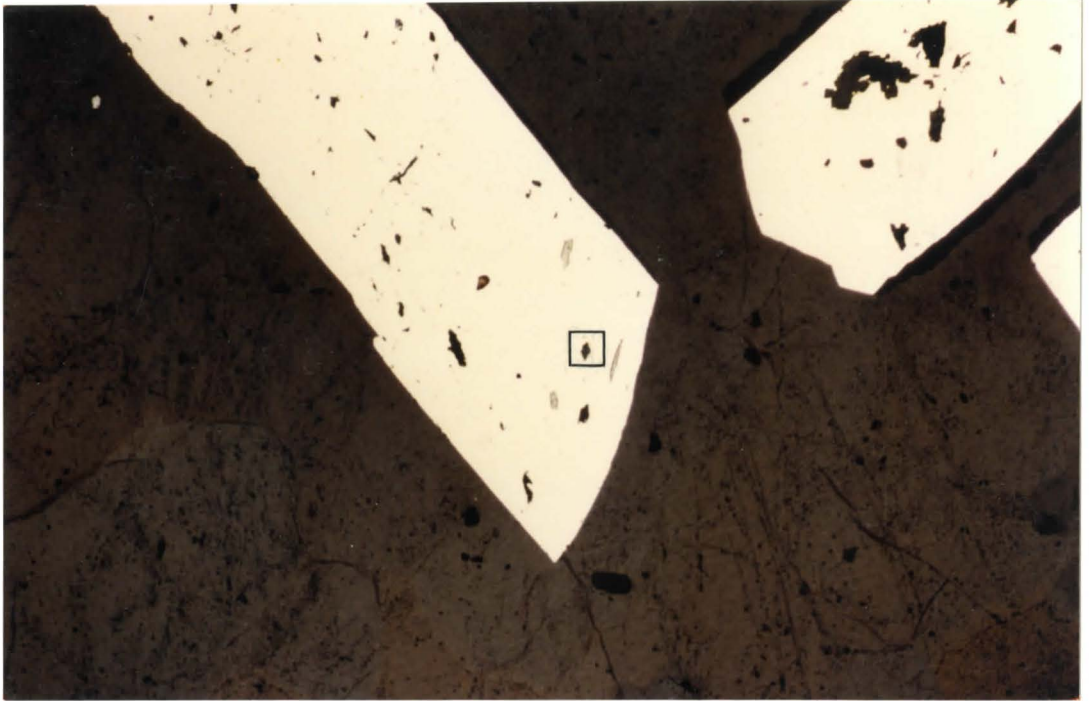
The andesite dykes in general appear to be oriented north to northwest whereas the rhyolite dykes are concordant to the Laforma structure and trend to the northeast except where the dyke trend is an expression of deformation along the Pal fault.

#### 7.1.1 Mineralogy

Polished thin sections were prepared from vein material obtained throughout the vertical extent of the mine. These were studied for progressive mineralogical variations which have been reported at other epithermal precious metal deposits (Buchanan, 1981). The Laforma deposit contains arsenopyrite, pyrite, tourmaline, gold, galena, sphalerite and chalcopyrite, tennantite, barite, Fe-Mg carbonate, sericite and calcite. There is a vertical zonation in mineralogy. Tourmaline, galena, Fe-rich sphalerite and chalcopyrite are present in drill core at and beneath Level 4 but are virtually absent above this level. Tennantite has only been noted above Level 4. Fe-Mg carbonate and sericite are only present within a zone where liquid-vapour immiscibility (boiling) has occurred. Coarse grained, euhedral arsenopyrite (Photo 21) and pyrite occur throughout the mine. Gold is present in thin section as tiny inclusions within arsenopyrite (Photo 22) and isolated fine

Photo 21. Euhedral arsenopyrite within the Laforma vein.  
Grey elongated inclusions are boulangerite.  
Arsenopyrite grain is 1 mm wide.

Photo 22. Close-up of boxed area in Photo 21 showing 8  $\mu\text{m}$   
gold inclusion.



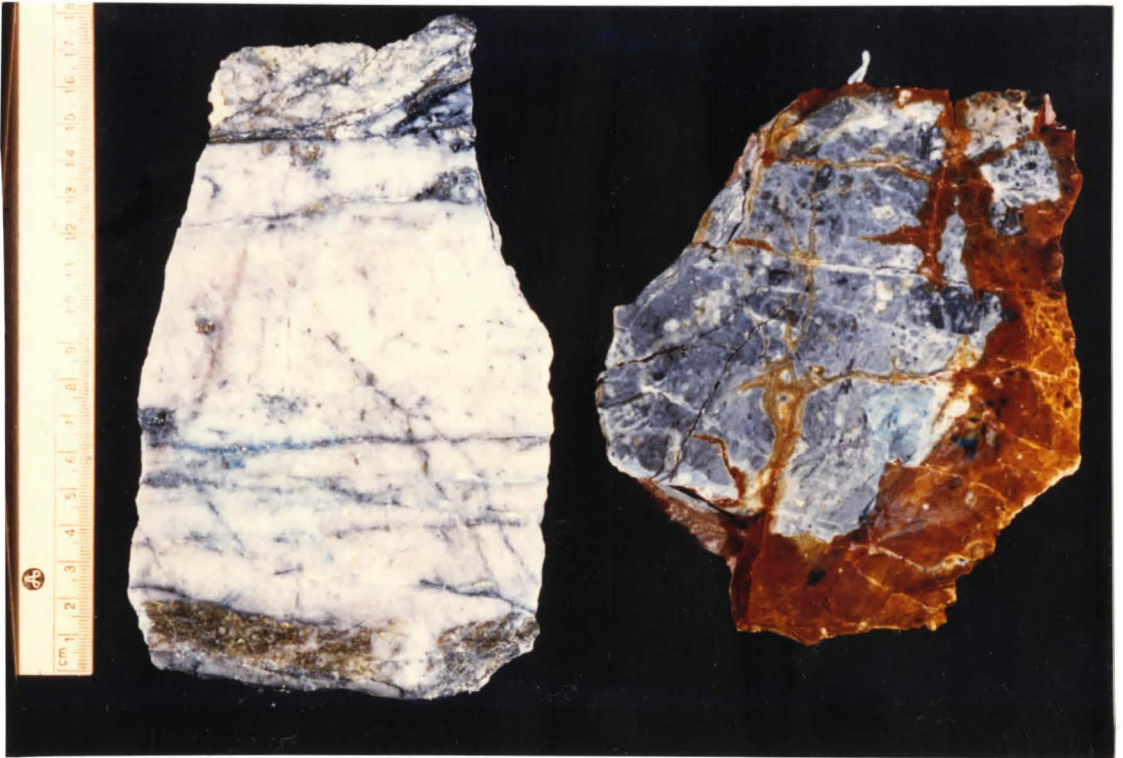
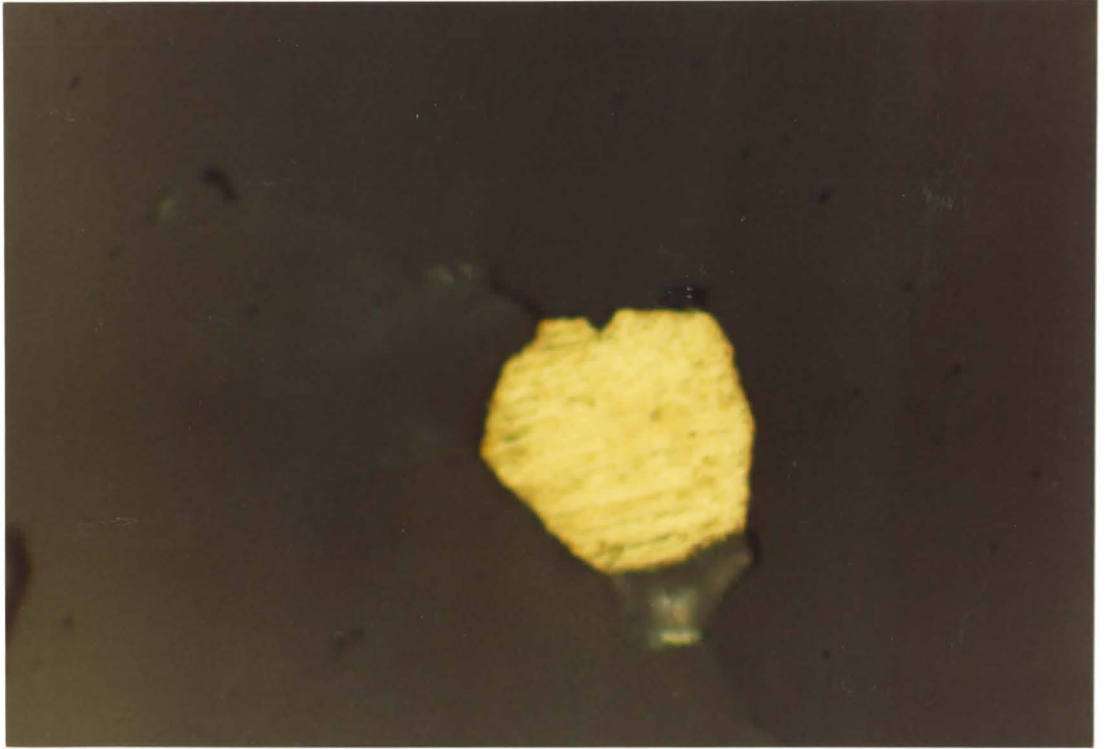
grains (Photo 23), although visible gold is not uncommon. Qualitative analysis of gold particles by a SEM equipped with an energy dispersive x-ray analysis unit, located at the Geological Survey of Canada, indicates a very low silver content ( $< 5\%$  Ag). Barite and calcite are post-ore minerals precipitating in late stage fractures during downward percolation of surface waters.

The vein is dominantly massive white quartz with sulfides and tourmaline providing a bluish colouration from Level 2 to depth. The part of the vein where boiling is observed has a vuggy, cockscomb texture with Fe-Mg carbonate, sericite and euhedral sulfides filling the vugs (Photos 24 and 25). Cockscomb texture is indicative of crystal growth in an open fissure and supports the premise that both an extensional and shear component occur on the Laforma fault.

The vein exposed at the surface has a dark blue coloration with abundant fine grained sulfides (Photo 24 and 26). It has undergone numerous brecciation and silicification events. The quartz clasts are coarsely granular while the matrix is composed of fine-grained silica. The quartz clasts in the vein breccia have fluid inclusion assemblages similar to those found in Level 4 vein. A possible genesis for the vein breccia is that violent eruptive venting of trapped  $\text{CO}_2$  and  $\text{H}_2\text{O}$  vapour, evolved during immiscibility processes at depth, caused vein material from lower down in the vein system to be carried

Photo 23. Fine-grained gold within 2nd level quartz vein.

Photo 24. A sample of the Laforma vein at the 4th level (left), and 200 metres above, at surface (right). The blue colouration in the surface sample is due its fine-grained nature and high sulphide content.



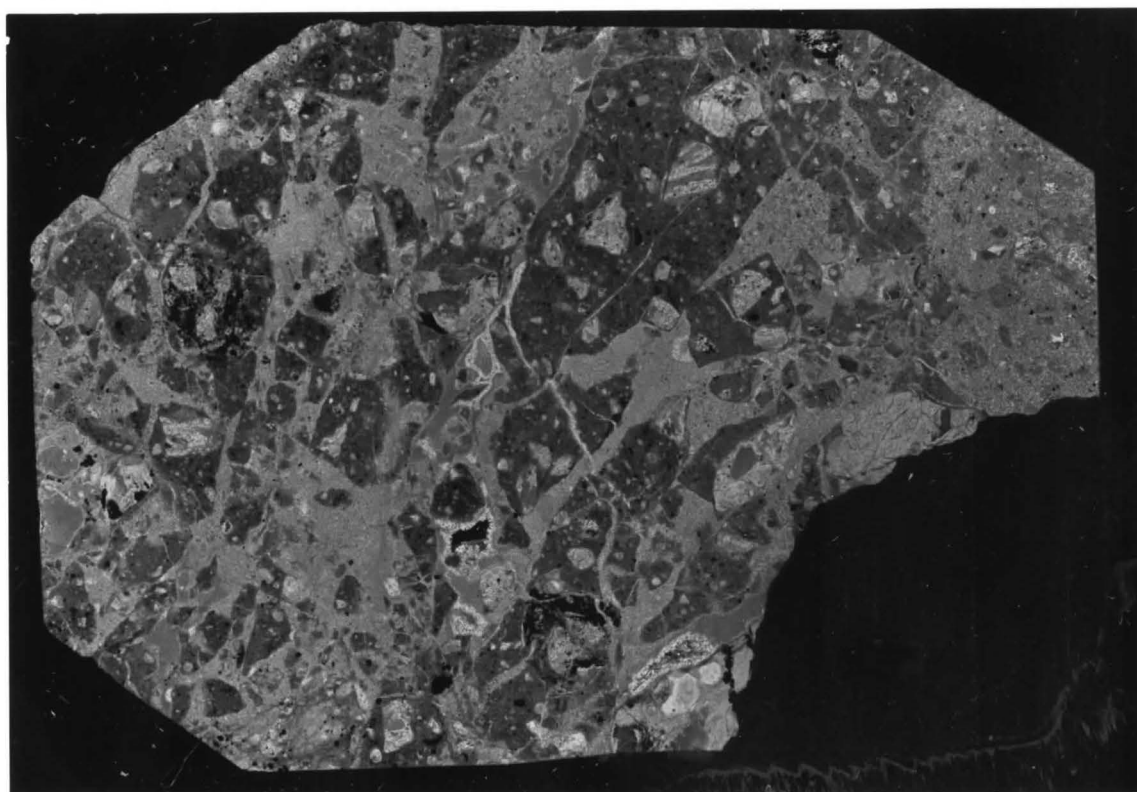
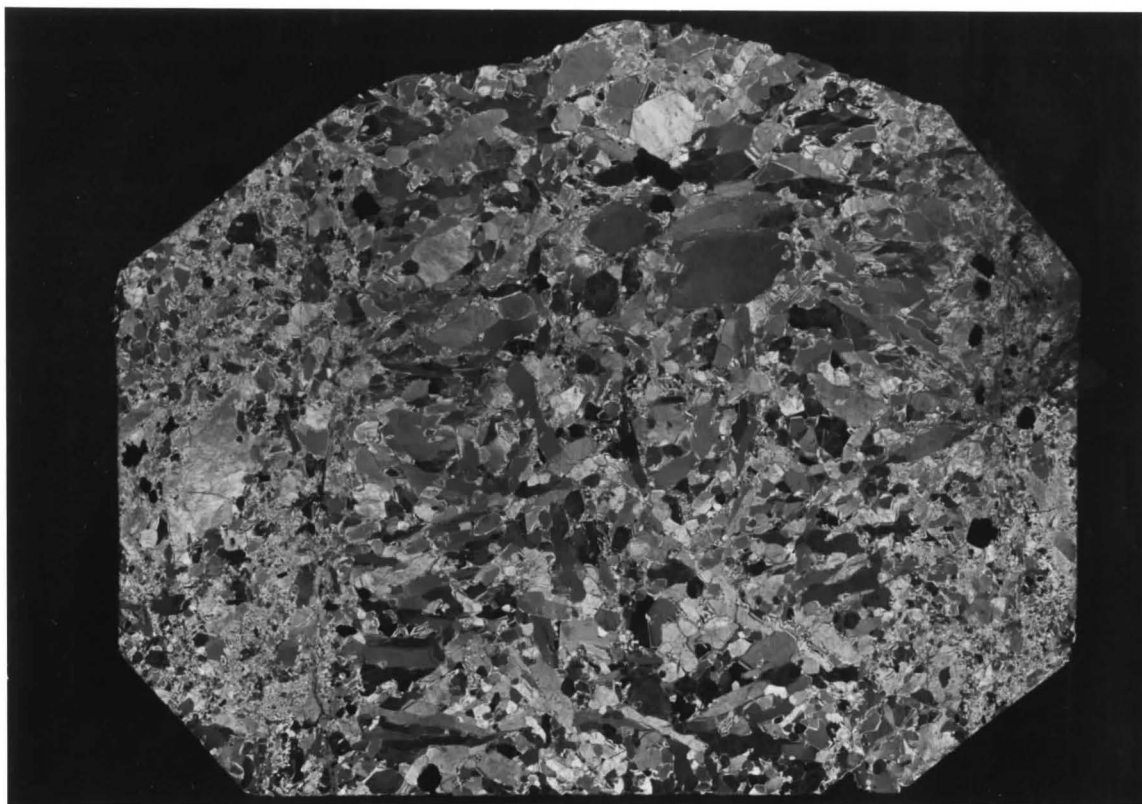
upward by the escaping gases. The fine grained nature of the silica cement is due to quenching of silica-rich fluids flowing upwards after the volatile escape. This process is similar to hydrothermal eruption breccias documented at geothermal fields at Waiotapu, New Zealand (Hedenquist and Henley, 1985; Nelson and Giles, 1985).

During fluid boiling, silica saturation is reached and quartz will precipitate (Fournier, 1983), sometimes sealing the hydrothermal system. When the fluid trapped below the seal begins to boil, the evolved gases (predominantly CO<sub>2</sub> and H<sub>2</sub>O) accumulate in a cavity below the seal, building up fluid pressure. Decompression of the high-pressure fluid can result from either hydraulic fracturing (fluid pressure exceeds confining pressure) or by tectonic fracturing. When an overpressured hydrothermal fluid rapidly decompresses, water will flash to steam resulting in an explosive eruption.

This condition is likely to have occurred at the Laforma mine because vein breccias at surface and at Level 2 have been found above a zone of boiling (Level 4) identified by fluid inclusion character (Chapter 8). Although fault associated, these vein breccias are not considered to be of tectonic origin, for several reasons. Firstly, adjacent clasts contain a variation of fluid inclusion populations, resulting from the upward transport of some clasts. Secondly, the clasts are cemented by fine-grained rapidly quenched quartz and sulfides whereas the fault-brecciated

Photo 25. Photomicrograph of central portion of 4th level vein, from Photo 24.

Photo 26. Photomicrograph of surface vein, from Photo 24.



clasts are cemented by coarse-grained quartz. The presence of halite-bearing fluid inclusions in clasts from the surface exposure of the vein indicates that upward transport of material may have been as much as 200 m, since halite-bearing inclusions are predominant in the boiling zone at Level 4. Brecciation was confined to the fissure and only minor amounts of wallrock appear to have been transported. Wallrock fragments identified in the vein breccia are altered to sericite and clay and have abundant sulfide.

As many as three types of vein material have been identified in samples taken from the surface immediately above Level 1. An early white coloured massive 'bull' quartz with no sulfide is cut by a massive bluish-gray quartz with sulfide mineralization. Both are veined by small lenses of reddish-brown chalcedonic quartz. No assays are available on these three types of quartz but the bluish-gray type is similar to ore-grade material in the lower levels, while the white and brown varieties are generally barren of mineralization.

The granodiorite wallrocks are hydrothermally altered to a sericite-dominant mineralogy. Silicification and carbonatization of the wallrocks are not significantly developed but do occur sporadically. Alteration is more intense in the hanging wall relative to the footwall granodiorite. Clay alteration is limited to a narrow width where intense shearing along the fault zone has occurred.

## 7.2 Antoniuk Deposit

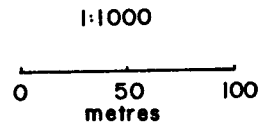
The Antoniuk deposit is a large sub-oval body of matrix supported brecciated country rock intruded by andesite and rhyolite dykes. In 1985, bulldozer trenches were excavated over a large area (Photo 27) of anomalous Au and As (Cathro and Main, 1986) concentrations discovered during a soil geochemical survey. Diamond drilling of the breccia in 1986 (Photo 28) provided information on geological relationships at depth and allowed the estimation of tonnage and grade. Mapping of these trenches (Figure 18, Map 2 (in pocket)) and interpretation of surface features with drill hole information allowed the interpretation of the geology of the deposit from cross-sections along the trenches as in Figure 19 (in pocket).

### 7.2.1 Geology

Figure 18 shows that the deposit is semi-elliptical in plan view. The breccia complex is dominated by large volumes of predominantly heterolithic breccia, composed of angular to subrounded clasts of granodiorite, syenite, andesite, rhyolite and quartz within a matrix of indurated rock flour (Photos 29 and 30). Rock flour and fragment rounding developed by interfragment attrition. No clasts of metasediments are present in the breccia. This indicates that during brecciation, either metasediments did not overlie the area if the breccia breached the surface, or that the breccia did not break the paleosurface. The

Figure 18. Geology of the Antoniuk Breccia deposit  
(1: 1,000).

Geology by  
B. McInnes, 1986



ANTONIUK BRECCIA  
MT. FREEGOLD, YUKON

-  Rhyolite
-  Andesite
-  Syenite
-  Granodiorite
-  Breccia Complex
-  Fault



Photo 27. Aerial view of the Antoniuk Breccia deposit.

Photo 28. Diamond drilling of the Antoniuk deposit.



presence of carbonized wood (Sillitoe, 1985) in some diatremes provides evidence that brecciation intersected the surface, although no such surficial material has been found at Antoniuk.

Monolithic breccia is minor and limited to the outer margins of the breccia complex where the breccia clasts are similar to the neighboring country rock, suggesting limited mixing of material. The breccia pipe contains large blocks of country rock along the north side of the deposit. These blocks are interpreted to have slumped into the breccia and were isolated into 'islands' by vertical stoping processes (see drill sections 16N, 18N and 20N (Fig. 19)). Stopping is thought to account not only for the large (50-100 m) blocks to the north but also for smaller (10-30 m) blocks surrounded by breccia and by rhyolite dykes interpolated from drill core intersections in sections 20N, 22N, 24N and 26N (Figure 19).

The breccia body is dissected by a major swarm of east-west trending rhyolite dykes. The largest continuous dyke, known as the Baseline dyke because of its close proximity to the surveyed baseline, is over 600 m long. This dyke is interpreted to be an apophysis of a large rhyolitic stock situated below the eastern end of the breccia pipe. The rhyolite becomes porphyritic and coarser grained at depth and in the wider dyke units at the eastern portion but is essentially cryptocrystalline to the west. Although some of the dykes clearly cut into the country rock from the breccia

Photo 29. Sample of heterolithic breccia from the oxidized supergene zone. Large clast in the centre is syenitic and the small triangular clast at the base is rhyolitic.

Photo 30. Sample of heterolithic breccia from the oxidized supergene zone containing clasts of andesite (top) and many rhyolite clasts.



pipe, others appear to terminate at the breccia-country rock contact. The dykes were intruded into the breccia body while it was relatively unconsolidated (Photos 31 and 32), and there appears to be no structural control on the attitude of the rhyolite dykes. Their linearity may be controlled by the shape of the underlying magma body, although evidence is not available to evaluate this supposition.

Individual fragments range from centimeters to tens of meters in size, but are commonly pebble to cobble size. Only one period of brecciation has occurred because no clasts of brecciated material have been identified (c.f. Golden Sunlight, Montana; see Porter and Ripley, 1985). The larger clasts are country rock fragments detached from the walls of the diatreme during active stoping. Syenite blocks up to 150 m long are vertically oriented along the breccia margin in drill section 26N. The presence of such large, vertically oriented fragments is also common at the Montana Tunnels diatreme (Sillitoe et al., 1985).

The presence of rhyolite (Photo 33) and andesite fragments in the breccias along with andesite and rhyolite intrusives indicates that breccia formation was temporally, spatially and probably genetically related to intrusive volcanism. Clasts of angular quartz fragments, some with sulfide mineralization, suggest that prior to brecciation either a quartz vein or a quartz lens may have been present. At Panasqueira, Portugal, a lensoid mass of quartz

Photo 31. Rhyolite dyke (R) intruding into breccia (B).  
Undulating contact indicates the breccia was  
unconsolidated during dyke intrusion.

Photo 32. Close-up of Photo 31.



precipitated in a cavity at the top of a granite cupola (Kelly and Rye, 1979). Sillitoe (1985) suggests that this 14 m zone of quartz may be a remnant of a failed breccia pipe. The presence of quartz fragments in the Antoniuk breccia complex (Photo 34) may indicate that a similar lens of quartz was developed above a silicic magma body that was the source of the rhyolite dykes. The temporal relationship of the breccia body with rhyolitic volcanism would signify an age of formation about 78 Ma.

The walls of the diatreme are essentially vertical with minor deviations evident in various sections. Country rock near the margin is brecciated and hydrothermally altered but has not undergone any fragment attrition or rock flour development. The heterolithic breccia is rock flour supported, and in places rock flour makes up the majority of the material present (Photos 35 and 36). Open space features are not common and occur only where multiple clasts are in contact, creating a cavity. These voids were subsequently filled with euhedral quartz, carbonate and sulfide crystals during hydrothermal fluid flow (Photo 37). Photo 38 shows drill core with the development of layers of different sized particles of rock flour. This layering is thought to arise by grain size sorting during upward fluid streaming (Warnaars et al., 1985; Arnold and Fitzgerald, 1977; Sillitoe, 1985).

Post-brecciation fault structures are commonly observed in outcrop and in drill core. Observed displacement on some

Photo 33. Abundant rhyolite clasts within hypogene zone.

Photo 34. Quartz clasts within silicified rock flour.

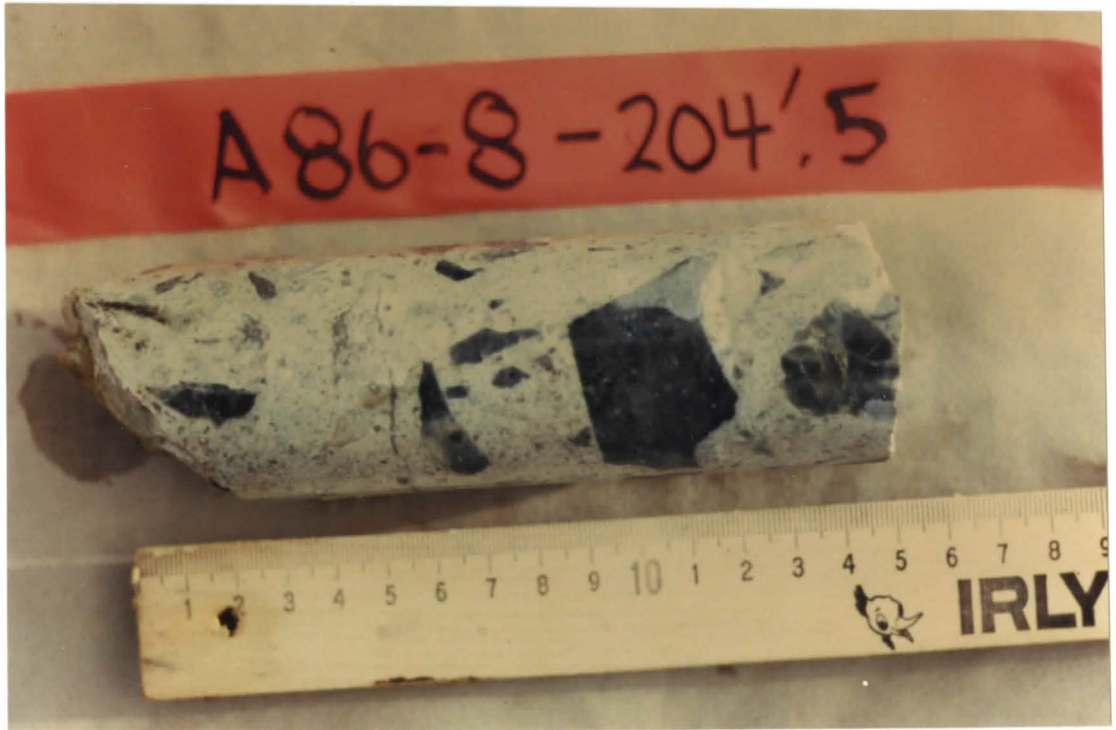


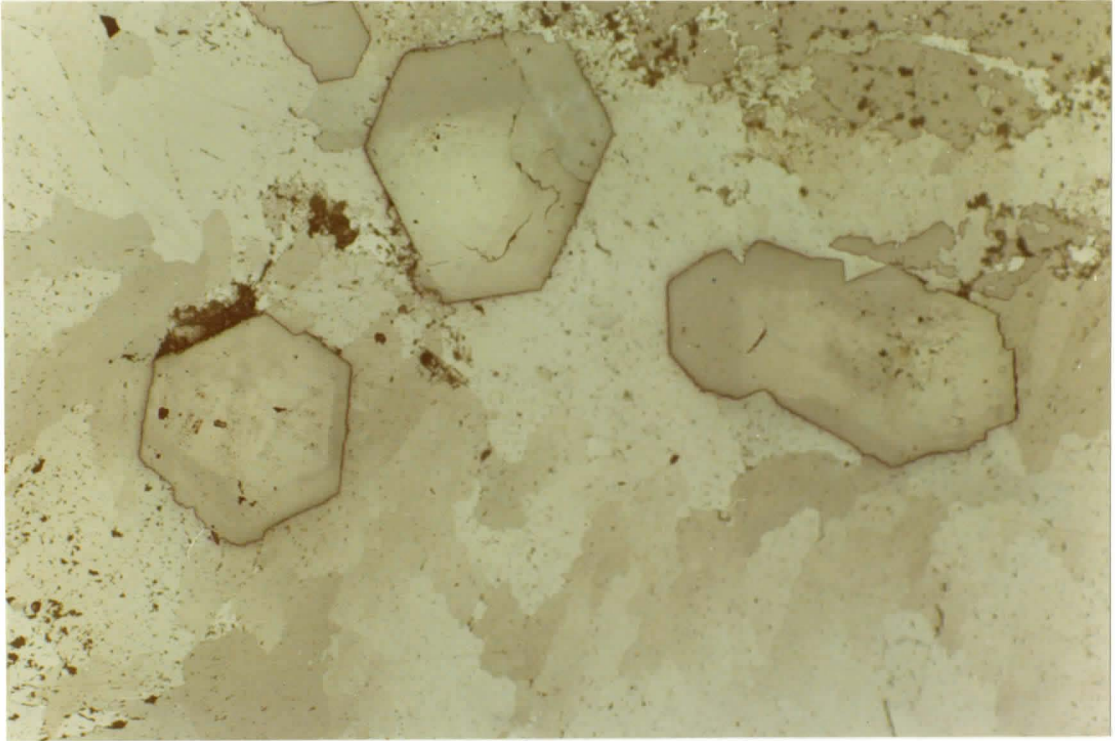
Photo 35. Varying proportion of clasts within silicified rock flour.

Photo 36. Varying proportion of clasts within silicified rock flour.



Photo 37. Euhedral quartz surrounded by calcite and pyrite (not shown) in a vug.

Photo 38. Banded texture in rock flour is interpreted to arise from particle sorting during fluid streaming.



fractures was generally less than 1 m and these are not interpreted to be major structural features. Alteration is intense and kaolinite is commonly present. Supergene oxidation by surface waters is deep at Antoniuk, varying from 5-60 m. Where the breccia is traversed by vertical faults the oxidation generally attains a greater depth. Ring fractures, dykes, veins and other structural phenomenon observed in the country rock around other diatremes (eg. Kidston, Australia (Mustard, 1986)) were not observed, but may be obscured by cover.

The northwesterly trend of the Antoniuk, Cabin and Revenue breccias (Figure 2), parallel to and possibly between major regional faults indicates a spatial and possible genetic relationship between breccia pipe formation and structure. Sillitoe (1985, p. 1473) concluded that,

"major regional structures play little part in breccia pipe formation and, if structural control is significant, it is likely to be by minor faults, fractures and joints."

He does concede, however, that diatremes at Montana Tunnels, Cerro de Pasco (Peru), and Wau (Papua New Guinea) are located on major regional faults. The location of the Antoniuk breccia near the contact of major syenite and granodiorite plutons is thought to be coincidental. Observed contacts between the two rock types are solid and do not suggest a penetrable zone of weakness. Although it is not clear what, if any, control structure exerts on the locations of the Antoniuk and other breccia bodies in the Freegold Mountain area, the spatial and temporal

relationships between rhyolitic volcanism and major faults suggests that explorationists should exploit such features for their ore potential.

### 7.2.2 Genetic Implications of Breccia Formation

Ore calculations at the Antoniuk indicate an ore mass of 3.7 Mt (million tonnes). The total volume of rock (ore + waste) originally brecciated before intrusion of the rhyolite dykes has been calculated using a simplified and conservative block estimation method as approximately 16,000,000 m<sup>3</sup>. This is equivalent to 41 Mt of rock (density = 2600 kg/m<sup>3</sup>) brecciated. The amount of energy necessary to brecciate this mass of rock can be estimated by the scaling of underground nuclear blasts (Johnson et al., 1971). For large blasts such as nuclear explosions or volcanic eruptions, the amount of explosive necessary to produce a certain crater radius can be calculated from the crater radius of a small tonnage explosive using the formula:

$$R_A = r_A (Y/Y_0)^{1/4}$$

where  $R_A$  = crater radius for charge weighing  $Y$  tons

$r_A$  = crater radius for charge weighing  $Y_0$  tons

A charge of 100 tons of TNT at a depth of 13 m will create a crater with radius 25 m. The surface area of the Antoniuk breccia converts to a crater with radius 193 m. To create such a crater an explosive equivalent to 410,000 of TNT would be necessary, 20 times more powerful than the bombs dropped on Hiroshima and Nagasaki, Japan. This minimum

estimate is only a first-order approximation of the energy required to produce brecciation of a body near the surface. The actual amount of energy may be an order of magnitude larger. The energy produced by an explosive charge of TNT weighing 400 Kt to 4 Mt is  $1.7 \times 10^{22}$  to  $1.7 \times 10^{23}$  ergs. The Mt. St. Helens explosion of May 8, 1980 was produced by an equivalent of 7 Mt of TNT (Kieffer, 1981). Therefore the amount of energy required to produce the Antoniuk Breccia is consistent with that produced by volcanic eruptions.

The presence of rhyolite clasts within the breccia body and a rhyolite stock with associated dykes intruding the breccia indicate that brecciation process is temporally related to a period of rhyolitic volcanism. The abundance of quartz clasts and the estimation of the energy needed to produce brecciation suggests that the brecciation process may be related to the exsolution of a vapour phase from a magma which became supersaturated with volatiles during ascent into high crustal levels by a second-boiling process.

The creation of breccias by the explosive venting of exsolved vapors was first discussed by Norton and Cathles (1973), and has been mathematically modelled by Burnham (1985) and Blake (1984). Burnham's model (1985) proposes that energy is dissipated from  $H_2O$ -saturated magmas during the exsolution of volatiles (mostly water) by the second boiling reaction (water-saturated melt  $\rightarrow$  crystals + aqueous fluid (Sillitoe, 1985)). This fluid would accumulate in a carapace above the magma.

As discussed previously, an aqueous cap above a magma can precipitate quartz as at Panasqueira, and ubiquitous clasts of quartz within the Antoniuk may indicate a stage of quartz deposition above a magma undergoing second boiling processes. Decompression of an overpressured exsolved fluid that has accumulated at the top of a cupola leads to the further exsolution of gases from the water-saturated residual melt.

Decompression may result from magma withdrawal, fracture propagation along existing structures (hydrofracturing), or by tectonic movement along a fault zone piercing either the fluid-filled cupola or fracture. Thus it is difficult to assess the role of fault systems in the initiation of breccia pipes. The linear relationship of breccia bodies in the Freegold Mountain area, concordant to known fault zones (Figure 2) may be the result of magma exploitation of previously existing fracture systems. Decompression, therefore, is related either to fluid pressure exceeding confining pressure in a zone of weakness or to movement along these faults that has caused a sudden decompression of the overpressured cupola.

Such a sudden decompression would lead to a rapid and violent expulsion of fluid from the carapace and magma. The fluid would at first "stream" through the original failure zone, continually stopping and spalling the walls of the zone, leading to the mixing and milling of fragments causing attrition and rock flour development (Burnham, 1985). The

unconsolidated breccia would then be susceptible to intrusion of dykes of fresh rhyolitic melt rising to equilibrate with the low pressure conditions following the brecciation event.

The low initial water content of parent rhyolite magmas (<1.2% H<sub>2</sub>O for Nisling Range alaskites, Lynch and Pride, (1984); and <2% H<sub>2</sub>O for granites, Maaloe and Wyllie, (1975)) coupled with their apparently minor volumes in the Freegold Mountain area indicates that volatile overpressure leading to brecciation must have occurred at relatively shallow levels in the crust, probably less than 1.5 km (Blake, 1984; Burnham, 1985).

### 7.2.3 Mineralogy

Polished thin sections were prepared to investigate the mineralogy of the ore bearing breccia. Unfortunately, no gold was observed in the 12 sections prepared, even from relatively high grade material (> 3 g/t Au). A private metallurgical report (Karklin et al., 1986) did identify gold grains by preparing polished sections from heavy mineral separates.

The breccia can be subdivided into two mineralogical zones. A lower hypogene zone characterized by sulfide mineralization and an upper oxide zone where supergene alteration by meteoric water has oxidized the majority of sulfides. The hypogene zone is characterized by abundant pyrite, averaging about 1-3% but occasionally accounting for

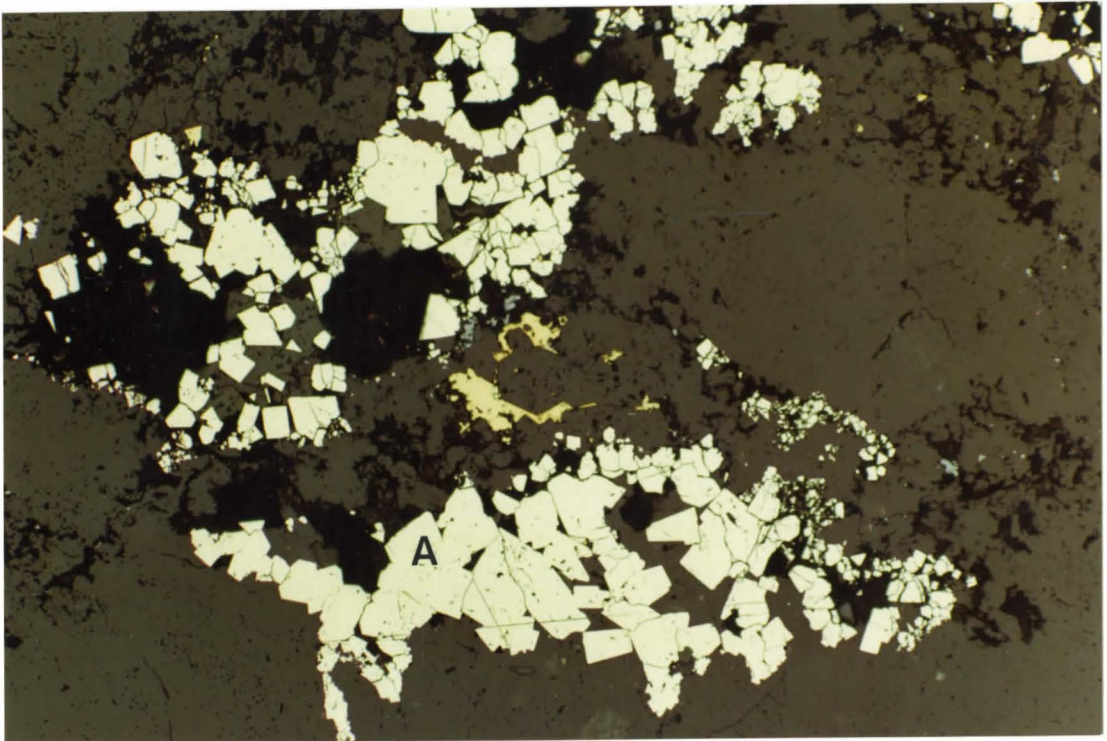
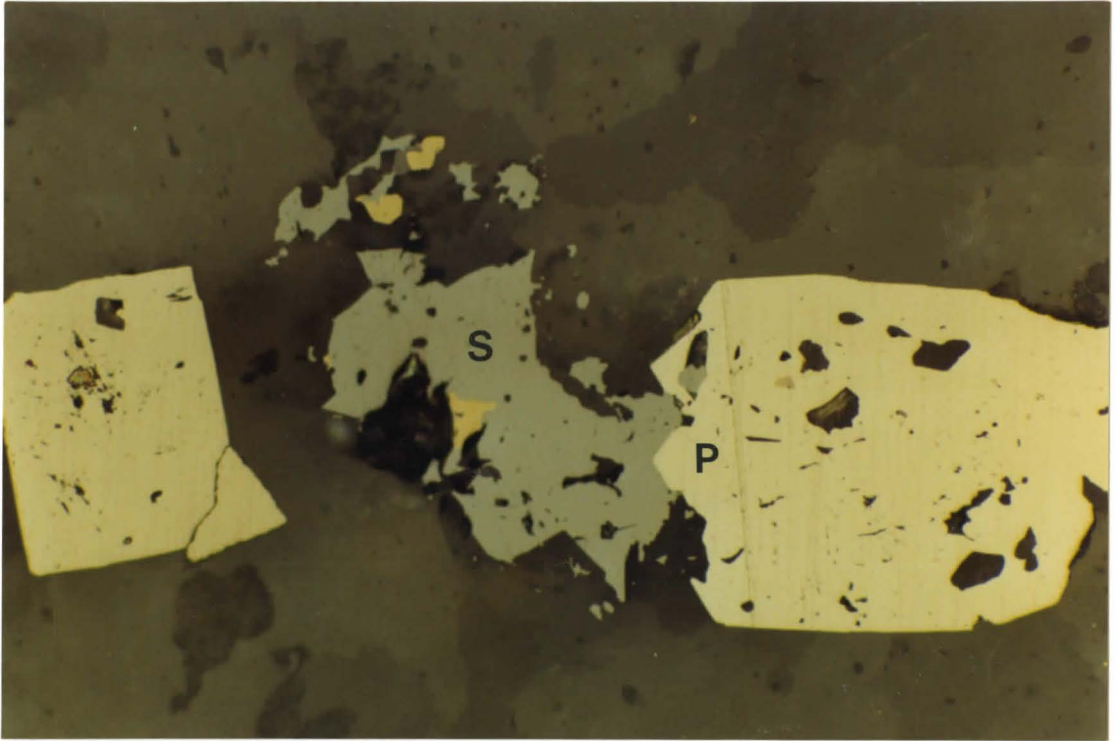
as much as 5% of the rock volume, particularly in areas of high permeability. Pyrite occurs as a replacement of Fe-bearing silicates in breccia fragments and in void spaces coprecipitating with other sulfides, quartz and carbonate. Arsenopyrite is locally abundant (Photo 40), but no physiochemical control on arsenopyrite deposition is discernible. Chalcopyrite, sphalerite, galena and pyrrhotite occur in trace amounts, occurring as minute intergrowths (Photo 39) or as inclusions within pyrite.

Gold grains are reported by Karklin et al., (1986) to occur as "angular to smooth, subrounded to lenticular particles" which average 35- 40  $\mu\text{m}$  in diameter, with grains as large as 250  $\mu\text{m}$ . One particle of gold was observed to have an inclusion of pyrrhotite.

Gold occurs in anomalous concentrations throughout the entire breccia body, but zones of continuous, and therefore potentially economic concentrations, are difficult to define. In general, gold concentration is higher in the heterolithic breccia (where fluid permeability was greater) than in the rhyolite dykes. Assay values from intensely altered, late stage fracture zones are significantly higher than from the rest of the breccia, and suggest that as the breccia became silicified and indurated, hydrothermal fluid flow was restricted to these later features. The passage of large volumes of fluid through these features would account for their higher gold concentration and intensely altered character relative to the rest of the breccia.

Photo 39. Inclusion-rich pyrite (P) intergrown with sphalerite (S) and chalcopyrite.

Photo 40. Arsenopyrite (A), chalcopyrite (centre) and quartz filling a void space between breccia clasts.



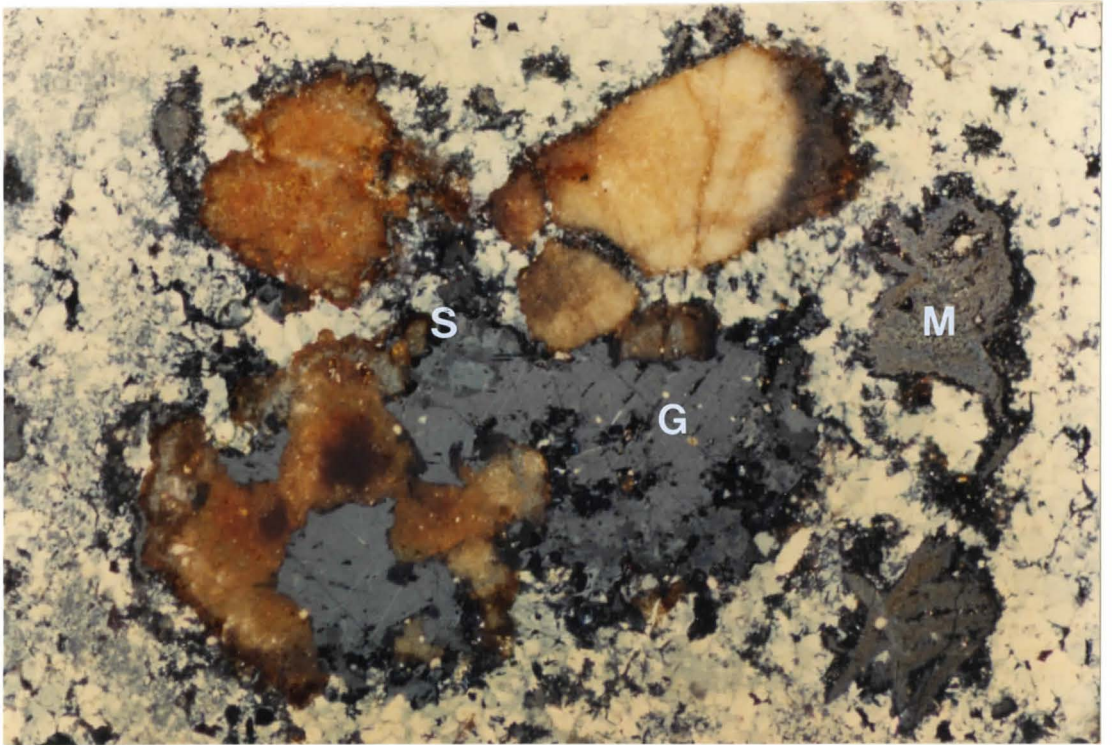
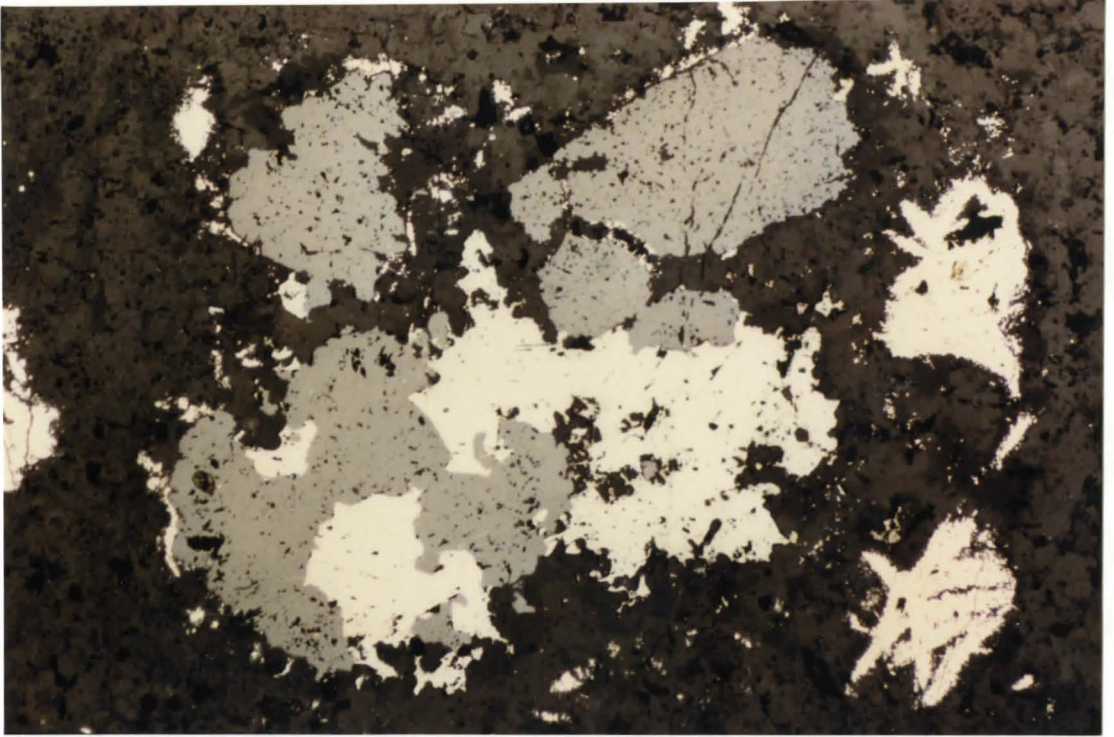
### 7.3 Emmons Hill

The Emmons Hill prospect is a series of trenches around an abandoned shaft located north of Emmons Hill. The shaft was reported to be 92 feet deep, with crosscuts at 40 and 92 feet (Johnston, 1937) driven along a northwesterly trending vein/breccia structure. Gold values ranging from 1.5 to 2 oz/ton were reported at a depth of about 60 feet, but grade was erratic. Samples collected from trenches dug to the west of the adit, from drill core and from the dump around the adit contain highly brecciated and altered clasts of metasediments and rhyolite in a matrix of sulphides, sulphates, carbonates and silica. This mineral suite is distinct compared to other precious metal properties in the thesis area. The mineralogy consists of barite, stibnite, marcasite, galena, sphalerite, cinnabar, orpiment, Fe and Mn carbonates and quartz.

This mineral assemblage is similar to those forming at hot springs in geothermal areas in the Taupo Volcanic Zone, New Zealand (Ewers and Keays, 1977; Weissberg, 1969) and at Steamboat Springs, Nevada (Weissberg et al., 1979). Precious metal ore deposits interpreted to be from near surface epithermal systems (Buchanan, 1981; Berger and Eimon, 1983) also have mineral assemblages and elemental concentrations similar to those at the Emmons Hill prospect.

Details of the paragenetic sequence of mineral deposition are complicated by multiple periods of

Photo 41, 42. Intergrowths of low-Fe sphalerite (orange), galena (G) and stibnite (S). Late stage marcasite (M) surrounds the intergrowth. (Photo 41 = PP, Photo 42 = XP). Field of view is 0.5 cm wide.



brecciation. Galena and low Fe-sphalerite are the earliest sulphide phases (Photos 41 & 42). Stibnite, barite, marcasite and quartz are roughly coeval.

Paragenesis of minerals at Emmons Hill

---GALENA---

-SPHALERITE-

--BARITE-----

--STIBNITE-----

--MARCASITE---

-CINNIBAR-

-ORPIMENT-

--FE & MN CARBONATES--

----- SILICA -----

Cinnibar and orpiment (Photos 43 & 44) are intergrown and coeval with stibnite deposition. Stibnite is the most abundant sulphide mineral present. Deformation twinning in the stibnite (Photo 45) records post-depositional deformation. The deformation at the Emmons Hill prospect is similar to that in the vein breccia at the Laforma Mine. Photo 46 shows a stibnite supported breccia with clasts of rhyolite, metasediments and silica. Photo 47 is a closeup of the silica clast in Photo 46 and reveals the finely banded nature of the silica. This banded silica strongly resembles material from silica sinters, which apron surficial geothermal discharge areas such as hot springs and

Photo 43, 44. Intergrown cinnabar (C) and orpiment  
(yellow) (Photo 43 =PP, Photo 44 = XP).  
Field of view is 0.25 cm.

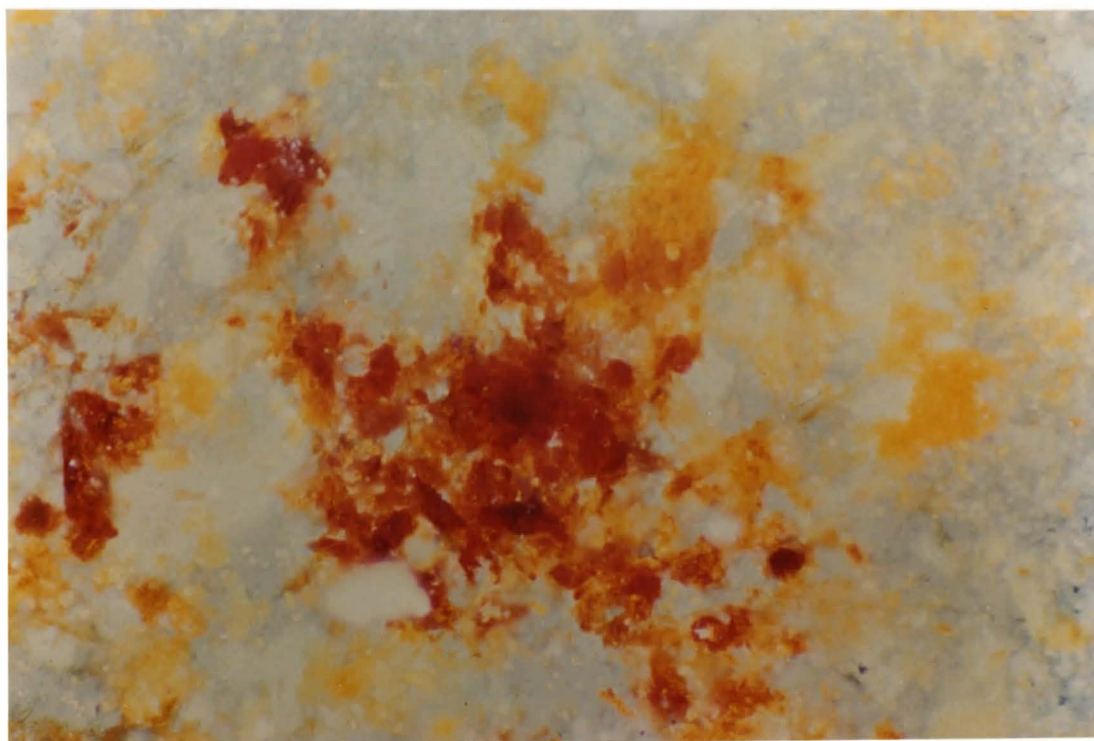
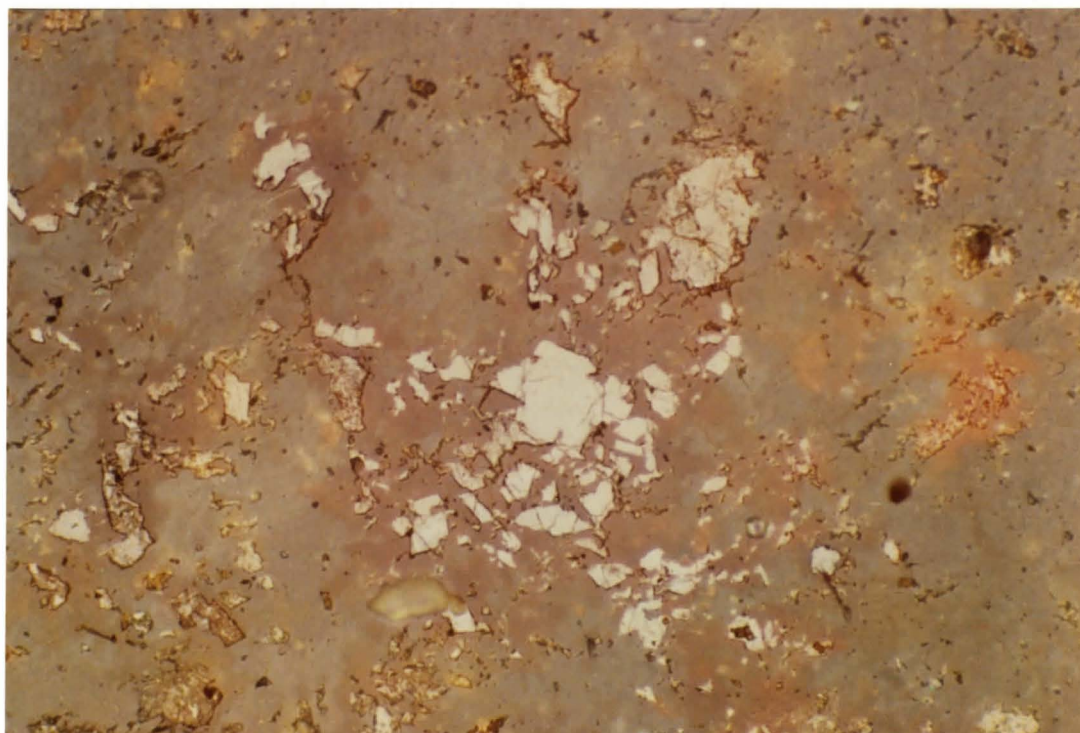


Photo 45. Deformation twinning in stibnite. Field of view is 0.6 cm (XP).

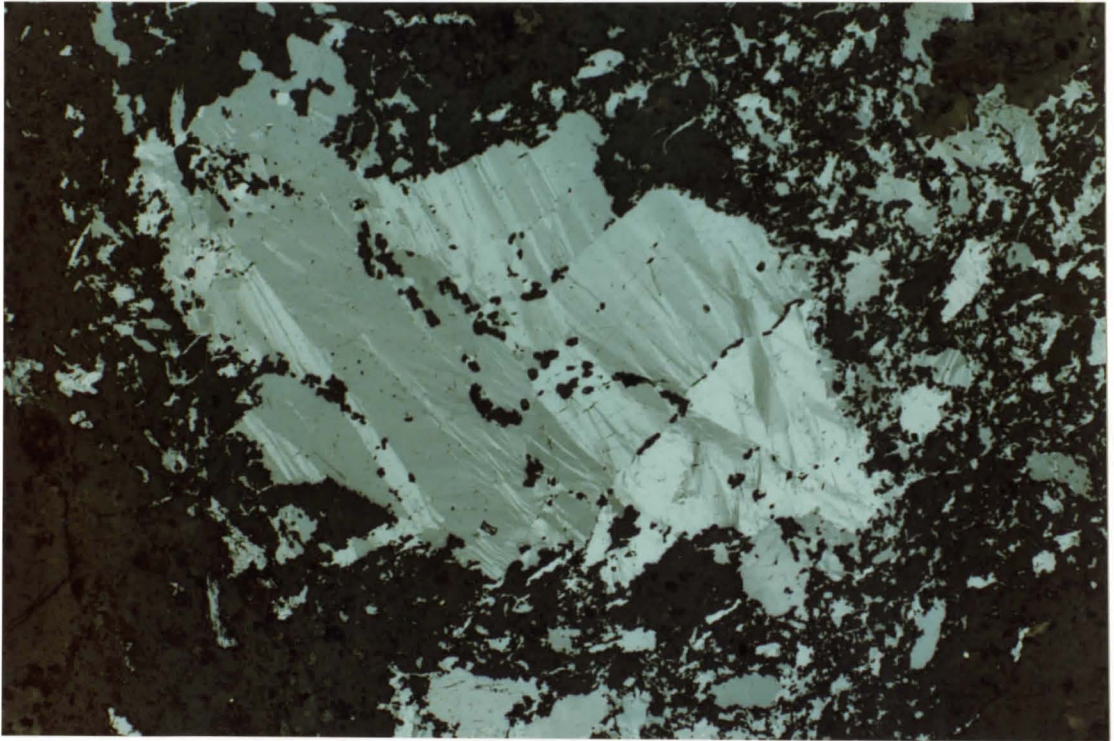
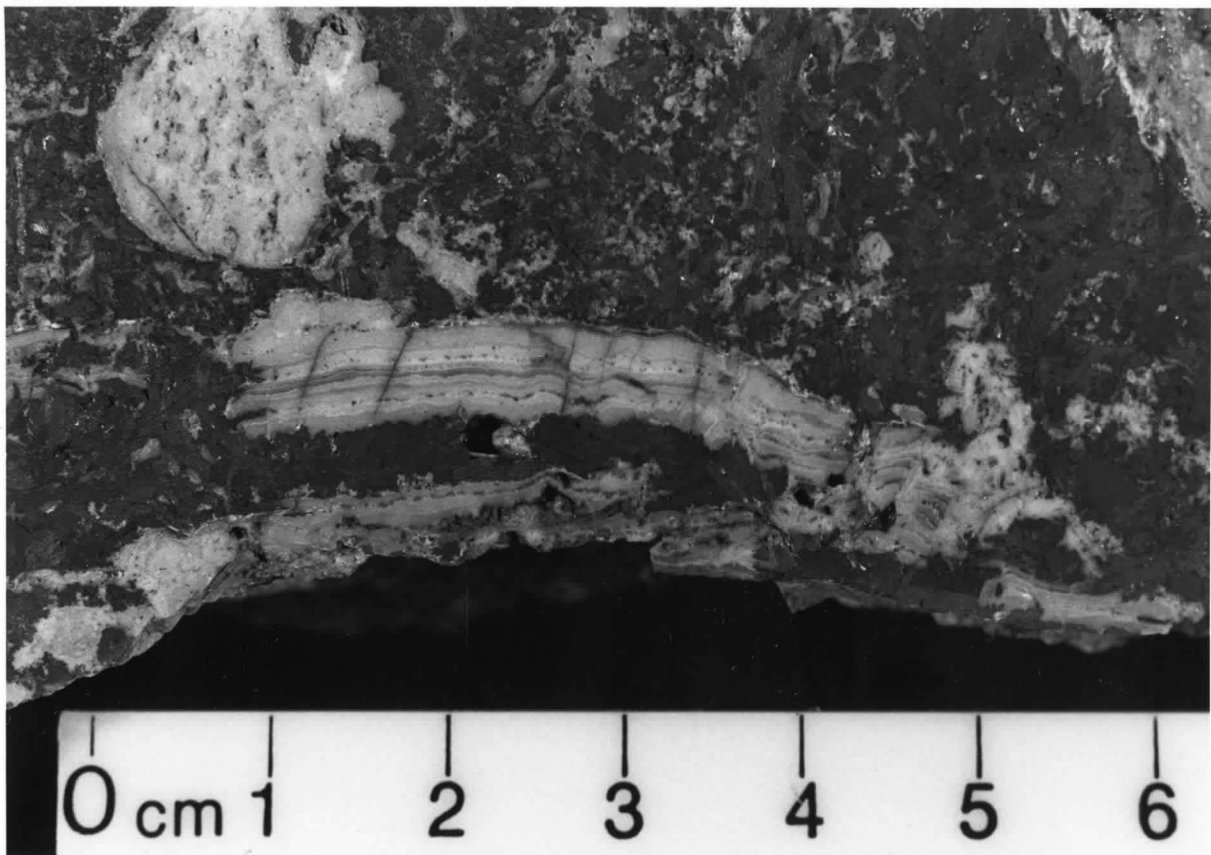


Photo 46. Clasts of rhyolite (R), metasediments (M) and sinter (S) within stibnite matrix.

Photo 47. Close-up of sinter clast with fine-grained banding.



geysers. That multiple clast types from different environments are present in the brecciated samples again suggests deformation is not solely tectonic but can be attributed to a hydrothermal eruption process.

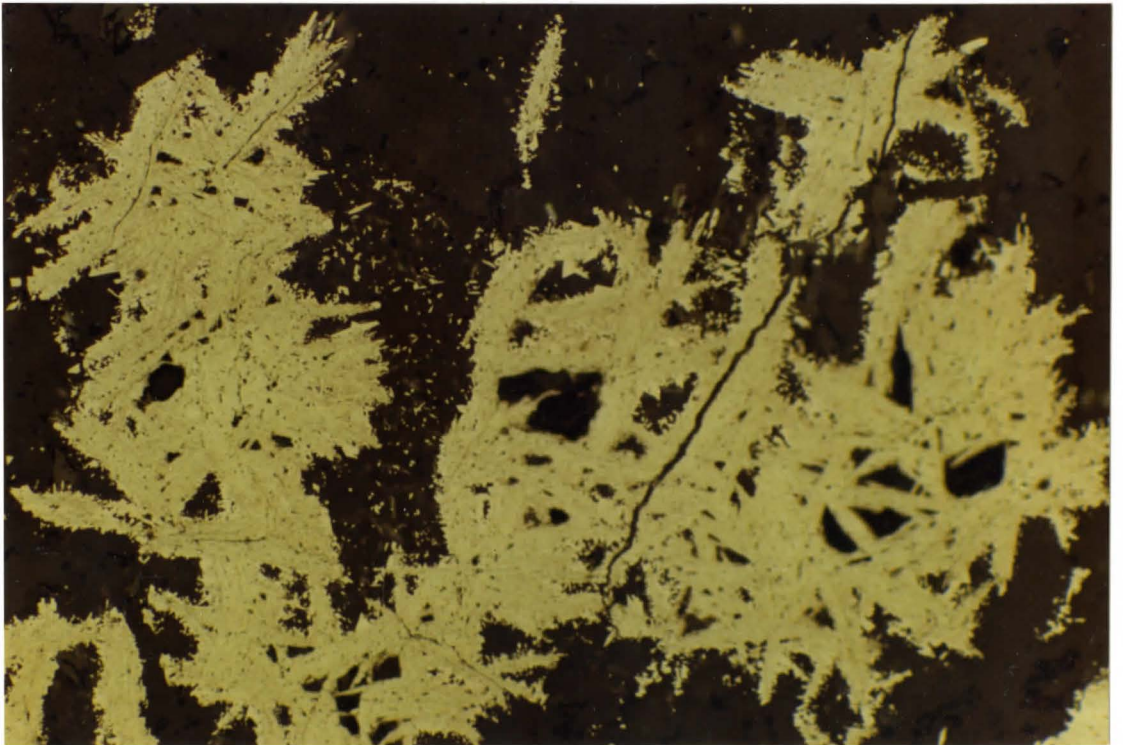
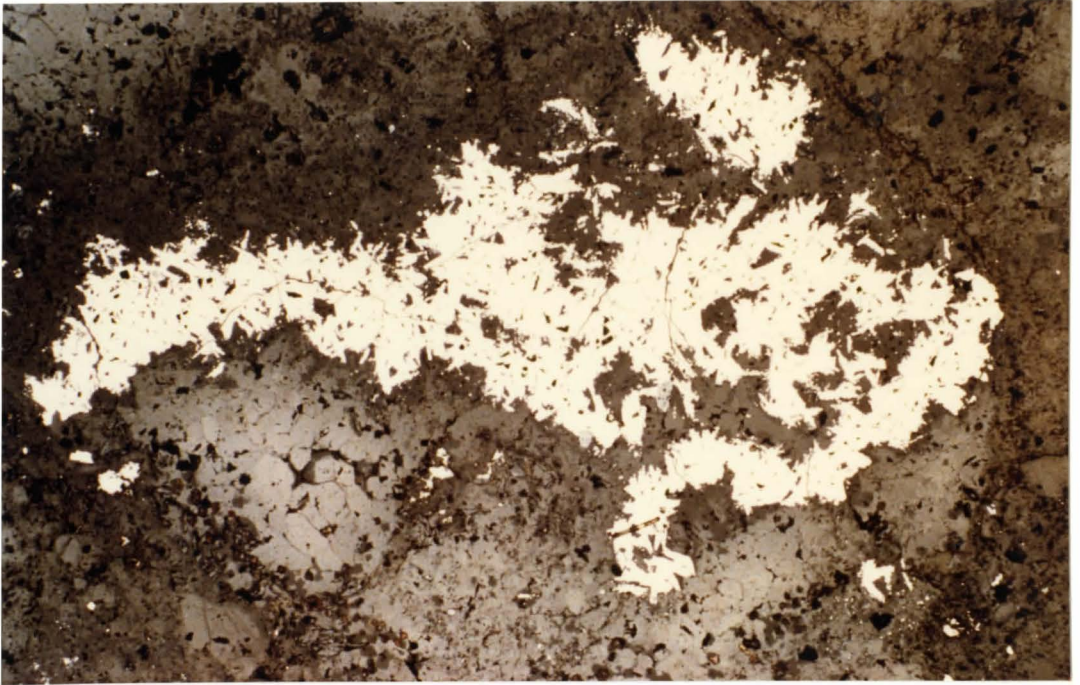
The occurrence of such an unusual mineralogy in comparison to the Laforma Mine suggests that a different physiochemical environment was prevalent at Emmons Hill. Marcasite (Photos 48 & 49) formation (rather than pyrite) is pH dependant (Murowchick and Barnes, 1986), and marcasite is stable only when  $\text{pH} < 5$  and where  $\text{H}_2\text{S}_2$  is available.  $\text{H}_2\text{S}_2$  is formed in hydrothermal environments by the partial oxidation of aqueous  $\text{H}_2\text{S}$ , which lowers the pH of the fluid. Intense kaolinite generation in the nearby metasediments indicates low pH conditions for the hydrothermal fluid and supports the requirements for marcasite generation. The presence of clasts resembling silica sinter suggests a near surface environment and oxidizing conditions. The preservation of marcasite over millions of years requires post-depositional temperatures below  $150^\circ \text{C}$ .

Cinnabar is a low temperature mineral often occurring in modern day hot spring deposits near the surface. White (1981) reports that cinnabar is restricted to the upper 50 m of the Steamboat Springs geothermal system in Nevada.

Barite is commonly found in near surface epithermal deposits and results from the oxidation of  $\text{H}_2\text{S}$  vapour by ground water (Bethke, 1984). This reaction produces acidic conditions favourable for marcasite deposition and which

Photo 48. Wispy laths of marcasite. Field of view is 0.4 cm (PP).

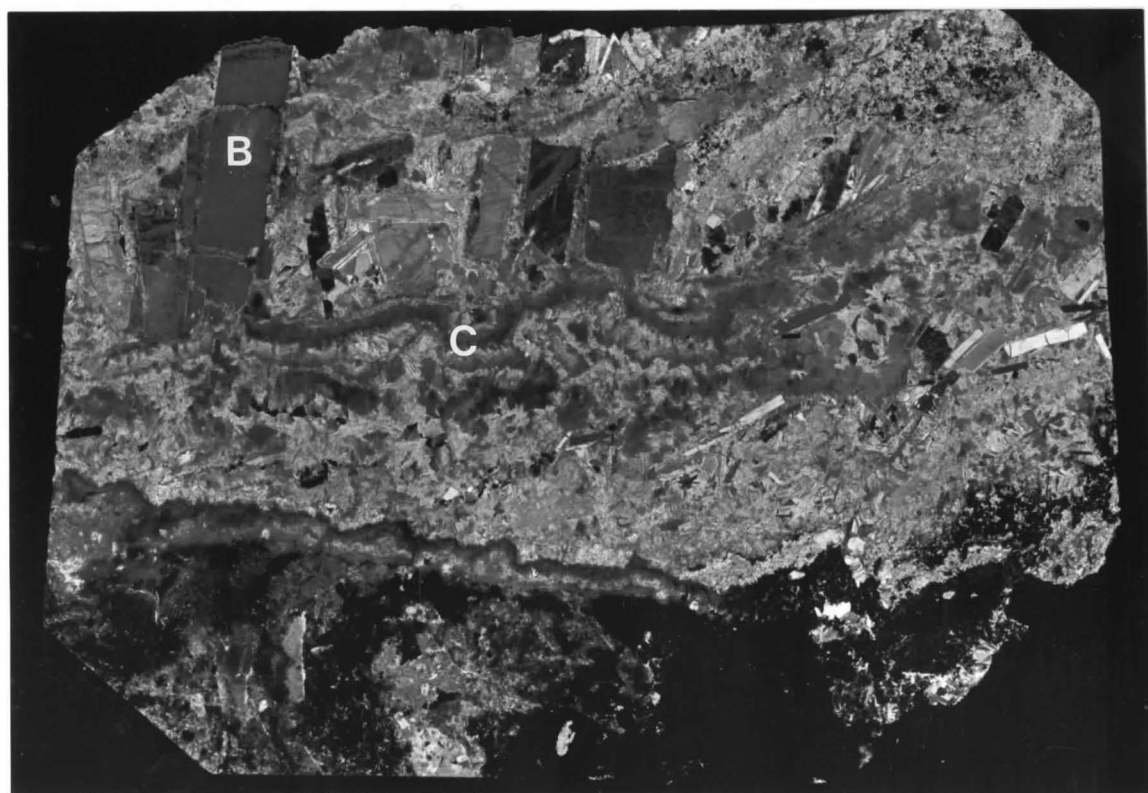
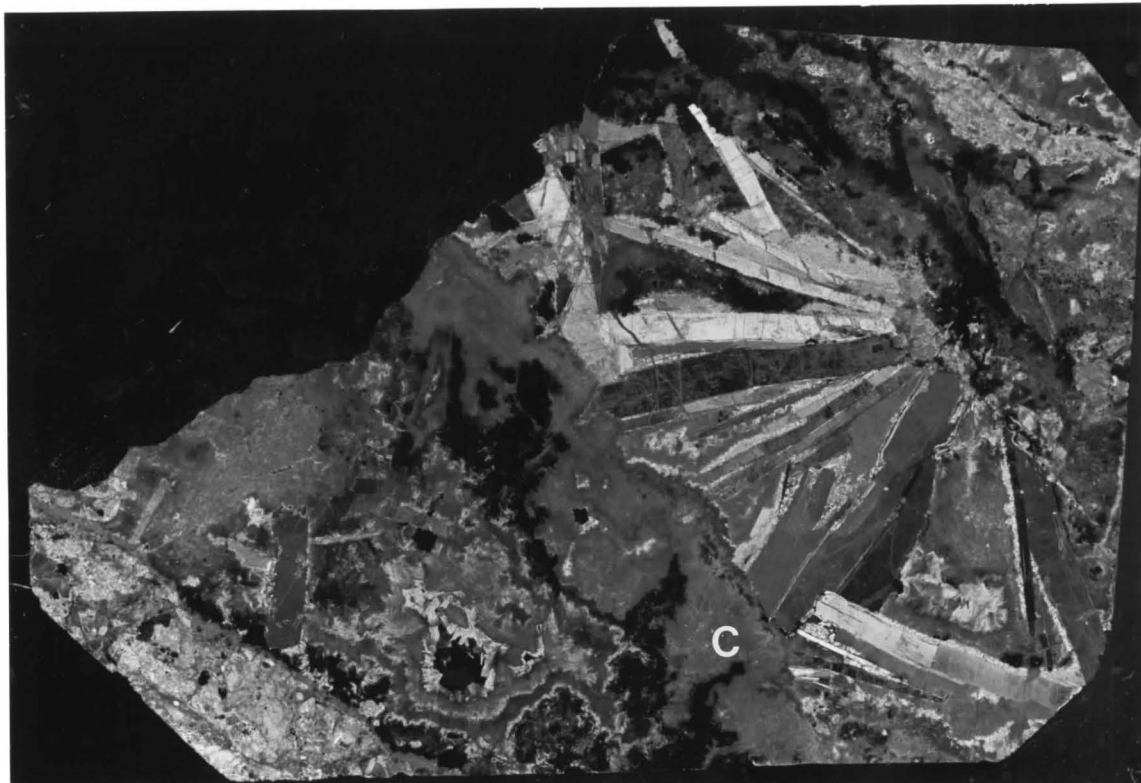
Photo 49. Close-up of marcasite laths. Field of view is 0.1 cm (PP).



would account for the intense clay alteration in the vicinity of the Emmons Hill showing. Cyclical changes in fluid pH are indicated by layered deposition of barite and calcite (Photos 50 and 51)

The mineral assemblage at Emmons Hill is similar to those found in the upper portions of modern hot springs and Acid-Sulphate type epithermal deposits. These are near surface phenomenon and if the Emmons Hill prospect is a fossil hot spring system and coeval with rhyolite volcanism (as is suggested by rhyolite clasts in the vein breccia) as the Laforma and Antoniuk deposits are, then the area has undergone an extremely slow rate of denudation since late Cretaceous time.

Photo 50, 51. Photomicrographs showing growth layering of calcite (C) and barite (B). Sections are 2.5 cm wide.



## CHAPTER 8. FLUID INCLUSION STUDY

Fluid inclusions are samples of fluid trapped within a mineral during its crystallization from an aqueous phase. Hydrothermal fluids at Freegold Mountain were important in the transport and deposition of silica, precious metals and other solutes. To understand the physiochemical conditions of the ore transporting fluids, fluid inclusions hosted within minerals deposited from these fluids were studied using a heating/cooling stage recently installed at McMaster University. The theories and methods of fluid inclusion analysis are not discussed in detail and the reader is referred to Roedder (1984) for authoritative discussion of this topic.

The McMaster fluid inclusion stage is a USGS type gas-flow stage manufactured by Fluid Inc., Denver, Colorado (Roedder, 1984, p.196; Wood et al., 1981). This stage allows the cooling of samples via liquid nitrogen cooled gases, and heating of samples by an electrical resistance heater over a temperature range of  $-196^{\circ}\text{C}$  to  $+700^{\circ}\text{C}$ . The inclusions are viewed with a Nikon Optiphot microscope specially fitted with a L32/0.40 Leitz objective. This objective has a long working distance since the sample is encapsulated within a metal chamber covered by three silica windows, and the sample is never closer to the objective than 4 mm.

The sample is placed inside this multiple silica-window

insulated metal chamber with gas intake and outlet ports. A thermocouple inserted through the chamber rests on the sample, and acts to hold the sample down so it will not become dislodged by the  $N_2$  gas flow. The thermocouple was calibrated regularly using commercially available standards and house standards prepared by J. Inman and R. Moritz. Table 7 lists the calibration standards used to test the accuracy and precision of the McMaster fluid inclusion stage.

The listed temperature of melting ( $T_m$ ) for each substance is from Roedder (1984, p. 208-210). The "observed  $T_m$ " column shows the lowest, average and highest temperatures observed for that particular substance during calibration runs. The final two columns show the standard deviation and number of runs made for each particular substance.

Figure 20 is a plot of Listed  $T_m$  versus Observed  $T_m$  from Table 7. It is apparent that accuracy and precision for substances 3, 4, 5, and 6 are quite good, with measured melting temperatures differing only by  $0.1^\circ C$  from quoted melting temperatures, and deviating from the quoted temperatures by less than  $0.2^\circ C$ . At low temperatures ( $<-60^\circ C$ ), accuracy was within  $1.0^\circ C$ . At high temperatures ( $>300^\circ C$ ) temperatures were accurate to within  $1-3^\circ C$  for a particular substance. Substances 7 and 9 may be impure, and these impurities have probably raised the melting temperature. Since the critical behaviour of  $H_2O$  (8) is the

Table 7. Temperature data for standard substances used in calibrating the McMaster University heating-freezing stage.

SUBSTANCE	LISTED T <sub>m</sub>	OBSERVED T <sub>m</sub>	S.D.	n
1 n-HEXANE	-95	-91.8	1.1	8
	-95	-94		
	-95	-95		
2 n-HEPTANE	-90.6	-88.6	0.8	10
	-90.6	-89.7		
	-90.6	-90.4		
3 CO <sub>2</sub> (25 MOL%)	-56.6	-56.5	0.16	14
	-56.6	-56.7		
	-56.6	-57		
4 n-DECANE	-29.7	-29.4	0.1	10
	-29.7	-29.6		
	-29.7	-29.7		
5 H <sub>2</sub> O+NACL (10%)	-6.6	-6.3	0.14	7
	-6.6	-6.6		
	-6.6	-6.7		
6 H <sub>2</sub> O PURE	0	0	0	6
	0	0		
	0	0		
7 NaNO <sub>3</sub>	306.8	307.8	0.33	7
	306.8	308.4		
	306.8	308.9		
8 H <sub>2</sub> O (C.P.)	374.1	374.1	0.6	14
	374.1	375.2		
	374.1	375.8		
9 TELLURIUM	449.5	448	3.6	4
	449.5	452.8		
	449.5	456.3		

# CALIBRATION CURVE FOR MCMASTER

FLUID INCLUSION STAGE

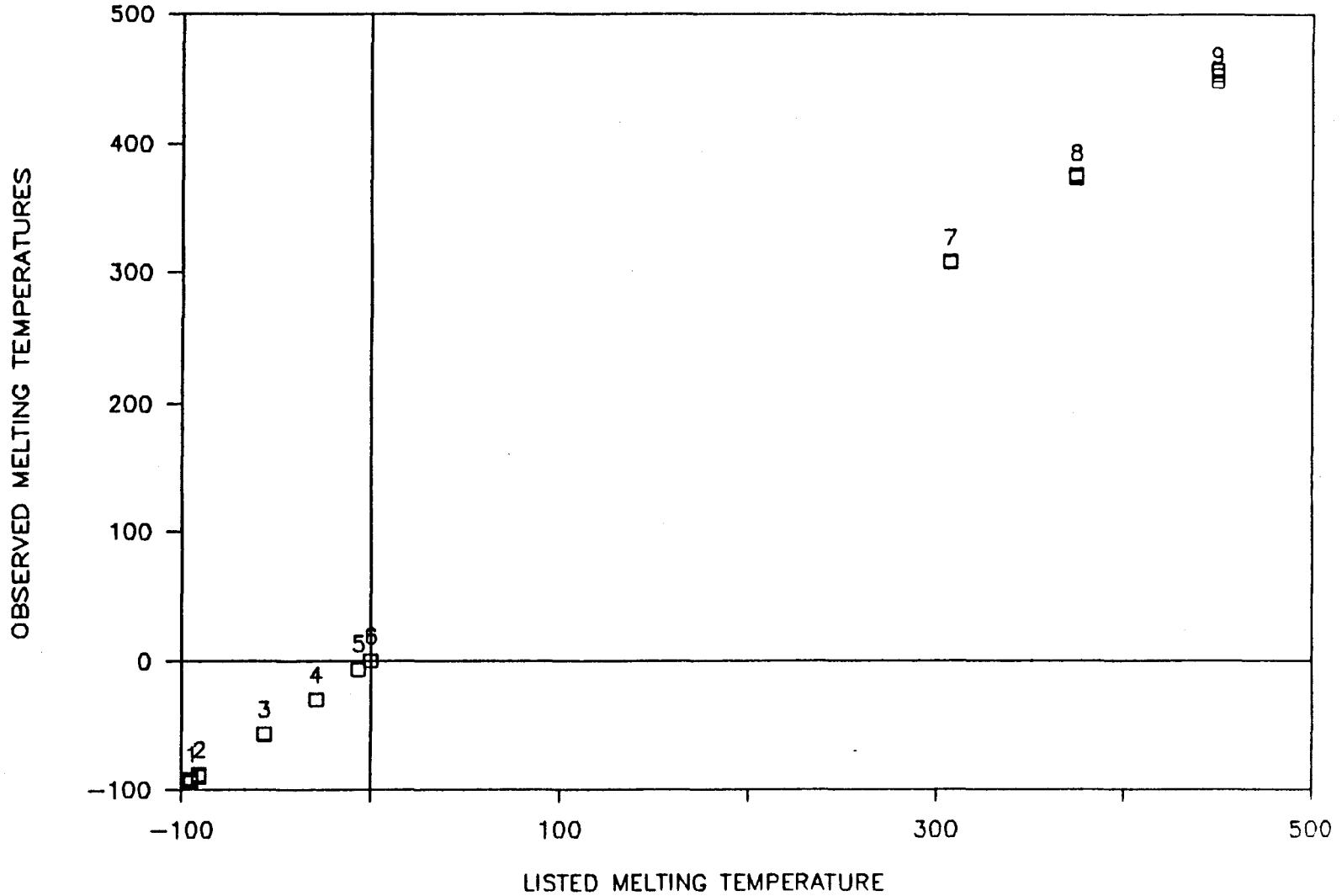


Figure 20. Temperature calibration curve for McMaster USGS-type fluid inclusion stage using standard substances listed in Table 7.

most reliable high temperature standard, accuracy and precision at high temperatures is believed to be  $\pm 1^{\circ}\text{C}$ .

The optimum inclusion size for study using the McMaster apparatus is 10  $\mu\text{m}$  or larger. Inclusions smaller than this are workable but time consuming because of the difficulty in observing phase changes, and therefore multiple runs are often required. The addition of a colour video camera (Nikon model GXS 700 UCH) and high-resolution RGB monitor to the microscope lessens eye strain and fatigue on the inclusion worker. The microscope is also equipped with a camera to photograph inclusions and inclusion behaviour.

### 8.1 Method of Study

The material to be studied is first observed in standard thin section to discern if the inclusions are usable based on their size, abundance, and inferred origin. Samples are prepared for analysis by doubly polishing a 100  $\mu\text{m}$  plate of fluid inclusion bearing material. Depending on the optical quality of the material, the thickness of the samples may range from 50  $\mu\text{m}$  to 200  $\mu\text{m}$ . A photograph is taken of the entire sample (enlarged to 8 x 10 in. size), then petrography is conducted using the photo as a map to orient growth zones, fracture zones and individual inclusions of interest. After petrography the polished section is broken into small (ca. 5  $\text{mm}^2$ ) chips with each subsample located on the photograph.

The sample is ready for analysis at this stage. Before

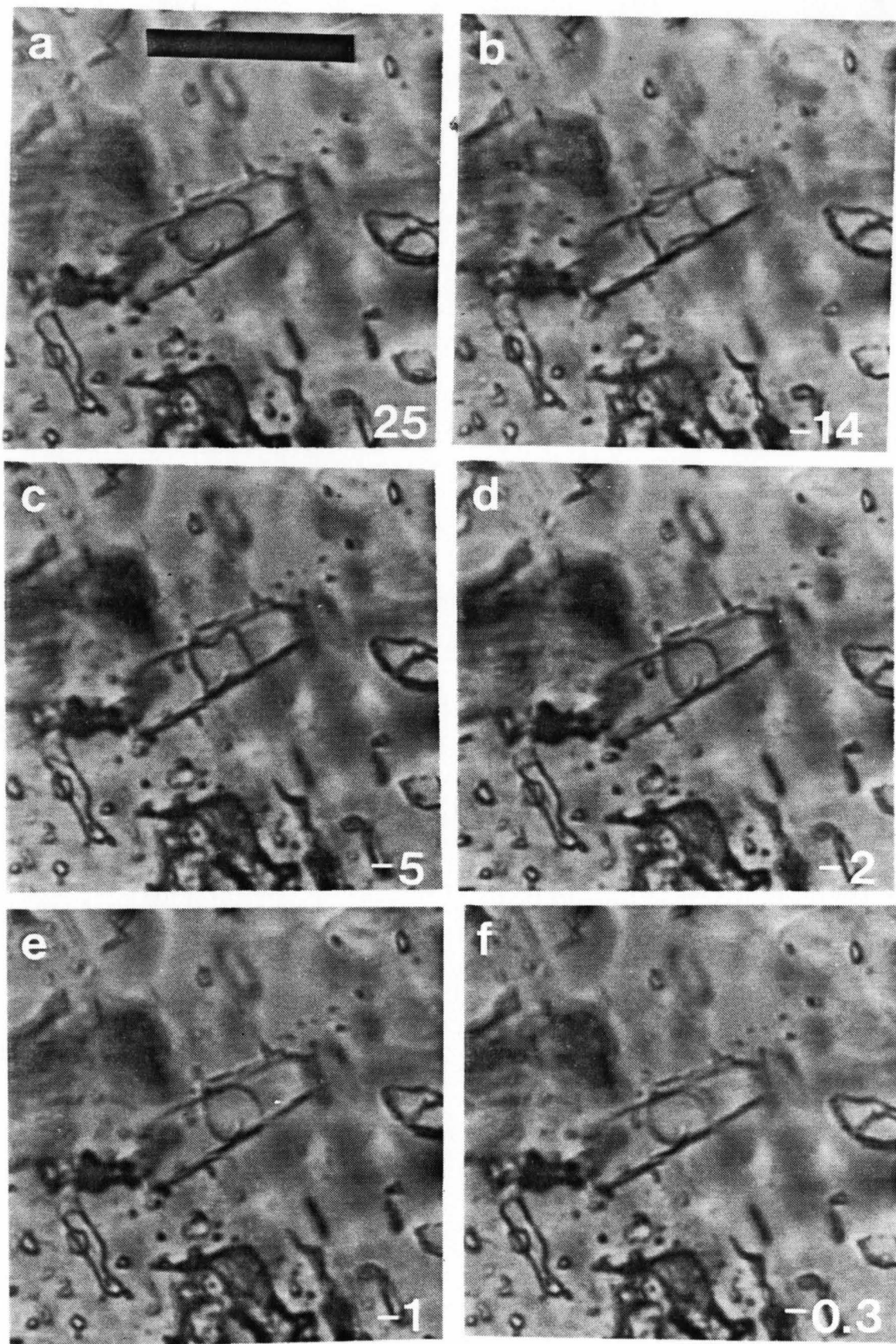
analysis each inclusion should be classified as to probable origin: primary, secondary, or pseudosecondary following the criteria recommended by Roedder (1984, p. 43-45). For quartz hosted inclusions the sample should undergo freezing runs prior to heating runs since heating the specimen may decrepitate or stretch inclusions in the sample, changing their volume and possibly destroying the whole chip (Roedder, 1984). The exception to this rule is when the inclusions are hosted by barite (or other easily deformed minerals, eg. fluorite). Freezing runs will transform water to ice, causing a concomitant volume expansion. If the vapour bubble (ie. vacuole) in the inclusion cannot account for this volume change then the inclusions can stretch or decrepitate (Ulrich and Bodnar, 1984). This phenomenon has been observed by the author during freezing runs on barite samples from Emmons Hill.

Freezing runs can determine the salinity of an aqueous fluid, using the freezing point depression of water by NaCl to obtain an approximation of the concentration of total dissolved salts in the solution. The contribution of individual solutes to the salinity of the solution cannot be determined by this method, but the dominant salt in most hydrothermal systems is NaCl (Roedder, 1984) and quoting the salinity in terms of weight percent NaCl equivalent closely approximates the true NaCl concentration. Freezing runs are also useful to identify CO<sub>2</sub> inclusions, as the melting point for CO<sub>2</sub> is -56.6°C.

Figure 21a-f shows a typical freezing run for salinity determination of a 40  $\mu\text{m}$  long inclusion hosted in barite, where the inclusion is cooled from room temperature until it freezes at around  $-35^{\circ}\text{C}$  and its appearance observed on warming up. The number in the lower right hand corner is the temperature of the sample. The appearance of the inclusion at room temperature is shown in Figure 21a. The sub-oval shape in the centre of the inclusion is the  $\text{H}_2\text{O}$  vapour bubble (essentially a vacuum), surrounded by liquid. Cooling the inclusion to  $-35^{\circ}\text{C}$  causes the liquid to freeze. There is a sudden "jerk" in the vapour bubble as it shrinks due to volume loss. Figures 21b-e show the changing appearance of the bubble as the ice progressively melts (the ice particles cannot be distinguished in these photographs). Figure 21f shows the vapour bubble in the process of attaining its original shape as the final particles of ice melt at  $-0.3^{\circ}\text{C}$ . This  $0.3^{\circ}\text{C}$  depression in freezing point (with respect to pure water) indicates that the liquid has a concentration of 0.5 wt. % NaCl (Potter et al., 1978).

Heating runs determine the homogenization temperature of the fluid in the inclusion. At room temperature, two or more phases are present within a given inclusion. Figure 22a shows a 20  $\mu\text{m}$  primary quartz-hosted inclusion at room temperature containing three phases: liquid  $\text{H}_2\text{O}$ , vapour  $\text{H}_2\text{O}$  and a cubic daughter mineral of halite. Heating the inclusion in Figures 22b-d causes the vapour bubble to vibrate rapidly and decrease in diameter, while the halite

Figure 21. Typical freezing run for salinity determination on a barite-hosted fluid inclusion (see text for details). Scale bar is 40  $\mu\text{m}$  long.



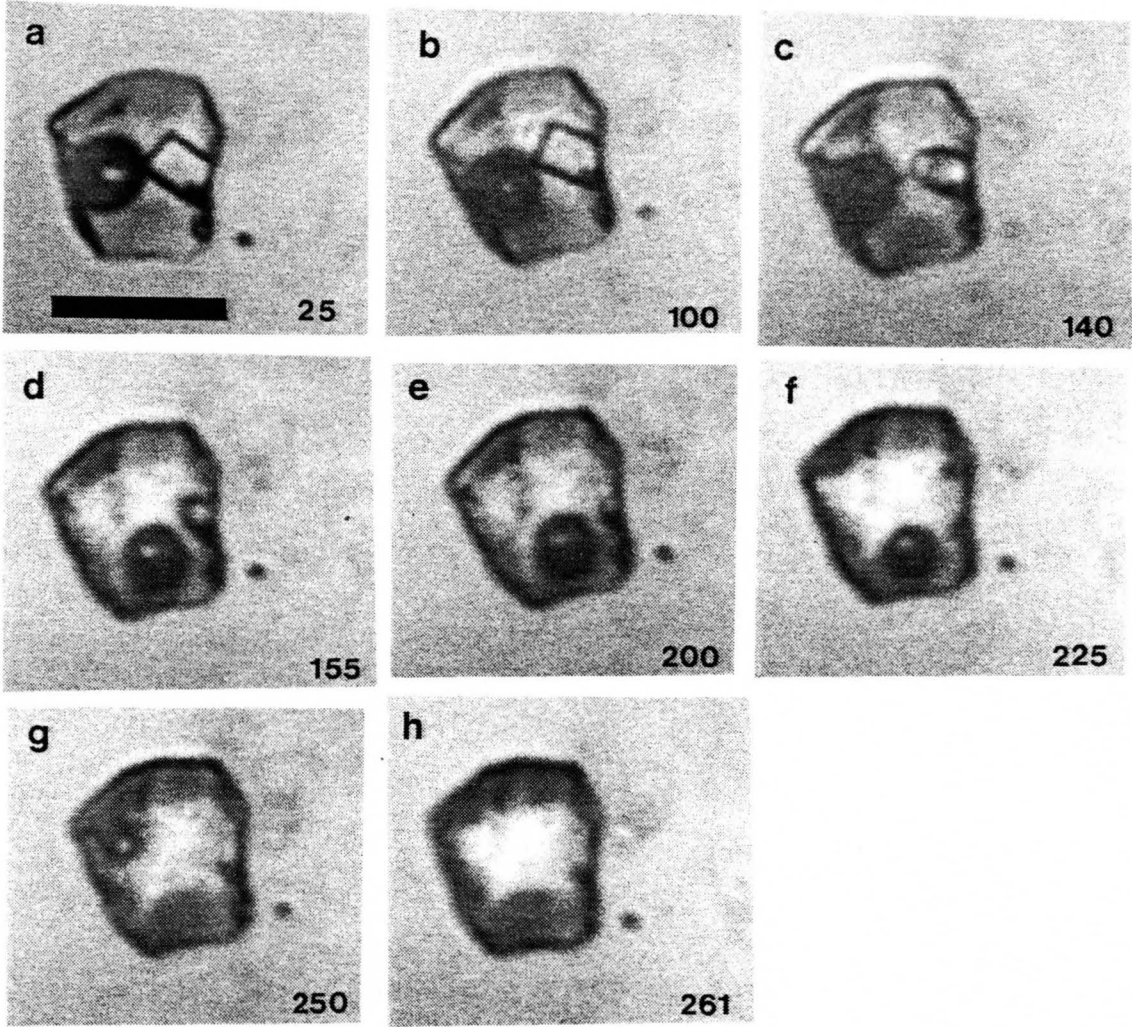
slowly dissolves into liquid. The halite is totally dissolved at 225°C corresponding to a salinity of approximately 31 wt. % NaCl (Sourirajan and Kennedy, 1962). The vapour phase gets smaller with continual heating (Figure 22f-h) and at 263°C the inclusion homogenizes to the liquid phase.

The presence of boiling zones in the deposits at Freegold Mountain and the near surface mineralogy at Emmons Hill indicates that the homogenization temperatures are indicative of the trapping temperature and that no pressure corrections are necessary. The temperature of 263°C is therefore the trapping temperature of the fluid and the temperature of crystallization of the quartz. The homogenization of CO<sub>2</sub> inclusions is conducted in a similar manner although at much lower temperatures (the critical temperature of CO<sub>2</sub> is + 31.0°C). For more detailed information on heating/cooling measurements the reader is referred to Roedder (1984).

## 8.2 Fluid Inclusion Studies of Ore Deposits and Quartz Veins at Freegold Mountain

A total of 529 measurements from 370 individual inclusions represents the database for this chapter (Appendix C). Fluid inclusions from the Laforma Mine, Emmons Hill, Antoniuk Breccia and from a barren "bull" quartz vein were studied to identify the temperature of the ore fluids and their chemical nature. Quartz was the host

Figure 22. Typical heating run for homogenization temperature determination of a quartz-hosted halite-bearing fluid inclusion (see text for details). Scale bar is 10  $\mu\text{m}$  long.



mineral for all inclusions studied except for Emmons Hill, where only barite provided adequate inclusions.

#### 8.2.1 Laforma Mine

Fluid inclusions were studied in the Laforma vein from diamond drill samples TU10-271 and TU6-248 and from the 2nd and 4th levels of the mine as indicated on Figure 15. Banding in the vein is indistinct and only two periods of quartz deposition can be discerned in the main ore zone from the sample on level 4 (see Photos 24 and 25). This sample has a relatively simple paragenesis, the outer zones are early and the central zone represents the late and final stages of deposition of quartz until the hydrothermal system sealed itself. The lack of distinct paragenetic relationships and the narrow width of the Laforma vein indicates that the hydrothermal system operated for a relatively short period of time and that the inclusion samples throughout the mine were essentially contemporaneous.

##### 8.2.1.1 TU10-271

Sample TU10-271 represents the deepest ore sample studied. It is a moderately brecciated quartz vein sample with about 5% pyrite and trace arsenopyrite, sphalerite and chalcopyrite. Inclusions are generally small, averaging around 5  $\mu\text{m}$  diameter but occasionally reaching 15  $\mu\text{m}$ . Two types of inclusions are present:  $\text{H}_2\text{O}$  liquid and  $\text{CO}_2$  vapour.

Figure 23 is a histogram of 48 primary H<sub>2</sub>O fluid inclusions measured in the sample. The strong peak between the 165°-180°C interval coincides with the average homogenization temperature ( $T_{hom}$ ) of  $176^{\circ} \pm 26^{\circ}$  C (range 150°-260°C). These inclusions had average salinities of  $4.3 \pm 1.1$  wt. % NaCl.

CO<sub>2</sub> vapour inclusions were sporadically present in the sample (Figure 24A). The average melting point of CO<sub>2</sub> was -57.3°C (range -57.6° to -56.9°C). Pure CO<sub>2</sub> has a melting point of -56.6°C and CO<sub>2</sub> standards were checked during analysis to verify the accuracy of the thermocouple and trendicator (temperature indicator). The lowering of the melting point of CO<sub>2</sub> is probably due to the presence of other gases in the hydrothermal system (Burruss, 1981). Possible candidates having melting points below -56.6°C are SO<sub>2</sub>, H<sub>2</sub>S, COS and CH<sub>4</sub>. Analyses of modern hydrothermal systems suggests that CO<sub>2</sub>, H<sub>2</sub>S and CH<sub>4</sub> are the only gases of significance, and therefore the contaminant may be H<sub>2</sub>S and/or CH<sub>4</sub>. The presence of such volatile components with the CO<sub>2</sub> phase indicates the fluid has undergone immiscibility reactions or effervescence (liquid->liquid + vapour). This should not be confused with "boiling". Immiscibility or effervescence is the degasification of dissolved volatile components (CO<sub>2</sub>, H<sub>2</sub>S and CH<sub>4</sub>) and not the production of H<sub>2</sub>O vapour.

The CO<sub>2</sub> inclusions homogenize to the liquid phase around +29°C and have densities of approximately 0.63 g/cm<sup>3</sup>

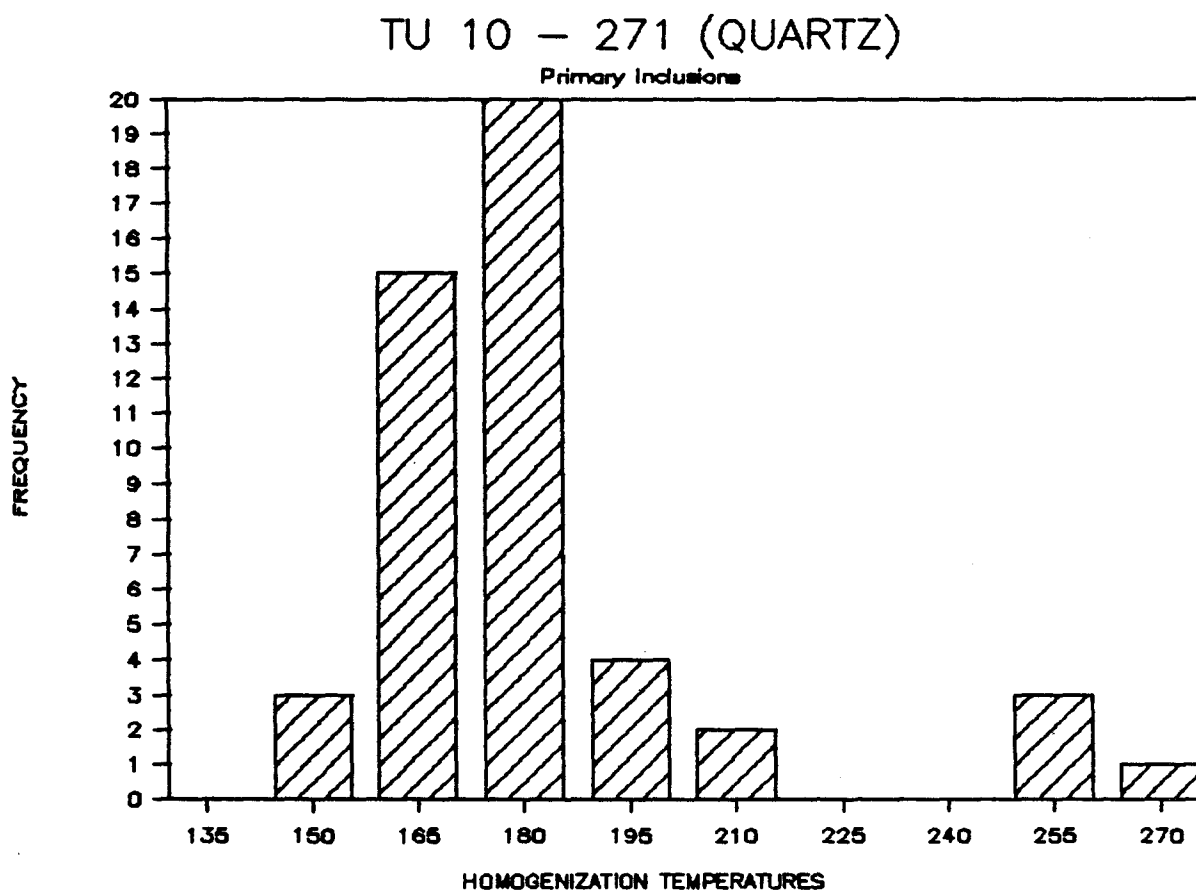
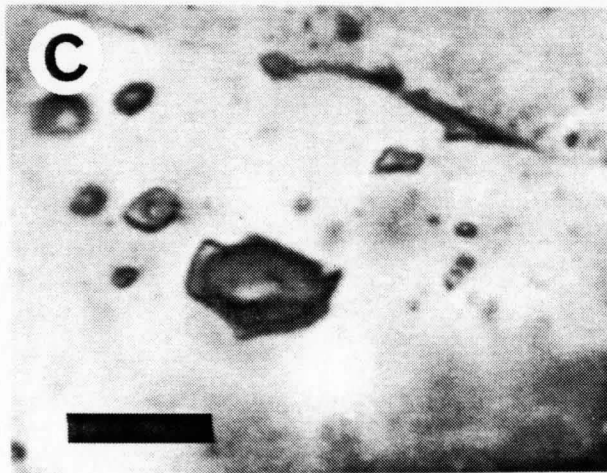
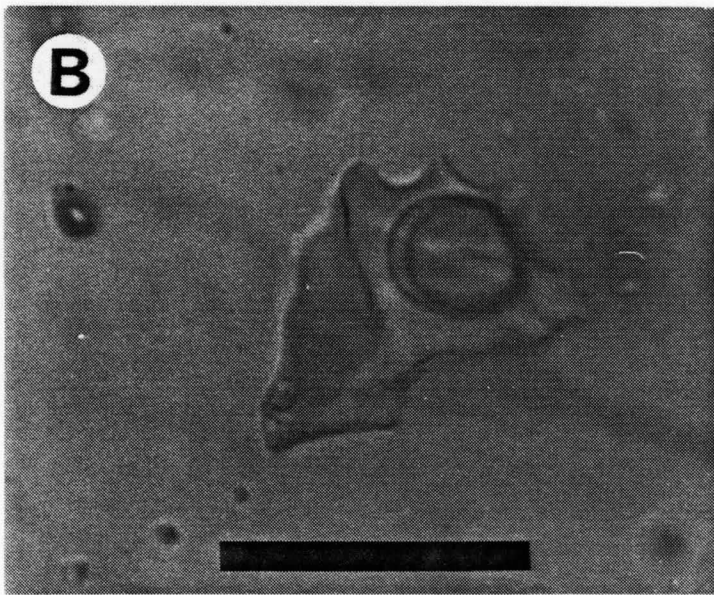
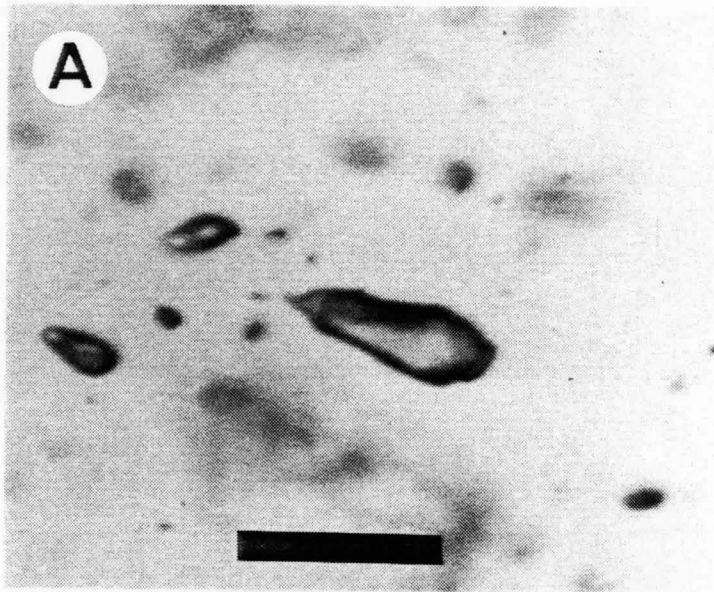


Figure 23. Histogram of homogenization temperatures for Laforma sample TU 10-271.

Figure 24. (a) CO<sub>2</sub> inclusions within TU 10-271. Scale bar is 15 μm long.

(b) Three phase CO<sub>2</sub>-H<sub>2</sub>O inclusion from 4th level. This rare type of inclusion contains a CO<sub>2</sub> vapour phase surrounded by CO<sub>2</sub> and H<sub>2</sub>O liquid. Scale bar is 15 μm long.

(c) Vapour-rich H<sub>2</sub>O inclusion (centre) surrounded by liquid-rich H<sub>2</sub>O inclusions. Sample is from the 4th level boiling zone. Scale bar is 10 μm long.



(Bodnar et al., 1985).

#### 8.2.1.2 TU6-248

This sample is from the vein approximately 120 m above TU10-271, and is comparable in mineralogy and character. Figure 25 is a histogram of homogenization temperatures of 43 primary inclusions in TU6-248. The data show more dispersion (ie. higher standard deviation) than Figure 23, but are similar in that the mean,  $188^{\circ} \pm 31^{\circ}\text{C}$ , is between the interval  $165^{\circ}$  to  $195^{\circ}\text{C}$ . A possible reason for the wider spread in this sample is that increasing effervescence of the liquid occurs as the fluid ascends into lower pressure regions. Such effervescence raises the vapour pressure of a fluid (Bodnar et al., 1985) and may induce true boiling (the production of  $\text{H}_2\text{O}$  vapour). The spread in the data is therefore interpreted to represent the initiation of boiling of  $\text{H}_2\text{O}$  in the hydrothermal fluid. The average salinity is  $3.9 \pm 1.0$  wt. % NaCl and is similar to that for TU10-271.

The analysis of  $\text{CO}_2$  inclusions again indicates contamination by other volatile components in that the average melting temperature is  $-57.3^{\circ}\text{C}$ . Homogenization of  $\text{CO}_2$  inclusions to the vapour phase at approximately  $+30.6^{\circ}\text{C}$  suggests a bulk density of  $0.38 \text{ g/cm}^3$  for  $\text{CO}_2$ . The change in density from  $0.68 \text{ g/cm}^3$  to  $0.38 \text{ g/cm}^3$  with elevation reflects the increasing volatility of the hydrothermal system since the volume of volatile constituents increases

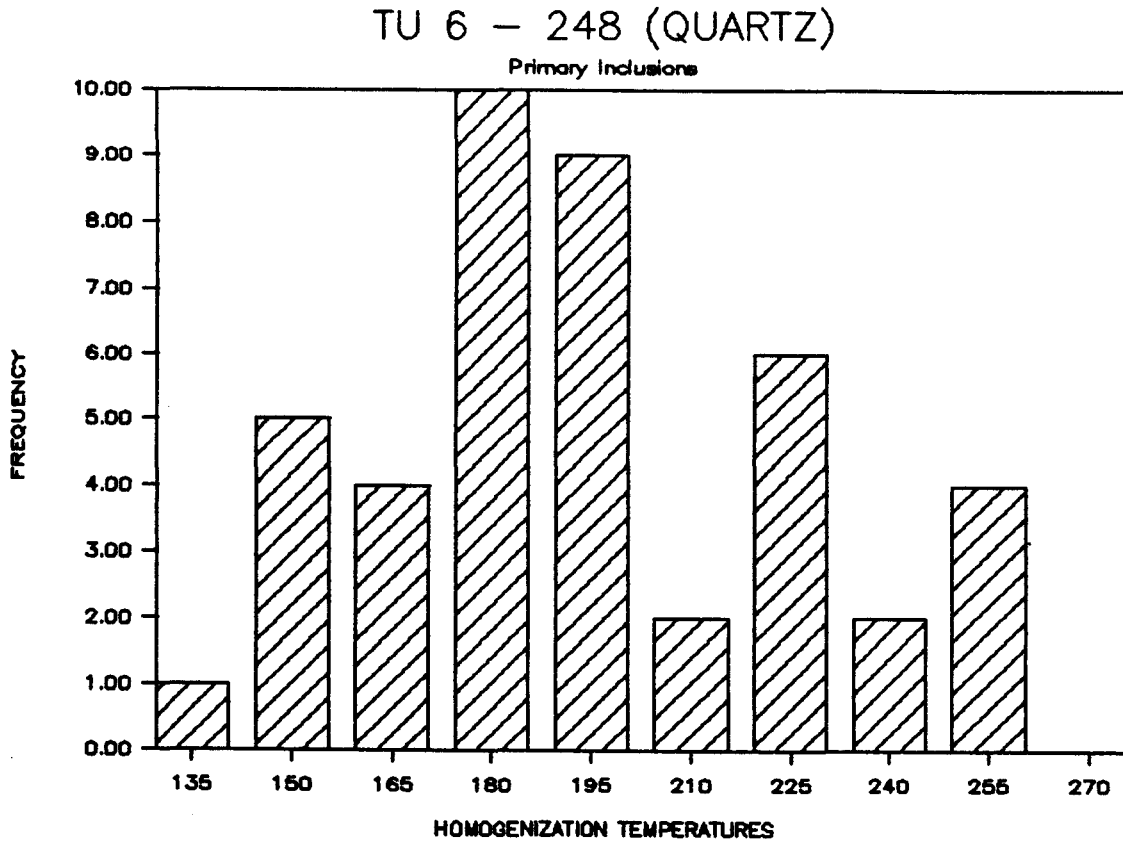


Figure 25. Histogram of homogenization temperatures for Laforma sample TU 6-248.

with decreasing pressure upon ascent. The increase in volatility accounts for the initiation of boiling and the spread in the homogenization data in Figure 25.

#### 8.2.1.3 4TH LEVEL

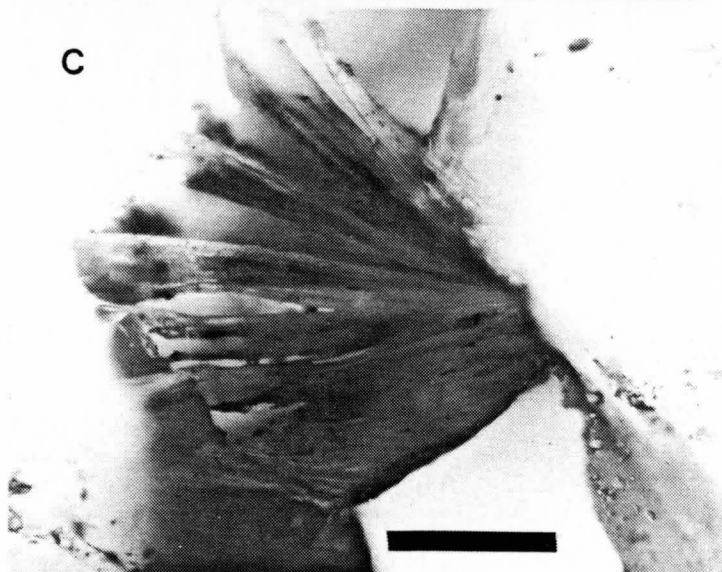
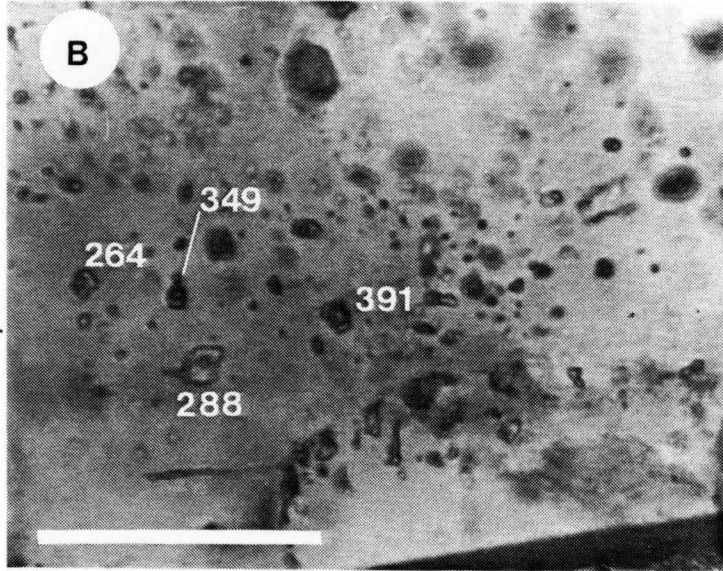
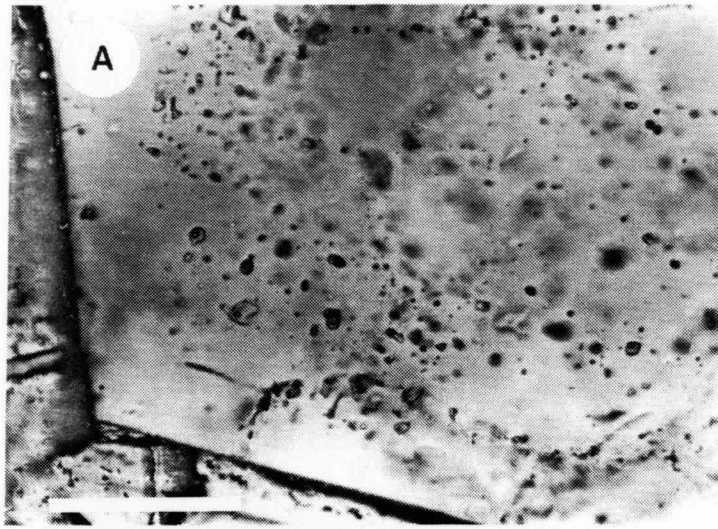
Photo 25 is from a polished section of the central portion of the Laforma vein at Level 4 in Photo 24. The thin section shows outer zones of randomly oriented, anhedral, slightly brecciated, medium grained quartz and an inner zone of coarser, euhedral, undeformed quartz grains with long axes oriented towards the interior of the vein. This orientation is a classic textural example of fissure filling common in epithermal systems. This central zone however shows fluid inclusion characteristics unlike any epithermal system reported in the literature.

The central zone records a history of fluid boiling resulting in extreme increases in salinity and the deposition of carbonate, silicate, sulfide minerals and gold. The evidence for boiling is provided in Figure 26A-C. Figure 26A shows a portion of a euhedral quartz grain near the termination which is surrounded by Fe and Mg-rich calcite (qualitative microprobe analysis). The quartz grain has not been deformed and the inclusions within are all primary in nature and display growth zoning. A closeup of the inclusions in Figure 26B reveals that the inclusions have varying liquid/vapour ratios and vastly different temperatures of homogenization. If the fluid precipitating

Figure 26. (a) Euhedral termination of inclusion-rich quartz crystal surrounded by Fe-Mg carbonate within 4th level boiling zone. The absence of deformation in this sample indicates that these inclusions are primary. Scale bar is 50  $\mu\text{m}$  long.

(b) Enlargement of (a) showing primary inclusions with variable vapour/liquid ratios and extreme ranges in homogenization temperatures indicative of fluids trapped under boiling conditions. Scale bar is 45  $\mu\text{m}$  long.

(c) Hydrothermal sericite growing in vug from the 4th level boiling zone. Scale bar is approximately 1 mm long.



the quartz was homogeneous the liquid/vapour ratio and  $T_{hom}$  of the inclusions would be relatively constant. The presence of highly variable liquid/vapour ratios and  $H_2O$  vapour inclusions (Figure 24C, c.f. Roedder, 1984, p. 257) indicates that a heterogeneous "boiling" fluid deposited the minerals in this zone.

Arsenopyrite is the dominant sulfide mineral in this sample with lesser amounts of pyrite, sphalerite, galena and chalcopyrite. The sphalerite is an Fe-rich variety as compared to that at Emmons Hill. Sulphide minerals occur as intergrowths with quartz (Photo 21) and in vugs along with other minerals such as carbonate (Fig. 26A) and sericite (Fig. 26C). Gold is coeval with arsenopyrite deposition (Photo 22). These observations corroborate theoretical calculations by Drummond and Ohmoto (1985) which indicate that the process of hydrothermal fluid boiling enhances mineral deposition.

Figure 27 is a histogram of homogenization temperatures of fluid inclusions within the boiling zone. It is evident that there is a large range in trapping temperatures. This is the result of the trapping of fluids along the  $H_2O$  liquid-vapour curve and measuring  $T_{hom}$  on inclusions with varying liquid/vapour ratios which produce inaccurately high  $T_{hom}$  (Roedder, 1984, p. 256). Only inclusions which have trapped either 100% liquid or 100% gas will provide accurate temperatures of trapping. This condition is rare in boiling systems (Roedder, 1984, p. 256) and therefore the minimum

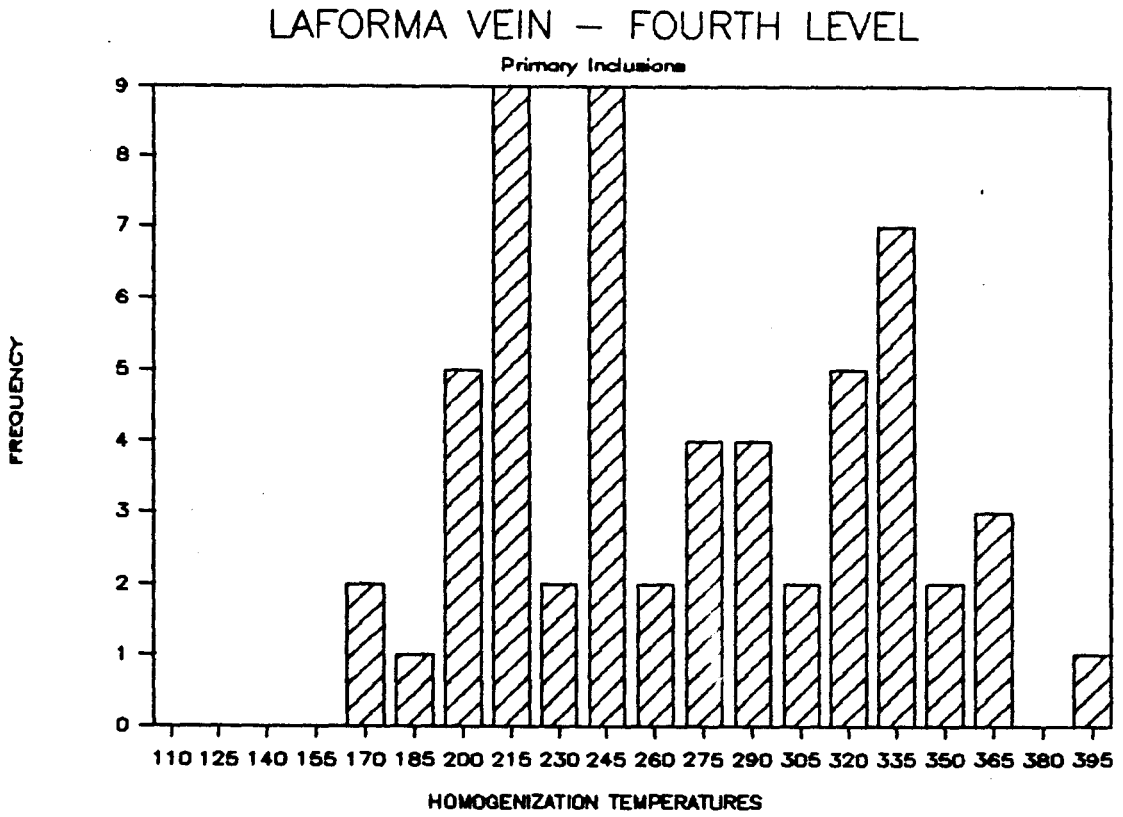


Figure 27. Histogram of homogenization temperatures for fluid inclusions for the 4th level Laforma sample.

Them is used to estimate the temperature of the boiling fluid. This would indicate a temperature between 175° - 200° C which is in agreement with homogenization temperatures in the lower portions of the vein.

The unusual aspect of this zone, apart from boiling, is the presence of high salinity inclusions with daughter minerals. The range in compositions for most epithermal gold-silver deposits is 0-3 wt.% NaCl (Henley, 1985). Salinities within the 4th Level boiling zone range from 4 to 42 wt.% NaCl. These inclusions have multiple daughter and accessory minerals precipitated from the hydrothermal fluid and are shown in Figure A-H.

An attempt was made to analyze the composition of daughter minerals using a SEM equipped with an energy dispersive X-ray analysis unit at the Geological Survey of Canada following the method of Metzger et al., (1977), and was successful in identifying the long, black rods in Figure 28A and F as tourmaline (t). Other mineral phases hosted within inclusions could not be identified due to their small size (generally less than 2  $\mu\text{m}$ ). Some of the inclusions were empty, probably due to the high vapour pressure within the inclusion which may have caused the minerals to be blown out of the inclusion upon fracturing. Figure 28A shows a group of inclusions associated with tourmaline. These rod-shaped minerals are not true daughter minerals (ie. minerals that have precipitated from the solution within the inclusion) since only portions of the rod are within the

Figure 28. Multiphase inclusions hosted within quartz from the Laforma 4th level boiling zone.

(A) A group of fluid inclusions containing tourmaline (t), halite (h), opaque minerals (o) and a vapour phase (v). Note that the tourmaline, which is not a true daughter mineral, passes through the inclusion into the quartz. Scale bar is approx. 15  $\mu\text{m}$  long.

(B) A rare hexagonal form of halite, which may have an octahedral form (c.f. Roedder, 1984, p. 364). Scale bar is 5  $\mu\text{m}$  long.

(C) A halite bearing fluid inclusion which has another unidentified rod-shaped daughter mineral (not tourmaline). Scale bar is 10  $\mu\text{m}$  long.

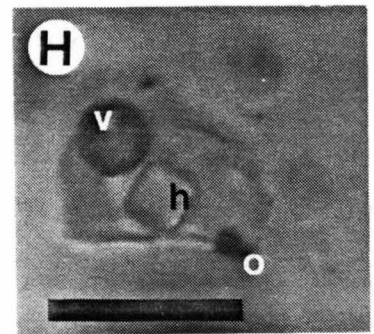
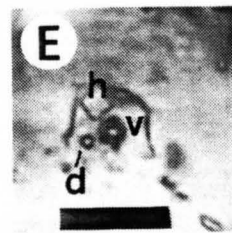
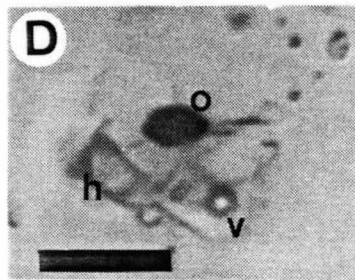
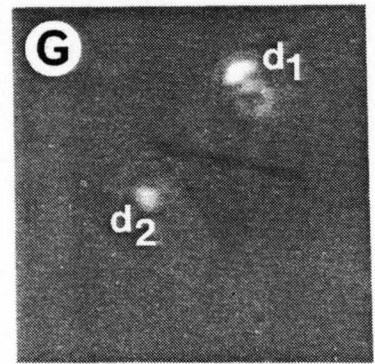
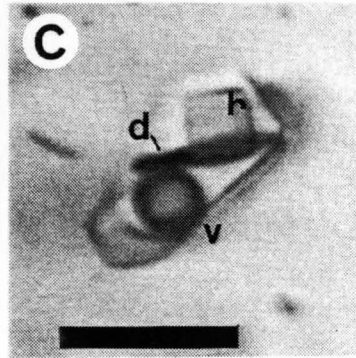
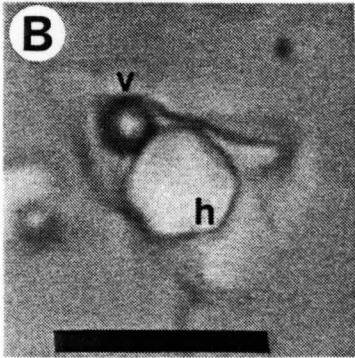
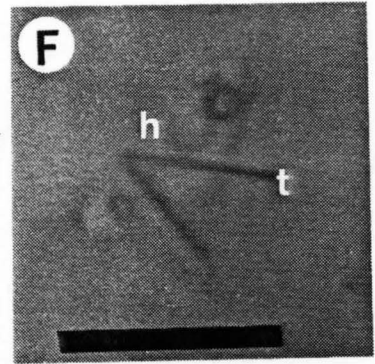
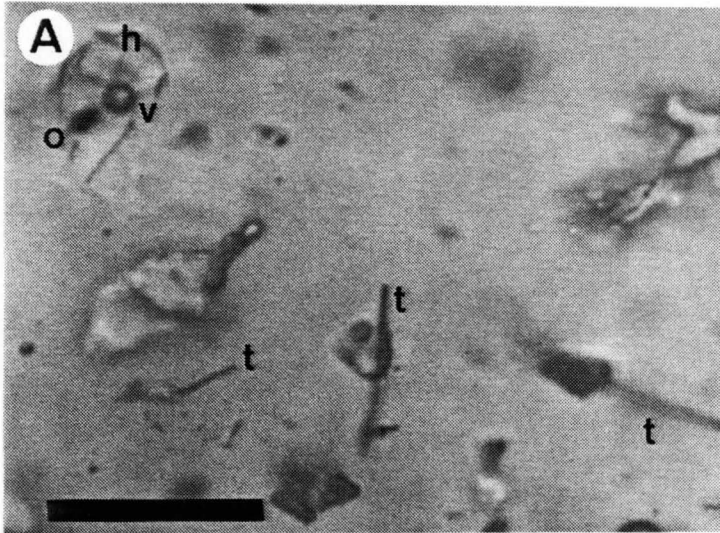
(D) An inclusion containing halite and an opaque mineral (arsenopyrite?). Scale bar is 10  $\mu\text{m}$  long.

(E) An inclusion containing halite and an unidentified smaller daughter mineral (d). This mineral has a higher relief and stronger birefringence compared to halite. Scale bar is 12  $\mu\text{m}$  long.

(F) A small inclusion with two rods of tourmaline growing from left to right. This texture indicates that tourmaline continued to grow after the fluid was trapped and is not a true daughter mineral. Due to the small size of the inclusion halite and two other daughter minerals are barely discernible. Scale bar is 3  $\mu\text{m}$  long.

(G) Same as (f) under cross polarized light showing the highly birefringent nature of unidentified daughter minerals ( $d_1$  and  $d_2$ ). Halite has low birefringence and cannot be seen. The vapour phase is located to the right and below  $d_1$ .

(H) A large inclusion containing a halite (h) and an unidentified opaque (o) daughter mineral. Scale bar is approx. 20  $\mu\text{m}$  long.



inclusion, with the ends protruding into and intergrown with quartz. Figure 28F shows two rods of tourmaline that have grown from one nucleation point within the inclusion and terminate within the quartz host. Daughter minerals are completely enclosed within the inclusion; therefore, these tourmaline rods have precipitated directly from the ore fluid, causing an imperfection in the quartz crystal and allowing the original fluid to be trapped within an inclusion.

There are true daughter minerals in the inclusions in Figure 28A-H. The most common daughter is a cubic mineral optically identified as halite (h). The presence of halite was confirmed by Sherriff et al., (1987), using a newly developed nuclear magnetic resonance technique. A rare form of halite (Figure 28B) with an hexagonal outline (c.f. Roedder, 1984, p. 364) was identified. The actual shape of the halite is probably an octahedron, but the reason for the development of non-cubic halite is unknown (Roedder, 1984).

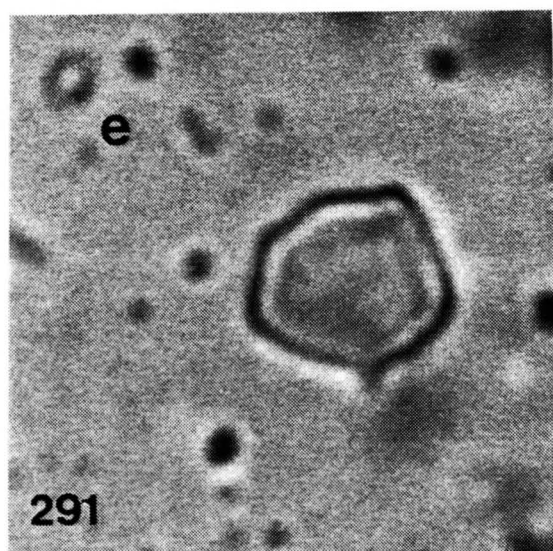
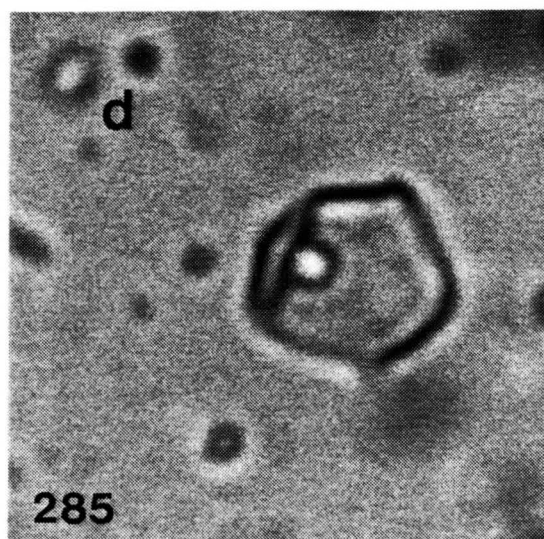
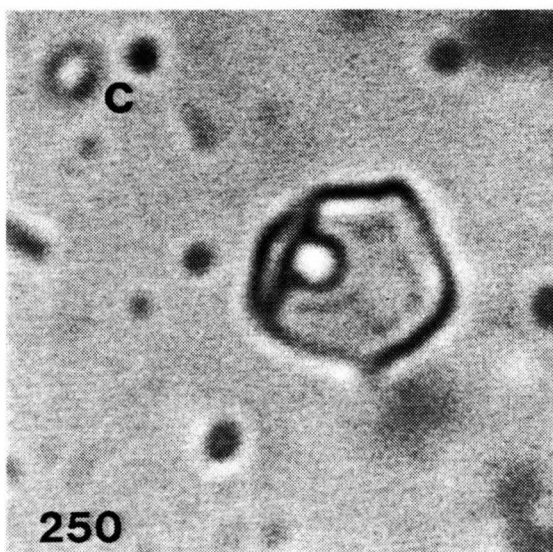
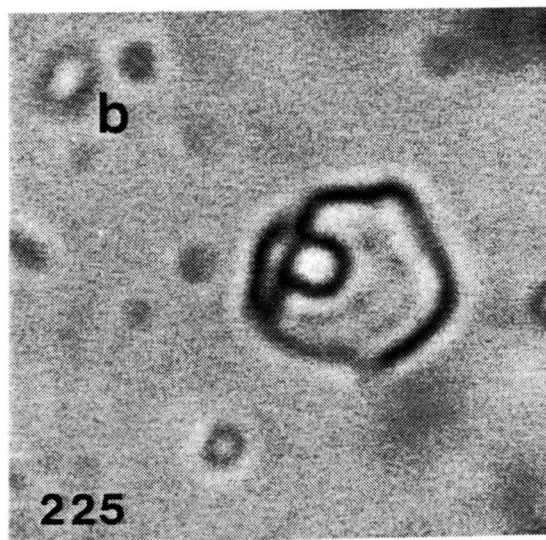
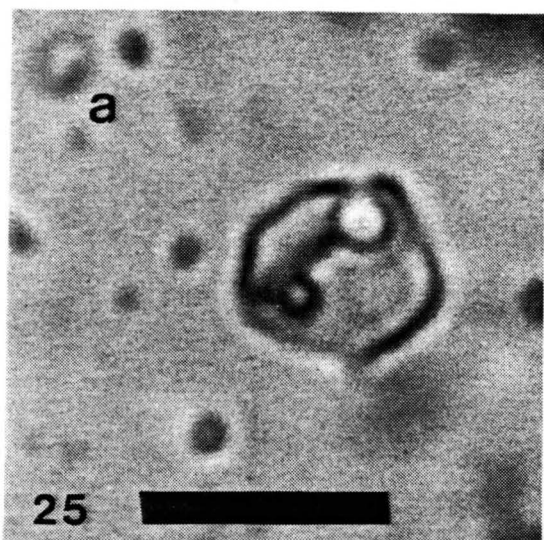
The majority of halite-bearing fluid inclusions homogenized by daughter mineral dissolution. This suggests that the hydrothermal brine was supersaturated with respect to NaCl (and other components) when trapped. The interpretations put forward to explain this phenomenon are not particularly convincing in light of the data from these samples. Roedder (1984, p. 276) discounts the possibility that this behaviour is due to kinetic effects ( $H_2$  loss), and that halite was trapped as a solid phase precipitating from

the hydrothermal fluid, and suggests that it may be due to trapping under "high pressure" conditions. Those inclusions containing halite at Laforma have a uniform phase ratio and halite precipitation directly from the hydrothermal fluid during boiling is not considered a practical explanation. The presence of boiling fluids and of hot spring type mineralogy in the area indicates that the fluids were not trapped at high pressure.

Other daughter minerals present could not be positively identified. Figure 28C is of an inclusion with a vapour phase, a cube of halite and an unidentified translucent rod-shaped mineral (not tourmaline). This daughter phase was also present in a similar inclusion (6  $\mu\text{m}$  diameter) depicted in Figure 29a-e undergoing a heating run. The vapour phase disappears at 216°C and the halite shows evidence of dissolving to 285°C while the other phase does not appear to be affected. At 290°C both phases dissolve and the inclusion homogenizes. All three phases renucleate upon cooling of the inclusion and attain the shape depicted in Figure 29a.

Figures 28E, F and G exhibit inclusions which contain minerals of high relief (E) and high birefringence (G) compared to halite. These phases were slow to dissolve and occasionally would not dissolve at temperatures of 450°C sustained for one hour. Quite often the fluid inclusion would decrepitate due to internal overpressures before the highly birefringent phase was dissolved.

Figure 29. Heating run on an inclusion containing halite and an unidentified rod-shaped mineral. This inclusion homogenized by daughter mineral dissolution, with both halite and the unknown mineral dissolving at the same temperature (290°C). (see text for details) Scale bar is 7  $\mu\text{m}$ .



The other daughter mineral phase noted was an opaque mineral (Figure 28A, D, and H) which was found only in larger inclusions ( $>10 \mu\text{m}$ ). This opaque mineral is thought to be arsenopyrite based on physical shape, white reflections in reflected light, and the abundance of arsenopyrite intergrown with quartz in the boiling zone. This mineral did not dissolve at high temperatures for periods of one hour although this is not uncommon for such low solubility daughter minerals (Roedder, 1984, p. 53). Possible reasons for this behaviour are: necking down of the inclusion,  $\text{H}_2$  leakage, and accidental trapping of the crystal; that is, it is not a true daughter phase. The first condition is not applicable because no evidence of strain deformation of these euhedral quartz grains was observed. The second condition is possible but hydrogen loss is difficult to ascertain. It is possible that the opaques are not true daughter minerals as they are relatively rare phases compared to halite and they do not show uniform phase ratios with respect to other components in the inclusions.

These highly saline fluids are interpreted to be the residual brines left from a period of extensive boiling of a hydrothermal fluid with initial concentration of approximately 4 wt.% NaCl. To change a fluid from 4 to 42 wt.% NaCl requires that 90% of the water to be removed in the form of steam. This requires a relatively closed system (to avoid dilution by 'fresh' water) with a high enthalpy.

The system could be closed by self-sealing of the hydrothermal conduit either by mineral deposition or by tectonic movement along the fracture zone. The cooling of a rhyolite dyke adjacent to the Laforma vein could provide the heat requirements for a high enthalpy system.

Other possibilities for obtaining such high salinities in natural systems include the leaching of an evaporite source rock, and input of magmatic-water. The absence of evaporites in the Freegold Mountain area discounts the first possibility, and a significant contribution of magmatic water is ruled out on the basis of stable isotope studies of the water within fluid inclusions. Therefore, a model of extensive and uninhibited boiling of a low salinity fluid in a high enthalpy system eventually producing a high salinity fluid, remains a viable possibility. This thesis is discussed in more detail in the context of stable isotope studies in Chapter 9.

Carbon dioxide inclusions were relatively more abundant in the Level 4 samples than the deeper ore samples. The melting point of  $\text{CO}_2$  was still depressed averaging around  $-57.1^\circ\text{C}$ , indicating the presence of volatile contaminants. The majority of  $\text{CO}_2$  inclusions homogenized to the vapour phase and had corresponding average densities of  $0.32 \text{ g/cm}^3$ . The density decrease from the lower levels is due to increasing devolatilization of the fluid with decreasing pressure.

Figure 24B is a rare example of a three phase  $\text{CO}_2\text{-H}_2\text{O}$

inclusion present in the boiling zone. It contains a central CO<sub>2</sub> vapour phase surrounded by a CO<sub>2</sub> liquid phase and a large volume of H<sub>2</sub>O liquid. The presence of such three phase inclusions indicates that the minimum CO<sub>2</sub> concentration of the hydrothermal fluid was 1.0 mole-% CO<sub>2</sub> (Bodnar et al., 1985). Using the calculation method of Nesbitt (1984), the maximum solubility of CO<sub>2</sub> in a the liquid phase of a hydrothermal fluid at 200°C, 100 bars pressure, and salinity of 4 wt.% NaCl is approximately 1.0 mole-% CO<sub>2</sub>, while the vapour phase contains approximately 80.3 mole-% CO<sub>2</sub> and 19.7 mole-% H<sub>2</sub>O. The presence of volatile contaminants in CO<sub>2</sub> inclusions suggests that the CO<sub>2</sub> content of the vapour phase is slightly less than 80.3 mole-%.

Quantifying the CO<sub>2</sub> content of the Laforma fluid aids in establishing paleodepth estimates from the boiling point-depth relationship for H<sub>2</sub>O-NaCl fluids. Commonly, the depth of boiling is calculated knowing the temperature and salinity of the boiling solution (Haas, 1971). Neglecting the affect of dissolved gases however, leads to a depth to boiling estimate too shallow, since the presence of volatile components raises the vapour pressure of a hydrothermal solution (Bodnar et al., 1985).

The calculation of the depth to boiling for gaseous fluids is given by Henley et al., (1984, p. 53). The total pressure ( $P_{TOT}$ ) of a gaseous hydrothermal system is equivalent to the pressure of steam-saturated liquid water

( $P_w$ ) and the pressure of the  $CO_2$  calculated using Henry's Law,

$$P_{TOT} = P_w + P_{GAS} = P_w + (K_H, (T^{\circ}C) \times X_{CO_2})$$

where  $X_{CO_2} = 0.010$  mole %,  $K_H$  (Henry's Law coefficient for  $CO_2$ ) = 7500, and  $P_w = 10$  bars (Haas, 1971). The total pressure of the Laforma hydrothermal fluid is therefore 85 bars, which is equivalent to a hydrostatic depth of 1070 m. The depth of boiling from surface when the hydrothermal system was operating was therefore approximately 1070 m. The effect that  $CO_2$  has on lowering the boiling point of the fluid is dramatic. If the  $CO_2$  concentration was not estimated and a pure  $H_2O$  fluid was assumed the fluid pressure would be 10 bars, giving a depth to boiling approximation of only 100 m.

#### 8.2.1.4 2ND LEVEL AND SURFACE EXPOSURES OF THE LAFORMA VEIN

The vein at these levels contains fluid inclusions with varying liquid-vapour ratios, high salinities, and daughter minerals similar to those found at the 4th level. At the 2nd level the vein was texturally similar to the 4th level except for the occurrence of limited portions of brecciated vein material. The samples from the surface exposure of the vein are extremely brecciated (Photo 26) and contain many clasts with different fluid inclusion populations as discussed in Chapter 7. The abundance of  $CO_2$  inclusions and

the estimated amount of CO<sub>2</sub> present in the hydrothermal fluid support the premise that the breccia textures present at 2nd level and at the surface are derived from gas overpressure in a self-sealed hydrothermal system.

### 8.2.2 Antoniuk Deposit

#### **ANT 86-1-91.4**

Quartz veining in the Antoniuk Breccia is rare and fluid inclusions were measured from quartz euhedra (Figure 30a and Photo 37) growing in vugs with calcite and pyrite. This sample was obtained from diamond drill hole 86-1 at a depth 91.4 m from the collar. The drill hole is located on Fig. 19, drill section 20N. Primary inclusions at the Antoniuk (Photo 30c) consist of liquid-rich H<sub>2</sub>O and vapour-rich CO<sub>2</sub> inclusions. The H<sub>2</sub>O inclusions homogenize to the liquid phase at temperatures ranging from 154° to 337°C (Figure 31A) but show a strong maximum at 305°C. The lower temperature inclusions were present within the interior portions of quartz euhedra with the higher temperature inclusions occurring on outer growth zones suggesting that the temperature of the hydrothermal fluid increased during the deposition of quartz, and that the deposition of calcite and pyrite occurred at temperatures around 300°C. The salinity of these primary inclusions is 4.5 ± 2.1 equivalent wt. % NaCl. There is no apparent salinity change throughout the history of inclusion trapping (Figure 32).

CO<sub>2</sub> inclusions are present but uncommon relative to the

Figure 30. Fluid inclusions from intergrown quartz-carbonate-pyrite within vugs in the Antoniuk Breccia gold deposit.

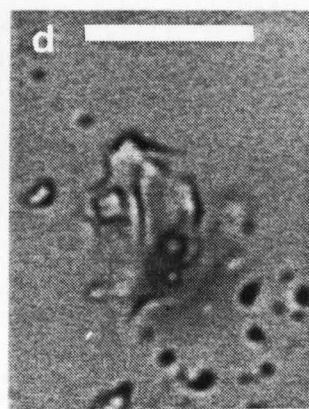
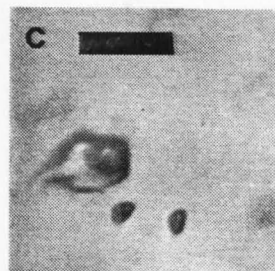
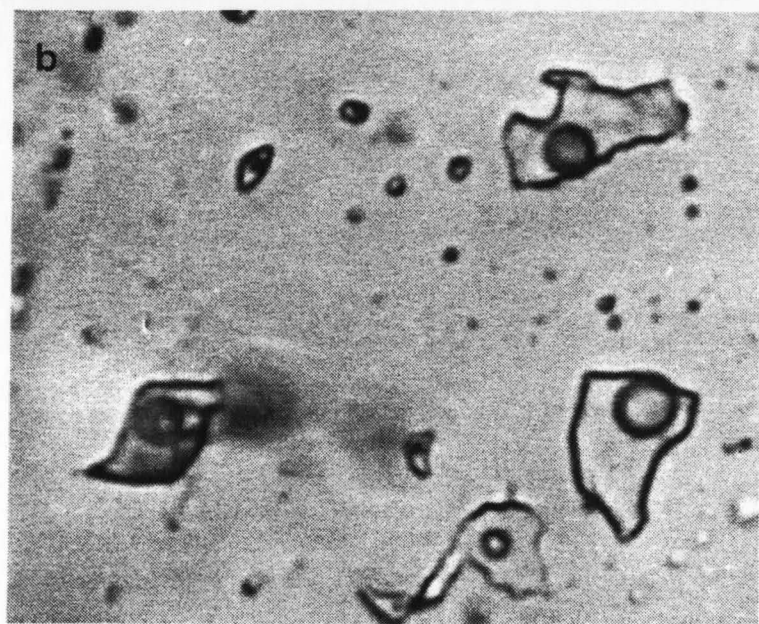
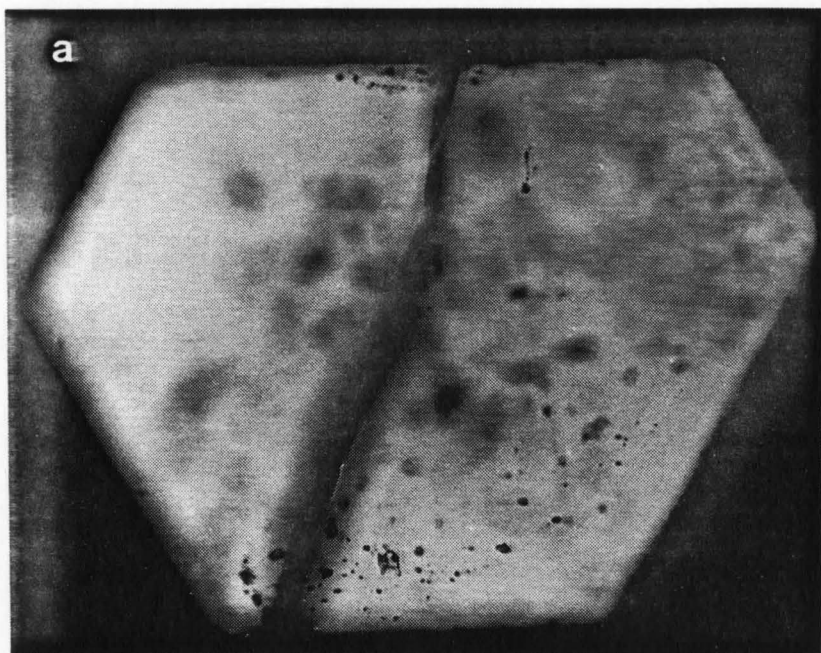
(a) A euhedral crystal of fluid inclusion-bearing quartz surrounded by carbonate. The diameter of the crystal is about 5 mm.

(b) A group of large secondary inclusions formed along a healed fracture plane. The inclusion at top right is approximately 20  $\mu\text{m}$  long.

(c) A group of small primary inclusions from a growth zone in (a). The scale bar is 5  $\mu\text{m}$  long.

(d) High salinity secondary inclusion containing cubic halite and an unidentified high relief daughter mineral similar to those found at Laforma. Scale bar is 15  $\mu\text{m}$  long.

(e) Same as (d) under cross polarized light showing strong birefringence of unidentified daughter mineral.



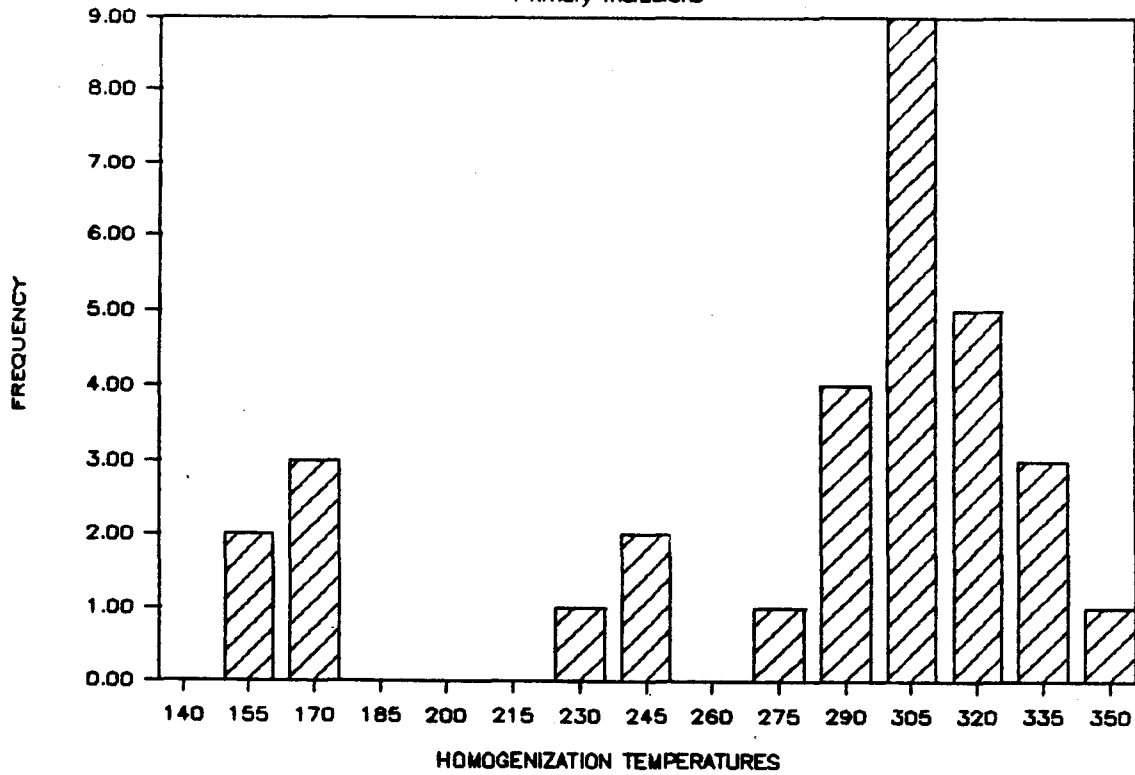
Laforma samples. Three inclusions had CO<sub>2</sub> melting temperatures around -57.2°C indicating the presence of either CH<sub>4</sub> or H<sub>2</sub>S gas to lower the melting temperature of CO<sub>2</sub> (-56.6°). One of the CO<sub>2</sub> inclusions was observed to homogenize to the vapour phase at +18°C, indicating a CO<sub>2</sub> vapour density of 0.16 g/cm<sup>3</sup>. As previously discussed, the presence of CO<sub>2</sub> inclusions suggest that immiscibility (effervescence) has occurred. Since indications of true boiling were not observed in any primary fluid inclusions from the Antoniuk, it is not possible to estimate paleodepths using the method of Henley et al., (1984). It is possible to make a minimum estimate of the paleodepth by using the immiscibility diagram (Figure 33) of Bodnar et al., (1985). Assuming an initial molar concentration between 0 and 1.0 mole-% dissolved CO<sub>2</sub> (ie. H<sub>2</sub>O-rich phase) in a hydrothermal fluid at 300°C, the CO<sub>2</sub> will undergo immiscibility and separate into two phases (CO<sub>2</sub>-rich and H<sub>2</sub>O-rich phases) at pressures between 80 and 125 bars. If the breccia was open to the surface and under hydrostatic pressure, the depth of CO<sub>2</sub> immiscibility would be between 1 and 1.6 km. Therefore the quartz in sample 86-1-91.4 precipitated within 1.6 km of the paleosurface according to the above assumptions. Although the original depth of initiation of breccia development is difficult to assess, the condition of CO<sub>2</sub> immiscibility in the hydrothermal fluid concurs with the geological evidence (Chapter 7) to suggest that the Antoniuk Breccia was generated in the upper crust

Figure 31. a) Homogenization temperatures for quartz-hosted primary inclusions within the Antoniuk Breccia.

(b) Homogenization temperatures for late stage secondary fluid inclusions at the Antoniuk deposit.

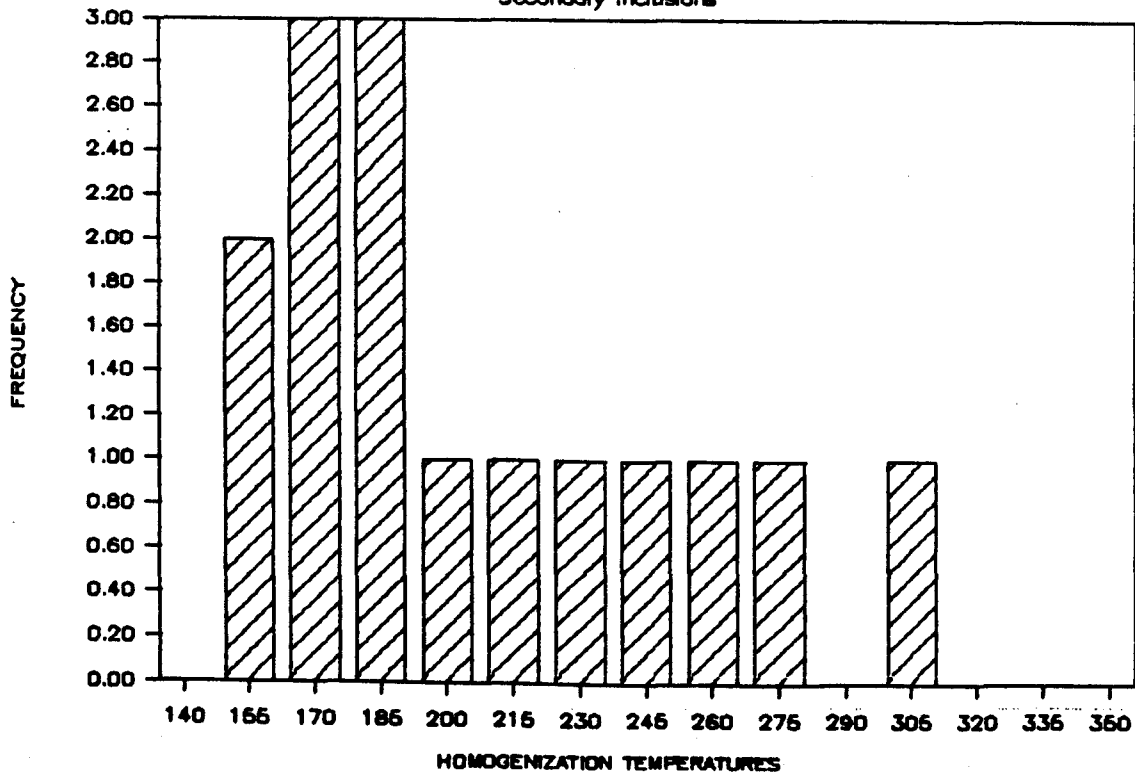
### ANTONIUK BRECCIA

Primary Inclusions



### ANTONIUK BRECCIA

Secondary Inclusions



(< 1.6 km). The higher temperatures recorded for the Antoniuk Breccia in comparison to the Laforma Mine must reflect differences in the physical environment since samples from both deposits are located near rhyolite dykes, which are the heat sources driving the hydrothermal systems. The obvious dissimilarity between the Laforma and the Antoniuk is the host rock for the quartz, and the relationship between the host rock and the rhyolite dykes. The hydrothermal fluids at Laforma are insulated from the heat source by the granodiorite wallrock, and heat transfer is by conduction. Heat is transferred more efficiently by convection, and the permeability of the Antoniuk breccia allows for more efficient heat transfer between the dykes and the fluid, and therefore leads to higher fluid temperatures and mineral deposition.

Fracturing of the quartz grains after their growth has allowed later fluid to be trapped as linear inclusions within the fracture. These secondary inclusions (Fig. 30b) are samples of a later fluid postdating quartz deposition. The homogenization temperatures of these inclusions are provided in Figure 31B. These temperatures are low compared to Figure 31A but do not necessarily reflect true trapping temperatures due to the possibility of 'necking down' of such inclusions.

Figure 32 is a graph of salinity vs. homogenization temperatures for primary and secondary inclusions. It is obvious that the secondary inclusions are highly saline (12-

### ANTONIUK BRECCIA

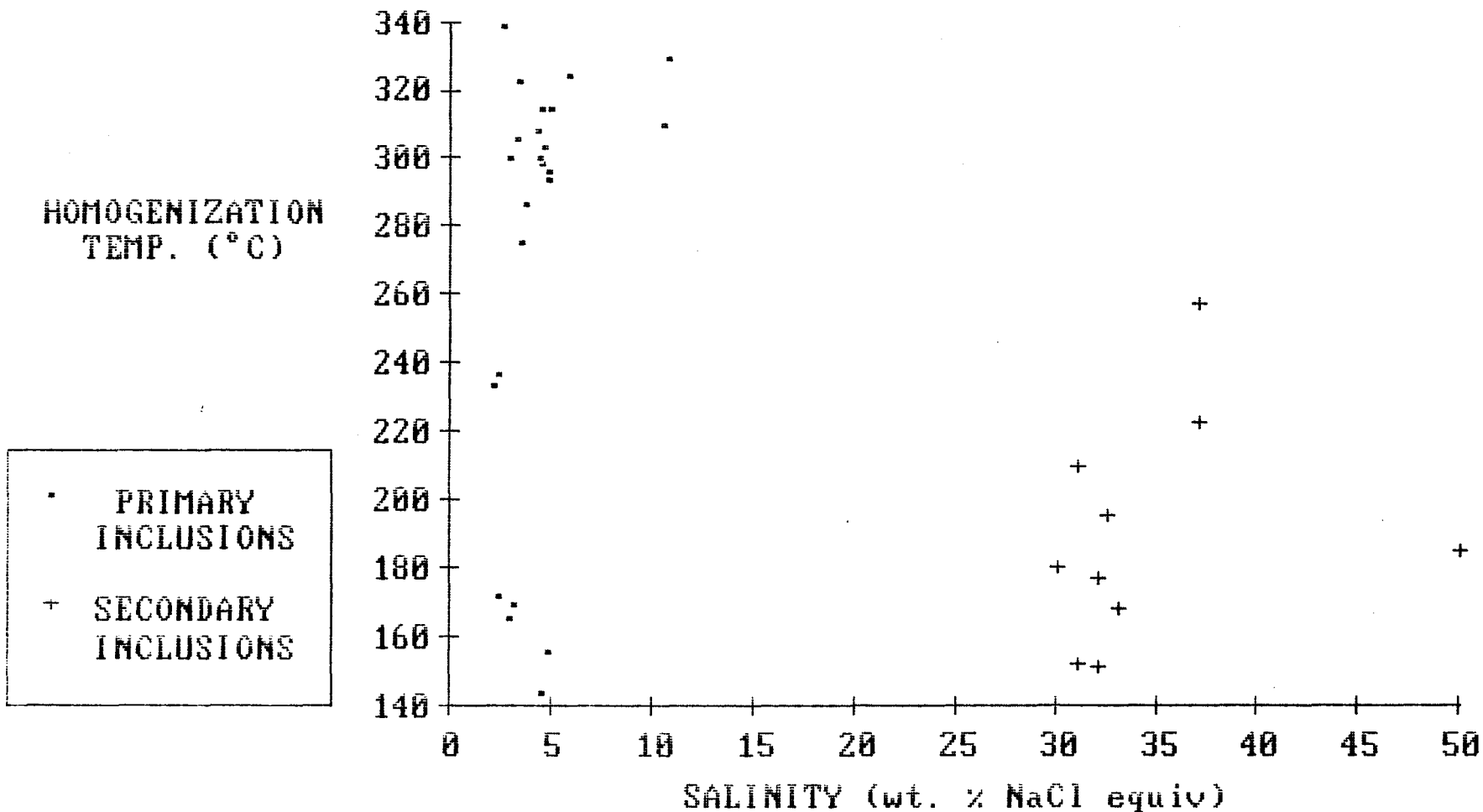
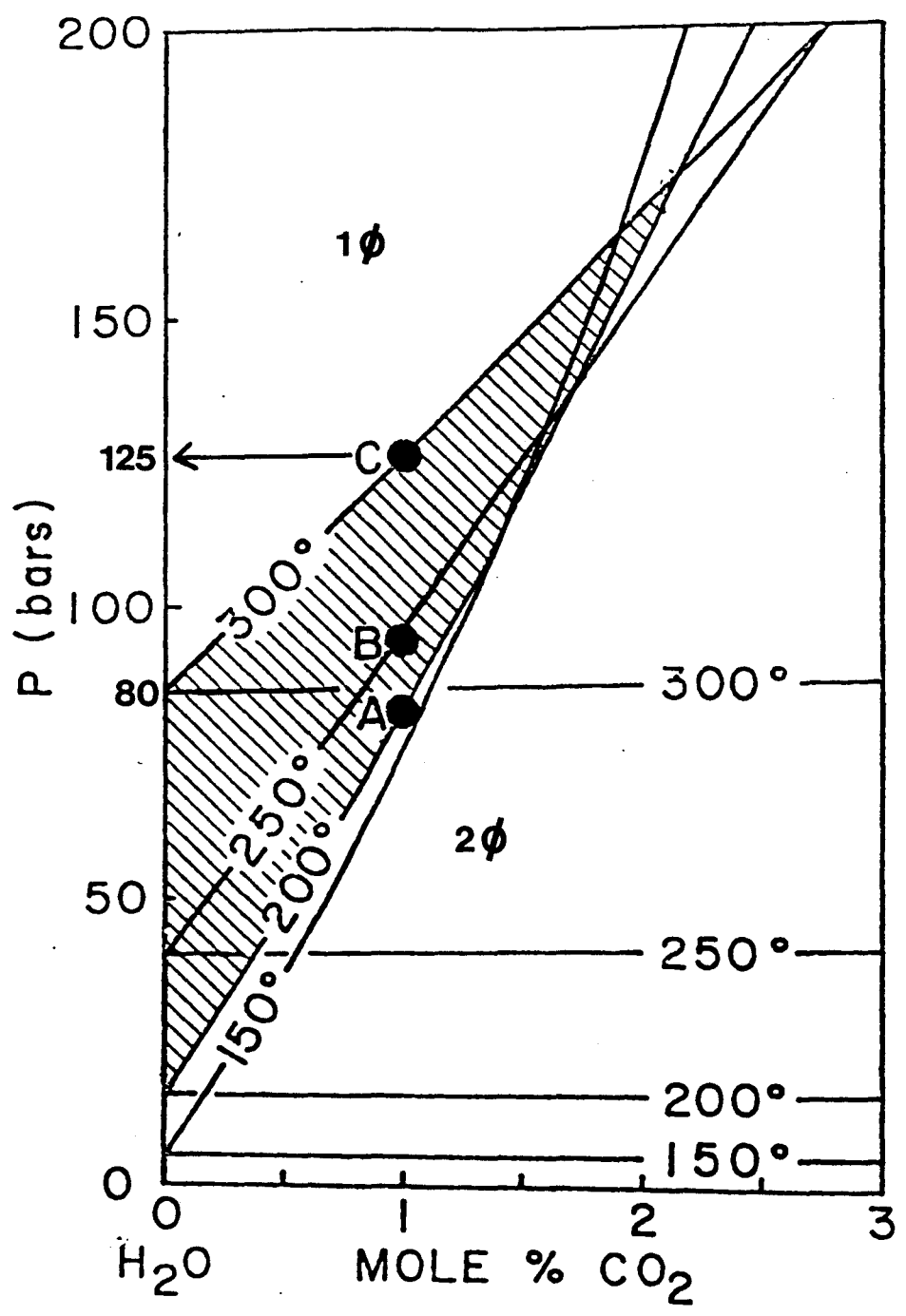


Figure 32. Homogenization temperature vs. salinity diagram for primary and secondary inclusions at the Antoniuk Breccia deposit.

Figure 33. The 150°C, 200°C, 250°C, and 300°C isotherms in the low pressure, water-rich portion of the CO<sub>2</sub>-H<sub>2</sub>O phase diagram suitable for gold deposits at Freegold Mountain. The isotherms represent the boundaries between the one-phase field (ie. CO<sub>2</sub> is dissolved) and the two-phase (H<sub>2</sub>O liquid and CO<sub>2</sub> vapour) field. Point C at 1 mole % CO<sub>2</sub> to 0 mole % CO<sub>2</sub> represents the conditions at Antoniuk where immiscibility has likely occurred at pressures equivalent from 125 to 80 bars (modified from Bodnar et al., (1985)).



38 wt.% NaCl) in comparison to primary inclusions (2-11 wt.% NaCl). Figure 30d and e are photographs of a high-salinity secondary inclusion with a daughter mineral of cubic halite, a vapour phase, and a highly birefringent unidentified daughter mineral similar to those found at Laforma (Figure 28E and G).

The origin of these high salinity late-stage fluids is interpreted similarly to those high-salinity inclusions in the Laforma deposit. Unfortunately, no stable isotope evidence to indicate the origin of the water could be obtained due to the problem of separating sufficient quantities of quartz with only one population of fluid inclusions.

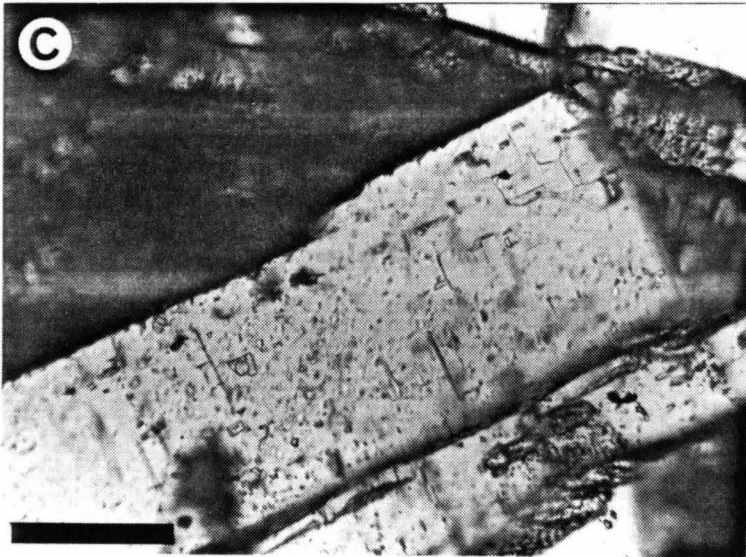
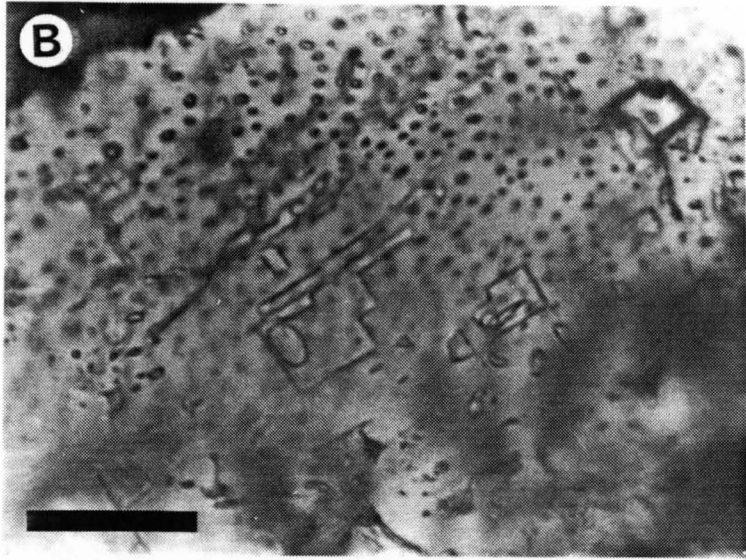
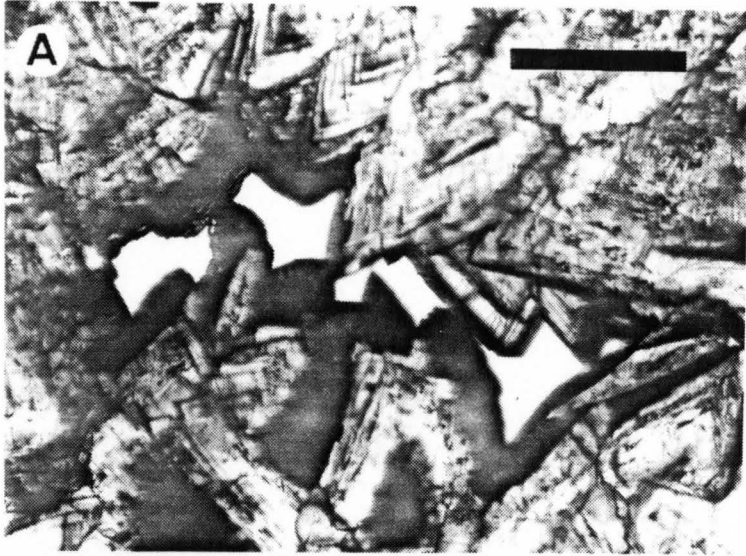
### 8.2.3 Emmons Hill

#### EHA-A

Usable fluid inclusions from this prospect were present only in samples of barite. Fe and Mn carbonates, Figure 34A, although showing euhedral crystals growing into void spaces, did not prove suitable for fluid inclusion analysis, since only small inclusions (<2  $\mu\text{m}$ ) were present. No inclusions were hosted within the fine-grained silica, which is not uncommon for a deposit of this type (Bodnar et al., 1985).

The inclusions hosted within the barite were quite large, generally between 15 and 50  $\mu\text{m}$  (Figure 34B and C). Heating runs were conducted to determine the homogenization

- Figure 34. (A) Euhedral Fe-Mn rich carbonate crystals at Emmons Hill. These minerals contain small fluid inclusions ( $< 2 \mu\text{m}$ ) which are inadequate for heating-freezing measurements.
- (B) Large primary inclusions hosted within barite. A plane of secondary inclusions cuts behind the primary inclusions. Scale bar is  $50 \mu\text{m}$  long.
- (C) Euhedral crystals of barite containing large, regularly shaped primary inclusions, surrounded by Fe-Mn carbonate. Scale bar = 1 mm.



temperatures, which show formation temperatures between 170-210°C as depicted on Figure 35a. The accuracy of these temperatures is somewhat suspect however, since many of the inclusions within the barite did not have a vapour phase. Failure to nucleate a vapour phase in inclusions of this size generally indicates trapping of a fluid below 150°C (Roedder, 1984, p.292). This does not apply to the Emmons Hill barite as inclusions containing a vapour phase are found adjacent to inclusions without a vapour phase.

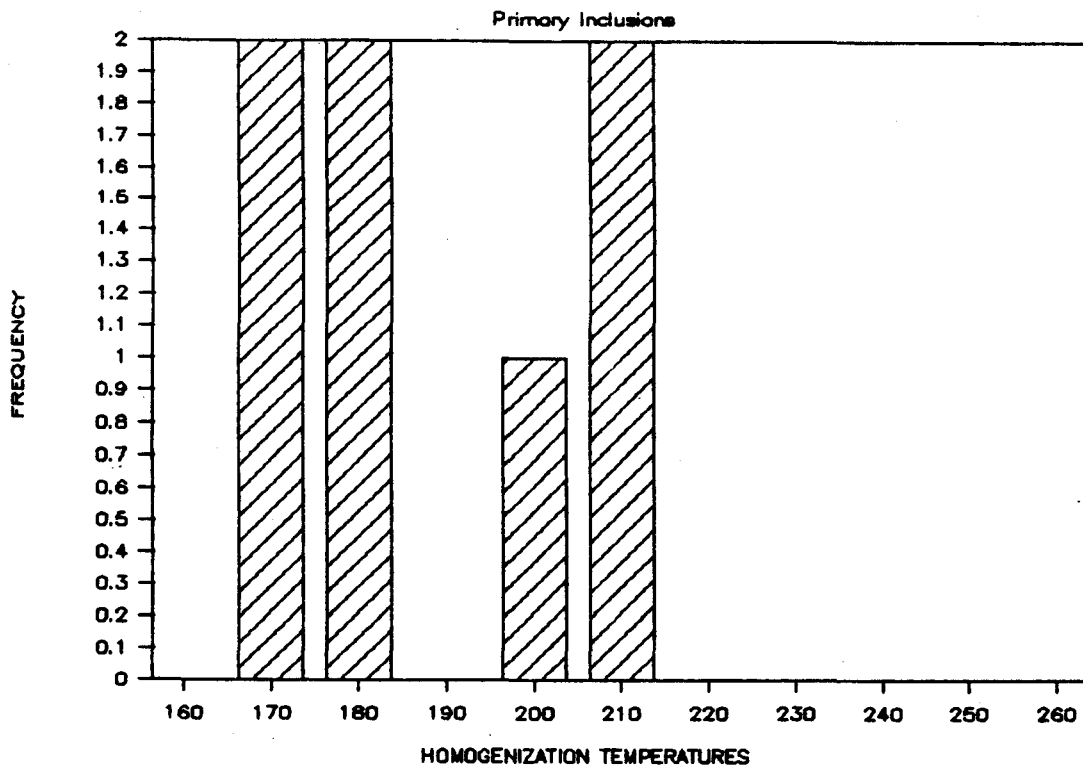
Another explanation for the absence of a vapour phase in some inclusions is that the barite host has yielded under volume expansion during freezing of the water (Ulrich and Bodnar, 1984), resulting in stretching and concomitant volume increase of the inclusion cavity. The resultant volume change generates a low or negative internal pressure (Roedder, 1984, p.293), causing a failure to nucleate a vapour phase. Since the samples were collected from a surface exposure of the showing, and long periods of sub-zero temperatures are experienced at these latitudes, it is probable that volume expansion of the barite occurred during freezing of inclusion water during winter months.

Temperatures of homogenization for inclusions which did have a vapour phase would be minimum temperatures of formation since volume expansion would result in the reduction in size of the vapour bubble. Inclusions with relatively large vapour bubbles (Figure 34B) may not be affected by freezing since the volume increase of water

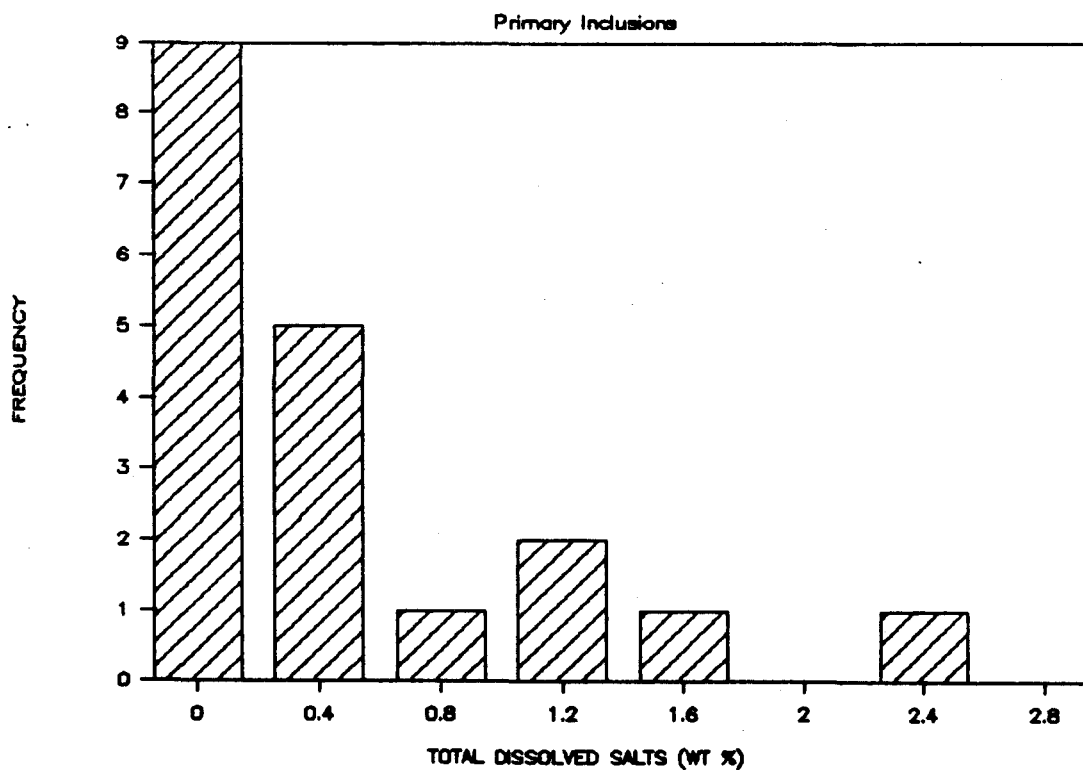
Figure 35. (A) Homogenization temperatures for inclusions within Emmons Hill barite.

(B) Salinity of fluids within barite-hosted inclusions at Emmons Hill.

## EMMONS HILL BARITE



## EMMONS HILL BARITE



during freezing can be accommodated by the volume of the vapour bubble. This was verified in the laboratory as barite hosted inclusions with small vapour bubbles fractured more often during supercooling than did inclusions with larger volume bubbles.

Stretching of the inclusions will not affect salinity determination via the freezing point depression method if the inclusion has a vapour phase present (Roedder, 1984). Figure 35b shows that the salinity of the inclusion water is very low (< 1 wt.% NaCl), with many of the inclusions containing essentially pure water (ice melted at 0°C). A traverse of fluid inclusions along the long axis of a barite crystal (Photo 50) from its nucleation point to its termination point demonstrated no change in salinity (all inclusions < 1 wt.% NaCl) during crystal growth. These dilute, static solutions may represent a groundwater dominated environment, and therefore support the mineralogical evidence that this deposit is a near surface phenomenon.

#### 8.2.4 Barren Quartz Veins

F85-27

A sample of a 25 cm. wide barren quartz vein hosted in metasedimentary rocks was taken from a trench south of Emmons Hill. The vein was barren of sulfides and gold, and contained coarse-grained white quartz commonly referred to as "bull" quartz. Fluid inclusions within this sample were

analyzed to determine whether the temperatures and salinities of the fluid precipitating barren quartz were significantly different from those precipitating gold and sulfides.

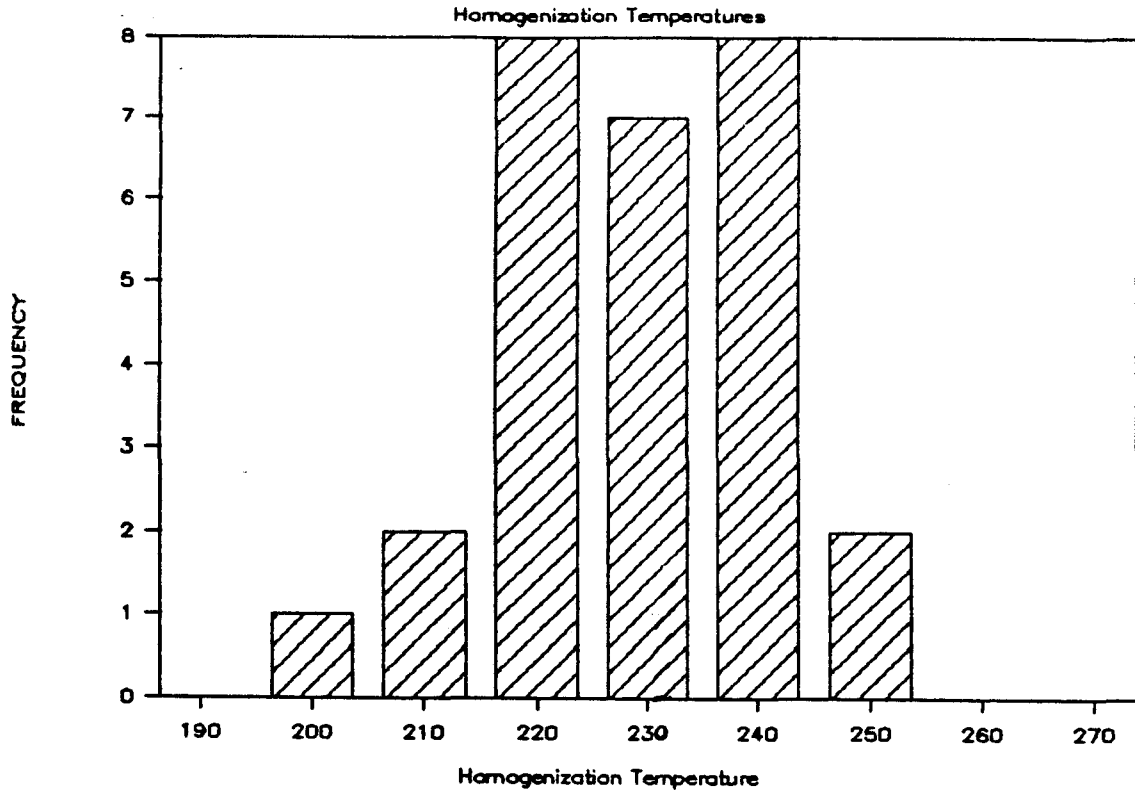
Fluid inclusions within this sample were relatively large (ave. diameter  $\approx 12 \mu\text{m}$ ) and abundant, accounting for the white coloration of the quartz. Figure 36A shows that the majority of inclusions homogenized between 220 and 240°C, with the average  $T_{\text{hom}} = 225^\circ \pm 12^\circ\text{C}$ . The salinity of the fluids (Fig. 36B) ranges from 0-5 wt.% NaCl, but averages around 1 wt% NaCl.  $\text{CO}_2$  inclusions were not detected in the sample, suggesting the molar volume of  $\text{CO}_2$  is lower than that found at Laforma and Antoniuk, and that if  $\text{CO}_2$  is present it is dissolved in the liquid and has not undergone immiscibility reactions.

Although comparisons between auriferous and barren veins may be meaningless due to the uncertainty of their age relationships, it is apparent from fluid inclusion analysis that the major differences between the two types are the presence of  $\text{CO}_2$  (and other gases) and the salinities of the fluid. The relative absence of  $\text{CO}_2$  and dissolved salts in the 'bull' quartz may be a detriment to the fluid's ability to complex and transport metals. That these constituents are absent reflects a fundamental relative difference in fluid history, and origin.

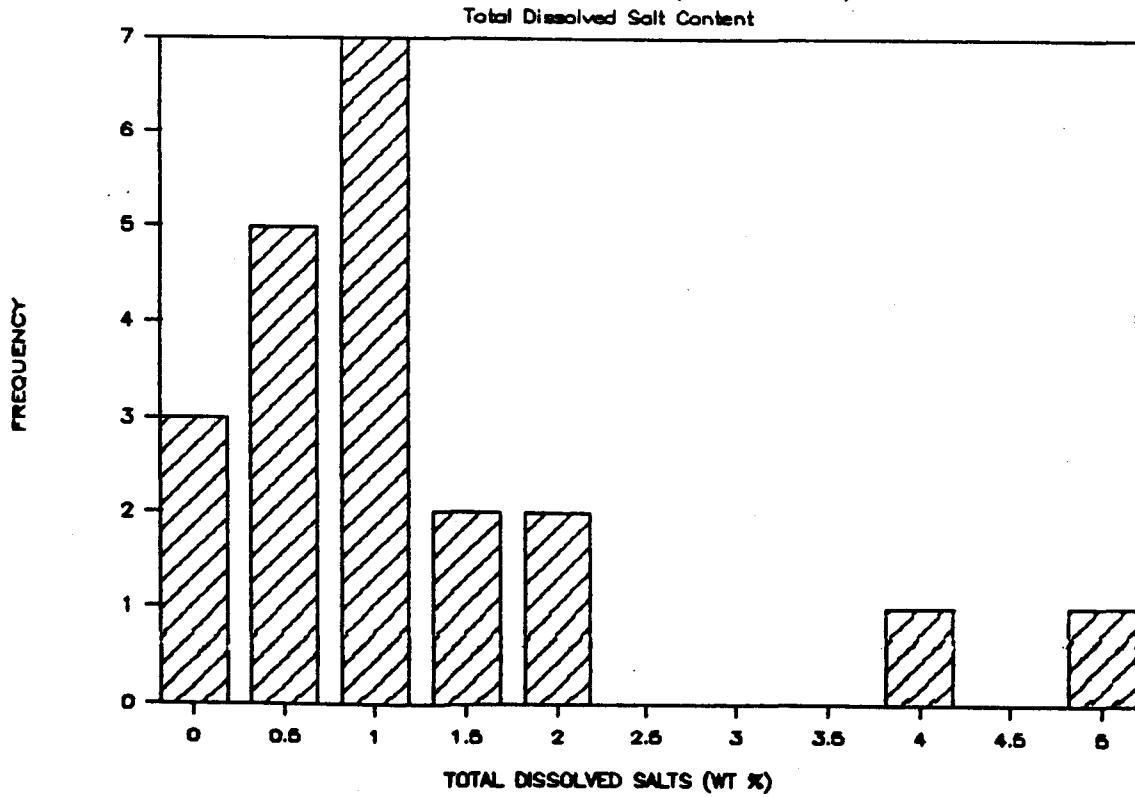
Figure 36. (A) Homogenization temperatures for inclusions within a barren quartz vein (Sample F-27).

(B) Salinity of fluid inclusions in barren quartz sample (F-27).

### SAMPLE F-27 (QUARTZ)



### SAMPLE F-27 (QUARTZ)



## CHAPTER 9. STABLE ISOTOPE STUDIES

### 9.1 Introduction

Stable isotope studies of ore deposits have been fundamental to the understanding of deposit genesis and the nature of ore deposition. This chapter will investigate the application of isotopic studies to deposit genesis at Freegold Mountain. For a detailed discussion of the use of stable isotopes in epithermal Au-Ag deposit research, the reader is referred to Field and Fifarek, (1985).

Oxygen and hydrogen isotope data suggest that epithermal Au-Ag deposits show many similarities to modern geothermal fields. Waters sampled from both show marked deuterium and  $^{18}\text{O}$  depletion and an isotopic signature similar to local meteoric water (O'Neil et al., (1973); O'Neil and Silberman, (1974); White et al., (1973)). As a result, it is widely accepted that ground water driven by igneous activity in large scale hydrothermal convection cells is important in the formation of epithermal Au-Ag deposits.

The ultimate source of the precious metals is unknown, although two possibilities exist:

1. The gold is leached from the country rock in large scale convection systems.
2. The gold originates from a magmatic source and the isotopic signature of the magmatic fluid is diluted by

immense volumes of groundwater.

Generally, the first premise is accepted based on the lack of a magmatic isotopic signature for ore fluids, although a few studies (Robinson, (1974); Kamilli and Ohmoto, (1977)) do show evidence of a magmatic water contribution. The common occurrence of igneous intrusives in epithermal areas leads to the speculation that they are not only heat engines driving convection cells, but that their associated waters may introduce metals into the area. The contribution of dissolved components ( $H_2S$ ,  $SO_2$ ,  $CO_2$ ,  $NaCl$ ) to geothermal systems is linked to magma bodies (Henley et al., 1984, p. 155), and since these species are associated with metal transport, it is not unreasonable to suspect that they may have provided metals.

Stable isotopic data is also useful in revealing processes that occur within the hydrothermal solution, particularly those which cause mass-dependant elemental fractionation, such as boiling. Exchange of oxygen between  $^{18}O$ -depleted meteoric water and  $^{18}O$ -enriched rocks causes the  $\delta^{18}O$  value of the water to shift away from the meteoric water line, and this shift enables the water:rock ratio to be determined.

## 9.2 Analytical Methods

### 9.2.1 Hydrogen

Water trapped within fluid inclusions in quartz and barite was obtained by crushing 15 to 30 mg of sample

material in an evacuated stainless steel tube. This method was modified by Ghazban (1987), from a technique utilized by Yonge (1982).

The sample for analysis was handpicked from a cut slab of rock, acid washed, weighed, and then crushed in the tube. The released fluid was frozen in dry ice in order to trap H<sub>2</sub>O. The gaseous phases released were then pumped away. When a vacuum was again achieved the tube was gradually heated and the H<sub>2</sub>O released was collected in a glass tube immersed in liquid nitrogen. The amount of H<sub>2</sub>O collected ranged from 1 to 10 µl.

The water collected was analyzed for hydrogen isotopic composition (via the production of H<sub>2</sub> gas by Zn-reduction of water) at the stable isotope facility at the University of Calgary, Calgary, Alberta.

### 9.2.2 Oxygen and Carbon

#### Quartz

Eleven samples of quartz from the Laforma and one from the Emmons Hill deposit were analyzed for oxygen. The quartz was reacted with BrF<sub>3</sub> to produce O<sub>2</sub>, which was reacted with a carbon rod at 550°C to produce CO<sub>2</sub>, following the method of Longstaffe (1977), modified from Clayton and Mayeda (1963).

#### Calcite

The carbon and oxygen isotopic compositions of CO<sub>2</sub> gas, liberated during acid dissolution (100% H<sub>3</sub>PO<sub>4</sub>) of powdered

calcite (McCrea, 1950), was determined. All  $\delta^{13}\text{C}$  and  $\delta^{18}\text{O}$  analyses were performed on a Micromass 602D mass spectrometer.

### 9.2.3 Sulfur

Ten samples of pyrite were analyzed for  $\delta^{34}\text{S}$ . Pyrite was heated at 1025°C in the presence of CuO to produce  $\text{SO}_2$  gas, which was analyzed for  $\delta^{34}\text{S}$ . Duplicate samples of pyrite show reproducibility of  $\delta^{34}\text{S}$  to be  $\pm 0.1$  per mil.

### 9.2.4 Analytical Standards

The standard against which the oxygen isotope abundance ratios of quartz and calcite, and the hydrogen isotopic ratios of fluid inclusion waters, are reported is SMOW (Standard Mean Ocean Water; Craig, 1961). The reference standard for  $\delta^{13}\text{C}$  abundance is PDB (belemnite from the Peedee Formation; Craig, 1957). Canon Diablo Troilite (CDT), is the standard for sulfur (Macnamara and Thode, 1950).

## 9.3 Laforma Mine

### Hydrogen and Oxygen Isotope Results

The  $\delta\text{D}$  of the fluid ( $\delta\text{D}_{\text{H}_2\text{O}}$ ) was determined directly by analysis of the water trapped within the fluid inclusions. The  $\delta^{18}\text{O}$  of the hydrothermal fluids ( $\delta^{18}\text{O}_{\text{H}_2\text{O}}$ ) associated with ore deposition was inferred from the determination of  $\delta^{18}\text{O}$  of quartz, and a calculation of the equilibrium

isotopic fractionation of  $^{18}\text{O}$  between quartz and water at known temperatures and salinities, derived from fluid inclusion analysis. Fractionation is essentially a temperature dependant phenomenon, but the presence of dissolved salts in a hydrothermal fluid has been shown experimentally (Truesdell, 1974) to effectively deplete the fluid in  $^{18}\text{O}$ . The cations in solution have strong bonding abilities and concentrate the heavy isotope of oxygen, thereby causing the residual liquid to become enriched in the lighter isotope of oxygen (Truesdell, 1974). This effect is minimal for fluids of low salinity (ie. 4 wt.% NaCl) and within analytical uncertainty ( $\pm 0.2\text{‰}$ ). For the high salinity fluids encountered in the boiling zone of the Laforma deposit (4-40 wt.% NaCl), a correction factor of +2.5‰ is added to the fractionation equation for quartz- $\text{H}_2\text{O}$ .

Table 8 shows the isotopic values of oxygen and hydrogen for Laforma quartz samples. The  $\delta^{18}\text{O}_{\text{H}_2\text{O}}$  was calculated using the equation for quartz-water fraction of Matsuhisa et al., (1979),

$$\Delta_{\text{qtz-H}_2\text{O}} = 3.34 (10^6/T^2) - 3.31.$$

It must be noted that the temperature range of this equation is between 250°-500°C, and therefore the calculation of  $\delta^{18}\text{O}_{\text{H}_2\text{O}}$  for the Laforma deposit at temperatures of 180°C requires extrapolation of the equation outside the limits of previous experimental measure.

Figure 37 is a graph of  $\delta\text{D}$  vs.  $\delta^{18}\text{O}$  for the Laforma

Table 8. Isotopic Composition of Laforma Ore Fluid

Sample	Salinity	$\delta^{18}\text{O}_{\text{Oz}}$ (‰)	$\delta^{18}\text{O}_{\text{H}_2\text{O}}$ (‰)	$\delta \text{D}$ (‰)	Elevation (m)	Au (ppb)
1 F85-13*	0.8-7 m	9.4	-10.2 to -7.7	-97	1204	1500
2 F85-14*	0.8-7 m	10.0	-9.6 to -7.1	-90	1204	1400
3 LAF-2-1*	0.8-7 m	11.1	-8.5 to -6.0	-139	1110	4400
4 LAF-2-2*	0.8-7 m	12.3	-7.3 to -5.0	-105	1110	690
5 LAF-4-3-M*	0.8-7 m	10.0	-8.0 to -6.3	-54	1025	860, 2700
6 LAF-4-3-LS	0.7 m	11.8	-7.0	-131	1025	510
7 LAF-4-3-RS	0.7 m	10.3	-9.3	-149	1025	640
8 LAF-4B	0.7 m	7.3	-12.3	-133	1025	NA
9 TU4-233	0.7 m	10.4	-9.2	-151	975	3400
10 TU13-278	0.7 m	11.5	-8.1	-134	950	10000
11 TU20-390	0.7 m	9.9	-9.7	-142	905	44

NA = not analyzed      \* = boiling zone      T = 180°C for all samples  
 $\delta^{18}\text{O}$  of water calculated using Matsuhisa et al., (1979), with salinity correction factor  
of Truesdell, (1974)

hydrothermal fluid, from data presented in Table 8.

Reference points on this graph are SMOW, the meteoric water line (MWL), derived from the relationship;

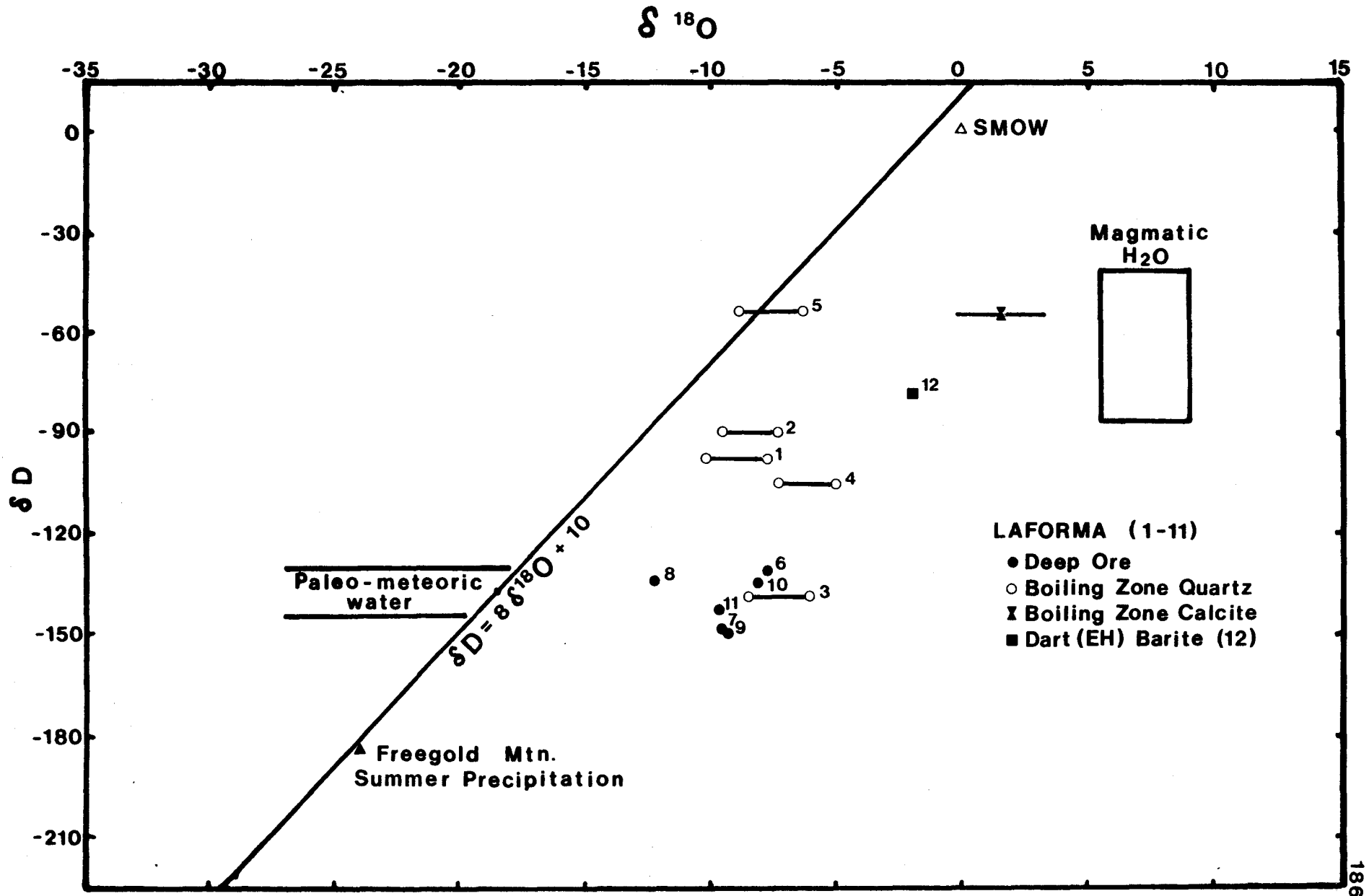
$$\delta D = 8\delta^{18}O + 10 \quad (\text{Craig, 1966; Taylor, 1974})$$

and the magmatic water box (Taylor, 1974;1979).

Precipitation collected at Freegold Mtn. during the period July-August, 1986 plots on the MWL with a  $\delta D$  of  $-184 \pm 1.5\text{‰}$  and  $\delta^{18}O$  of  $-24.1\text{‰}$ . The cluster of closed circles represents deep ore samples (6-11) whose fluid inclusion populations do not show indications of boiling. The average  $\delta^{18}O_{H_2O}$  and  $\delta D_{H_2O}$  for this cluster is  $-9.4 \pm 1.5\text{‰}$  and  $-138 \pm 7\text{‰}$  respectively. These values are isolated from the magmatic water box and more closely represent a meteoric signature in  $\delta D$ . From the MWL relationship defined above, such a water would have a  $\delta^{18}O$  of  $-18.4\text{‰}$ , implying that the water has been enriched in  $^{18}O$  by 9 per mil. This trend of enrichment, known as the "oxygen isotope shift", has been documented at many geothermal systems (Craig, 1966; White et al., 1973 and Truesdell and Hulston, 1980). The shift is due to exchange of  $^{18}O$  between  $^{18}O$ -deficient meteoric water and  $^{18}O$  enriched country rocks. An isotopic mass balance equation to model water-rock interactions, derived by Ohmoto and Rye (1974) is used to determine the water:rock mass ratio;

$$\delta^{18}O^{FINAL} = \frac{\delta^{18}O_{ROCK} - \Delta_{r-w} + (1.8R)(\delta^{18}O^{INITIAL})}{(1 + 1.8R)}$$

Figure 37. Stable isotopic signature of fluid inclusion hosted waters from the Laforma and Emmons Hill deposits.



where R is the water:rock mass ratio,

$\delta^{18}\text{O}_{\text{FINAL}} = -9.4 \text{ ‰}$  (calculated hydrothermal fluid composition)

$\delta^{18}\text{O}_{\text{ROCK (GRANODIORITE)}} \approx 7 \text{ ‰}$

$\delta^{18}\text{O}_{\text{INITIAL}} = -18.4 \text{ ‰}$  (local paleo-meteoric water)

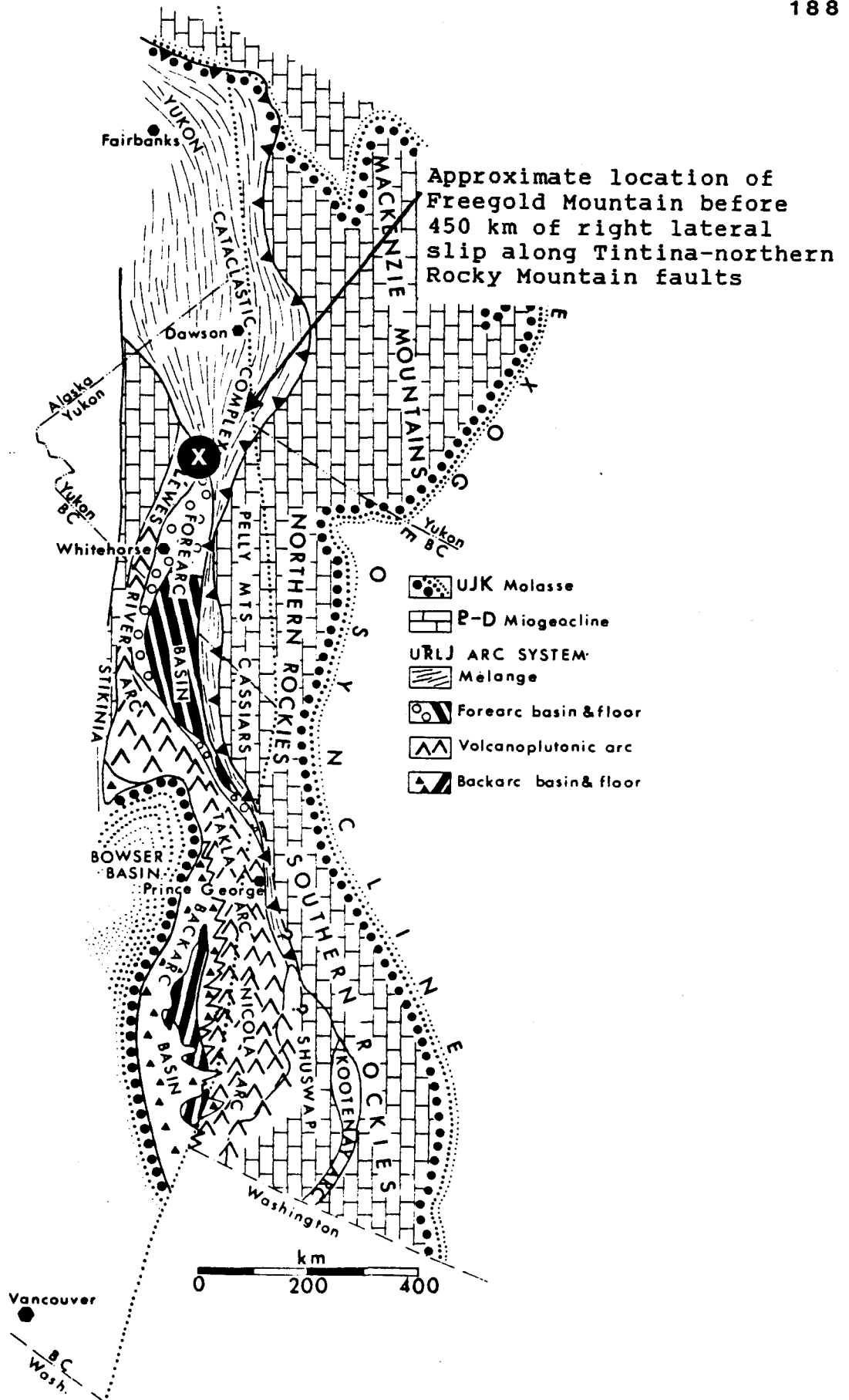
$\Delta_{r-w} = \Delta_{(\text{An}_{20}\text{-H}_2\text{O})}$  (fractionation equation for feldspar-water interaction, (O'Neil and Taylor, 1967))

T = 180°C.

This equation indicates an R value of approximately 0.4. Temperatures of 300°C would give an R value of 0.7. This ratio is within the range observed for epithermal districts in Western U.S.A. (0.2 to 2, Taylor, 1974) and to those of geothermal systems (0.15 to 1.3, Field and Fifarek, 1985).

Because hydrogen is much less abundant in igneous rocks than oxygen, water:rock ratios as low as 0.4 will not affect the initial  $\delta\text{D}$  of the water through water-rock interaction, therefore a paleo-meteoric water for Freegold Mountain during the late Cretaceous can be defined at approximately  $\delta\text{D} = -138$  and  $\delta^{18}\text{O} = -18.4 \text{ ‰}$ . That the isotopic composition of the new paleo-meteoric water is heavier than present-day meteoric water implies a climatic and/or geographic change. Figure 38 is a geological reconstruction of the Cretaceous Canadian Cordillera by Templeman-Kluit (1979) before 450 km of left-lateral movement on the Tintina fault. The approximate location of Freegold Mountain at this time, as indicated on Figure 38, is 100 km south of the present Yukon-British Columbia border and 180 km south of present

Figure 38. Reconstruction of Canadian Cordillera before 450 km of right lateral slip along the Tintina fault (fine dotted line) showing the approximate location of Freegold Mountain in late Cretaceous time. (from Templeman-Kluit, 1979)



day Whitehorse. The  $\delta D$  and  $\delta^{18}O$  of precipitation from Whitehorse is approximately -158 and -20 per mil, respectively (IAEA, 1970).  $\delta D$  and  $\delta^{18}O$  values determined in this study for Freegold Mountain paleo-meteoric waters support this reconstruction, as they are correspondingly higher (-138 and -18‰) than those found in Whitehorse today. The only possible conclusion, then, is that the Freegold Mountain paleo-latitude was south of present-day Whitehorse.

### 9.3.2 The Effects of Boiling on Isotopic Ratios

As previously mentioned, samples 6-11 on Fig. 37 show no evidence of fluid boiling. Fluid inclusion evidence, however, suggests that samples 1-5 formed in zones of active boiling. The effect of boiling on solutions is to partition the lighter isotopes into the vapour phase, and enrich the residual liquid in deuterium and  $^{18}O$ . The average composition of the deep ore fluids can be taken as the initial fluid composition ( $\delta D = -138‰$  and  $\delta^{18}O = -9.4‰$ ). Boiling should cause a shift in  $\delta D$  and  $\delta^{18}O$  parallel to the meteoric water line, towards the magmatic water box (ie., increasing  $\delta D$  and  $\delta^{18}O$ ). A significant increase in  $\delta D$  is observed in samples 1, 2, 4 and 5. Although sample 3 shows evidence of boiling, this is not reflected in its isotopic composition perhaps because the sample may have undergone fractionation during extraction. The extreme enrichment in  $\delta D$  in the remaining samples is in accord with extreme

enrichments in salinity (Table 8).

Although far less dramatic, there is a slight increase in  $\delta^{18}\text{O}$  for the samples from the boiling zone. The less pronounced increase in  $\delta^{18}\text{O}$  relative to  $\delta\text{D}$  could be a reflection of their mode of determination.  $\delta\text{D}$  is quantified directly from the water extracted from the fluid inclusions, while  $\delta^{18}\text{O}$  is calculated indirectly, from analysis of quartz, using a fractionation equation which assumes equilibrium conditions. It is probably erroneous to assume equilibrium conditions prevail when vapour-liquid fractionation and precipitation of quartz occur simultaneously in a zone of intense boiling where salinity increases by an order of magnitude. In addition, a larger shift in  $\delta\text{D}$  can be expected since deuterium is more strongly fractionated into the vapour phase than  $^{18}\text{O}$  (Truesdell et al., 1977).

To test for the existence of equilibrium conditions in the boiling zone, it is useful to compare the fractionation of  $^{18}\text{O}$  between contemporaneous mineral phases. The  $\delta^{18}\text{O}$  of calcite intergrown with quartz has values between 9.8 and 13.3‰ as shown in Table 9. The average  $\delta^{18}\text{O}$  of calcite is  $12.3 \pm 1.8$ ‰. This is greater than the  $\delta^{18}\text{O}$  of intergrown quartz. Under equilibrium conditions,  $\Delta_{\text{QUARTZ-CALCITE}}$  at 180°C should be +2.3‰ (Friedman and O'Neil, 1977; Matsuhisa et al., 1979). Instead, the actual value is -1.5‰, and therefore quartz and calcite precipitated under disequilibrium conditions.

Table 9. Isotopic Composition of Calcite at Laforma Mine.

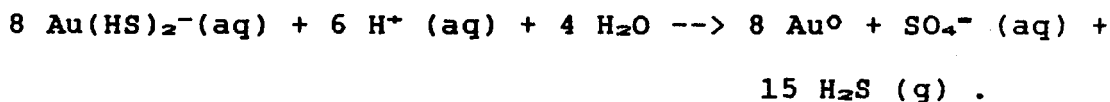
SAMPLE	$\delta^{13}\text{C}_{\text{(CALCITE)}}$	$\delta^{18}\text{O}_{\text{(CALCITE)}}$	$\delta^{18}\text{O}_{\text{(H}_2\text{O)}}$	$\delta\text{D}$
BZCAL1	-3.3	13.3	2.6	-54
BZCAL2	-3.8	9.8	-0.8	-54
BZCAL3	-3.9	11.8	1.2	-54
BZCAL4	-5.4	15.2	4.6	-54
BZCAL5	-3.9	11.2	0.6	-54
x	$-4.1 \pm .7$	$12.3 \pm 1.8$	$1.6 \pm 1.8$	

$$\Delta_{\text{CAL-H}_2\text{O}} = 2.78(10^6/T^2) - 2.89 \quad (\text{Friedman and O'Neil, 1974})$$

$$T = 180^\circ\text{C}$$

### 9.3.3 The Effect of Boiling on Gold Deposition

The effect of boiling is to concentrate solutes in the residual liquid, and more significantly to remove dissolved volatile components. Boiling of an auriferous fluid, where gold is probably transported as a bisulfide complex (Seward, 1973), has been proposed as a mechanism for the deposition of gold, by the reaction,



The deposition mechanism is the partitioning of the  $\text{H}_2\text{S}$  into the vapour phase, resulting in an unstable Au-bisulfide complex and subsequent Au precipitation. Mathematical modelling of this reaction by Drummond and Ohmoto (1985) shows this to be an effective mechanism, but direct physical evidence of the association between boiling and Au deposition is difficult to obtain.

A boiling zone within two non-boiling peripheral zones has been identified by fluid inclusion and stable isotopic analysis at the Laforma 4th level. Table 8 shows that gold concentrations are markedly higher in the boiling zone (diagrammatically represented in Figure 39).

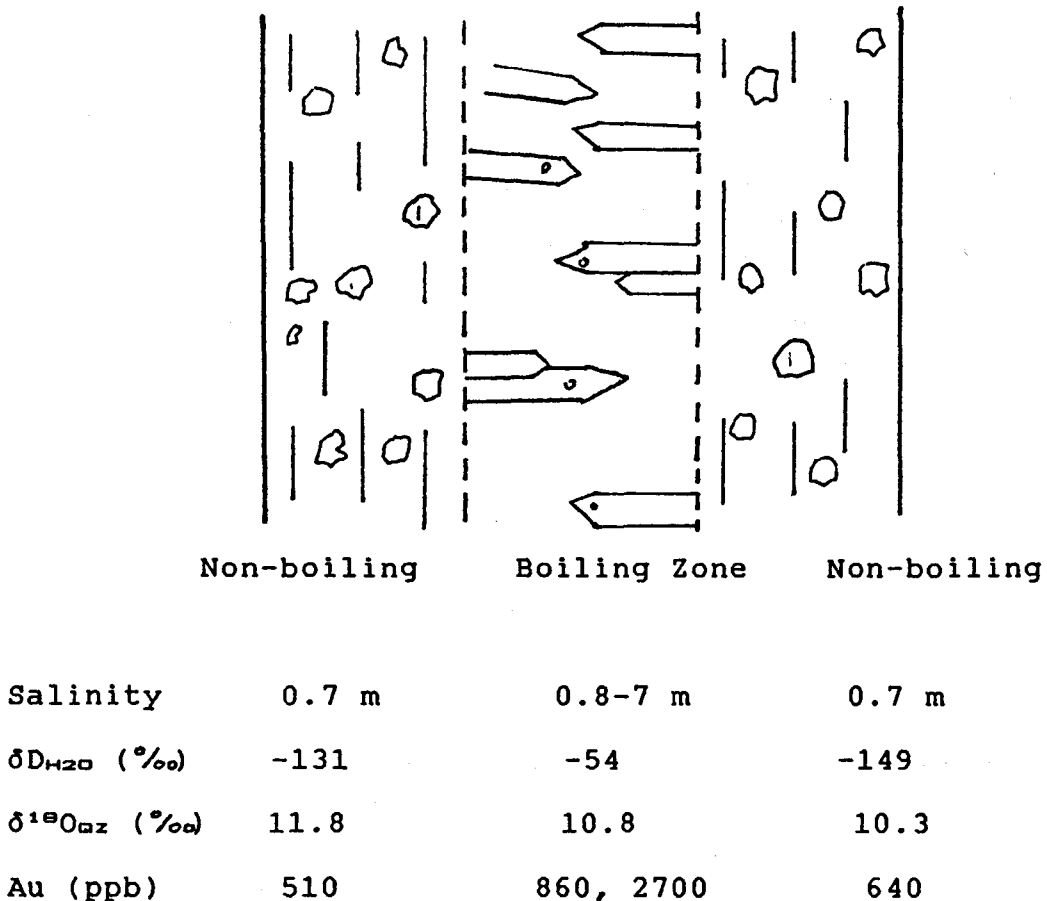


Figure 39. Schematic cross-section of 4th level Laforma Vein.

If the peripheral zone gold concentrations represent the original depositional capacity of the fluid under non-boiling conditions, the one to five-fold increase in gold values within the boiling zone supports the mechanism outlined above. However, no appreciable vertical variation in gold concentration is evident at the Laforma Mine, which

suggests that boiling is not the only depositional process operating.

#### 9.3.4 Carbon Isotope Results

Interpretations from carbon isotope data are limited due to the limited occurrence of calcite. Primary calcite is present only in the boiling zone located on the 4th level. The carbon isotopic values for this calcite (listed in Table 9) show a restricted range in  $\delta^{13}\text{C}$ , from -3.3 to -5.4‰. These values resemble values determined from other epithermal deposits and geothermal systems (Field and Fifarek, 1985) and are interpreted as being indicative of magmatic carbon (-5 to +2‰; Ohmoto and Rye, 1979).

#### 9.3.5 Sulphur Isotope Results

Five samples of pyrite from the Laforma deposit were analyzed for  $\delta^{34}\text{S}$  as indicated in Table 10. Three samples from the 4th level boiling zone have  $\delta^{34}\text{S}$  ranging from 1.9-2.2‰. The remaining two samples were obtained from the vein at surface (220 m above the 4th level) and have  $\delta^{34}\text{S}$  values of 2.8-2.9‰. Boiling tends to enrich the residual liquid in the heavier isotopes. The increase in  $\delta^{34}\text{S}_{\text{PYRITE}}$  with elevation is consistent with a Rayleigh fractionation process, in that upon boiling (4th level)  $^{32}\text{S}$  is preferentially taken into the vapour phase ( $\text{H}_2\text{S}$  gas) and removed from the system. The proportion of vapour phase increases with increasing elevation so that pyrite

crystallizing from the residual liquid at 1210 m is heavier in  $^{34}\text{S}$  than that crystallizing at 1025 m.

Table 10. Sulphur Isotope Data for the Laforma Mine

Sample	Elevation (m)	$\delta^{34}\text{S}_{(\text{PYRITE})}$
F85-13	1204	2.8
F85-14	1204	2.9
LAF-4-1	1025	1.9
LAF-4-2	1025	2.0
LAF-4-3	1025	2.2

#### 9.4 Antoniuk Breccia

Due to a lack of quartz veining, inadequate sample material was available for deuterium and oxygen isotope determination.

##### 9.4.1 Sulphur Isotopes

Five samples of pyrite from one diamond drill hole in the Antoniuk Breccia were analyzed for sulphur as shown in Table 11.

Table 11. Sulphur Isotope Data for the Antoniuk Deposit.

Sample	$\delta^{34}\text{S}_{(\text{PYRITE})}$	Au(ppb)
AR75-9-160	2.6	2540
AR75-9-165	2.3	488
AR75-9-219	1.7	679
AR75-9-344	2.0	196
AR75-9-381	2.9	1070

$$\bar{x} = 2.1 \pm 0.4$$

There does not appear to be a correlation between sulphur isotopic composition and gold concentration. No significant

conclusions can be drawn from this data without complimentary analysis of coexisting sulphur-bearing minerals, which were too small to isolate and analyze. The origin of the sulphur cannot be discriminated as it could have been derived from either a magmatic source or leached from the granitic country rock.

## 9.5 Emmons Hill

### 9.5.1 Oxygen and Hydrogen Results

One sample of intergrown barite and calcite was analyzed for oxygen and deuterium. The deuterium value ( $\delta D = -78\text{‰}$ ) was derived from water removed during the crushing of barite and the oxygen value ( $\delta^{18}O_{\text{CALCITE}} = 9.1\text{‰}$ ;  $\delta^{18}O_{\text{H}_2\text{O}} = -1.5\text{‰}$  at  $\approx 180^\circ\text{C}$ ) from the co-precipitated calcite. Sample 12 on Figure 37 represents the results of these determinations. Although this area has been identified previously (Chapter 7) as a near surface occurrence, the isotopic signature does not suggest a meteoric water-dominated system. It is possible that the meteoric signature has been altered by boiling, which enriched the residua in the heavier isotopes, a situation similar to that of the boiling zone samples from the Laforma Deposit.

## 9.6 Metal Inventory - Considering the Genesis of Gold Deposits at Freegold Mountain

It is possible to make first-order approximation calculations to assess the ability of meteoric water to

leach gold from the country rock and concentrate it in a deposit such as the Laforma. The Laforma deposit contains 180, 000 tonnes of ore. It is known that the ore is hosted exclusively within quartz and that the wallrock is not considered ore. Therefore, 180, 000 tonnes of gold-bearing quartz has been deposited by hydrothermal solutions. The solubility of quartz at 180°C is 102 mg/kg (Fournier, 1985). Assuming that all the quartz present in the solution is deposited, the minimum amount of H<sub>2</sub>O needed to deposit ore at Laforma is  $1.8 \times 10^{12}$  l. (This is equivalent to the amount of water flowing over Niagara Falls in 7 days.)

Stable isotopic measurements for the deep ore waters suggest that the bulk of the water at Laforma is of meteoric origin. The genetic implications are therefore, that meteoric water has been prominent in the transportation and deposition of gold. But the question as to the ultimate source of the gold has not been discussed. As previously mentioned, the probable source is thought to be country rock gold leached by groundwater or that Au is from magmatic fluids associated with the intrusive rocks ubiquitous in epithermal environs.

Conservative derivation of the minimum amount of fluid flow through the Laforma system is  $1.8 \times 10^{12}$  l of H<sub>2</sub>O. The oxygen isotope shift of the paleo-meteoric waters is the result of oxygen exchange between 4 mass units of water with 10 mass units of rock (R = 0.4). Thus,  $1.8 \times 10^{12}$  l of H<sub>2</sub>O ( $1.8 \times 10^{12}$  kg) has interacted with  $4.5 \times 10^{12}$  kg of rock.

Assuming that igneous rocks in the Freegold Mountain area had an average gold concentration of 2 ppb (Crocket, 1974), the hydrothermal fluids had a gold leaching capability of 25%, and 100% of the gold in solution was deposited with quartz in the Laforma vein (reasonable estimates following the data of Hedenquist and Henley, (1985)), a convecting groundwater system operating at Freegold Mountain could transport and deposit  $2.25 \times 10^6$  g of Au. The Laforma deposit is estimated to contain a total of  $2.034 \times 10^6$  g of Au (110,000 tonnes of ore @ 11.3 g/t Au).

This calculation suggests that it is feasible to generate gold deposits such as the Laforma by meteoric water dominated convection cells and that the rhyolite intrusives in the area are only heat engines, and not the ultimate gold sources. This leads to the conclusion that the rhyolite also does not contribute dissolved constituents ( $H_2S$ ,  $CO_2$ , Cl) to the system. Unfortunately, sulfur and carbon isotopes cannot differentiate between sulfur and carbon of magmatic origin and that derived from leaching of igneous rocks.

A genetic interpretation of the Laforma deposit is that upper crustal circulation of meteoric water in large-scale hydrothermal convection systems driven by rhyolitic intrusives leached gold from the country rocks, and deposited it in structurally prepared fissure systems. Although no evidence is available to support a more integral role for the rhyolite in ore genesis, it is possible that a contribution of magmatic constituents was diluted by the

large volumes of meteoric water present in the hydrothermal system.

## CHAPTER 10. CONCLUSIONS AND SUMMARY

The geological evolution of the Freegold Mountain area should be considered within the evolutionary framework of the Northern Cordillera since large scale tectonic events have affected, and are reflected in, the Freegold system. Chronologically summarized below are the major broad-scale geologic and tectonic events, the results of which are seen in the Freegold geology today.

Triassic granodiorite and early Cretaceous syenite ( $138 \pm 10$  Ma) plutonic rocks intruded into Paleozoic sediments during consumption of oceanic plate in a westward dipping subduction zone under an island arc accreted onto<sup>the</sup> North American continent (165 Ma - 125 Ma) (Templeman-Kluit, 1979, p.23). Following arc-continent collision, subduction of the N-NE moving Kula plate under the North American craton along an E-NE dipping Benioff zone initiated transcurrent movement along the Tintina fault around 90 Ma (Templeman-Kluit, 1979). The Dawson Range experienced a period of predominantly dacitic volcanism beginning around 80 Ma, resulting from the melting of subducted oceanic plate material and contamination by crustal material. This period of intermediate volcanism was followed by rhyolitic volcanism around  $77.5 \pm 6.2$  Ma, which is interpreted to have been caused by partial melting of upper crustal rocks. These rhyolitic melts exploited N to NE-oriented extensional fractures and faults which are conjugate to large scale

northwesterly trending major structures such as the Tintina and Big Creek faults.

Gold mineralization at Freegold Mountain is temporally and spatially related to rhyolitic volcanism. Meteoric waters, driven in large scale hydrothermal convection cells, utilized extensional environments to form high-grade gold-quartz veins such as the Laforma and Rambler. Fluid inclusion temperatures (175°-195°), salinities (2-4.5 wt. % NaCl equivalent), CO<sub>2</sub> contents and the presence of boiling zones indicate that gold deposition at Laforma occurred 1 to 1.5 km below the late Cretaceous surface.

The boiling zone contains euhedral quartz, carbonate, pyrite and arsenopyrite in vugs. The extreme ranges in temperatures of homogenization (165-430°C) and salinities (4-43 wt. % NaCl equiv.) within this zone indicate that boiling of an original low salinity fluid has occurred in a 'closed' system where no additional fluid has diluted the saline brine. Gold concentration in the inner boiling zone increases 150% to 450% relative to the outer non-boiling zones, however there is no apparent vertical zonation in gold grade at the mine. Intergrown carbonate and quartz show isotopic disequilibrium.

The upper ore zone, 200 m above the boiling zone, has undergone multiple periods of brecciation and silicification. The vein breccia is interpreted to have formed by the explosive eruption of CO<sub>2</sub> and H<sub>2</sub>O vapour

trapped within the closed boiling system. Movement along the Laforma fault may have triggered the vapour release, with clasts of material within the boiling zone transported upward by the gases.

The Antoniuk diatreme consists of heterolithic and monolithic breccias intruded by rhyolite dykes. Diamond drilling indicates that a large body of fine to medium grained alaskite is present beneath the auriferous breccia. The deposit is interpreted to have formed by the explosive escape of volatile components, evolved from the retrograde boiling of a silicic magma chamber. Gold mineralization in the breccia is associated with pyrite and arsenopyrite formed at temperatures around 305°C and salinities of about 5 wt. % NaCl. The northwesterly alignment of mineralized diatremes suggests that their genesis is structurally controlled by transcurrent faults.

The Emmons Hill gold-bearing vein-breccia deposit has a mineral assemblages of barite, stibnite, cinnabar, orpiment, Fe and Mn carbonates and chalcedonic silica. Fluid inclusions from these deposits homogenize between 140-185° with salinities of 0-0.5 wt. % NaCl. This deposit shows marked similarities to epithermal precious metal deposits in New Zealand and western United States.

The diversity of precious metal deposits at Freegold Mountain requires that the exploration geologist not restrict him/herself to any one specific style of gold

occurrence. Exploration criteria for the Dawson Range should concentrate on areas where rhyolites occur.

Structural zones oriented N-NE and NW in the vicinity of the Big Creek and Tintina faults, should be explored for potential vein and breccia deposits, particularly where these structures are associated with felsic magmatism.

Fluid inclusion and mineralogical evidence suggests that the area has undergone a relatively minor degree of erosion since the late Cretaceous, probably less than 1 km. The presence of stibnite, arsenopyrite, orpiment and cinnibar in gold deposits at Freegold Mountain indicates that Sb, As, Hg, and Au should be useful pathfinder elements during geochemical exploration for these deposits.

References Cited

- Albuquerque, C.A.R. 1977. Geochemistry of the tonalitic and granitic rocks of the Nova Scotia southern plutons. *Geochim. Cosmochim. Acta*, 41, pp. 1-13.
- Antoniuk, T. 1975. A report on the 1975 diamond drilling program at the Laforma property, Mt. Freegold, Yukon. Private report, Rayrock Mines Ltd., on file Dept. Ind. Nor. Affairs, Whitehorse.
- Arnold, G.O., and Fitzgerald, F. 1977. Igneous rock types and their alteration, Mt. Fubilan porphyry copper deposits. Papua New Guinea Geol. Survey Rept. 77/5, 11p.
- Arth, J.G. 1976. Behavior of trace elements during magmatic processes—a summary of theoretical models and their applications. *J. Res. U.S. Geol. Surv.*, 4, pp. 41-47.
- Atherton, M.P., McCourt, W.J., Sanderson, L.M. and Taylor, W.P. 1979. The geochemical character of the segmented Peruvian Coastal Batholith and associated volcanics; in Origin of Granite Batholiths; Geochemical Evidence, Atherton, M.P and Tarney, J. (eds.), Shiva Pub. Ltd, Orpington, Kent., pp. 45-64.
- Atwater, T. 1970. Implications of plate tectonics for the Cenozoic tectonic evolution of western North America. *Geological Society of America Bulletin*, v.81, pp.3513-3536.
- Bateman, P.C. 1983. A summary of critical relations in the central part of the Sierra Nevada batholith, California, U.S.A. *Geol. Soc. Am., Mem.*, 159, pp. 241-254.
- Beakhouse, G.P. and Heaman, L.M. 1980. The chemical separation of Rb and Sr for mass spectrometric analysis. McMaster Univ. Tech. Memo 80-6.
- Beavan, A.P. 1963. Evaluation of Laforma Property, Ormsby Mines Ltd., Private Unpublished Report, Dept. Indian Nor. Affairs, Whitehorse.
- Berger, B.R., and Eimon, P.I. 1983. Conceptual models of epithermal precious-metals deposits, in Shanks, W.C. III(ed.), Cameron Volume on Unconventional Mineral Deposits, Society of Mining Engineers, pp. 191-205.
- Bethke, P.M. 1984. Controls on base- and precious-metal mineralization in deeper epithermal environments: U.S. Geological Survey, Open File Report 84-890, 40 p.

- Blake, S. 1984. Volatile oversaturation during the evolution of silicic magma chambers as an eruption trigger. *J. of Geophys. Res.*, v. 89, no. B10, pp. 8237-8244.
- Bodnar, R.J., Reynolds, T.J., and Kuehn, C.A. 1985. Fluid-inclusion systematics in epithermal systems. *in* Berger, B.R. and Bethke, P.M.(eds.), *Reviews in Economic Geology*, V. 2, *Geology and Geochemistry of Epithermal Systems*, pp. 73-98. Society of Economic Geologists.
- Bostock, H.S. 1935. Carmacks District, Yukon. Geological Survey, Canada, Memoir 189, pp. 1-67.
- Buchanan, L.T. 1981. Precious metal deposits associated with volcanic environments in the southwest, *in* Dickinson, W.R. and Payne, W.D. (eds.), *Relation of Tectonics to Ore Deposits in the South Cordillera*. Arizona Geological Society Digest, v. 14, pp. 237-262.
- Buddington, A.F. 1927. Coast Range intrusives of southeastern Alaska. *J. Geol.*, 35(3), pp. 224-246.
- Burnham, C.W. 1979. Magmas and hydrothermal fluids; *in* Barnes, H.L. (ed.), *Geochemistry of Hydrothermal Ore Deposits*, 2nd Edition: John Wiley and Sons, New York, pp. 71-136.
- 1985. Energy release in subvolcanic environments: Implications for breccia formation. *Econ. Geol.*, v. 80, pp. 1515-152.
- Burruss, R.C. 1981. Analysis of phase equilibria in C-O-H-S fluid inclusions. *in* Short Course in Fluid Inclusions, Hollister, L.S. and Crawford, M.L.(eds.). Mineralogical Association of Canada.
- Cairnes, D.D. 1914. South Western Yukon. Geological Survey, Canada, Summary Rept.
- Cathro, R.J., and Main, C.A. 1986. Report on drilling program, Antoniuk property, Mt. Freegold, Yukon Territory. Archer, Cathro and Associates Ltd., Vancouver. Unpublished Report.
- Chayes, F. 1975. *Statistical Petrology*. Carnegie Inst. Wash., Yearb., 74, pp. 542-550.
- Clayton, R.N., and Mayeda, T.K. 1963. The use of bromine pentafluoride in the extraction of oxygen from oxides and silicates for isotopic analysis. *Geochim. Cosmochim. Acta*, v. 72, pp. 43-52.

- Cole, J.W. 1979. Structure, petrology, and genesis of Cenozoic volcanism, Taupo Volcanic Zone, New Zealand—a review. *N.Z. Jour. of Geol. and Geophys.*, v.22 (6), pp. 631-657.
- Coney, P.J. 1978. Mesozoic - Cenozoic Cordilleran plate tectonics. *Geological Society of America, Memoir 152*, pp. 33-50.
- Craig, H. 1957. Isotopic standards for carbon and oxygen and correction factors for mass spectrometric analysis of carbon dioxide. *Geochim. Cosmochim. Acta*, v. 12, pp. 133-149.
- . 1961. Standards for reporting concentrations of deuterium and oxygen-18 in natural waters. *Science*, v. 133, pp. 1833-1834.
- . 1966. Isotopic composition and origin of the Red Sea and Salton Sea geothermal brines. *Science*, v. 154, pp. 1544-1548.
- Crocket, J.H. 1974. Gold, in Wedpohl, K.H. (ed.), *Handbook of Geochemistry*, Chap. 79, Sections B-O, v. II/5, Springer-Verlag, Berlin.
- Cross, W.C., Iddings, J.P., Pirsson, L.V., and Washington, H.S. 1902. A quantitative chemico-mineralogical classification and nomenclature of igneous rocks. *Journal of Geology*, 10, pp. 555-690.
- Dalrymple, G.B., and Lanphere, M.A. 1969. Potassium-Argon Dating: Principles, techniques and applications to geochronology, W.H. Freeman and Company, San Francisco, 258 p.
- Drummond, S.E., and Ohmoto, H. 1985. Chemical evolution and mineral deposition in boiling hydrothermal systems. *Econ. Geol.*, v. 80, pp. 126-147.
- Ewart, A. 1979. A review of the mineralogy and chemistry of Tertiary-Recent dacitic, latitic, rhyolitic, and related salic volcanic rocks, in Trondhjemites, Dacites, and Related Rocks, edited by F. Barker, Elsevier, Amsterdam, pp. 13-121.
- Ewers, G.R., and Keays, R.R. 1977. Volatile- and precious-metal zoning in the Broadlands geothermal field, New Zealand. *Econ. Geol.*, v. 72, pp. 1337-1354.
- Ewing, T.E. 1980. Paleogene tectonic evolution of the Pacific Northwest. *Journal of Geology*, v. 88, n. 6, pp. 619-638.

- Faure, G. and Powell, J.L. 1972. Strontium Isotope Geology. Springer-Verlag, New York. 188p.
- Field, C.W., and Fifarek, R.H. 1985. Light stable-isotope systematics in the epithermal environment; in Berger, B.R., and Bethke, P.M. (eds.), Geology and Geochemistry of Epithermal Systems: Reviews in Economic Geology, V.2, Soc. Econ. Geologists, pp. 99-128.
- Fournier, R.O. 1983. Self-sealing and brecciation resulting from quartz deposition within hydrothermal systems: Extended abstracts, Fourth International Symposium on Water-Rock Interaction, Misasa, Japan, pp. 137-140.
- . 1985. The behaviour of silica in hydrothermal solutions; in Berger, B.R., and Bethke, P.M. (eds.), Geology and Geochemistry of Epithermal Systems: Reviews in Economic Geology, V.2, Soc. Econ. Geologists, pp. 45-61.
- Friedman, I., and O'Neil, J.R. 1977. Compilation of stable isotope fractionation factors of geochemical interest; in Fleischer, M. (ed.), Data of Geochemistry, 6th Edition: US Geological Survey, Professional Paper 440-KK, pp. KK1-KK12.
- Gabrielse, H. 1985. Major dextral transcurrent displacements along the Northern Rocky Mountain Trench and related lineaments in north-central British Columbia. Geological Society of America Bulletin, v. 96, pp. 1-14.
- Ghazban, F. 1987. Geochemistry of Carbonate-hosted Pb-Zn deposits, Baffin Island, NWT. Unpublished Ph.D. Thesis, McMaster University. (in prep.)
- Gilbert, L.A., and Foland, K.A. 1986. The Mont Saint Hilaire plutonic complex: occurrence of excess  $^{40}\text{Ar}$  and short intrusion history. Canadian Journal of Earth Sciences, v. 23, pp. 948-958.
- Godwin, C.I. 1975. Alternative interpretations for the Casino Complex and Klotassin Batholith in the Yukon Crystalline Terrane. Can. J. Earth Sci., 12, pp. 1910-1916.
- Gromet, L.P., and Silver, L.T. 1983. Rare earth element distribution among minerals in a granodiorite and their petrogenetic implications. Geochim. Cosmochim. Acta., 47, pp. 925
- Grond, H.C., Churchill, S.J., Armstrong, R.L., Harakal, J.E., and Nixon, G.T. 1984. Late Cretaceous age of the Hutshi, Mount Nansen, and Carmacks groups, southwestern

- Yukon Territory and northwestern British Columbia. Can. Jour. Earth Sci., v. 21, pp.554-558.
- Gwilym Roberts, R. 1987. Ore Deposit Models #11. Archean Lode Gold Deposits. Geoscience Canada, v. 14, no. 1, pp. 37-52.
- Haas, J.L., Jr. 1971. The effect of salinity on the maximum thermal gradient of a hydrothermal system at hydrostatic pressures. Econ. Geol., v.66, pp. 940-946.
- Hannington, M.D., and Scott, S.D. 1985. A caldera-hosted silica-sulfate-sulfide deposit, Axial Seamount, central Juan de Fuca Ridge, N.E. Pacific Ocean [abstr.]. GAC-MAC Joint Ann. Mtg. Prog. Abstr., 10, A24.
- Hedenquist, J.W. and Henley, R.W. 1985. Hydrothermal eruptions in the Waiotapu geothermal system, New Zealand: Their origin, associated breccias, and relation to precious metal mineralization. Economic Geol., v. 80, pp. 1640-1668.
- Henley, R.W., Truesdell, A.H., Barton, P.B., Jr., and Whitney, J.A. 1984. Fluid-Mineral Equilibria in Hydrothermal Systems. Reviews in Economic Geology, v. 1, Society of Economic Geologists, p. 267.
- Henley, R.W. 1985. The geothermal framework of epithermal deposits, in Berger, B.R. and Bethke, P.M.(eds.), Geology and Geochemistry of Epithermal Systems. Reviews in Economic Geology, V. 2, Society of Economic Geologists, pp. 1-21.
- IAEA, 1970. Environmental Isotope Data No. 2: World Survey of Isotope Concentration in Precipitation (1964-65). Technical Reports Series No. 117, International Atomic Energy Agency, Vienna.
- Irvine, T.N. and Baragar, W.R.A. 1971. A guide to the chemical classification of the common volcanic rocks. Can. Jour. Earth Sci., v. 8, pp. 523-549.
- Johnson, S.M., Bourque, R.F., and Day, W.C. 1971. Explosive Excavation Technology. U.S. Army Engineer Nuclear Cratering Group, Livermore, California, 246 p.
- Johnston, J.R. 1937. Geology and Mineral Deposits of Freegold Mountain, Carmacks District, Yukon. Geological Survey of Canada, Memoir 214, pp. 1-21.
- Kamilli, R.J., and Ohmoto, H. 1977. Paragenesis, zoning, fluid inclusion, and isotope studies of the Finlandia vein, Colqui district, central Peru. Econ. Geol., v. 72, pp. 950-982.

- Karklin, G.A., Davison, G., and Viianen, M. 1986. Dawson Range Heap Leach Project: Phase I, Metallurgical Test Work and Mineralogical Evaluation. Unpublished private report. Witteck Development Inc., Missisauga, Ontario., 32 p.
- Kieffer, S.W. 1981. Blast dynamics at Mount St Helens on 18 May, 1980. *Nature*, v. 291, pp. 568-570.
- Kelly, W.C. and Rye, R.O. 1979. Geologic, fluid inclusion, and stable isotope studies of the tin-tungsten deposits of Panasqueira, Portugal. *Econ. Geol.*, v. 74, pp. 1721-1822.
- Le Couteur, P.C. and Templeman-Kluit, D.J. 1976. Rb/Sr ages and a profile of initial Sr 87/ Sr 86 ratios for plutonic rocks across the Yukon Crystalline Terrane. *Canadian Journal of Earth Sciences*, v. 13, pp. 319-330.
- Le Maitre, R.W. 1976. The chemical variability of some common igneous rocks. *J. Petrology.*, 17(4), pp. 589-637.
- Lerbekmo, J.F. and Campbell, F.A. .1969. Distribution, composition, and source of the White River Ash, Yukon Territory. *Canadian Journal of Earth Sciences*, v. 6, n. 1, pp. 109-116.
- Longstaffe, F.J. 1977. The oxygen isotope and elemental geochemistry of Archean rocks from northern Ontario. Unpublished Ph.D. Thesis. McMaster University, 564 p.
- Lynch, G.V., and Pride, C. 1984. Evolution of a high-level, high-silica magma chamber: the Pattison pluton, Nisling Range alaskites, Yukon. *Can. J. Earth Sci.*, v. 21, pp. 407-414.
- Maaloe, S., and Wyllie, P.J. 1975. Water content of a granite magma deduced from the sequence of crystallization determined experimentally with water undersaturated conditions. *Contrib. Mineral. Petrol.*, v. 52, pp. 175-191.
- Macnamara, J., and Thode, H.G. 1950. Comparison of the isotopic constitution of terrestrial and meteoric sulfur. *Phys. Rev.*, v. 78, pp. 307-308.
- Mahood, G., and Hildreth, W. 1983. Large partition coefficients for trace elements in high-silica rhyolites. *GCA*, v. 47, pp. 11-30.

- Matsuhisa, Y., Goldsmith, J.R., and Clayton, R.N. 1979. Oxygen isotopic fractionation in the system quartz-albite-anorthite-water. *Geochim. Cosmochim. Acta*, v. 43, pp. 1131-1140.
- McCrea, J.M. 1950. On the isotope chemistry of carbonates and a paleotemperature scale. *Jour. Chem. Phys.*, v. 18, pp. 849-857.
- Metzger, F.W., Kelly, W.C., Nesbitt, B.E., and Essene, E.J. 1977. Scanning electron microscopy of daughter minerals in fluid inclusions. *Econ. Geol.*, v. 72, pp. 141-152.
- Middlemost, E.A.K. 1985. Magmas and Magmatic Rocks: An introduction to igneous petrology. Longman Group Ltd., Essex. 266 p.
- Miller, C.F., and Mittlefehldt, D.W. 1982. Depletion of light rare-earth elements in felsic magmas. *Geology*, 10, pp. 129-133.
- Mitcham, T.W. 1974. Origin of breccia pipes. *Econ. Geol.*, v.69, pp. 412-413.
- Monger, J.W.H. and Price, R.A. 1979. Geodynamic evolution of the Canadian Cordillera - progress and problems. *Canadian Journal of Earth Sciences*, v. 16, pp. 770-791.
- Monger, J.W.H., Price, R.A. and Templeman-Kluit, D.J. 1982. Tectonic accretion and the origin of the two major metamorphic and plutonic belts in the Canadian Cordillera. *Geology*, v. 10, pp. 70-75.
- Monger, J.W.H., Souther, J.G., and Gabrielse, H. 1972. Evolution of the Canadian Cordillera: a plate tectonic model. *American Journal of Science*, v. 272, pp. 577-602.
- Murowchick, J.B., and Barnes, H.L. 1986. Marcasite precipitation from hydrothermal solutions. *Geochim. Cosmochim. Acta*, v. 50, pp. 2615-2629.
- Mustard, H. 1986. Geology and genesis of the Kidston gold deposit, Australia in *Proceedings Volume of Gold '86 Symposium*, Toronto. pp. 404-415.
- Nash, W.P., and Crecraft, H.R. 1985. Partition coefficients for trace elements in silicic magmas., *Geochim. Cosmochim. Acta*, v. 49, pp. 2309-2322.
- Nelson, C.E. and Giles, D.L. 1985. Hydrothermal eruption mechanisms and hot spring deposits. *Econ. Geol.*, v. 80, pp. 1633-1639.

- Nesbitt, W.H. 1984. Calculation of the solubility of CO<sub>2</sub> in NaCl-rich hydrothermal solutions using regular solution equations. *Chemical Geology*, v. 43, pp. 319-330.
- Norton, D.L., and Cathles, L.W. 1973. Breccia pipes-products of exsolved vapor from magmas. *Econ. Geol.*, v. 68, pp. 540-546.
- Ohmoto, H., and Rye, R.O. 1974. Hydrogen and oxygen isotopic compositions of fluid inclusions in the Kuroko deposits, Japan. *Econ. Geol.*, v. 69, pp. 947-953.
- 1979. Isotopes of sulfur and carbon; in Barnes, H.L. (ed.), *Geochemistry of Hydrothermal Ore Deposits*, Second Edition: John Wiley and Sons, New York, pp. 509-567
- O'Brien, B.H. 1985. The formation of veins in greenschist facies rocks and the early deformation of the Meguma Group, eastern Nova Scotia. Nova Scotia Department of Mines and Energy, Paper 85-2, 35 p.
- O'Neil, J.R., Silberman, M.L., Fabbi, B.P., and Chesterman, C.W. 1973. Stable isotope and chemical relations during mineralization in the Bodie mining district, Mono County, California. *Econ. Geol.*, v. 68, pp. 765-784.
- , and Silberman, M.L. 1974. Stable isotope relations in epithermal Au-Ag deposits. *Econ. Geol.*, v. 69, pp. 902-909.
- , and Taylor, H.P., Jr. 1967. The oxygen isotope and cation exchange chemistry of feldspars. *Amer. Mineral.*, v. 52, pp. 1414-1437.
- Peccerillo, A., and Taylor, S.R. 1976. Geochemistry of some calc-alkaline volcanic rocks from the Kastamonu area, northern Turkey. *Contrib. Mineral. Petrol.*, 58, pp. 63-81.
- Porter, E.W., and Ripley, E. 1985. Petrologic and stable isotope study of the gold-bearing breccia pipe at the Golden Sunlight deposit, Montana. *Econ. Geol.*, v. 80, pp. 1689-1706.
- Potter, II, R.W., Clynne, M.A., Brown, D.L. 1978. Freezing point depression of aqueous sodium chloride solutions. *Econ. Geol.*, v. 73, 284-285.
- Pride, M.J., and Clark, G. 1985. An Eocene Rb-Sr isochron for rhyolite plugs, Skukum area, Yukon Territory. *Can. J. Earth Sci.*, v. 22, pp. 1747-1753.

- Ramsay, J.G. 1980. Shear geometry: a review. *J. of Structural Geology*, v. 2, pp. 83-99.
- Reynolds, R.C. 1963. Matrix corrections in trace element analysis by X-ray fluorescence. Estimation of mass absorption coefficient by compton scattering. *American Mineral.*, 48, pp. 1133-1143.
- Reynolds, R.C. 1967. Estimation of mass absorption coefficients by compton scattering. Improvements and extensions of the method. *American Mineral.*, 52, pp. 1493-1502.
- Robinson, B.W. 1974. The origin of mineralization at the Tui mine, Te Aroha, New Zealand, in the light of stable isotope studies. *Econ. Geol.*, v. 69, pp. 910-925.
- Roddick, J.A. 1967. The Tintina Trench. *J. of Geology*, v. 75, pp. 23-33.
- Rodgers, J.W., Burchfiel, B.C., Abbot, F.W., Anepohl, J.K., Ewing, A.H., Koehnken, P.J., Novitsky-Evans, J.M., and Talukdar, S.C. 1974. Paleozoic and Lower Mesozoic volcanism and continental growth in the western United States. *Geol. Soc. Am. Bull.*, 85, pp. 1913-1924.
- Roedder, E. 1984. Reviews in Mineralogy (Ribbe, P.H., ed), Volume 12, Fluid Inclusions. Mineral. Soc. Amer.
- Seward, T.M. 1973. Thio complexes of gold and the transport of gold in hydrothermal ore solutions. *Geochim. Cosmochim. Acta*, v. 37, pp. 379-399.
- Sherriff, B.L., Grundy, H.D., and Hartman, J.S. 1987. Analysis of fluid inclusions using nuclear magnetic resonance. *Geochim. Cosmochim. Acta.*, v. 51, pp. 2233-2235.
- Sillitoe, R.H. 1985. Ore-related breccias in volcanoplutonic arcs. *Econ. Geol.*, v. 80, pp. 1467-1514.
- , R.H., Graubeger, G.L. and Elliot, J.E. 1985. A diatreme-hosted gold deposit at Montana Tunnels, Montana. *Econ. Geol.*, v. 80, pp. 1707-1721.
- Smith, M.J. 1982. Petrology and geology of high level rhyolite intrusives of the Skukum area, 105D SW, Yukon Territory in Yukon Exploration and Geology 1981, Dept. Ind. Aff. Nor. Dev., Whitehorse, Yukon, pp. 62-73.
- Sourirajan, S., and Kennedy, G.C. 1962. The system H<sub>2</sub>O-NaCl at elevated temperatures and pressures. *Am. J. Sci.*, 260, pp. 115-141.

- Streckeisen, A. 1975. To each plutonic rock its proper name. *Earth-Science Reviews.*, 12, pp. 1-33.
- Streckeisen, A., and LeMaitre, R.W. 1979. A chemical approximation to the modal QAPF classification of the igneous rocks. *Neues Jahrbuch für Mineralogie Abhandlungen.*, 136, pp. 169-206.
- Souther, J.G. 1977. Volcanism and tectonic environments in the Canadian Cordillera - a second look; in W.R.A. Barager, L.C., Coleman and J.M. Hall (eds.), *Volcanic Regimes in Canada*, Geological Association of Canada, Special Paper No. 16, pp. 3-24.
- Taylor, H.P., Jr. 1974. The application of oxygen and hydrogen isotope studies to problems of hydrothermal alteration and ore deposition. *Econ. Geol.*, v. 69, pp. 843-883.
- 1979. Oxygen and hydrogen isotope relationships in hydrothermal mineral deposits; in Barnes, H.L. (ed.), *Geochemistry of Hydrothermal Ore Deposits*, Second Edition: John Wiley and Sons, New York, pp. 236-277.
- Tchalenko, J.S. 1968. The evolution of kink-bands and the development of compressive textures in sheared clays. *Tectonophysics*, v. 6, pp. 159-174.
- Templeman-Kluit, D.J. 1984. Geology of the Snag and Carmacks Map Sheets, Geological Survey of Canada, Open File 1101.
- 1979. Transported cataclastite, ophiolite and granodiorite in Yukon: Evidence of arc-continent collision. Geological Survey of Canada Paper 79-14, 27 p.
- 1976. The Yukon Crystalline Terrane: Enigma in the Canadian Cordillera. *Geological Society of America Bulletin*, v. 87, pp. 1343-1357.
- , and Wanless, R.K. 1975. Potassium-Argon age determinations of metamorphic and plutonic rocks in the Yukon Crystalline Terrane. *Canadian Journal of Earth Sciences*, v. 12, pp. 1895-1909.
- Truesdell, A.H. 1974. Oxygen isotope activities and concentrations in aqueous salt solutions at elevated temperatures--consequences for isotope geochemistry. *EPSL*, v. 23, pp. 387-396.

- , Nathenson, M., and Rye, R.O. 1977. The effects of subsurface boiling and dilution on the isotopic compositions of Yellowstone thermal waters. JGR, v.82, no. 26, pp. 3694-3704.
- , and Hulston, J.R. 1980. Isotopic evidence on environments of geothermal systems; in Fritz, P., and Fontes, J. (eds.), Handbook of Environmental Isotope Geochemistry: Elsevier Scientific Publishing Co., New York, pp. 179-226
- Turek, A., Riddle, C., and Smith, T.E. 1977. Determination of Rb and Sr by X-ray fluorescence in the measurement of radiometric ages. Canadian Jour. Spectroscopy, v. 22, No. 1, pp. 20-24.
- Ulrich, M.R., and Bodnar, J.R. 1984. Systematics of stretching of fluid inclusions in barite at 1 atm confining pressure [abs.]: Geological Society of Amer., Abstracts with Programs, v. 16, no. 6, p. 680.
- Wanless, R.K., Stevens, R.D., Lachance, G.R., and Delabio, R.N. 1970. Age determinations and geological studies, K-Ar isotopic ages. Report 9. Geological Survey of Canada Paper 69-2A, 78 pp.
- Warnaars, F.W., Holmgren, D.C., and Barassi, F.S. 1985. Porphyry copper and tourmaline breccias at Los Bronces-Rio Blanco, Chile. Econ. Geol., v. 80, pp. 1544-1565.
- Weissberg, B.G. 1969. Gold-silver ore-grade precipitates from New Zealand thermal waters. Econ. Geol., v. 64, pp. 95-108.
- Weissberg, B.G., Browne, P.R.C., and Seward, T.M. 1979. Ore metals in active geothermal systems, in Barnes, H.L. (ed.), Geochemistry of Hydrothermal Ore Deposits, Second Edition. John Wiley and Sons, New York, pp. 739-780.
- White, D.E. 1955. Thermal springs and epithermal ore deposits; in Bateman, A.M. (ed.), Economic Geology, 50th anniversary volume, pp. 99-154.
- , Barnes, I., and O'Neil, J.R., 1973. Thermal and mineral waters of nonmeteoric origin, California coast ranges. GSA Bull., v. 84, pp. 547-560.
- Wilson, G.H., Smith, J.G., and Shew, N. 1985. Review of radiometric data from the Yukon Crystalline Terrane, Alaska and Yukon Territory. Canadian Journal of Earth Sciences, v. 22, pp. 525-537.

- Woods, T.L., Bethke, P.M., Bodnar, R.J., and Werre, R.W., Jr. 1981. Supplementary components and operation of the U.S. Geological Survey gas-flow heating/freezing stage. U.S. Geol. Survey Open File Rept. 81-954, 12p.
- Yonge, C.J. 1982. Stable isotope studies of water extracted from speleothems. Unpublished Ph.D. Thesis, McMaster University, 298 p.
- York, D. 1969. Least squares fitting of a straight line with correlated errors. Earth Planet. Sci. Lett., v. 5, pp. 320-324.

APPENDIX A. GEOCHEMICAL DATA

GEOCHEMICAL ANALYSES OF FREEGOLD SAMPLES

\*\*\*\*\* RHYOLITES \*\*\*\*\*

SAMPLE #	RHYOLITES							TR16N-0	TR22N
	TR24-235W	ANT86-12-333F85-33A	F85-33B	F86-57	TR18-60E	F86-29	*1151869005	*1151869006	
SiO2	80.8	80.6	81	79.8	81.8	77.7	79.5	76.2	80.1
TiO2	0.1	0.1	0.07	0.08	0.08	0.04	0.11	0.07	0.13
Al2O3	11.6	11.5	12	11.9	11.9	11.6	11.9	12.8	12.6
FeZ naa	0.43	0.47	0.34	0.43	0.27	0.63			
Fe2O3T	0.68	0.95	0.51	0.66	0.39	1.03	1.13	1.15	0.33
MnO	0.01	0.01	0.01	0.01	0.01	0.01	0.01	0.02	0.01
MgO	0.24	0.18	0.08	0.11	0.18	0.3	0.22	0.25	0.14
CaO	0.09	0.09	0.08	0.08	0.06	0.07	0.14	0.05	0.05
NaZ naa	BLD (.05)	BLD (.05)	0.05	0.05	BLD (.05)	0.06			
Na2O	0.11	0.12	0.11	0.12	0.11	0.14	1.95	0.05	0.05
K2O	3.71	3.23	3.63	4.29	3.46	5.74	4	6.2	3.58
P2O5	0.02	0.03	0.03	0.02	0.01	0.02	0.04	0.02	0.02
H2OT	2	1.8	3.1	2.4	2	2	1.3	1.3	1.5
CO2T	0.1	0.1	0.1	0.1	0	0.1	0.1	0.1	0.1
S	0.04	0.53	0	0.01	0.04	0.03	0.56	0.3	0.01
C(org)								0.4	0.3
Ag	0	0	0	2	0	0	0	BLD (1)	BLD (1)
Au ppb naa	400	930	12	31	940	53	-	392	1685
As naa	790	330	61	38	250	56	-	-	-
Ba	480	620	100	550	770	6800	2100	-	-
Be	1.9	1.8	1.2	1.4	2	1.2	1.3	-	-
Co	-	-	-	-	-	-	-	BLD (1)	BLD (1)
Co	71	86	39	42	39	28	5	BLD (5)	BLD (5)
Cr	4	5	3	4	3	3	5	30	30
Cu	8	14	9	8	8	15	12	134	4
Hf naa	2	2	BLD (1)	3	3	2	-	-	-
La	21	21	14	18	18	16	23	-	-
Ni	3	3	4	0	0	0	0	8	10
Pb	0	20	19	59	72	23	69	40	20
Rb naa	150	130	180	190	180	200	-	220	160
Sr	30	5	61	44	5	57	130	60	10
Sb naa	19	11	37	50	6.6	45	-	-	-
Sc naa	1.9	1.8	2.8	2.7	2.8	1.8	-	-	-
Se naa	BLD (5)	BLD (5)	BLD (5)	BLD (5)	BLD (5)	BLD (5)	-	-	-
Th naa	18	29	27	29	9.7	5.9	-	-	-
U naa	2.2	8.8	4.9	5.4	1.9	3.2	-	-	-
V	6	3	2	1	0	1	9	-	-
W naa	BLD (4)	BLD (4)	130	81	16	47	-	-	-
Yb	0.8	1.2	1.9	1.6	1.1	0.8	0.5	-	-
Zn	15	16	23	96	9	31	94	88	10
Zr	83	82	71	80	68	61	68	20	70
La naa	20	19	14	18	19	15			
Ce naa	42	30	27	29	33	22			
Sm naa	1.8	1.9	2.4	2.3	2.6	1.4			
Eu naa	0.4	0.2	0.4	0.5	0.4	0.3			
Gd naa	1.9	2.1	3	2.9	3.1	1.5			
Yb naa	1.1	1.2	2.2	1.7	1.6	0.9			
Lu naa	0.12	0.28	0.37	0.3	0.2	0.13			

SAMPLE #	***** ANDESITES *****			
	F86-54	F85-1	F86-40	F86-41
SiO2	67.5	66.1	51.1	61.2
TiO2	0.39	0.4	0.89	0.65
AL2O3	13.5	15.5	14.4	17.1
FEZ naa	1.91	2.49	5	3.51
FE2O3T	3.22	3.76	8.17	6.36
MNO	0.08	0.09	0.15	0.09
MGO	1.05	1.53	8.34	2.69
CAO	3.23	2.81	7.97	5.25
NAZ naa	0.98	2.9	1.5	2.7
NA2O	1.49	4.33	2.31	3.83
K2O	4.26	2.84	2.46	2.35
P2O5	0.21	0.2	0.38	0.21
H2OT	3.1	1.8	3.3	1
CO2T	2.2	0.2	0.7	0.1
S	0.02	0.01	0.01	0.15
AG	1	0	0	3
AU ppb naa	BLD (5)	BLD (8)	BLD (9)	BLD (8)
AS naa	7	6	5	2
BA	1100	2100	1000	1200
BE	2.5	1.5	2.6	1.7
CO	17	26	41	20
CR	16	15	380	16
CU	14	20	57	19
HF naa	4	BLD (1)	4	2
LA	37	28	37	30
NI	4	0	160	13
PB	23	19	15	200
RB naa	220	130	BLD (60)	90
SR	290	460	740	770
SB naa	4.8	3.1	1.3	0.9
SC naa	5.1	6.2	22.5	11.4
SE naa	7	15	BLD (9)	BLD (9)
TH naa	13	11	25	13
U naa	7.5	5.3	9.3	5.2
V	48	54	160	120
W naa	9	22	4	BLD (4)
YB	0.9	1.5	1.7	1.8
ZN	67	53	69	61
ZR	170	180	200	180
LA naa	37	27	37	29
CE naa	46	29	69	35
SM naa	2.9	1.7	4	2.1
EU naa	1	BLD (1)	1.8	1.5
GD naa	3.6	2.9	5	3.3
YB naa	0.9	1	1.6	1.3
LU naa	0.13	0.27	0.27	0.28

SAMPLE #	***** GRANDIORITES *****					
	F86-16	F86-16d	F86-18	TR18-660E	TR18-660Ed	F85-18
SI02	67.2	66	67	65.2	65.4	61.9
TI02	0.44	0.41	0.44	0.41	0.41	0.05
AL203	15.6	15.7	15.4	14.7	16.1	2.11
FEZ naa	2.42		2.45	2.22		
FE203T	4.02	4.02	3.9	3.79	3.75	1.4
MNO	0.09	0.09	0.09	0.09	0.09	0.02
MGO	1.92	1.78	1.91	1.59	1.58	0.1
CAO	3.47	3.57	3.65	3.01	2.99	1
NAZ naa	2.5		2.5	2.4		
NA20	3.76	3.76	3.81	3.75	3.6	0.05
K2O	3.16	3.3	3.02	3.62	3.66	0.45
P2O5	0.15	0.14	0.14	0.17	0.17	0.07
H2OT	1.1	0.8	0.9	1.8	1.8	
CO2T	0.2	0.1	0.1	0.7	0.7	0.4
S	0	0.01	0	0.01	0.01	6.77
C(org)						
AG	0	0	0	2	3	9
AU ppb naa	BLD (8)		BLD (9)	BLD (5)		
AS naa	3		3	2		
BA	1400	1400	1300	2300	2300	650
BE	1.6	1.5	1.6	1.6	1.6	0.7
CO	35	11	45	42	42	8
CR	20	18	20	18	16	84
CU	11	9	12	19	20	100
HF naa	BLD (1)		BLD (1)	2		
LA	29	23	26	22	23	9
NI	3	2	7	0	0	110
PB	15	12	16	17	19	62
RB naa	90		140	120		
SR	580	580	590	420	430	110
SB naa	0.3		0.5	1.8		
SC naa	7.3		7.6	6.4		
SE naa	BLD (9)		11	BLD (5)		
TH naa	15		15	11		
U naa	4.8		5.1	4.3		
V	67	66	68	67	67	56
W naa	79		200	BLD (4)		
YB	1.4	1.3	1.3	1.4	1.4	0.7
ZN	47	47	45	170	45	400
ZR	140	140	130	170	150	21
LA naa	31		25	19		
CE naa	BLD (3)		36	20		
SM naa	BLD (.1)		1.7	1.7		
EU naa	BLD (1)		1.5	1		
GD naa	2.4		2.8	3.4		
YB naa	1		1.2	0.9		
LU naa	0.25		0.12	0.16		

SAMPLE #	***** SYENITES *****				
	HBITE	F86-59	F85-200	F85-100	F86-62 (naa)
SIQ2	39.6	52.2	60.3	61	
TIQ2	1.81	1.18	0.61	0.6	
AL203	9.49	10.6	14.3	14.8	
FEZ naa	14	7.83	4.75	3.35	9.2
FE203T	22.5	13.5	7.34	6.75	
MNO	0.24	0.42	0.14	0.14	
NGO	9.27	6.75	2.64	2.52	
CAO	10.5	8.07	4.22	4.18	5
NAZ naa	1	1.6	2.4	2.8	1.6
NA2O	1.52	2.32	3.4	3.58	
K2O	1.12	2.06	4.29	4.29	
P2O5	0.38	0.52	0.38	0.42	
H2OT	2.1	1.9	1.3	1.1	
CO2T	0.9	0.9	0.1	0.2	
S	0.02	0.12	0.02	0.01	
C(org)					
AG	0	0	0	0	BLD (5)
AU ppb naa	BLD (11)	BLD (11)	42	BLD (9)	BLD (11)
AS naa	3	21	11	3	4
BA	1100	380	1800	2000	700
BE	1.3	3.8	2.5	0.24	
CO	60	36	76	14	43
CR	6	26	22	21	40
CU	19	47	16	15	
HF naa	BLD (1)	BLD (1)	BLD (1)	2	9
LA	8	36	29	31	
NI	23	23	0	0	
PB	6	13	14	6	
RB naa	BLD (50)	150	80	BLD (70)	
SR	360	240	910	1000	
SB naa	1.9	7.4	6.5	0.6	1.9
SC naa	56.8	42.5	16.4	12.2	35.3
SE naa	16	17	BLD (11)	BLD (9)	15
TH naa	0.9	5.9	6.7	3.9	5.8
U naa	BLD (1.5)	2	BLD (1.6)	BLD (1.3)	3.2
V	670	250	150	130	
W naa	40	120	210	BLD (4)	100
YB	0.4	3.6	1.8	2	
ZN	170	770	75	67	
ZR	83	210	140	190	
LA naa	10	40	31	27	58
CE naa	28	68	71	37	108
SH naa	2.5	6.5	3.7	2.7	8.9
EU naa	2	2.6	BLD (.2)	1.9	2.8
GD naa	4.5	10.2	5.8	5.3	12.5
YB naa	1	3.6	1.9	1.4	4.1
LU naa	0.12	0.46	0.19	0.19	0.41

APPENDIX B. STRUCTURAL DATA

## APPENDIX B. STRUCTURAL DATA

## FRACTURE PLANE ORIENTATIONS

LOCATION	STRIKE	DIP	:	LOCATION	STRIKE	DIP	:	LOCATION	STRIKE	DIP
ANTONIUK	166	E82	:	ANTONIUK	25	W80	:	LAFORMA	145	E80
ANTONIUK	175	E80	:	ANTONIUK	160	E70	:	LAFORMA	158	E72
ANTONIUK	10	E67	:	ANTONIUK	160	E77	:	LAFORMA	158	W70
ANTONIUK	75	N72	:	ANTONIUK	175	E78	:	LAFORMA	150	W80
ANTONIUK	80	N30	:	ANTONIUK	125	S70	:	LAFORMA	151	W42
ANTONIUK	160	E55	:	ANTONIUK	15	E80	:	LAFORMA	135	E65
ANTONIUK	95		90 :	ANTONIUK	45	N82	:	LAFORMA	42	S77
ANTONIUK	165	E75	:	ANTONIUK	150	E80	:	LAFORMA	23	E60
ANTONIUK	165	E70	:	ANTONIUK	170	E70	:	LAFORMA	159	E76
ANTONIUK	165	E70	:	ANTONIUK	165	E77	:	LAFORMA	112	N65
ANTONIUK	168	E71	:	NABOB GULCH	120		90 :	LAFORMA	105	S80
ANTONIUK	175	E79	:	FAIRCLOUGH	150	E70	:	LAFORMA	157	E68
ANTONIUK	175	E80	:	FAIRCLOUGH	145	W70	:	LAFORMA	118	S87
ANTONIUK	172	E46	:	FORREST GUL	145		90 :	LAFORMA	29	W65
ANTONIUK	180	E59	:	GRIZZLY GUL	115	E40	:	LAFORMA	48	W53
ANTONIUK	15	E63	:	GRIZZLY GUL	115	E64	:	LAFORMA	45	N75
ANTONIUK	175		90 :	GRIZZLY GUL	12	W66	:	LAFORMA	118	S76
ANTONIUK	155	E64	:	GRIZZLY GUL	50		90 :	LAFORMA	21	W74
ANTONIUK	165	E58	:	MCLEOD GULC	0	W76	:	LAFORMA	65	N66
ANTONIUK	175		90 :	FAIRCLOUGH	52	N50	:	LAFORMA	0	W57
ANTONIUK	58	E47	:	63 VEIN	25	W75	:	LAFORMA	5	E60
FREEGOLD RD	175	W45	:	PAL FAULT	150	E75	:	LAFORMA	20	90
FREEGOLD RD	10	E59	:	LAFORMA	43		90 :	LAFORMA	11	E72
FREEGOLD RD	10	E78	:	LAFORMA	34	W75	:	LAFORMA	80	90
FREEGOLD RD	0	E87	:	LAFORMA	126	N70	:	LAFORMA	133	S35
ANTONIUK	175	E82	:	LAFORMA	166		90 :	LAFORMA	20	90
ANTONIUK	25	W70	:	LAFORMA	122	S85	:	LAFORMA	33	E85
ANTONIUK	125	N68	:	LAFORMA	28	W85	:	LAFORMA	58	W24
ANTONIUK	30		90 :	LAFORMA	149	W42	:	LAFORMA	51	W81
ANTONIUK	160	W84	:	LAFORMA	151	W80	:	LAFORMA	42	W75
ANTONIUK	50	W77	:	LAFORMA	28	W80	:	LAFORMA	10	W66
ANTONIUK	90	N62	:	LAFORMA	28	W70	:	LAFORMA	32	W56
ANTONIUK	35	W70	:	LAFORMA	170	E85	:	LAFORMA	156	W26
ANTONIUK	60	W84	:	LAFORMA	146	E60	:	LAFORMA	7	W56
ANTONIUK	125	N81	:	LAFORMA	15	W75	:	LAFORMA	166	E80
ANTONIUK	40	S12	:	LAFORMA	15	W68	:	LAFORMA	12	90
ANTONIUK	28	E24	:	LAFORMA	156	W60	:	LAFORMA	35	90
ANTONIUK	12	W75	:	LAFORMA	150	W42	:	LAFORMA	15	90
ANTONIUK	15	W87	:	LAFORMA	164	E72	:	LAFORMA	85	W73
ANTONIUK	155	E15	:	LAFORMA	164	W70	:	LAFORMA	153	W46
ANTONIUK	25	E74	:	LAFORMA	171	E85	:	LAFORMA	126	NN45
NABOB GULCH	175	E65	:	LAFORMA	18	W75	:	LAFORMA	165	E61
LAFORMA RD	75	S72	:	LAFORMA	43	W65	:	LAFORMA	14	90
LAFORMA	10	W63	:	LAFORMA	8	W79	:	LAFORMA	84	90
LAFORMA	20	W78	:	LAFORMA	106	S77	:	LAFORMA	25	W76
LAFORMA	170	W78	:	LAFORMA	25	W82	:	LAFORMA	15	W80
LAFORMA	161	E70	:	LAFORMA	28		90 :			

## APPENDIX B. DYKE ORIENTATIONS

LOCATION	TYPE	AZIMUTH	DIP	WIDTH(m)
ANTONIUK	QFP	130	90	3
ANTONIUK	QFP	10	90	3
ANTONIUK	QFP	175	90	3
ANTONIUK	QFP	45	90	2.5
ANTONIUK	QFP	55	90	5
GRIZZLY GUL	QFP	135 N51		13
GRIZZLY GUL	ANDESITE	78 E45		0.8
GRIZZLY GUL	QFP	95	90	
GRIZZLY GUL	QFP	160	90	5
ANTONIUK	AND	135	90	6.5
FREEAU ROAD	QFP	10 E59		2.5
FORREST CK	AND	150 E40		1.5
FOSTER CK	QFP	10 E78		2.5
ANTONIUK	QZ MONZ	145 E73		35
ANTONIUK	QFP	55	90	13
ANTONIUK	QFP	80	90	3
ANTONIUK	QFP	43 N60		6
ANTONIUK	QFP	122 N60		4.5
ANTONIUK	QFP	45 E60		
ANTONIUK	QFP	50	90	3.5
ANTONIUK	QFP	105	90	10
ANTONIUK	ANDESITE	105 N50		3
ANTONIUK	ANDESITE	75 N45		5
ANTONIUK	QFP	80 N60		9
ANTONIUK	QFP	15	90	18
ANTONIUK	QFP	90	75	16
E OF NABOB	QFP	15	90	UNKNOWN
E OF NABOB	ANDESITE	92	90	UNKNOWN
SW NABOB	QFP	20	90	UNKNOWN
ANTONIUK	QFP	142	90	3
ANTONIUK	HB AND	0	90	UNKNOWN
ANTONIUK	QFP	10	90	3
BASELINE	QFP	78	90	UNKNOWN
N OF BASEL	QFP	46	UNKNOWN	UNKNOWN
NE ANTONIUK	QFP	152	UNKNOWN	UNKNOWN
E OF GRIZZL	ANDESITE	48	UNKNOWN	UNKNOWN
MCLEOD GUL	QFP	116	UNKNOWN	UNKNOWN
E OF NABOB	QFP	28	UNKNOWN	UNKNOWN
NEAR BASEL	QFP	50	UNKNOWN	UNKNOWN
E OF NABOB	QFP	19	UNKNOWN	UNKNOWN
E OF NABOB	QFP	94	UNKNOWN	UNKNOWN
NABOB	QFP	120	UNKNOWN	UNKNOWN
RAMBLER	QFP	110	UNKNOWN	UNKNOWN
NW LAFORMA	QFP	153	UNKNOWN	UNKNOWN
NW LAFORMA	QFP	165	UNKNOWN	UNKNOWN
NE ANTONIUK	QFP	65	UNKNOWN	UNKNOWN
EAST GRIZZL	QFP	110	UNKNOWN	UNKNOWN

APPENDIX C. FLUID INCLUSION DATA

## FLUID INCLUSION ANALYSIS - FREEGOLD SAMPLES

TU10-271

SAMPLE ID	TYPE	Tm	Th	Hom.Phase	WT. % NaC	TmCO2	ThCO2	CLATHRATE	TmCLATH	COMMENTS
1	S	-2.3	148.4	V-L	3.832244					MS
2	P	-0.9	170	V-L	1.558675					MS
3	P	-2.6	180	V-L	4.323668					MS
4	P	***			ERR	-57.3	28.4	NO		CO2 V->L
5	P	-1.8	173	V-L	3.050997					MS
6	P	-2.9	206	V-L	4.788204					MS
7	P	-2.2	165	V-L	3.693557					MS
8	S	-2.4	166	V-L	4.010156					MS
9	S	-2.1	145	V-L	3.534092					MS
10	S	-2	144	V-L	3.373846					MS
11	P	-3.1	250	V-L	5.094110					MS
12	P	-2	150	V-L	3.373846					MS
13	P	-2.1	167	V-L	3.534092					MS
14	S	-0.5			0.874259					MS
15	S	-0.1			0.176534					MS
16	P	***	168	V-L	ERR					MS
17	P	-1.9	151	V-L	3.212815					MS
18	S	-1.1	173	V-L	1.895955					MS
19	P	-2.5	185	V-L	4.167296					MS
20	S	-1.1			1.895955					MS
21	P	***	166	V-L	ERR					MS
22	P	-0.9			1.558675					MS
23	P	-3.1	164	V-L	5.094110					MS
24	P	-3.1	158	V-L	5.094110					MS
25	P	-2.8	175	V-L	4.634119					MS
26	P	-3.2	164	V-L	5.245938					MS
27	S	-1.5			2.560787					MS
28	P	-3.1	181.6	V-L	5.094110					MS
29	P	***			ERR	-56.9	***			LS
30	P	***	163	V-L	ERR					MS
31	P	***	160	V-L	ERR					LS
32	P	-1.1	158	V-L	1.895955					MS
33	P	***	162	V-L	ERR					MS
34	P	-2.9	174	V-L	4.788204					MS
35	P	-2.1	158	V-L	3.534092					MS
36	P	-2.7	178	V-L	4.479274					MS
37	P	-2.9	164	V-L	4.788204					MS
38	P	***			ERR	-57.5	29.5			MS BUBB EXPANDS TO ONE PHAS
39	P	-3.5	166	V-L	5.696954					MS
40	P	***			ERR	-57.4	***			MS
41	P	***			ERR	-57.3	***			MS
42	P	***			ERR	-57.6	***			MS
43	P	***	174	V-L	ERR					MS
44	P	-2.7	261	V-L	4.479274					MS
45	P	-3.2	172	V-L	5.245938					MS
46	P	-3.2	178	V-L	5.245938					MS
47	P	-3.2	151	V-L	5.245938					MS
48	S	***	178	V-L	ERR					MS
49	P	-3.3	148	V-L	5.397019					MS
50	P	-3.1	147	V-L	5.094110					MS
51	P	-2.6	174	V-L	4.323668					MS
52	S	-1.5	147	V-L	2.560787					MS
53	P	***			ERR	-57.2				MS
54	P	-2.2	151	V-L	3.693557					MS
55	P	-3.2	176	V-L	5.245938					MS
56	P	-3.4	177	V-L	5.547356					MS
57	P	-2.7	254	V-L	4.479274					MS
58	P	-2.6	243	V-L	4.323668					MS
59	P	***	193	V-L	ERR					MS
60	P	***	162	V-L	ERR					MS
61	P	***	162	V-L	ERR					MS
62	P	***	167	V-L	ERR					MS
63	P	***	178	V-L	ERR					MS
64	P	***	183	V-L	ERR					MS
65	P	***	202	V-L	ERR					MS
66	P	***	180	V-L	ERR					LS
67	P	***	177	V-L	ERR					MS
68	P				0	-57				MS NO TH AT +160

## FLUID INCLUSION ANALYSIS - FREEGOLD SAMPLES

TU06-248

SAMPLE ID	TYPE	Tm	Th	Hom.Phase	WT. % NaCl	TmCO2	ThCO2	CLATHRATE	Tdiss	COMMENTS
1	S	-1.1	156		1.895955					MS
2	P	-2.4	242		4.010156					MS
3	P	-2.1	135		3.534092					
4	P	-2.8	150		4.634119					MS
5	P	-2.6	141		4.323668					MS
6	P	-2.5	161		4.167296					MS
7	P	***			ERR	-57.2				CRIT BEHAVIOUR NOT DISCERNI
8	P	-2.7	176		4.479274					MS
9	P	***	161		ERR					MS
10	P	****			ERR	-57.3	30.2	NO		L-->V
11	P	-2.6	240		4.323668					MS
12	P	***	224		ERR					MS
13	P	***	224		ERR					MS
14	P	***	245		ERR					MS
15	P	***	244		ERR					MS
16	P	-25.4	248		26.25163					MS
17	P	-2.2	191		3.693557					MS
18	P	-2.2	183		3.693557					MS
19	P	***	179		34				272	MS
20	P	***	185		ERR					MS
21	P	***	181		35				281	MS
22	P	***	148		ERR					MS
23	P	***	181		34				272	MS
24	P	***	182		ERR					MS
25	P	***	167		ERR					MS
26	P	***	137		ERR					MS
27	P	***	198		ERR					MS
28	P	-3	184		4.941534					
29	P	-2.5	222		4.167296					
30	P	-2.8	222		4.634119					
31	P	***	177		ERR					
32	P	-3	224		4.941534					
33	P	***	175		ERR					
34	P	***	179		ERR					
35	P	***	164		ERR					
36	P	***	207		ERR					
37	P	-2.3	172		3.852244					
38	P	-0.7	182		1.218118					
39	P	-3.1	179		5.094110					
40	P	-2.2	174		3.693557					
41	P	-2.1	158		3.534092					
42	P	-1	189		1.727723					
43	P	-3	171		4.941534					
44	P	-2.4	234		4.010156					
45	P	-2.5	225		4.167296					
46	P	-2.7	145		4.479274					
47	P	***	***		ERR	-57.3	30.9			
48	P	***	188		ERR					
49	P	***	164		ERR					
50	P	***	175		ERR					



M. FROM							
L4AA-50	P	349	V-L				INC # 10, 5
0-55 FR							
L4AA-51	P	264.3	V-L				
L4AA-52	P	391.4	L-V				
L4AA-53	P	335	V-L				
L4AA-54	P	390	V-L				NINE MICROM
. FROM							
L4AA-55	P	~400?	L-V				Th OBSCURRE
D BY IN							
L4AA-56	P	305	L-V	-57.1			
L4AA-57	P			-57.0			
L4AA-58	P			-57.0			
L4AA-59	P	166	V-L-H		1	CUBIC	294
L4AA-60	P	204	V-L-H		1	CUBIC	290
L4AA-61	P	207	V-L-H		1	CUBIC	288
L4AA-61B	P	210	V-L-H		1	CUBIC	296
L4AA-62	P	232	V-L				
L4AA-63	P	192	V-D1-L-D2		2	D1=CU	178 D2=? Tdiss=
310							
L4AA-64	P	319	V-L-H		1	CU	? INC LEAKED
@ 345							
L4AA-65	P	315	L-V				
L4AA-66	S	169	V-L		1	D	? INC LEAKED
L4AA-67	P	261	V-L				
L4AA-68	P	285	V-L				
L4AA-69	S?P?	325	V-L				
L4AA-70	P	272	V-L				
L4AA-70B	P	305	V-L		1	HI RE, BI	>425
L4AA-71	P	~320	D-V-L		1		118.5IMPOSS OBSE
RV HOMO							
L4AA-72	P	289	V-L				
L4AA-73	P	247	V-L				
L4AA-74	PS	195	V-L				
L4AA-75	P	170	V-L				
L4AA-76	P	238	V-L-D		1	HALITE	>338
L4AA-77	P	234	V-L				
L4AA-78	P	232	V-L				
L4AA-79	P	337	L-V				
L4AA-80	P	241	V-L-D		1	HALITE	287
L4AA-81	P	204	V-L-D2-D1		2	HA+?	HA=365, ?=315?
L4AA-82	P	275.2	V-L				
L4AA-83	P	211.4	V-L-D1=D2		2	HA+HA?	BOTH=228
L4AA-84	P	216	V-L-D1=D2		2	HA+HA?	BOTH=290
L4AA-85	P	201	V-L-D?		1	HALITE	?
L4AA-86	P	214	V-L				
L4AA-87	P	206	V-L				
L4AA-88	P	266	V-L				
L4AA-89	P	285	L-V				
L4AA-90	P	197	V-L				
L4AA-91	P	261	V-L				
L4AA-92	P	314	V-L				
L4AA-93	P	197.3	V-L				
L4AA-94	P	200	V-L				
L4AA-95	P	278.3	V-L				
L4AA-96	P	273.3	V-L				
L4AA-97	P	226	V-L				

ANT86-1-91.4A  
SAMPLE IDTYPE

	Tm	Th	V-L	Hom.Phase	WT. % NaCl	TmCO2	ThCO2	CLATHRATE	Tdiss	COMMENTS
1 P	-3.6	323	V-L		5.845815					EUHEDRAL QZ
2 P	-2.2	285	V-L		3.693557					EUHEDRAL QZ
3 S	-8.2	161	V-L		11.95165					EUHEDRAL QZ
4 P	-2.9	154	V-L		4.788204					EUHEDRAL QZ
5 P	-1.7	164	V-L		2.888389					EUHEDRAL QZ
6 S	-2.6	217	V-L		4.323668					EUHEDRAL QZ
7 P	-2.7	142	V-L		4.479274					EUHEDRAL QZ
8 P	-2.9	292	V-L		4.788204					EUHEDRAL QZ
9 S	-3.6	237	V-L		5.845815					EUHEDRAL QZ
10 P	-3	313	V-L		4.941534					EUHEDRAL QZ
11 P	-2.7	297	V-L		4.479274					EUHEDRAL QZ
12 P	-2.7	313	V-L		4.479274					EUHEDRAL QZ
13 P	***	295	V-L		ERR					EUHEDRAL QZ
14 P	***	277	V-L		ERR					EUHEDRAL QZ
15 P	***	281	V-L		ERR					EUHEDRAL QZ
16 P	***	286	V-L		ERR					EUHEDRAL QZ
17 P	-4.1	***	***		6.579178					EUHEDRAL QZ
18 S	-1.6	293	V-L		2.724986					EUHEDRAL QZ
19 P	-1.2	232	V-L		2.063375					EUHEDRAL QZ
20 P	-1.9	304	V-L		3.212815					EUHEDRAL QZ
21 P	-1.4	235	V-L		2.395787					EUHEDRAL QZ
22 P	-2	321	V-L		3.373846					EUHEDRAL QZ
23 S	***	167	V-L-H		33				230	EUHEDRAL QZ
24 S	***	179	V-L-H-D2		30				179	EUHEDRAL QZ
25 S	***	151	V-L-H		31				204	EUHEDRAL QZ
26 P	***	316	V-L		ERR					EUHEDRAL QZ
27 S	***	150	V-L-H		32				216	EUHEDRAL QZ
28 S	***	209	V-L-H		31				203	EUHEDRAL QZ
29 S	***	165	V-L		ERR					EUHEDRAL QZ
30 P	-2.1	274	V-L		3.534092					SUBHEDRAL
31 P	-1.5	337	V-L		2.560787					SUBHEDRAL
32 P	-1.7	299	V-L		2.888389					SUBHEDRAL
33 S	-40.5	256	V-L-H		37.20812	SAL BY	Tdiss=29%		157	SUBHEDRAL
34 S	-51	184	V-L-H?		50.01834					SUBHEDRAL
35 P	-7	308	V-L		10.49127					SUBHEDRAL
36 P	-7.2	328	V-L		10.74078					SUBHEDRAL
37 P	-40.5	222	V-L-H?		37.20812					SUBHEDRAL
38 S	***	176	V-L-H		32				213	SUBHEDRAL
39 S	***	194	V-L-H		32.5				222	SUBHEDRAL
40 S	***	261	V-L		ERR					SUBHEDRAL
41 P	-2.5	307	V-L		4.167296					EUHEDRAL
42 P	-1.4	170	V-L		2.395787					EUHEDRAL
43 P	-1.8	168	V-L		3.050997					EUHEDRAL
44 P	***	***	***		ERR	-57.2	CAN'T			EUHEDRAL
45 P	***	***	***		ERR	-57.2	DETECT			EUHEDRAL
46 P	-2.8	302	V-L		4.634119					EUHEDRAL
47 P	***	***	***		ERR	-57.4		18		EUHEDRAL
48 P	-2.9	295	V-L		4.788204					EUHEDRAL
49 P	-2.6	299	V-L		4.323668					EUHEDRAL
50 P	***	295	V-L		ERR					EUHEDRAL
51					0					
52					0					
53					0					

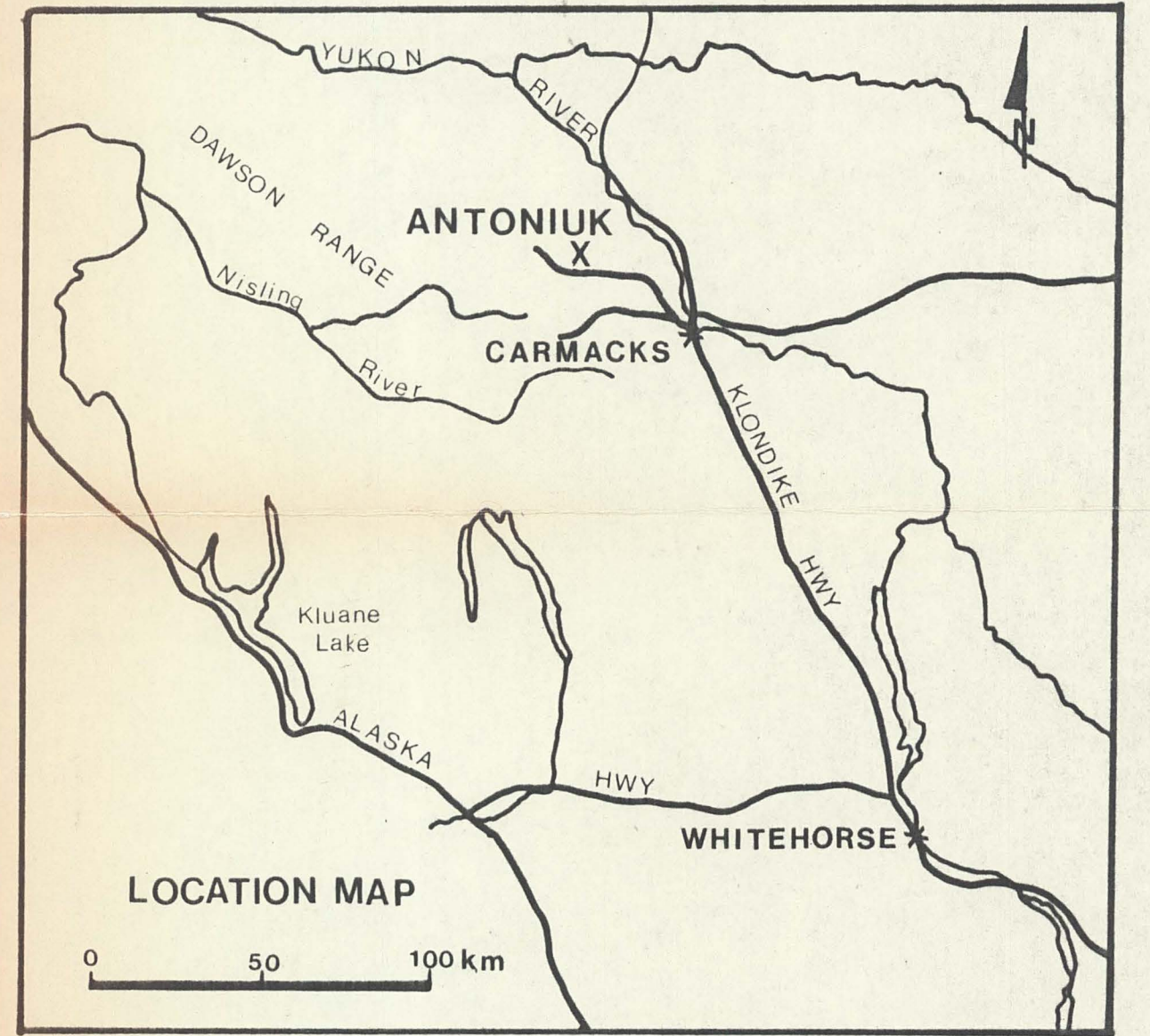
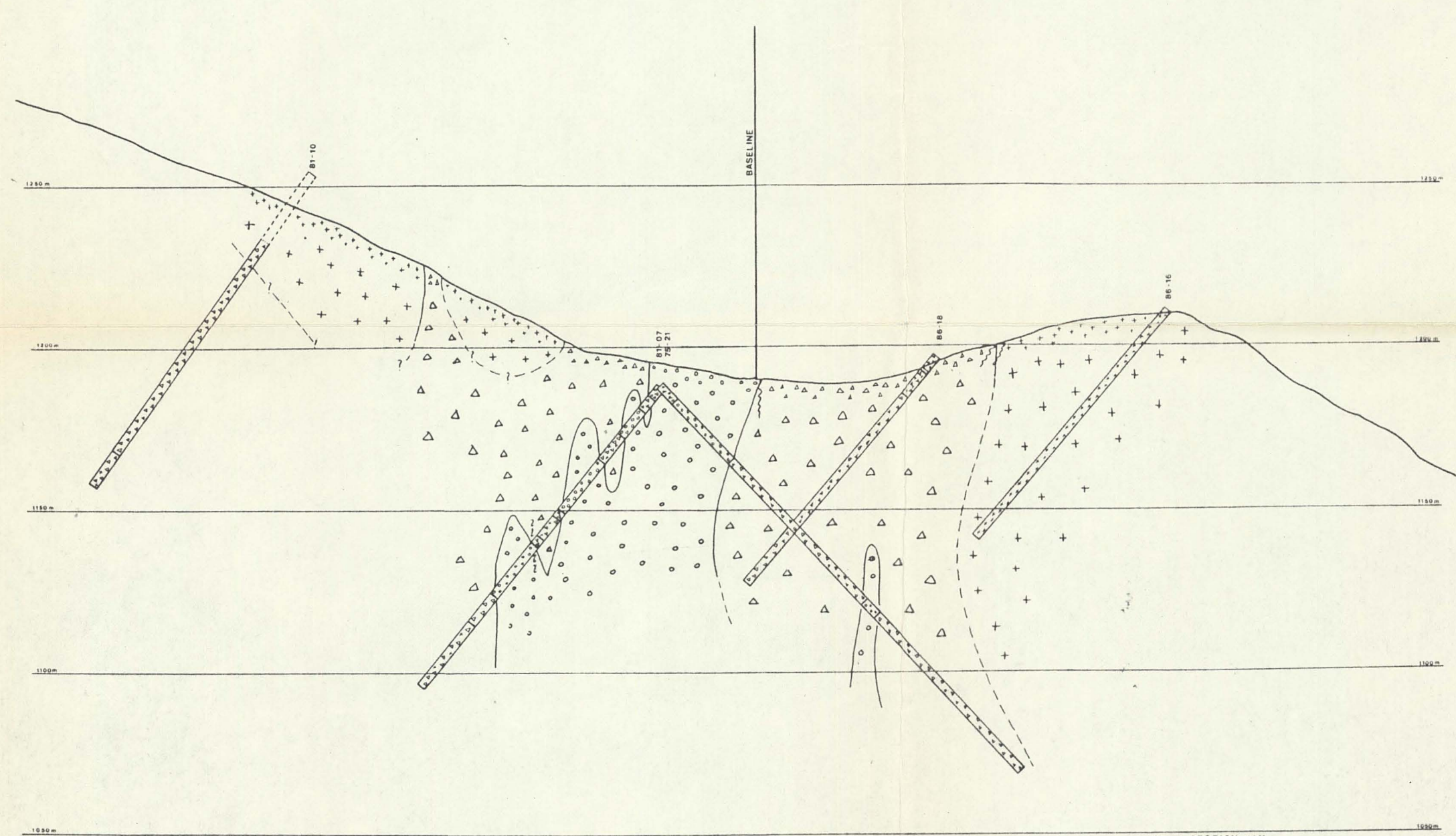
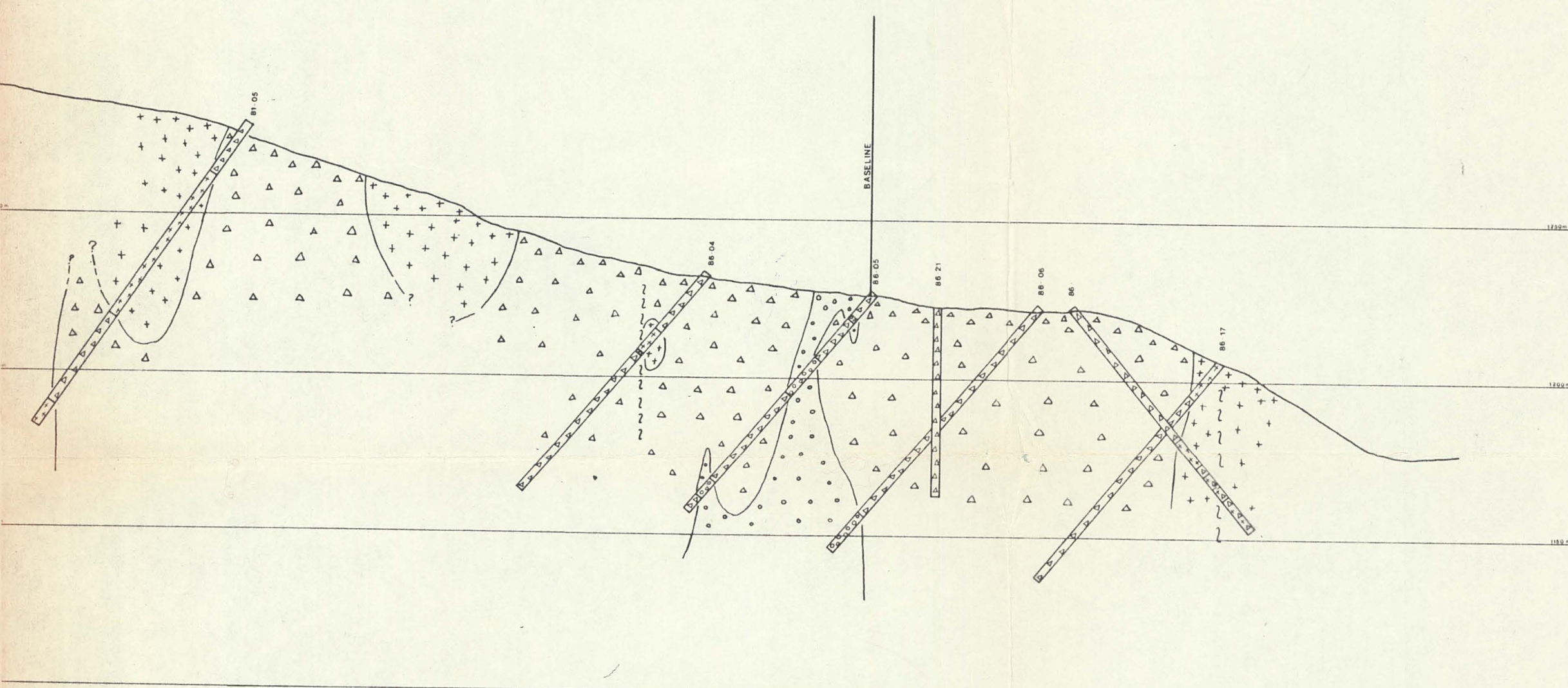
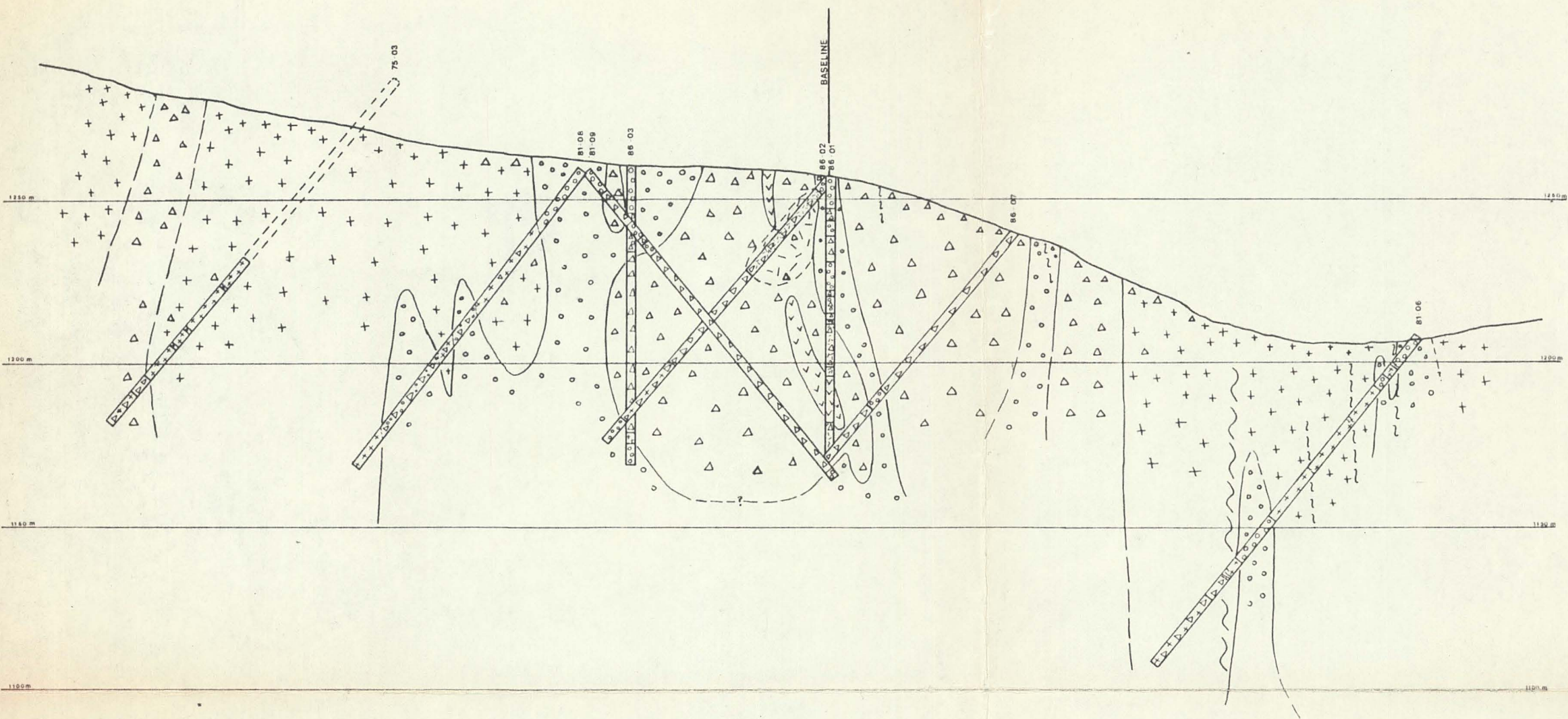
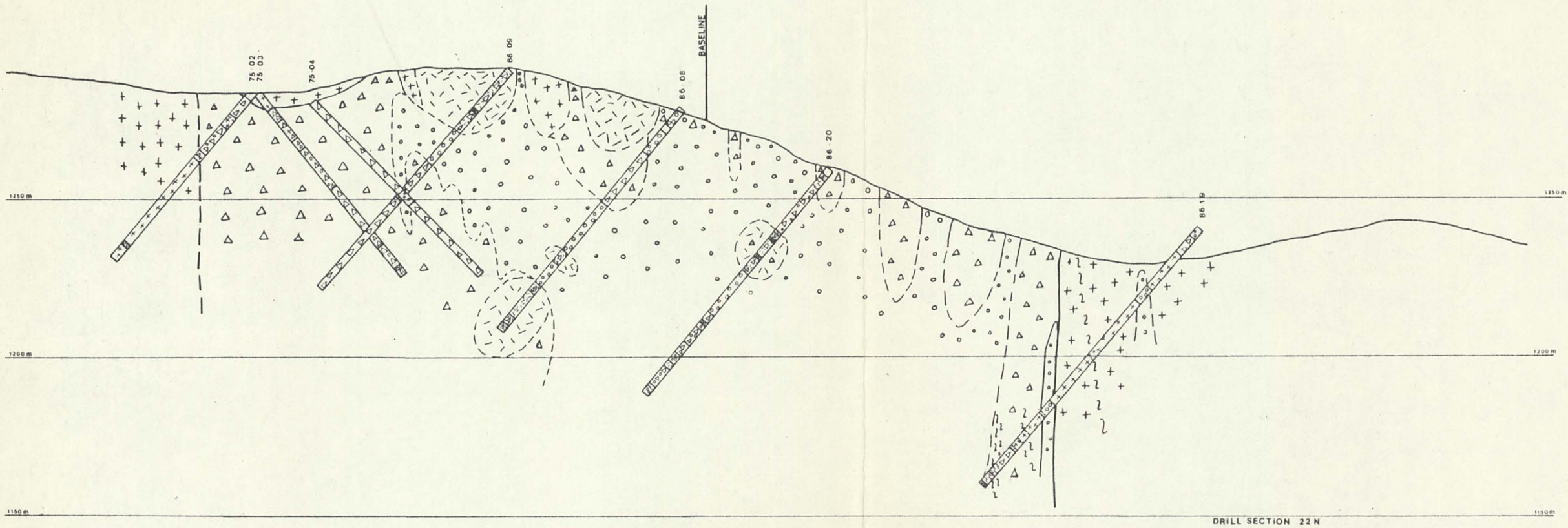
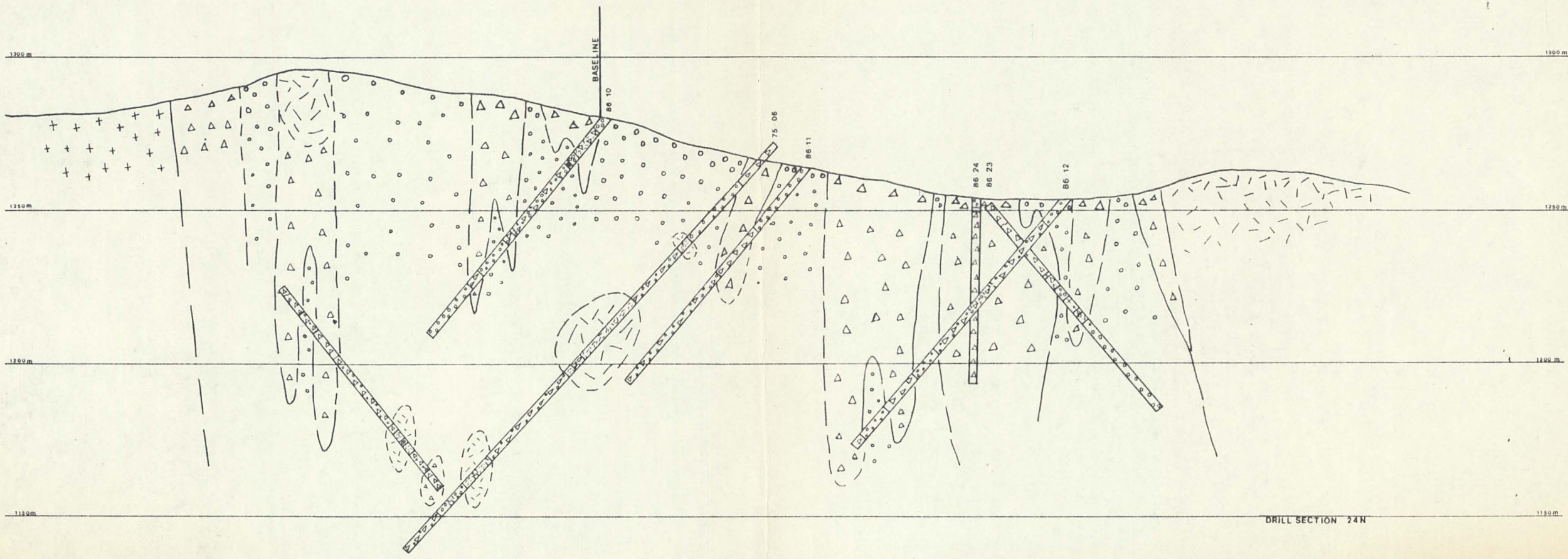
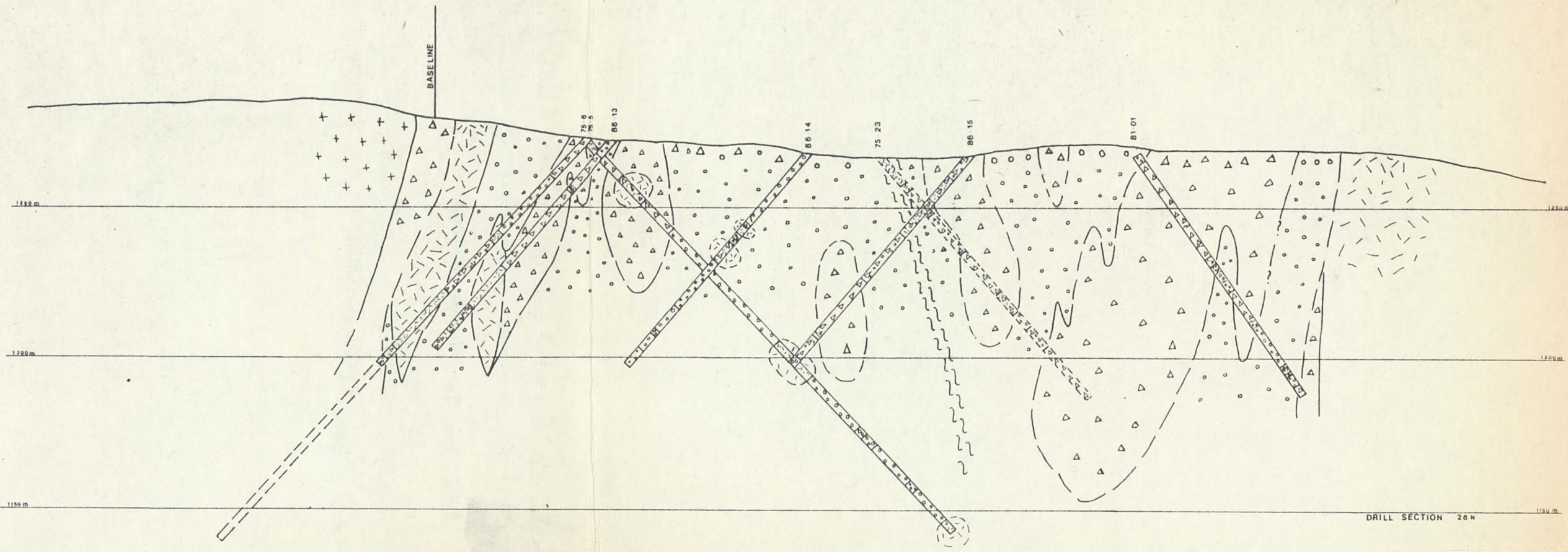
HALITE=17

## FLUID INCLUSION ANALYSIS - FREEGOLD SAMPLES

SAMPLE ID.		Tm	Th	WT. % NaC	MINERAL
EHA-A-1	S	-3.4	193.7	5.547356	BARITE
EHA-A-2	S	-0.7		1.218118	BARITE
EHA-A-3	S	-2.5		4.167296	BARITE
EHA-A-4	P	<del>0</del>		0	BARITE
EHA-A-5	S	-0.2		0.352224	BARITE
EHA-A-6	P	-0.2		0.352224	BARITE
EHA-A-7	S	-0.2		0.352224	BARITE
EHA-A-8	S	-1.2		2.063375	BARITE
EHA-A-9	S	-0.5		0.874259	BARITE
EHA-A-10		***	204	0	BARITE
EHA-A-11	F	-0.3	>250	0.527073	BARITE
EHA-A-12	S	-1.6	185	2.724986	BARITE
EHA-A-13	F	-0.2		0.352224	BARITE
EHA-A-14	F	-0.1	170.6	0.176534	BARITE
EHA-A-15	F	0	171	0	BARITE
EHA-A-16	S	0	137	0	BARITE
EHA-A-17	F	0	197	0	BARITE
EHA-A-18	S	-2.1	192	3.534092	BARITE
EHA-A-19	F	***	162	0	BARITE
EHA-A-20	F	0		0	BARITE
EHA-A-21	F	0	201.2	0	BARITE
EHA-A-22	F	0	166.9	0	BARITE
EHA-A-23	S	FRACTURED		0	BARITE
EHA-A-24	F	0	FRACTURED	0	BARITE
EHA-A-25	F	-0.5	FRACTURED	0.874259	BARITE
EHA-A-26	S	-1.9		3.212815	BARITE
EHA-A-27	S		219.7	0	BARITE
EHA-A-28	S		252.5	0	BARITE

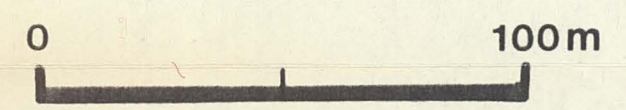
## FLUID INCLUSION ANALYSIS - FREEGOLD SAMPLES

SAMPLE ID.	T <sub>m</sub>	Th	WT. % NaCl	
F27-1	***	195	11	194.9
F27-2	-0.5	216	28	199.9
F27-3	-0.3	202.1	0.527073	204.9
F27-4	-0.4	217.3	0.701084	209.9
F27-5	0	224.2	0	214.9
F27-6	-0.5	221.1	0.874259	219.9
F27-7	***	233	ERR	224.9
F27-8	***	216.2	ERR	229.9
F27-9	-0.1	220	0.176534	234.9
F27-10	-0.2	***	0.352224	239.9
F27-11	-0.9	***	1.558675	244.9
F27-12	-0.1	241.5	0.176534	249.9
F27-13	0	***	0	
F27-14	-2.1	233.6	3.534092	
F27-15	-1	***	1.727723	
F27-16	-0.6	***	1.046603	
F27-17	***	216.2	ERR	
F27-18	***	220	ERR	
F27-19	***	207.2	ERR	
F27-20	***	217.5	ERR	
F27-21	***	229.1	ERR	
F27-22	***	237.7	ERR	
F27-23	-0.3	238.6	0.527073	
F27-24	-0.1	223.7	0.176534	
F27-25	-0.5		0.874259	
F27-26	-3	234	4.941534	
F27-27	-0.1		0.176534	
F27-28	-0.3		0.527073	
F27-29	0		0	
F27-30	-0.7		1.218118	
F27-31	***	216	ERR	
F27-32	***	222.4	ERR	
F27-33	***	226	ERR	
F27-34	***	221.1	ERR	
F27-35	***	237	ERR	
F27-36	***	237	ERR	
F27-37	***	244.1	ERR	
F27-38	***	235.8	ERR	
				0

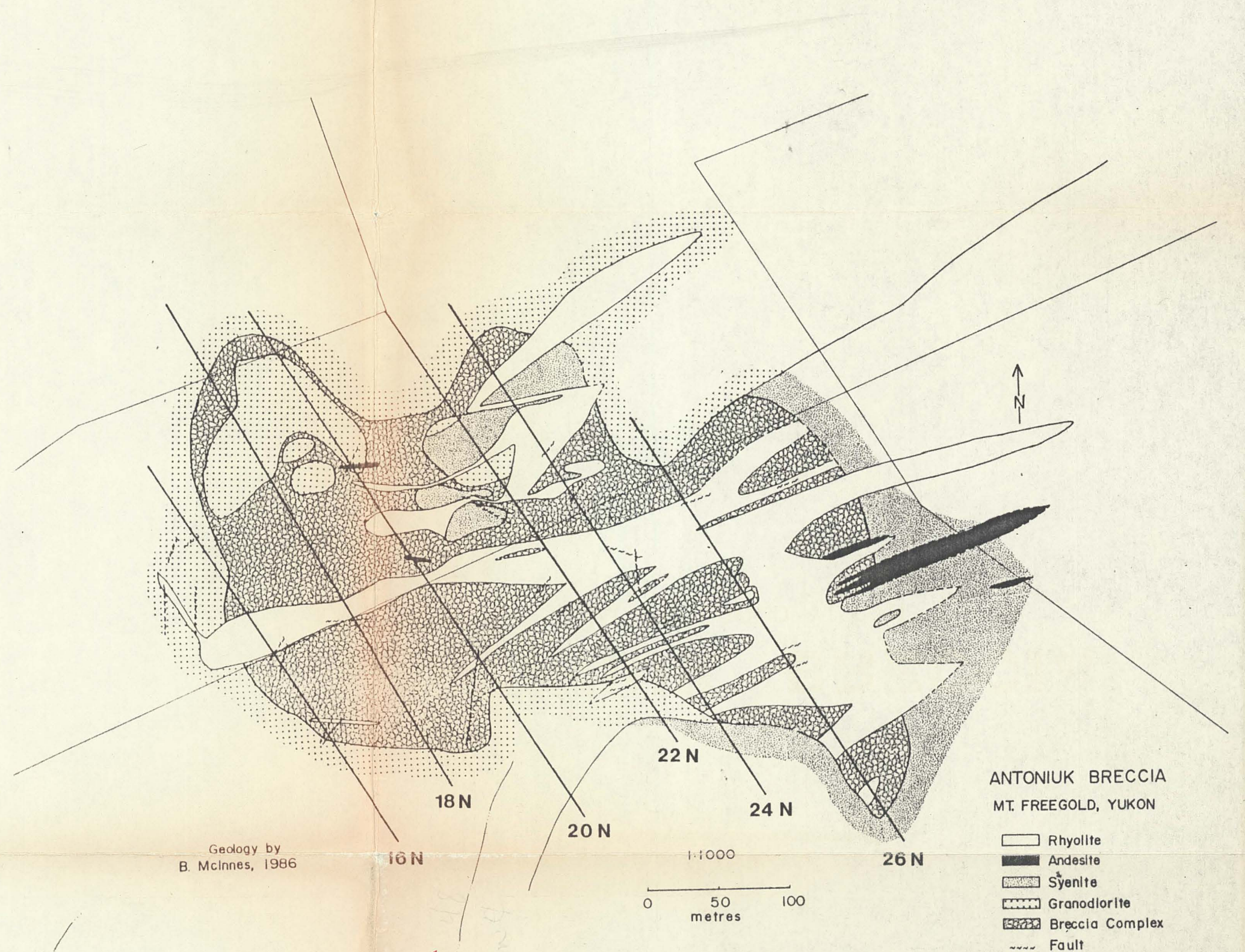


LEGEND

- RHYOLITE
- ANDESITE
- SYENITE
- GRANODIORITE
- BRECCIA COMPLEX
- FAULT



**ANTONIUK BRECCIA**  
MT. FREEGOLD, YUKON



Map 2 and Figure 19. Plan and cross-sections of the Antoniuik Breccia deposit.

with  
made  
GE  
390  
m36  
c-2

